A Study of Three Dimensional Effects in Induced Current Impedance Imaging

Timothy James Healey BEng.

A thesis presented for the degree of Doctor of Philosophy, Department of Electronic and Electrical Engineering University of Sheffield.

February 1995

IMAGING SERVICES NORTH
Boston Spa, Wetherby
West Yorkshire, LS23 7BQ
www.bl.uk

VOLUME CONTAINS CLEAR OVERLAYS

OVERLAYS HAVE BEEN SCANNED SEPERATELY AND THEN AGAIN OVER THE RELEVANT PAGE

A Study of Three Dimensional Effects in Induced Current Impedance Imaging

T. J. Healey

Summary

Previous studies of the induced current impedance imaging technique have been unable to reconstruct images of three dimensional (3-D) structures. In this study the cause of the problem is identified and the reconstruction algorithm of Purvis is adapted to facilitate the correct reconstruction of images of a limited class of structures which have the form of a long cylinder. The images produced by the algorithm are improved by a data filter based on that of Barber, Brown and Avis.

By consideration of the underlying field equations which govern 3-D induced current Electrical Impedance Tomography (EIT) systems, the finite element method (FEM) is used for the computation of the potential field for arbitrary conductivity distributions excited by various coil configurations. A phantom system is built to test the results of the FEM and particular attention is paid to the improvement of the instrumentation. A statistical comparison of the results of measurement and simulation is unable to detect any error in the FEM model. The FEM model is consequently used to develop the reconstruction algorithm but physical measurements are also used to test the algorithm in the presence of noise.

The behaviour of the 3-D algorithm is tested for its plane selectivity showing similar characteristics to those of injected current systems developed by other workers. A possible approach which could both reduce the volume to which the system is sensitive and generate extra measurements for the possible reconstruction of multi-layered images is investigated.

Acknowledgements

I would like to express my sincere thank to Professor Ian Freeston and Doctor Richard Tozer for their continual support and guidance throughout my study.

I am greatly indebted to my father for his assistance in proof reading my thesis.

I would also like to acknowledge the great help given to me by the late Nigel C. Cusworth in the form of his extremely skilled machine work used in the construction of the phantom and electrode ring.

I am very grateful to my fellow postgraduate colleagues for their humour and assistance throughout my project.

Finally I acknowledge with thanks the financial support of the Science and Engineering Research Council. Without their support such projects would not be possible.

Table of Contents

Chapter 1	**Introduction**		**1**
	1.1	Background	1
	1.2	Other imaging techniques	2
	1.3	Electrical impedance tomography	4
	1.3.1	APT	6
	1.3.2	ICT	7
	1.4	The 3D problem	7
	1.4.1	Experimental set up	8
	1.5	Outline of the thesis	10
Chapter 2	**The Forward Problem**		**12**
	2.1	The forward problem	12
	2.2	Methods of solving the forward problem	13
	2.2.1	Fundamental equations	13
	2.2.2	Solution using potentials	14
	2.2.3	Order of magnitude of quantities measured from human subjects	15
	2.2.4	Analytical method	16
	2.2.5	Finite difference method	17
	2.2.6	Finite element method	17
	2.2.7	The selection of the method used (FEM)	18
	2.3	Description of the method of finite elements	19
	2.4	Calculation of the induced electric field	23
	2.5	Mesh generation	24
	2.5.1	Problems with the mesh generation	26
	2.5.2	Dimensional scaling	30
	2.6	Results obtained from the FEM	32
	2.7	Summary	32
Chapter 3	**Design and Construction of a Laboratory Phantom and Instrumentation**		**35**
	3.1	Introduction	35
	3.2	Design of the phantom	35
	3.3	Electrical specifications	38
	3.3.1	Outline of the final system designed	42
	3.3.2	Buffers	43
	3.3.3	Multiplexers	45
	3.3.4	Subtractor	46
	3.3.4.1	Instrumentation amplifiers	47
	3.3.4.2	The long tailed pair	47

3.3.4.3 Results obtained from the subtractor 52
3.4 Procedure for removing magnetically induced 50 kHz noise 60
3.5 Conclusions 61

Chapter 4 Validation of the Finite Element Method 63

4.1 Introduction 63
4.2 Comparison between the current patterns obtained from the 2-D analytic solution and those of the FEM 64
4.3 Comparison of voltage profiles obtained from measurements and FEM simulations 68
4.3.1 Statistical procedures for the comparison of results obtained experimentally and from the FEM 71
4.3.2 Description of the measurement process and the measurement of the system's noise 74
4.3.3 Results 76
4.3.4 Consideration of the value of *b* - the gradient of the graph 98
4.4 Comparison of the results obtained from the 2-D analytic solution and those from the measuring system 99
4.5 Comparison of images reconstructed from data both measured from the phantom and generated by the FEM 104
4.6 Comparison of results obtained by FEM and measurements for axially displaced targets 108
4.7 Conclusions 109

Chapter 5 The three dimensional problem 111

5.1 Introduction 111
5.2 Analysis of the 3-D geometry by the method of finite elements 112
5.3 Dependence of the current patterns on the axial dimension 116
5.4 3-D magnetically induced current imaging 118
5.4.1 General 3-D reconstruction algorithms 119
5.4.2 Application specific algorithms 120
5.5 Generation of a 3-D reconstruction algorithm 120
5.5.1 Limits to the use of the 3-D algorithm 123
5.5.2 Calculation of a 3-D reconstruction algorithm 124
5.6 Other possible reconstruction techniques 128
5.7 Conclusion 128

Chapter 6 Image Filtering **130**

6.1 Introduction 130
6.2 The principle of the filter 130
6.3 Calculation of the filter 132
6.3.1 Singular value decomposition 133
6.4 The inversion of (FB) 134
6.5 Testing the robustness of the filtering technique for different systems 143
6.6 Conclusions 147

Chapter 7 Quantifying the effect of structures out of the plane of interest **148**

7.1 Introduction 148
7.2 The effect of out of plane structures 150
7.3 Sensitivity of the injected current technique to objects out of the measurement plane 154
7.4 Quantifying the effect of out of plane structures 154
7.5 Methods to improve the axial resolution for the system 163
7.5.1 Axially displaced coils 165
7.5.2 Techniques used to improve to the layer selectivity of the injected current system 170
7.5.3 Direct sensitivity method to reconstruct 3-D images 170
7.5.4 Modified reconstruction algorithm to generate multi layered images 171
7.6 Conclusions 172

Chapter 8 Conclusions **173**

8.1 Summary 173
8.2 Future work 174

List of references **176**

Appendix 1 **180**

A1 The effect of channel mismatch on cmrr 180

Appendix 2 **183**

A2 Images reconstruction 183

Chapter 1 Introduction

1.1 Background

This thesis investigates the problems associated with the reconstruction of conductivity maps from measurements made on a structure with a finite third dimension, using an induced current electrical impedance tomography system.

Electrical impedance tomography (EIT) is a technique, developed over the past sixteen years, for generating conductivity maps of a cross section of a body using measurements made on the periphery. The technique involves probing the region with current and detecting the resulting peripheral potential distribution which results. Any disturbance in the potential distribution from that expected for a homogeneous body provides information that can be used to reconstruct a conductivity map. The technique is being applied in medicine and in industry.

In 1978 Henderson and Webster[1] investigated the impedance distribution of the human thorax using a planar array of current sourcing electrodes. A significant development of this method was made in 1982 by Brown and Barber[2] who successfully imaged an arm by using a procedure known as applied potential tomography (APT). APT systems investigate the impedance distribution within the body by applying currents which pass through the surface of the body into its interior. They are presently the most successful of the impedance imaging techniques and are being considered for commercial production [3]. EIT is attractive as a medical imaging technique for a number of reasons:-

- it provides good soft tissue contrast
- there is high temporal resolution
- the system is comparatively cheap to implement
- there are no known hazards to the patient or the operator.

Currently impedance imaging is undergoing evaluation for a broad range of clinical applications and a few examples are given below:-

- lung ventilation and perfusion [4]
- gastric emptying and monitoring [5]
- brain action-potential activity [6]
- tissue temperature monitoring [7]
- quantitative assessment of pulmonary edema [8]

This list is not complete but it does indicate that there is wide interest in the technique and a wide range of potential applications.

A different method of generating the current within the structure of interest was developed by Purvis *et al* [9] who used time varying magnetic fields to induce currents in the region to be investigated. It is this induced current system which is to be studied in this thesis. Section 1.3.2 discusses in more detail the advantages and disadvantages of this system.

1.2 Other imaging techniques

In many fields of science the ability to investigate the internal structure of a body non-invasively has been found to be extremely useful. There have been many techniques developed for this purpose and the merits of some of these are described in this section.

The first imaging technique used for investigating the internal structure of a body was the planar X-ray, discovered by Röntgen in 1895 and published in 1896 [10]. The body to be interrogated was placed between a point source of X-rays and a photographic plate which recorded the attenuation of the X-rays in the form of a shadow-graph. X-rays are still the most widely used medical imaging technique. They are very good for imaging hard tissue such as bone, and are therefore suitable for investigating bone fractures, but they can also differentiate some soft tissues with much reduced sensitivity.

A major disadvantage of planar X-rays is that the whole 3-D structure is projected on to a single 2-D photographic plate which makes it very difficult to interpret. A further development of the use of X-rays for medical imaging is X-ray computed tomography (CT) which both improves the soft tissue contrast and reduces clutter from regions which are not of direct interest. It uses a fan of X-rays which passes through the structure to be imaged with sensors to detect the absorption. This process is repeated for many positions of the X-ray source. From the measurements made a computer, using a method known as backprojection, is able to reconstruct a map of X-ray absorption within a cross section of the structure. CT images only contain information about a single plane and if measurements are taken for multiple layers, a 3-D model of the structure can be made, aiding image interpretation.

A serious disadvantage of X-rays is that, along with all ionising radiation, they can damage DNA in living tissue. This damage to the DNA can have severe consequences. Usually the tissue will die but sometimes it will mutate and can cause cancerous growths. X-ray dosages must always be kept to a minimum and there must always be a cost benefit analysis as to whether the harmful effects of the X-rays are outweighed by the possible benefits of an accurate diagnosis. These disadvantages in the use of X-rays have encouraged the development of other techniques which improve imaging systems with respect to increased tissue definition or enhanced safety.

Ultrasound is a technique based on echo location. The images produced are constructed from the magnitude of the sonic echoes received after interrogating the region with ultrasound. The echoes mainly emanate from boundaries between different types of tissue. The technique is therefore sensitive to the edges of tissues. The images reproduced tend to be difficult to interpret and the operation of the equipment is very awkward because the operator has to optimise the position of the probe to produce acceptable images of the desired internal structures. Ultrasound has the great advantage of safety in that there is no substantiated evidence that ultrasound has any harmful effects on tissues at the power levels used [11].

Magnetic resonance imaging (MRI) is a technique capable of imaging the concentration of particular isotopes of chemical elements in 3-D. The nuclei of these isotopes have specific electromagnetic properties and the MRI technique exploits these properties. The isotope most frequently traced in medical applications is hydrogen (^{1}H) which is present in all body tissue. Because the hydrogen may be at different concentrations or its atoms may be in different electronic environments, different tissues respond differently and very good soft tissue contrast can be achieved. There are no known hazards with the technique and its main drawbacks are cost and poor temporal resolution.

Nuclear medical techniques have been used to provide images which are based on the way in which systems function in the body rather than on the anatomy of the body. They are based on the introduction into the body of chemical substances which are labelled with a radioactive component which emits gamma radiation. The physiological function of tissues is investigated by the way in which the labelled material becomes distributed. The dangers of this technique are similar to those of X-rays.

Electrical impedance tomography in comparison is safe, cheap and capable of real-time imaging, but has poor spatial resolution.

1.3 Electrical impedance tomography

Electrical impedance tomography produces maps of the electrical impedance of the region being imaged. For the technique to be applied the region must contain areas of different electrical conductivity. The spread of conductivities of different biological tissues extends over two orders of magnitude as can be seen from the values in table 1.3.1. Thus an imaging technique based on impedance could in principle be able to discriminate between different types of tissue. There are several possible methods that could be used to measure the impedance of body tissue and these can be divided into

two main groups. The first called APT involves injecting current through the surface of the body and taking potential difference measurements from the surface. The other, called induced current tomography (ICT), involves the use of time varying magnetic fields to induce current in the body and takes potential difference measurements at the surface.

Tissue	Conductivity Sm^{-1}	Notes
Cerebro-spinal fluid	1.5	-
Blood	0.67	-
Liver	0.29	-
Skeletal muscle	0.80 0.056	measured longitudinally measured transversely
Neural tissue	0.35 0.15	grey matter white matter
Lung	0.14 0.042	measured during expiration measured during inspiration
Fat	0.049	-
Bone	0.0060	-

Table 1.3.1 Conductivity values of some biological tissues [12]

Electrical current in most biological tissues has two main components; the first is the movement of ions and the other the displacement of bound charges. At high frequency the charge displacement current becomes increasingly significant whereas at low frequency the ionic movement dominates. The bound charge displacement current arises from many factors including cell membranes and the dielectric properties of the whole tissue, and this leads to a frequency dependent behaviour of the electrical properties of the tissue. This frequency dependence property is now being widely exploited in EIT systems because it is a possible means of characterising the tissue [13].

Reconstructed images can be classified into two categories as either static or dynamic images. The static image is a map based on the absolute impedance of a structure, whereas the dynamic imaging process requires a change in the impedance distribution between two sets of measurements. The first set of measurements is known as the background set and the second set is the foreground set. Using the method of APT some workers [14] are now using different frequencies for the background and foreground measurement sets and from these it is possible, using some *a priori* information about the frequency behaviour of tissue, to reconstruct static images. Scaife[15] has shown that it is possible using the ICT system to reconstruct static images of the permittivity distribution of a body.

1.3.1 APT

A system that was capable of generating tomographic conductivity maps *in vivo* was first demonstrated by Barber *et al* [16]. Current was injected through electrodes mounted on the surface of an arm and potentials were measured between electrode pairs. From potential measurements made using various drive configurations it was possible to reconstruct a tomographic map of the change in conductivity between two successive sets of measurements. The method used to reconstruct the map of potentials was similar to that used in the field of X-ray CT and is known as backprojection. In CT the X-rays travel through the body in straight line paths and the absorption of the X-ray beam is measured for many different paths. A reconstructed map of the X-ray attenuation is computed by the method of backprojection which involves summing for the attenuation of the X-ray paths which pass through the individual pixels forming the image. A similar technique has been used for the reconstruction of APT images where values of measured potential differences are backprojected along the curved isopotential lines as opposed to straight line paths of the X-ray in the technique of CT.

1.3.2 ICT

The magnetically induced current system is functionally similar to the injected current system in that the system still maps the variation in conductivity. The difference lies in the way in which current is introduced into the region to be investigated. As with the injected current system the peripheral potential distribution is measured but the currents are induced internally rather than being injected through the surface of the body. This system has several possible advantages:-

- The electrodes are required only for sensing potential and not for current injection. This allows the electrodes to be optimised for potential sensing.
- The number of independent measurements can be increased without using more electrodes simply by increasing the number of distinct exciting magnetic field configurations.
- It may be possible to gain information in regions separated from the electrodes by exciting these particular regions.
- A completely non-contact impedance imaging system can be constructed.

Using the method of ICT, Purvis[9] was able to show that conductivity images could be produced from 2-D models *in vitro*. Scaife *et al* [15] further developed the method and demonstrated the reconstruction of both permittivity and conductivity images *in vitro*.

1.4 The 3-D problem

The 3-D problem in ICT systems was first investigated by Purvis[17] when the induced current system was connected to a phantom which was in the form of a cylindrical tank that had a length which was significant in comparison with the diameter, and could not be considered as even approximately 2-D. For tanks other than those which could be considered 2-D the system of Purvis failed to reconstruct images correctly. In some cases the areas in which the conductivity had decreased were erroneously reconstructed as areas of increased conductivity. This was quite different from the injected current system which was able to reconstruct images from measurements taken from both 3-D

and 2-D phantoms without any alteration to the reconstruction algorithm. Structures which are to be imaged are almost always three dimensional and certainly in the human body there are no parts sufficiently thin for a 2-D reconstruction algorithm to function correctly with ICT. The work described in this thesis is an investigation of methods to produce images for a 3-D ICT system.

1.4.1 Experimental set up

The design of the experimental system in this work is described in detail in chapter 3. The system uses a cylindrical phantom, with a nominal diameter of 100 mm, whose depth can be adjusted and filled with saline to any desired height. A sketch of the functional components is shown in figure 1.4.1. The system has 16 electrodes mounted in a single ring round the circumference of the cylinder. Currents are induced in the phantom by a set of three coils in the plane of the electrodes and this plane is used as the datum from which both heights and depths are measured. The arrangement of these coils are shown in figure 1.4.1.

The peripheral measurements made on the system are of the voltage at the periphery and are quoted in the units of measurement which are volts. These peripheral voltage measurements are a function of the excitation current and so are a measure of transfer impedance with units Ω. Some measurements, such as noise in the system, are not dependent on the exciting current and for this reason it is more convenient to quote peripheral measurements in the units measured, which are volts.

Numerical calculations were performed by creating a finite element model of the physical system to aid analysis of the system's behaviour.

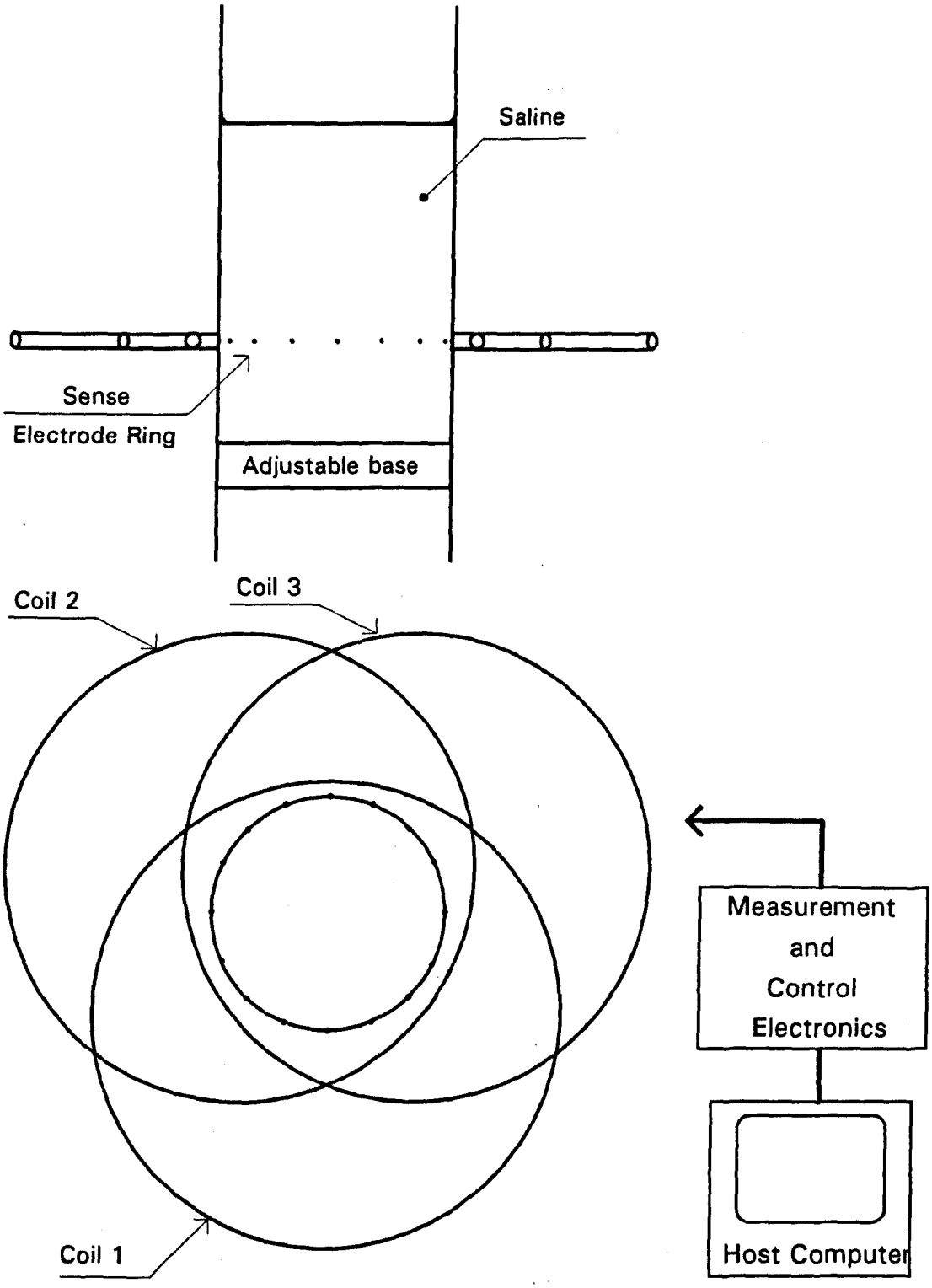

Figure 1.4.1 Plan and front elevation of the imaging system. *The system uses 3 drive coils and 16 equi-spaced potential sense electrodes. Measurements are taken under control of the host computer.*

1.5 Outline of the thesis

In chapter 2 a technique for modelling the behaviour of the system mathematically is developed. From this model it is possible to calculate:-

- the path of the currents in three dimensions for a 3-D phantom,
- the potential distribution throughout the phantom,
- the peripheral voltages that would be detected by electrodes placed on the surface.

In chapter 3 the design and construction of the instrumentation system is described and discussed. The overall structure of the measuring system was similar to that used by previous workers but many of the components of the system were developed and improved; in particular, the phantom, the multiplexers and the subtractor. Relationships are derived between the mismatch in the bandwidth of channels and the common mode rejection ratio.

In chapter 4 an experiment is described which was used to compare the results obtained by measurement with those found using the computational model. The measurements for the physical system are inevitably contaminated by experimental error and noise which necessitates the use of statistical methods to quantitatively test the agreement between the two systems.

In chapter 5 the origin of the problems experienced when working with 3-D subjects is explored, and it is shown that the backprojection algorithm calculated for the 2-D situation does not work for measurements taken from a 3-D body. A backprojection algorithm that is capable of correctly reconstructing images from 3-D systems is developed. Limitations to the types of physical bodies for which the new algorithm is successful are also discussed.

In chapter 6 image filtering of a type used by Barber *et. al.* [18] is developed. This filter is capable of improving the quality of the reconstructed images but in some

situations it can actually reduce the quality of the images reproduced. Examples of this are given.

In chapter 7 the corruption of images caused by structures out of the plane of measurement is investigated and this effect is compared with results from the injected current system. Methods which are not available using the injected current system, such as axially displacing the coils, are investigated and suggestions are made to show how they might be used to improve the plane selectivity of the system.

Conclusions are drawn in chapter 8.

Chapter 2 The Forward Problem

2.1 The forward problem

The forward problem in impedance tomography is that of determining the distribution of potentials and the currents within the body to be investigated in response to the time varying magnetic field. The ultimate aim of the EIT process is to find a method that can generate a map describing the impedance distribution within the body from measurements taken on the periphery. This is known as the reverse problem which, because the maps are usually presented in a visual form, is also known as imaging. The solution to the forward problem is the first step towards the solution of the reverse problem, and as discussed in chapter 1, the solution of the reverse problem requires knowledge of the current paths.

In the case of magnetically induced impedance tomography, the system is excited with a magnetic field generated by external current carrying coils. The investigation of effects associated with imaging 3-D objects requires detailed knowledge of the nature of the current paths and of the potential distribution within the 3-D structure. Purvis[17] developed methods to solve both the forward and reverse problems, but they were limited to the conductivity distribution within a bounded 2-D region and were not necessarily the most efficient or accurate. For most realistic situations a more general solution of the 3-D forward problem is needed and for this Purvis's method proved unsuitable. There are several methods that could be employed to find the field distribution within the body and three such methods are discussed in this chapter:-

- analytical {section (2.2.4)}
- finite difference {section (2.2.5)}
- finite elements {section (2.2.6)}

The method of finite elements was chosen for reasons to be discussed. The method used to calculate the electric field induced by the excitation coils is also described.

2.2 Methods of solving the forward problem

Some of the possible methods for solving the forward problem are now discussed. These all involve finding the solution to Maxwell's equations that fully describes the behaviour of the currents and potentials within the body being investigated.

2.2.1 Fundamental equations

Maxwell's equations are :-

$$\nabla . \mathbf{E} = \frac{\rho}{\varepsilon} \qquad 2.2.1$$

$$\nabla . \mathbf{B} = 0 \qquad 2.2.2$$

$$\nabla \times \mathbf{E} = -\frac{\partial \mathbf{B}}{\partial t} \qquad 2.2.3$$

$$\nabla \times \mathbf{B} = \mu \mathbf{J} + \mu\sigma \mathbf{E} + \mu\varepsilon \frac{\partial \mathbf{E}}{\partial t} \qquad 2.2.4$$

where

- ρ : electric charge density
- μ : permeability
- σ : conductivity
- ε : permittivity
- $\mathbf{B}$: magnetic flux density
- $\mathbf{E}$: electric field
- $\mathbf{J}$: electric current density

These are equations for **E** and **B** fields in the region of interest. ρ and **J** are the charge and source current densities respectively and for a uniform region are zero within the medium because there are no sources within the region. The conduction current is

$$\mathbf{J}_c = \sigma \mathbf{E} \qquad 2.2.5$$

and the displacement current is

$$\mathbf{J}_d = \varepsilon \frac{d\mathbf{E}}{dt} \qquad 2.2.6$$

The charge density ρ arises in the region of interest at boundaries between materials of different electrical properties in order to ensure current continuity. Away from these boundaries $\rho = 0$.

2.2.2 Solution using potentials

We can solve equation (2.2.1) - (2.2.4) using magnetic vector potential **A** and electric potential Φ. From (2.2.2)

$$\mathbf{B} = \nabla \times \mathbf{A} \qquad 2.2.7$$

and therefore from (2.2.3)

$$\mathbf{E} = -\frac{\partial \mathbf{A}}{\partial t} - \nabla \Phi \qquad 2.2.8$$

Putting (2.2.8) into (2.2.1) with ρ= 0, gives

$$-\frac{\partial}{\partial t}(\nabla \cdot \mathbf{A}) - \nabla^2 \Phi = 0 \qquad 2.2.9$$

and putting (2.2.7) and (2.2.8) into (2.2.4) with **J** = 0 gives

$$\nabla \times \nabla \times \mathbf{A} = \mu\sigma\left(-\frac{\partial \mathbf{A}}{\partial t} - \nabla \cdot \Phi\right) + \mu\varepsilon\left(\frac{\partial^2 \mathbf{A}}{\partial t^2} - \frac{\partial}{\partial t}(\nabla \Phi)\right) \qquad 2.2.10$$

or

$$\nabla(\nabla \cdot \mathbf{A}) - \nabla^2 \mathbf{A} = \mu\sigma\left(-\frac{\partial \mathbf{A}}{\partial t}\right) + \mu\varepsilon\left(\frac{\partial^2 \mathbf{A}}{\partial t^2}\right) + \left(-\mu\sigma - \mu\varepsilon\frac{\partial}{\partial t}\right)(\nabla \Phi) \qquad 2.2.11$$

so far $\nabla \cdot \mathbf{A}$ is unspecified, and setting

$$\nabla \cdot \mathbf{A} = \mu\sigma\Phi + \mu\varepsilon\frac{\partial \Phi}{\partial t} \qquad 2.2.12$$

yields

$$\nabla^2 \mathbf{A} + \mu\sigma\frac{\partial \mathbf{A}}{\partial t} + \mu\varepsilon\frac{\partial^2 \mathbf{A}}{\partial t^2} = 0 \qquad 2.2.13$$

$$\nabla^2 \Phi + \mu\sigma\frac{\partial \Phi}{\partial t} + \mu\varepsilon\frac{\partial^2 \Phi}{\partial t^2} = 0 \qquad 2.2.14$$

To find **E** and **B** in the region of interest we need to solve (2.2.13) and (2.2.14) for **A** and Φ subject to appropriate boundary conditions. It can also be shown that **E** and **B** satisfy equations similar in form to (2.2.13) and (2.2.14).

2.2.3 Order of magnitude of quantities measured from human subjects

Equations (2.2.7), (2.2.8), (2.2.13) and (2.2.14) are part of an exact solution to the problem *i.e.* the field must satisfy these equations in the region of interest. However not all the terms in (2.2.13) and (2.2.14) are equally important. For a 2-D region they can be written

$$\frac{\partial^2 \mathbf{A}}{\partial x^2} + \frac{\partial^2 \mathbf{A}}{\partial y^2} + \mu\sigma\frac{\partial \mathbf{A}}{\partial t} + \mu\varepsilon\frac{\partial^2 \mathbf{A}}{\partial t^2} = 0 \qquad 2.2.15$$

$$\frac{\partial^2 \Phi}{\partial x^2} + \frac{\partial^2 \Phi}{\partial y^2} + \mu\sigma\frac{\partial \Phi}{\partial t} + \mu\varepsilon\frac{\partial^2 \Phi}{\partial t^2} = 0 \qquad 2.2.16$$

The relative magnitudes of these terms are:-

L^{-2}, L^{-2}, $\omega\mu_0\sigma$, $\omega^2\mu_0\varepsilon$

where L is a length characteristic of the region being investigated

which correspond to the relative values of

10^2, 10^2, $8\cdot10^{-2}$, $9\cdot10^{-5}$

If typical values for a human subject at the frequency of operation of 50 kHz are taken as $\mu=\mu_0$, $L = 10^{-2}$ m, $\sigma = 0.2$ Sm^{-1} $\varepsilon = 80\varepsilon_0$

Hence in equations (2.2.13) and (2.2.14), it is the geometric terms and not the time dependent terms that are important, and for this problem they reduce to

$$\nabla^2 \mathbf{A} = 0 \qquad 2.2.17$$

$$\nabla^2 \Phi = 0 \qquad 2.2.18$$

Physically, this simplification arises because the magnetic field produced by the conduction current and the displacement current in the medium are much smaller than that due to the driving coils, and hence any effects that arise from fields due to conduction current induced in the region can be neglected.

Unfortunately there is no general solution to these partial differential equations for arbitrary geometries. **A** can be found directly as will be shown in section 2.4, but to determine Φ it is necessary to solve 2.2.18, subject to the boundary condition at the edge of the region of interest. For certain limited sets of conditions, direct solutions may be found but in most cases, formulating a solution requires the use of a numerical method. Various possible methods for solutions to the problem are discussed below.

2.2.4 Analytical method

Direct analytical methods involve the direct mathematical solution of the equations describing the system. There is no general solution of these equations although solutions can be found for a limited set of conditions, and Pidcock *et. al.* [19][20] have collected information about such solutions for the injected current EIT system. The computational efficiency of analytical methods is very good and once the analytic solution has been found, the numerical solution follows with little computational effort. The methods are usually applied to conductivity distributions which can be described by simple mathematical models such as a single circular target placed inside a circular phantom. The analytic solution to such a construct has been found [21] for the 2-D

induced current system. The method involves finding the solution to a circular target placed at the centre of the tank and then using a conformal transformation to find the solution when the target is moved to any desired position within the phantom. Usually conformal transformations can only be applied to two dimensional systems, making this method useless for finding the solution to a 3-D situation, and no equivalent analytic solution for 3-D geometries appears to be available. If there were one, it would be unlikely to be of sufficient generality for the solution of most of the problems encountered. This method for the solution of the forward problem was therefore abandoned although the computational intensity for the solution of 3-D structures by other methods would make an analytic approach very attractive.

2.2.5 Finite difference method

The finite difference method (FDM) involves breaking the problem up into a mesh of similar geometric shapes. The solution to the forward problem is achieved by replacing the derivatives of the describing Laplacian equation with simple algebraic approximations at discrete points. This yields a set of simultaneous equations which can be solved either directly or iteratively. FDM is simple to apply due to the mathematical simplicity of generating the required equations. These equations can also be formed by considering the physical principles of the problem. The solution to the equation is usually found by iteration and can be time-consuming.

2.2.6 Finite element method

The finite element method (FEM) is a well documented technique for the solution of field problems in both 2-D and 3-D structures [22]. The method can be computationally quite efficient and can be applied to general geometries; that is to say it can be used to find the electric fields induced within an arbitrary conductivity distribution by an external magnetic field. FEM involves dividing the system into small but finite elements of known shape. The division is arbitrary and any pattern of elements can be used. This flexibility is very useful because it allows a greater number

of elements to be placed where greater detail is required in the solution. Unlike FDM the potential at any point is represented as the linear interpolation of the potentials at the nodes. Because it is so flexible, FEM is also more complex than other methods. The fact that the elements can in effect be placed randomly means that the description of the elements and of the node positions have both to be generated and stored, and the generation of the mesh can be almost as complex as the problem to be solved. The formation of the solution using FEM is more complex than that of FDM and is discussed in section 2.3.

2.2.7 The selection of the method used (FEM)

As described in section 2.2.4, no analytical method has been found for the solution of the 3-D geometries. A further difficulty is that most analytical solutions can only be applied to very limited sets of problems, usually with only one object placed in the system. These two problems rule out the use of an analytical method.

The FDM is quite simple to implement but 3-D problems tend to have very large numbers of nodes which would make the finding of the solution very laborious. Purvis[17] used a polar mesh for the 2-D system since such a geometry made it possible to choose a mesh in which the nodes lay exactly on the electrodes. This would not have been possible with a Cartesian mesh because a mesh of square elements could not have provided nodes at sixteen equally spaced points on a circle. The disadvantage of the polar mesh is that the greatest node density is at the centre where the resolution is known to be poorest. Some of the simulations by Scaife[23] using FDM were solved only after 24 hr of computation on an HP 9000 work station, and for some simulations with a large number of nodes it could take up to two weeks. This computation was required for only one layer but the 3-D problem would have several layers and this would multiply the time to an unacceptable length. Although great savings could have been made by writing the code more efficiently, and for a 3-D geometry it may have been possible to improve the initial starting point so reducing the number of required

iterations, it would always have taken a lot longer than the few minutes that the FEM required.

The only other method considered which was capable of producing results in an acceptable time was the FEM. Finite element programmes designed to solve various problems are commercially available but since a finite element package written by Low[24] for magnetic field problems associated with electrical machines was available in the Department, it was this that was used in the present work. Finite element programmes with their equations buried deep inside the code are usually difficult to adapt for a particular set of describing equations. However, Low was able to adapt his FEM package to suit the needs of this problem. The major drawback of this package was the lack of mesh generation software and post-processing software to display the results but had the advantage that this software could be developed to suit this particular application.

2.3 Description of the method of finite elements

The FEM solver written and adapted by Low[24] was essentially used as a package and treated as a black box in which the required problem is placed at the input and the program generates the solution. Although the FEM solver was written by Low, software was required to set up the data in the appropriate form for the solver and then to process the results from the solver. Section 2.4 describes the calculation of the induced field and 2.5 the setting up of the mesh. For completeness a brief description of the method used by Low is given below.

There is a duality between satisfying Laplace's equation and minimising the total energy within the region. In the FEM the solution to Laplace's equation is found by the minimisation of the total energy within the region studied.

The interaction of the nodal potentials and total energy minimisation leads to a set of linear simultaneous equations of the form:-

$$[\mathbf{K}].[\Phi] = [\mathbf{S}] \qquad 2.3.1$$

$[\Phi]$ is a column matrix which lists the potential at each individual node of the mesh. The solution of the forward problem involves finding the solution to equation 2.3.1 for $[\Phi]$.

The square matrix [K] is defined as:-

$$\mathbf{K}_{ij} = \iiint_{\Omega} 2\sigma\left(\frac{\partial \mathbf{N}_i}{\partial x}\cdot\frac{\partial \mathbf{N}_j}{\partial x}+\frac{\partial \mathbf{N}_i}{\partial y}\cdot\frac{\partial \mathbf{N}_j}{\partial y}+\frac{\partial \mathbf{N}_i}{\partial z}\cdot\frac{\partial \mathbf{N}_j}{\partial z}\right)\cdot d\Omega \qquad 2.3.2$$

where Ω is the volume of the body. The solution to the forward problem involves the inversion of this matrix, and this is computationally the most expensive part of the FEM. The largest system investigated in this work contained approximately 22000 nodes which implies that [K] has 22000 by 22000 coefficients. Fortunately [K] is very sparse and the FEM only needed to store a fraction of the possible $4.84\cdot10^8$ elements of [K].

The column matrix [S] is defined as:-

$$S = \iiint_{\Omega} \sigma[\mathbf{E}_{ind.x}\cdot\frac{\partial \mathbf{N}_i}{\partial x}+\mathbf{E}_{ind.y}\cdot\frac{\partial \mathbf{N}_i}{\partial y}+\mathbf{E}_{ind.z}\cdot\frac{\partial \mathbf{N}_i}{\partial z}]\cdot d\Omega \qquad 2.3.3$$

$\mathbf{E}_{ind}$ is the induced electric field in the region and is calculated as described in section 2.4.

$\mathbf{N}_i$ is the shape function for each of the elements and is defined as an interpolating function of the potential in terms of the nodal potentials $[\Phi_i]$ over each element. The interpolated potential over the element is given by:-

$$\phi_{el}(x,y,z) = [\mathbf{N}_i][\Phi_i] \qquad 2.3.4$$

This interpolation approximates the exact smoothly varying solution with a piecewise planar function over the region of each element.

Equations 2.3.2 and 2.3.3 are derived by the global minimisation of the potential energy which is described by the functional:-

$$F(\phi) = \iiint_{element} \frac{1}{2}[\sigma \cdot \nabla\phi \cdot \mathbf{E}_{ind} - \sigma \cdot (\nabla\phi)^2]d(element) \qquad 2.3.5$$

This involves equating the sum of the differentials of the functional with respect to ϕ to zero. *i.e.*

$$\sum_{i=1}^{N} \frac{\partial F(\phi)}{\partial \phi_i} = 0 \qquad 2.3.6$$

All the results obtained from FEM used software written specifically for this purpose, including the following post-processing software:-

- calculation of the peripheral voltage profile;
- display of the peripheral voltage profile;
- display of the potential distribution on any plane of nodes;
- calculation of the currents at the centre of any element;
- the display of the current at any element.

Figure 2.3.1 shows the sequence of operations in the form of a flow chart required in the solution of the forward problem. There are many stages of processing required to find the potential distribution many of which are common to different problems. Control software was written, which would only run an individual stage of the process if any of the inputs to that stage had changed.

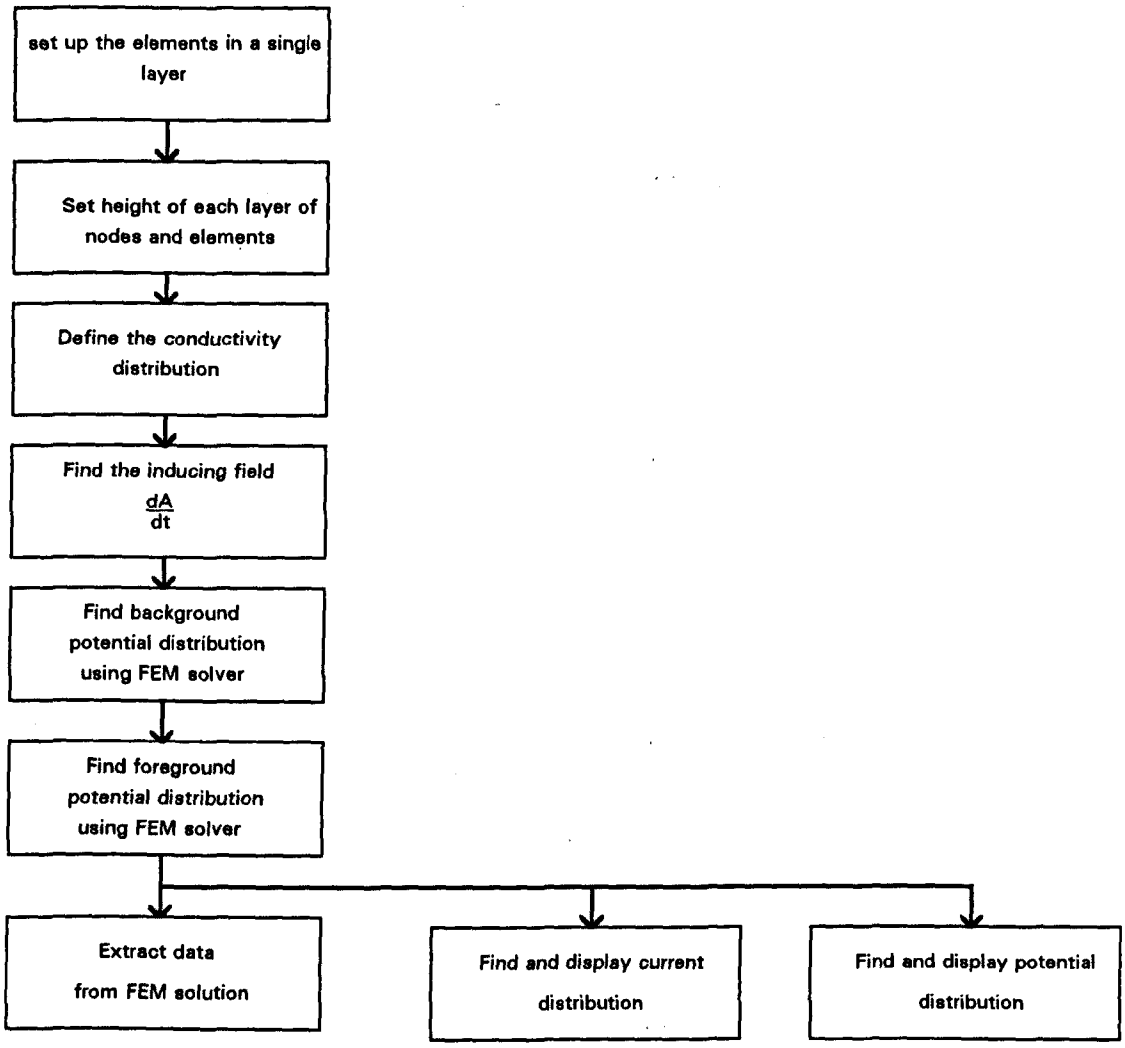

Figure 2.3.1 flow chart showing the sequence of processes required when the FEM solver is used.

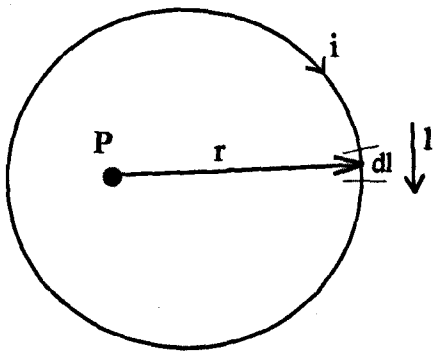

Figure 2.4.1 Arrangement of the coil. *The point P is in the region of interest.*

2.4 Calculation of the induced electric field

The induced electric field can be found from the magnetic vector potential **A**. For an elemental section of the coil of one turn (figure 2.4.1) carrying a current i at an angular frequency of ω radians per second :-

$$d\mathbf{A} = \frac{i\mu}{4\pi r}\mathbf{l}\,dl \qquad 2.4.1$$

where

A : magnetic vector potential

l : unit vector in direction of coil element *dl*

r : distance from the coil element

μ : permeability

i : $\hat{i}e^{j\omega t}$

The total value of **A** at any point is given by integration round the complete coil and this was evaluated by numerical methods. For this application Purvis[17] showed that a solution of sufficient accuracy could be determined by dividing the coil into 100 elements.

We have :-

$$\mathbf{A} = \oint \frac{\mu i(t)}{4\pi r}\mathbf{l}\,dl \qquad 2.4.2$$

The induced electric field is given by the rate of change of the magnetic vector potential.

$$\mathbf{E}_{ind} = -\frac{\partial \mathbf{A}}{\partial t} = -j\omega t\frac{\mu i}{4\pi}\oint\frac{\mathbf{l}}{r}dl \qquad 2.4.3$$

This expression for $\mathbf{E}_{ind}$ is approximated by assuming the circular coil is a centagon and summing over its 100 linear elements.

$$\mathbf{E}_{ind} \approx -j\omega t\frac{i\mu}{4\pi}\sum_{n=1}^{N}\frac{\mathbf{l}_n}{r} \qquad 2.4.4$$

where

$\mathbf{l}_n$: A vector representing the length of a coil element and the direction of the current flowing in the element.

The FEM requires that the induced electric field at the centre of each of the elements is determined. Each mesh element requires that equation (2.4.4) is evaluated 100 times for each coil element and to find $\mathbf{l}_n$ requires the calculation of two sines and cosines. This is a large computational demand. For example, a mesh of 22000 elements would require the calculation of $8.8 \cdot 10^6$ trigonometric functions. Computational efficiency can be greatly increased because the sine and cosine functions which are required to find the direction of each coil element are identical for each mesh element. The trigonometric functions only need to be found once and then stored in a table. The calculation of the magnetic vector potential for each element then simply involves looking up the value of the trigonometric function from this table instead of calculating it on every occasion.

2.5 Mesh generation

Most FEMs use triangular elements for the solution of 2-D problems and tetrahedral elements for 3-D problems. The solution to the 3-D problem requires very large numbers of both elements and nodes but the number of elements can be reduced by using hexahedrons instead of tetrahedrons. This reduces the memory required to solve the problem. The two meshes that were investigated are shown in figures 2.5.1a and b. The circular cross-section was divided into 12 regions, the outer eight having curved outer edges, and these were fitted together to make a circle. The space in the centre was filled by the four quadrilateral regions. Using this arrangement it is possible to produce a mesh which is circular and has elements of a similar size with nodes on the periphery in exactly the same position as the electrodes. This mesh can then be repeated at intervals in the direction perpendicular to its plane, in order to generate a

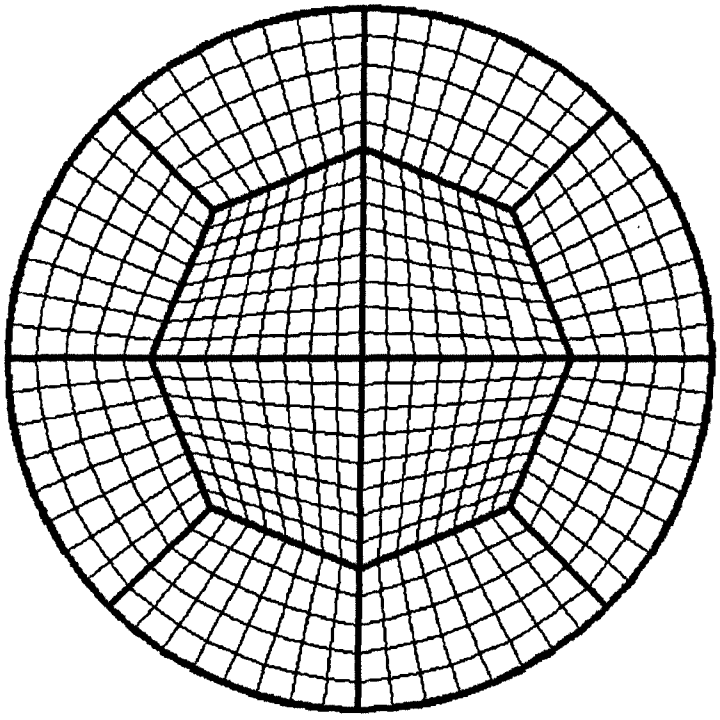

Figure 2.5.1a

Cross section of the first mesh used for finite element analysis. It is made up of 12 quadrilateral regions subdivided into elements.

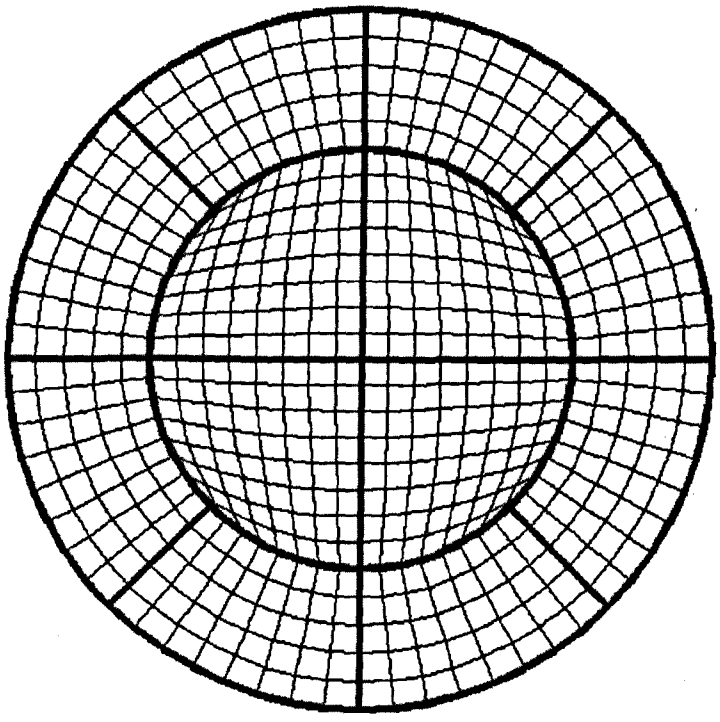

Figure 2.5.1b:- The final mesh which was successfully used for the finite element analysis. In common with the mesh shown above it is constructed using 12 quadrilateral regions but the 4 inner ones now have curved edges. This means that the outer elements are at the same radial displacement.

cylindrical arrangement of hexahedrons. This prismatic structure has the advantage that the amount of space required to store the whole mesh is reduced. Only the position of the nodes and elements in one plane need to be stored. The plane is then swept axially by variable distances in the axial or Z-direction with the only additional storage being the axial displacement. It was calculated that this method of storing the mesh would reduce the number of nodes (N) to be stored to approximately $N^{2/3}$, and as only the x and y position is required for each node, there would be a further reduction of 2/3. In this application the information stored was 609 node positions, 576 element structures and 41 layer heights.

The meshes used for the 3-D solver were generated by adapting 2-D triangular meshes. Software was available for the construction of these triangular meshes. Certain types of meshes constructed of triangular elements can be converted to meshes of quadrilateral elements because both possess nodes that are common. The meshes used up to 41 layers of nodes and the height of each layer was simply defined using a text editor. A graphic editor was written to edit the conductivity distribution within any region of the mesh.

2.5.1 Problems with the mesh generation

The first mesh used an arrangement which was of a similar form to that shown in figure 2.5.1a where the central region was octagonal and only the outer edge was circular. When this mesh was used to find the solution to the homogeneous case, it was found that the peripheral voltage profile was contaminated by noise and this noise had the same spatial frequency as that of the octagon. The problem was overcome by modifying the mesh so that both the centre and outer sections were circular. As shown in figure 2.5.1b. Figures 2.5.2a and 2.5.2b show the potential distribution for a thin phantom with the two different meshes of figure 2.5.1; each pair of images shows both a surface view and a plan view of the contours. These are both excited by a concentric coil and the conductivity distribution is homogeneous. In this configuration the

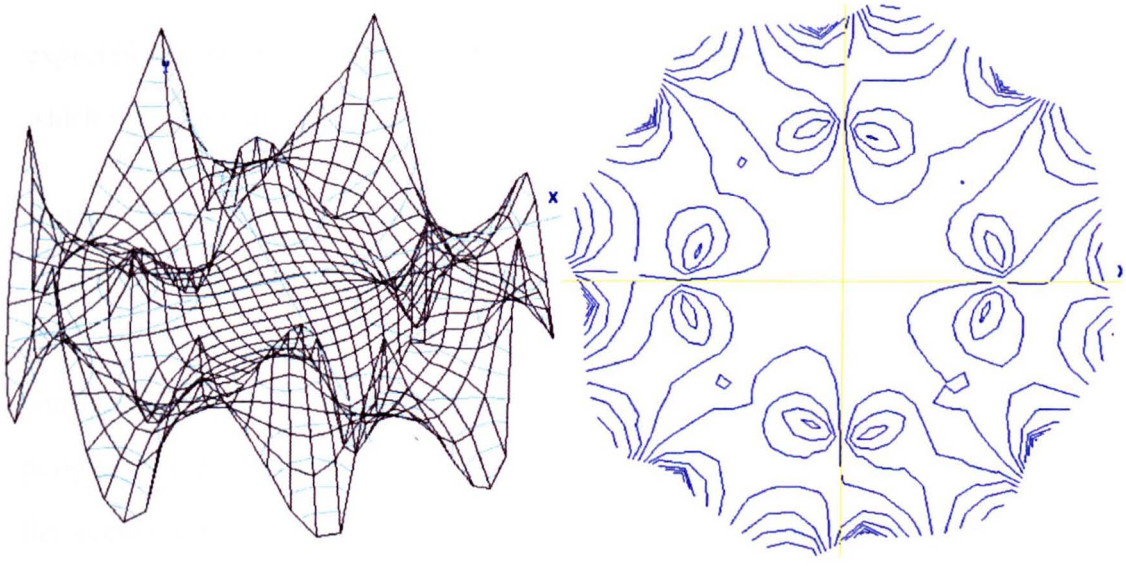

a

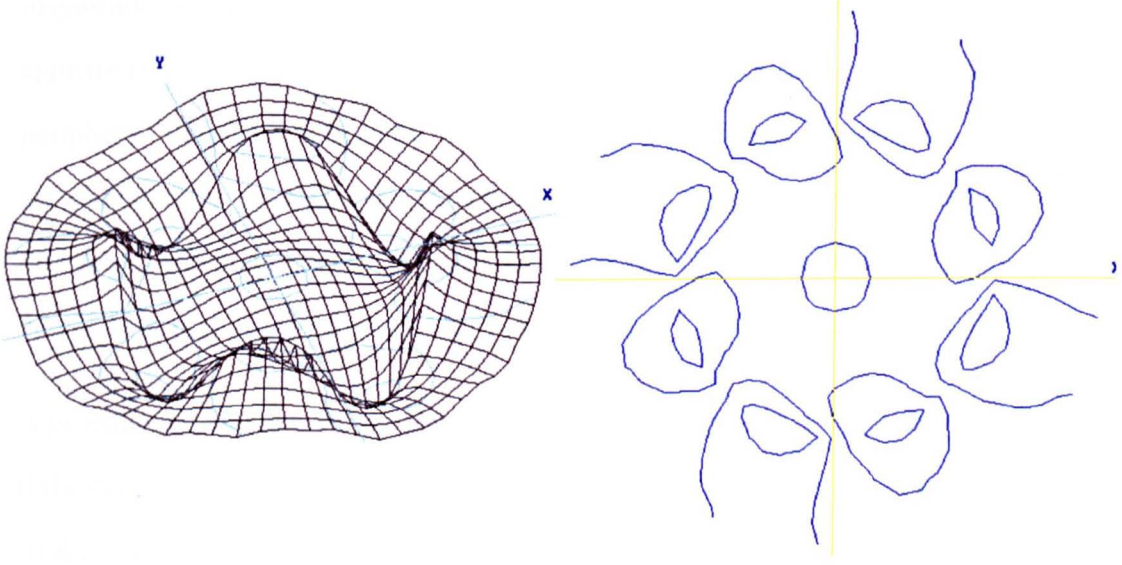

b

Figure 2.5.2 shows the calculated potential distribution using the two meshes in figure 2.5.1 with a concentric coil. *Both are shown to the same scale with contours separated by 50 nV. A concentric coil should generate a uniform potential distribution so these images show the error induced by the shape of the meshes. Figure 2.5.2a shows the potential distribution generated using an octagonal centred mesh and figure 2.5.2b shows the potential distributions generated using a circular centred mesh.*

expected potential is uniform and therefore any deviation from uniform must be noise which was generated in the calculation of the potential distribution.

Figures 2.5.2a and 2.5.2b show the noise from the octagonal centred mesh and the circular centred mesh respectively; they clearly show that there is noise generated by the FEM but in the case of the octagonal centred mesh the magnitude of the noise is considerably greater. In the real imaging system the potentials are measured at the periphery of the region and for the FEM to be a useful model of the system's behaviour, the accuracy is of greatest importance at the periphery. With the octagonal centred mesh it can be clearly seen that the FEM not only generates more noise but the magnitude of that noise is greatest at the periphery of the mesh. The circular mesh appears to generate the noise internally and this is attenuated by the time it reaches the periphery. Figures 2.5.2a and b, which are both plotted to the same scale show that the peripheral noise generated by the circular mesh is approximately 6 times smaller than that of the octagonal mesh. The two figures are plotted with contours equally spaced at 50 nV with both systems excited by a concentric coil carrying current of 1 A turn^{-1}.

A possible explanation of the differences between the results for the two meshes is that if the central region is octagonal, the elements in the outer rows are of different size and so the centres of the elements must have different radial displacements, whereas if the central region is circular, the centres of the elements in the outer row have the same radial displacements. This means that the calculated inducing field for each of the elements will vary. This causes step variations in the peripheral field and results in small errors in the calculated field in the peripheral region, so causing the noise.

An illustration of the way in which the nodal position affects the calculated nodal potentials can be shown by displacing one of the nodes. Figure 2.5.3a shows a mesh with one node radially displaced by 0.5 mm with a tank radius of 50 mm. For a homogeneous conductivity distribution this should still generate a uniform potential

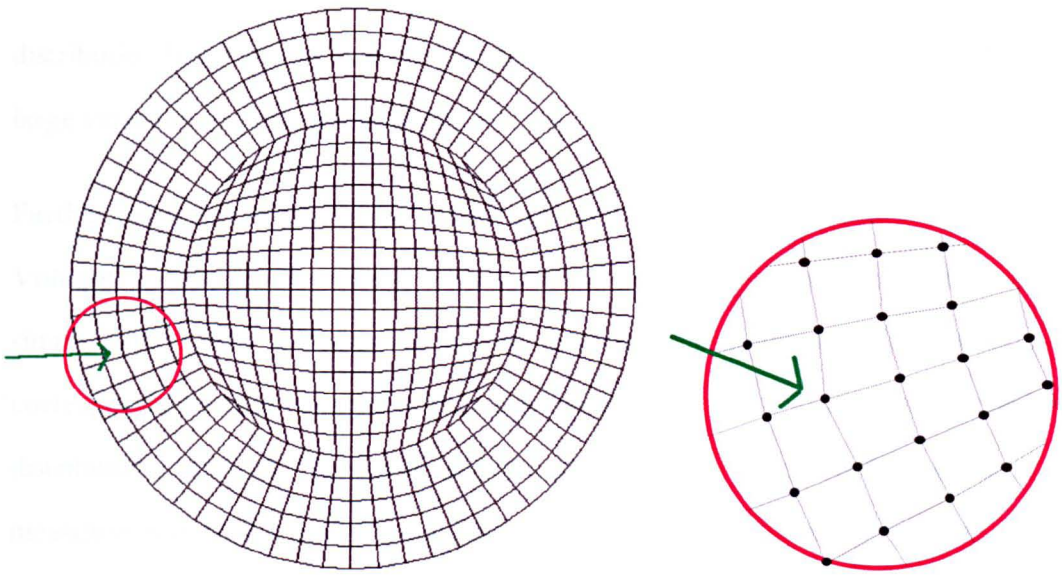

Figure 2.5.3a showing mesh with one node radially displaced by 0.5 mm. *The green arrow points to the displaced node. The radius of the region is 50 mm.*

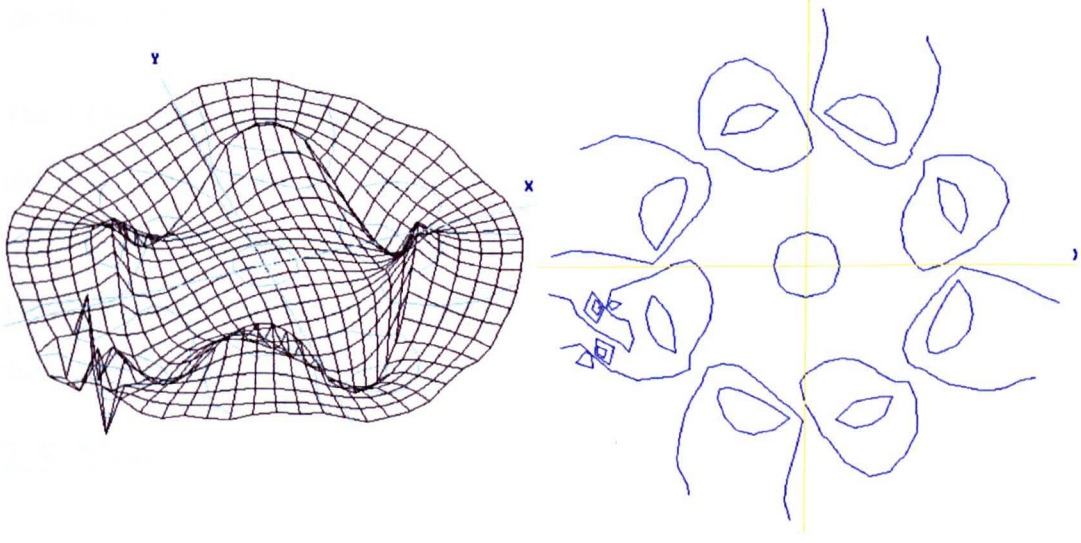

Figure 2.5.3.b shows the calculated potential distribution for a thin tank with one node displaced. *Contours are shown at a separation of 50 nV.*

distribution but it can be seen that in the region where the node was displaced, there is a large variation in potential of about 300 nV.

Further reduction of this noise can be achieved by the method used in the real system. Voltages induced in the wiring from the electrodes to instrumentation are removed by simply subtracting a reference set of voltage measurements. This reference set corresponds to the voltages which are measured for the homogenous conductivity distribution. In both the model and the phantom this is achieved by taking a set of measurements with a uniform conductivity distribution. Figure 2.5.4a shows an object of only 0.5% change in conductivity. The potential distribution shown in figure 2.5.4b has a significant contribution from noise similar to that shown in figure 2.5.2b for a uniform region. This can be dramatically attenuated by subtracting the potential distribution for a uniform medium and the result is shown in figure 2.5.4c.

The FEM used was developed by Low for the design of electrical machines, and meshing problems of the nature described above had not been noticed in these applications. The small errors induced by the exact location of the nodes as described above would be insignificant for many situations, but this is not the case when solving the forward problem to the accuracy required.

2.5.2 Dimensional scaling

The system has the property that it can be scaled without affecting the current paths. It is possible to utilise this property which allows the same mesh to be used to model different sized systems. To achieve this all the linear measurements are multiplied by a scaling factor which is determined by the ratio of the diameters of the two systems.

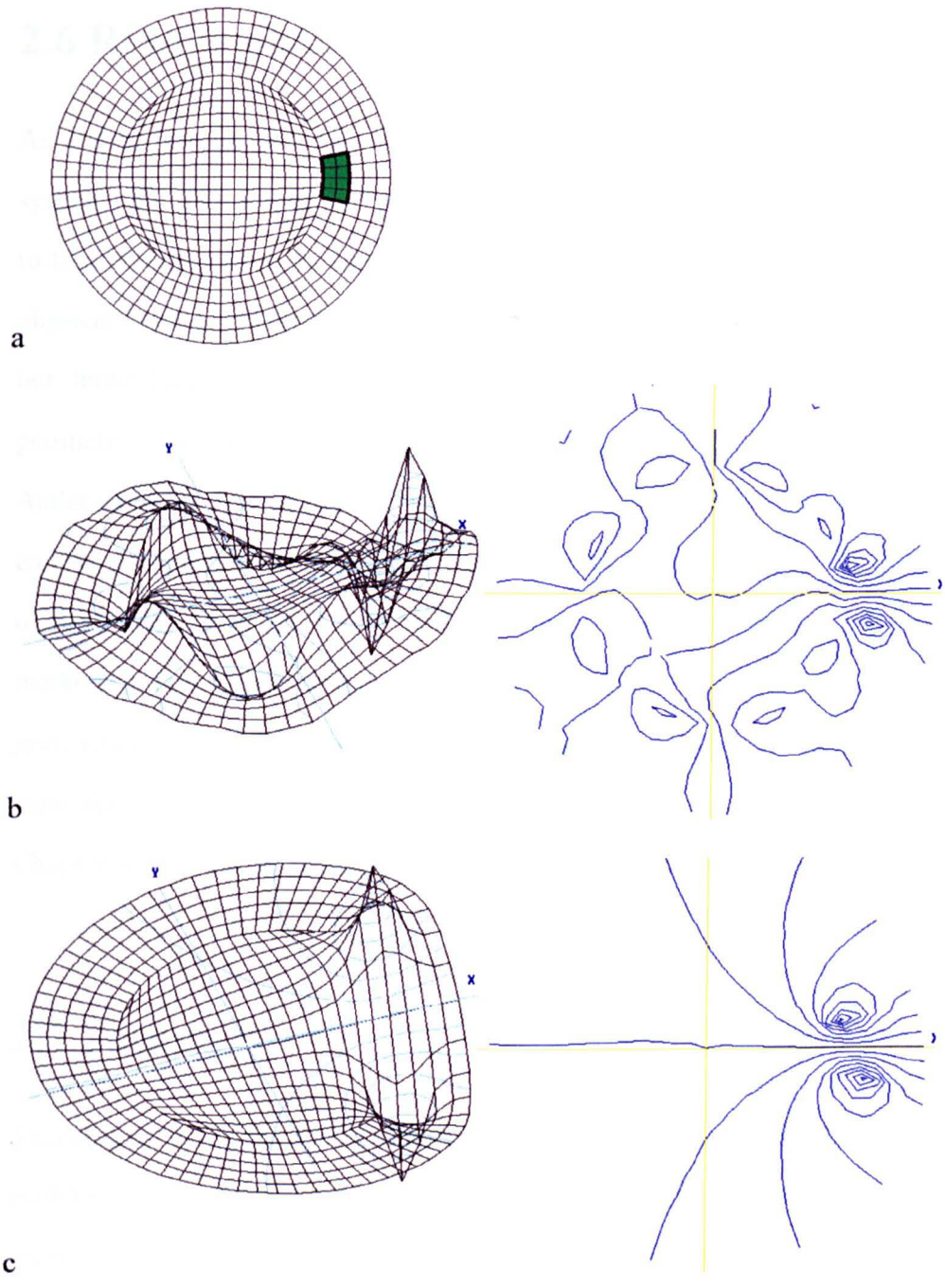

Figure 2.5.4 shows the potential distribution due to an inhomogeneity of 0.5% change in conductivity placed at the position shown in green. *Figure 2.5.4b shows the potential distribution found by the FEM for the conductivity distribution shown in figure 2.5.4a in which the green area is increased in conductivity by 0.5 %. The errors can be reduced by subtracting the potentials found for the homogeneous conductivity distribution which is shown in figure 2.5.2b. The result of this subtraction is shown in figure 2.5.4c. Contours are shown at a separation of 50 nV.*

2.6 Results obtained from the FEM

As a first test for the 3-D FEM the results were compared with results for a 2-D system. The FDM used by Purvis[17] for a 2-D system has produced data comparable to that resulting from an experimental system. Purvis's results compared well with the physical system, although the experimental system was only pseudo 2-D having a small but finite length. The 3-D FEM model was used to solve a similar pseudo 2-D geometry, and the solution was compared with the results of both the 2-D FDM and Anderson's[21] 2-D analytical method. Figure 2.6 shows the results obtained for the current pattern produced by the 2-D analytic solution of Anderson alongside the results of the FEM model for a thin tank. The only noticeable variation between the two methods is that for the analytical solution the current arrows are placed on a Cartesian grid, whereas the FEM solution places the arrows at the centre of the elements. The main features such as the current nulls appear to be in exactly the same positions. Chapter 4 describes in more detail the validation of the results from the FEM.

2.7 Summary

This chapter has given a brief description of the methods available to solve the forward problem; that is finding the potential and the current distribution of the system for a given drive configuration and conductivity distribution. The techniques used by Purvis and Scaife in the field of magnetically induced tomography were rejected because they are not suitable for the solution to the forward problem in 3-D. The Finite Difference Method which they used was constructed out of a mesh where the density was finest at the centre. To use this mesh to solve the 3-D forward problem would have required both an unacceptable amount of computer memory and of computation time. Anderson[21] has used conformal transformations to find an analytic solution for 2-D regions containing single circular targets, but conformal transformations can normally only be applied to 2-D problems.

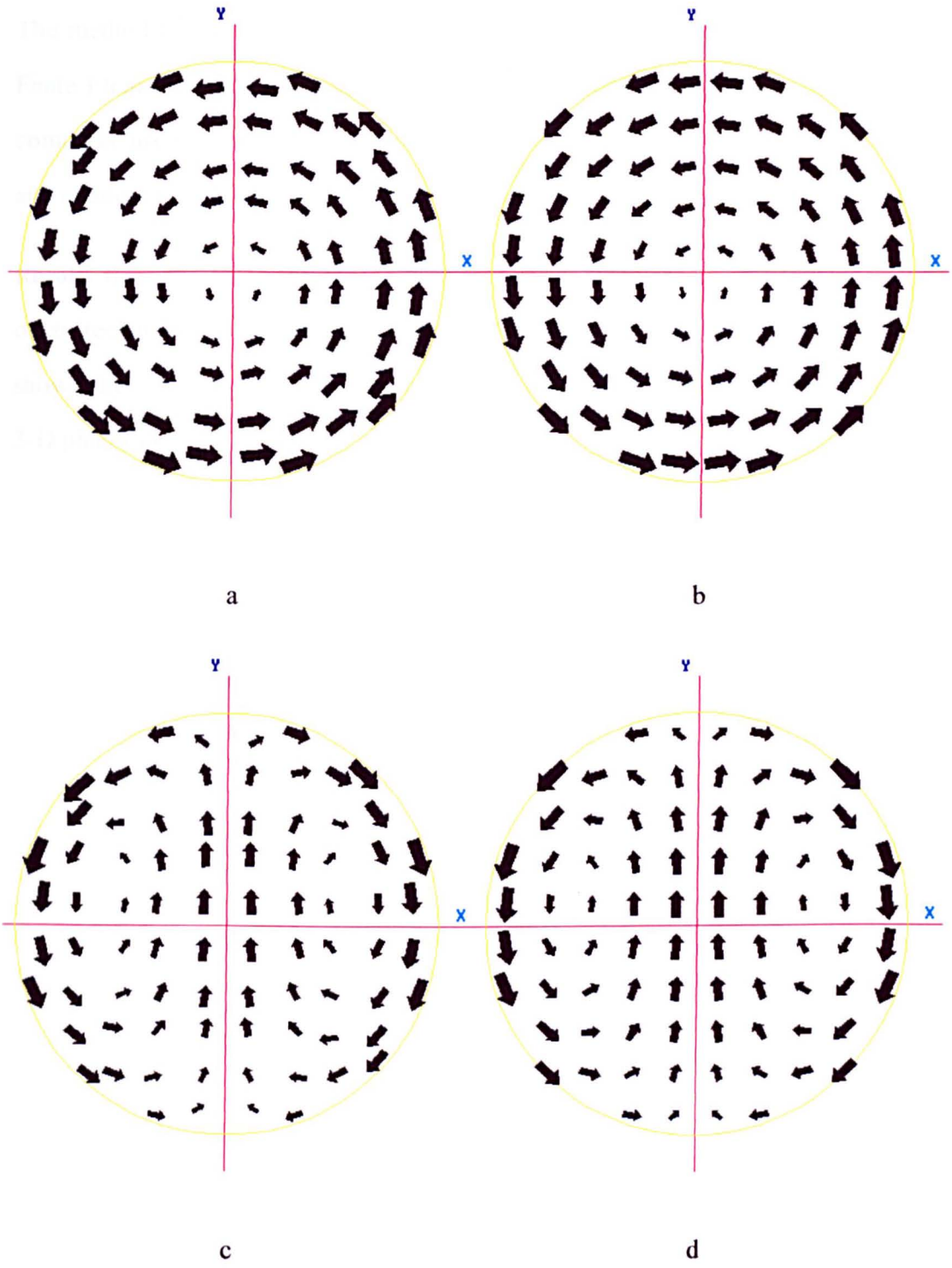

Figure 2.6 compares results obtained by the FEM and the analytic solution of Anderson [21]. *The analytic solution (figure 2.6 b and d) are for a 2-D phantom and the FEM solution (figure 2.6 a and c) are a pseudo 2-D phantom of length 20 mm. Figures 2.6 a and b show the current induced whilst exciting coil one and figures 2.6 c and d show the current induced with coils two and three excited in antiphase.*

The method that has been used to solve the forward problem in 3-D is the method of Finite Elements. The full implementation of this technique required a great amount of computer programming in order to provide the finite element program with the mesh and conductivity distribution and then to process the data generated by the program.

Results from the FEM for pseudo 2-D geometries were shown to compare well with other techniques which solve the forward problem for 2-D geometries. Chapter 4 shows the results obtained by comparing the FEM model with measured data from a 3-D phantom.

Chapter 3 Design and Construction of a Laboratory Phantom and Instrumentation

3.1 Introduction

In chapter 2 the method used to calculate the potential distribution in the phantom was discussed. In order to test the validity of the model it is necessary to make measurements on a phantom. Previous workers [17][25] constructed a simple system to evaluate the feasibility of taking measurements from a 2-D phantom with magnetically induced currents, using a nominal 100 mm diameter PVC soil pipe. However this phantom had to be modified in order to be suitable for making measurements on 3-D targets; the re-design is described in section 3.2. The elements of the electrical system also needed re-designing and these are described in section 3.3. These elements include the buffers, multiplexers and subtractor. The specification achieved for the new system is tabulated in section 3.5..

Results presented in chapter 4 compare the model discussed in chapter 2 with the measurements made using the equipment described in this chapter.

3.2 Design of the phantom

The original phantom design suffered from a number of problems which were associated with the mechanical design and construction of both the tank and electrodes.

The base was fixed in place by silicon rubber resin and the electrodes were in the form of stainless steel screws which fitted into tapped holes in the wall of the PVC pipe.

Although the electrodes were sawn to approximately the correct length there was no regularity to the shape of the sawn ends. Furthermore the thickness of the phantom wall varied with circumferential position so that the extent of electrode penetration was unpredictable. The fit between the tapped hole in the phantom and the threads of the screw was not tight enough to prevent leakage of saline which caused corrosion problems at the contacts and in the cables. Partly as a result of this corrosion and partly as a result of corrosion of the stainless steel itself, electrical contact to the electrodes was unreliable. In addition the length of the phantom was fixed so that it would have been impossible to carry out 3-D experiments.

These problems were overcome by the design and construction of a new phantom shown in figure 3.2.1. In the new design the electrodes were mounted in a short ring designed to mate with the PVC pipe used in the previous design. In this way the ease of availability of the standard PVC pipe could be exploited and design effort expended where it was most needed, *i.e.* in the electrode ring.

A diagram of the arrangement of the essential components of the phantom is shown in figure 1.4.1. The key element of the new design is the electrode ring, made of polymethylmethacrylate resin, which is shown in figure 3.2.1a. The top and bottom of this ring were designed to mate with the PVC soil pipe and the electrodes were mounted in the ring as shown. The seal between the electrode ring and the pipe was made using 'O' rings with a cross sectional diameter of 4 mm. The electrodes, one of which is shown in figure 3.2.1b, were machined out of 2 BA brass screws. The back of the head of the screw was machined to fit on a shoulder in the electrode ring so that the end of the electrode just penetrated into the tank to form a hemispherical electrode of 1 mm diameter. A second shoulder machined on to the electrode formed a sealing surface when fitted with a small 'O' ring. The back of the electrode was tapped to take an 8 BA screw to which a solder tag could be fitted to make electrical contact. After machining, the electrodes were gold plated to make them resistant to corrosion by the saline.

Fig 321

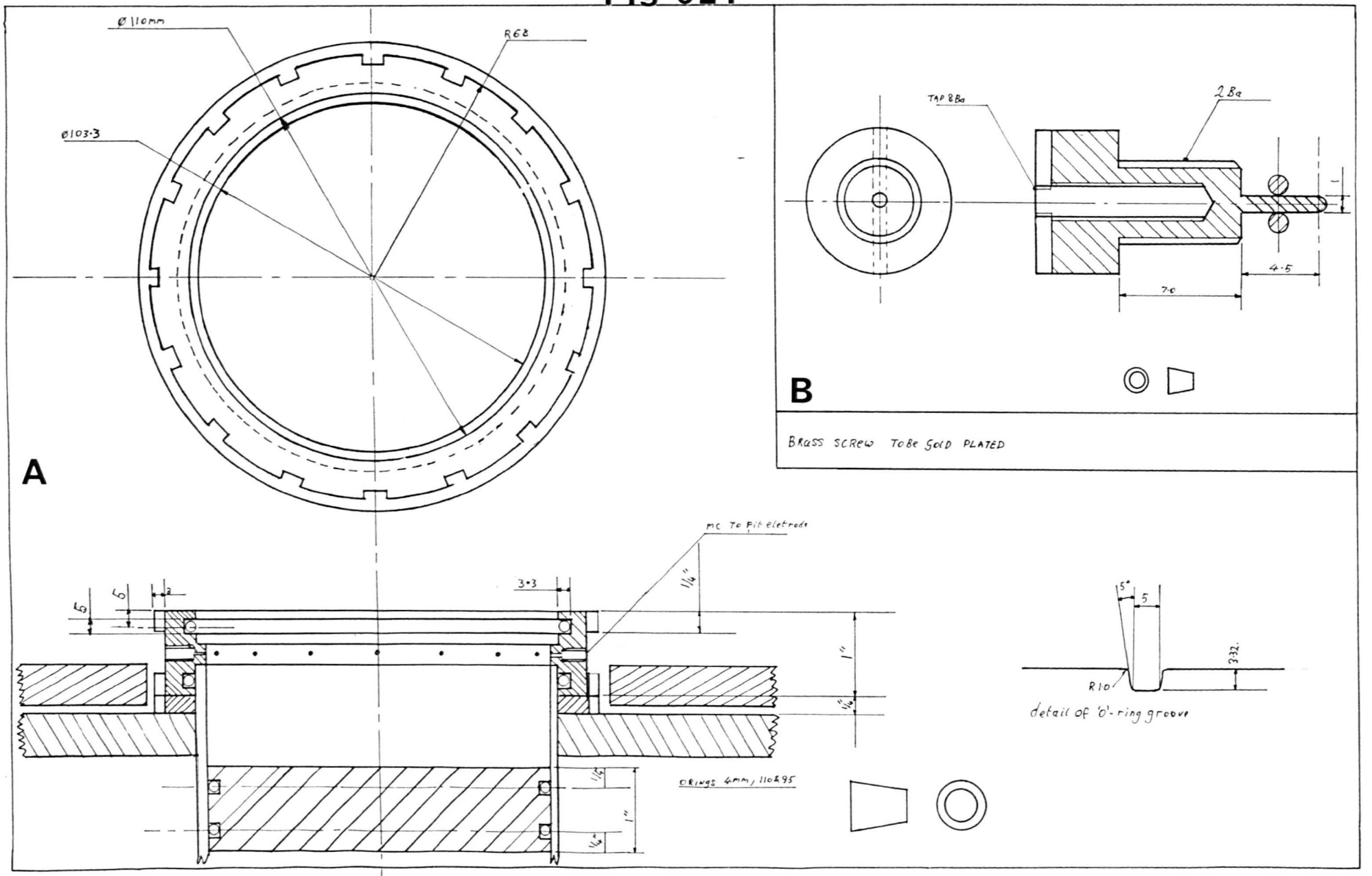
Ø 110mm
R68
Ø103·3
A
TAP 8Ba
2 Ba
4·5
7·0
B
BRASS SCREW TO BE GOLD PLATED
mc TO Pt electrode
3·3
1"
ORings 4mm, 110 & 95
5°
5
3·32
R1·0
detail of 'O'-ring groove

In order to be able to adjust the height of the tank, the base of the tank was made in the form of a plunger machined out of polymethylmethacrylate resin. The joint between the plunger and the pipe was sealed using two 'O' rings. By moving the plunger up or down the pipe below the electrode ring and filling the tank with saline up to the required level any height could be achieved. The height of the electrodes was used as a reference datum and all measurements are made with respect to this datum. For most experiments the height of the coils is set to this level. Thus the plane of the electrodes is regarded as height zero so that a tank described as having a height of ± 200 mm would have the plunger 200 mm below the electrodes and be filled with saline to a level of 200 mm above the electrodes; the total length of such a tank would be 400 mm. Figure 3.2.2 shows photographs of an electrode, the electrode ring, the phantom, sense electronics and the whole system. This phantom proved to be entirely satisfactory for all the experimental work.

To model this system, the FEM was used as described in chapter 2. The mesh had a nominal diameter of 100 mm whereas the phantom's diameter is 103.5 mm. To model the phantom a scaling factor of 3.5 % was used for all the system's linear measurements. Hence the coils were 3.5 % smaller and were centred 3.5 % closer to the centre of the phantom.

3.3 Electrical specifications

Although the electrical system was redesigned, the overall structure was not altered and a block diagram of this is shown in figure 3.3.1. The original instrumentation consisted of input buffers using TL081 op amps connected as voltage followers, a pair of DG506 multiplexers used to enable a subtractor circuit to sense the potential difference between any electrode pair and the subtractor circuit itself which was constructed from discrete transistors. The output of the subtractor was fed into one of

Figure 3.2.2 Experimental layout

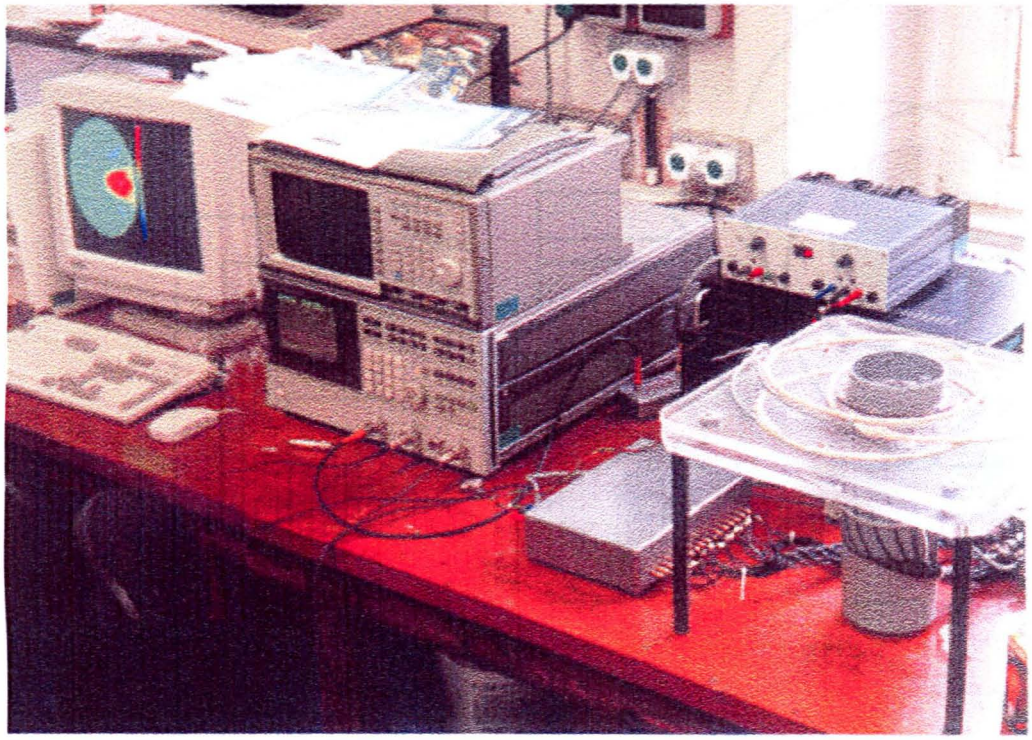

Instrumentation layout

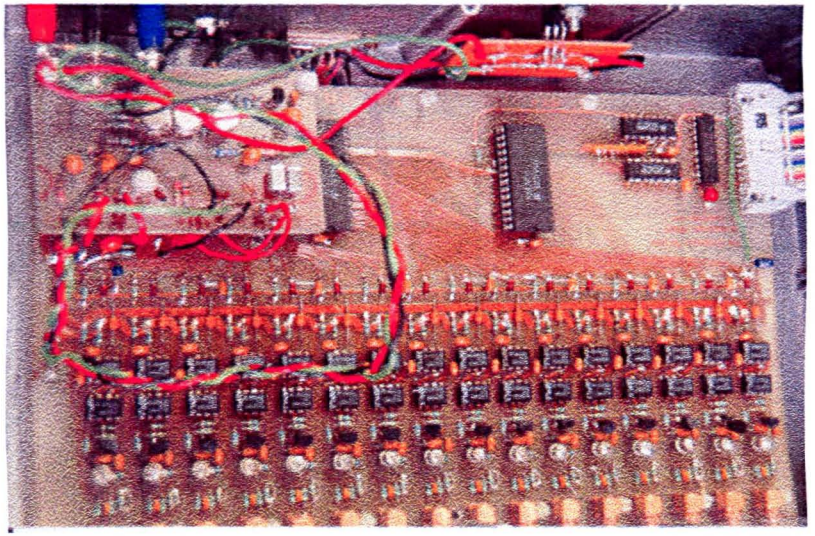

Phantom

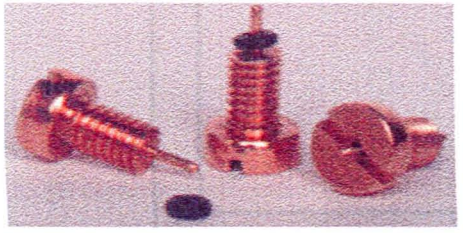

Electrodes and electrode ring

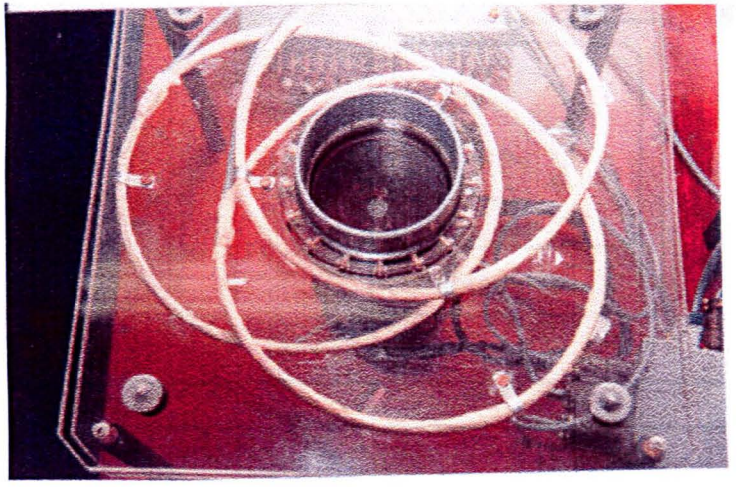

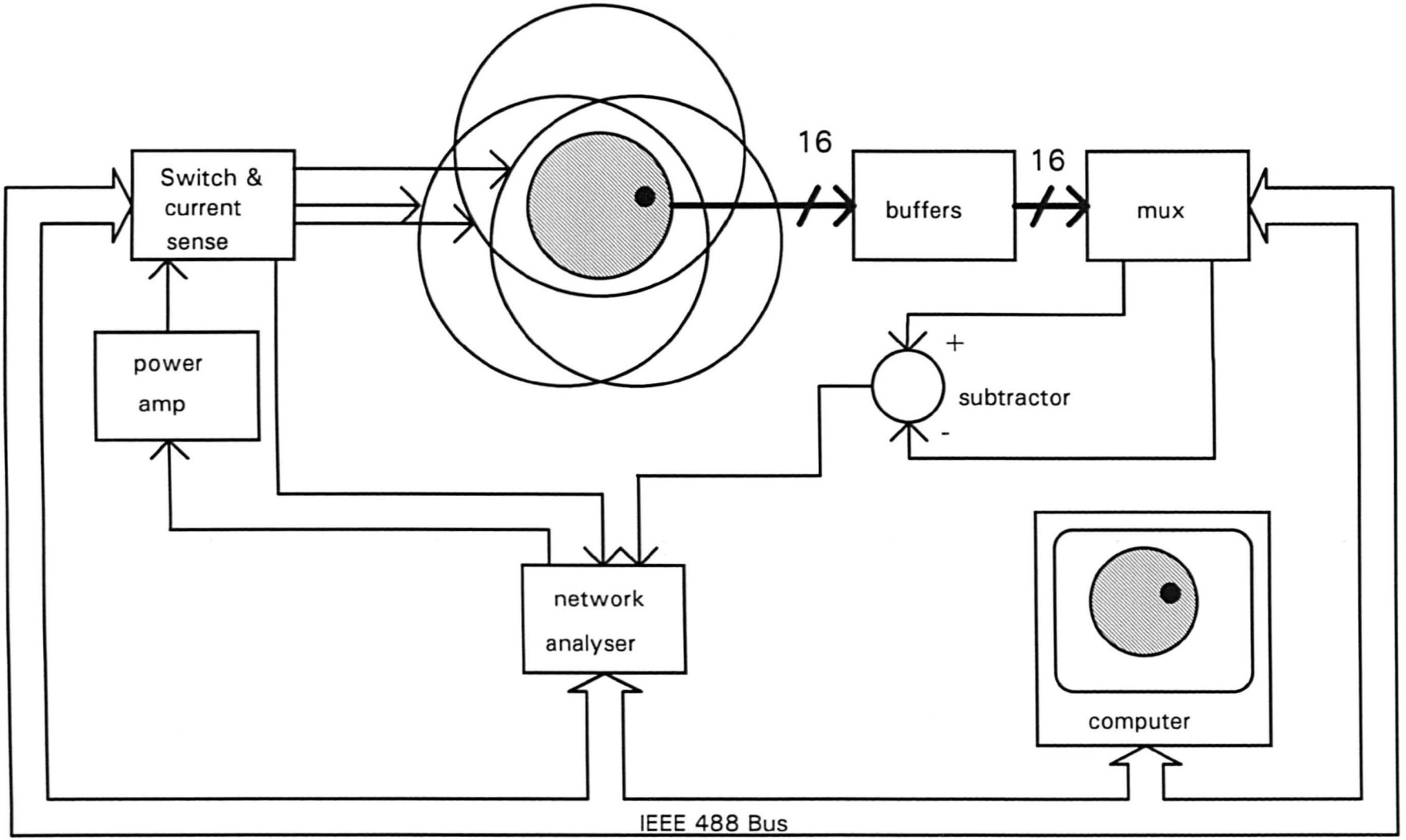

Figure 3.3.1 Block diagram of the data gathering system.

the input channels of an HP3577 network analyser, the coil current being used as a reference.

Unlike the phantom the original electrical system did not suffer from problems concerned with functionality. Using the system it was possible to take measurements but the performance of the system limited the quality of those measurements.

Before an improved system could be designed, it was necessary to define target specifications for the important functions of the system; essentially the differential mode gain, common mode rejection ratio, gain stability and phase shift stability.

The differential mode gain is defined as the ratio of the output voltage to the voltage applied between two inputs to the electrical system. The common mode rejection ratio (cmrr) is the ratio between the differential mode and the common mode (cm) gains, where the cm gain is the gain of the system for the average voltage with respect to earth and in this application contains no information of interest. The source of the cm voltage is from electrostatic pickup from the coils and from emfs generated by the time varying magnetic field.

Measurements between an adjacent pair of electrodes taken from the 2-D phantom indicated typical cm voltages of 10 mV and differential mode voltages of between 4 mV and 4 μV. These differential mode voltages were typical of a large insulating target (20 % of phantom diameter) at the periphery and of a small insulating target (5 % of phantom diameter) near the centre respectively.

To be able to detect and measure a signal of 4 μV, in the presence of a 4 mV signal, the system must measure and resolve signals to an accuracy of 1 part in 1000. There are two types of error which may occur within the measuring system. One is entirely random and can be attributed to phenomena such as noise in the electronics of the instrumentation system. Drift in the system during measurement will also give rise to errors of a random nature. The other is coherent noise arising from the inability of the

system to completely reject cm signals. This will be discussed in the next section. For each part of the system the errors must be sufficiently small so that the error for the total system does not exceed 1 part in 1000.

It can be seen that the cm signal is about 10 dB greater than the differential mode signal generated by a large insulating target placed at the periphery. If it was required to detect both the small target placed at the centre of the phantom and at the same time detect the large insulating target at the periphery, the system would be required to make measurements to an accuracy of 1 part in 1000. For a system to make measurements to this accuracy it must at least be capable of resolving to 1 part in 1000 which suggests a required dynamic range of >60 dB. To make measurements of this dynamic range in the presence of a cm signal 10 dB greater than the largest dm signal would require a cmrr of -70 dB at the operating frequency of 50 kHz. This specification is similar to that of Brown and Seagar[26] who found that if an injected current system was required to measure lung perfusion, measurements would have to made to the accuracy of 1 part in 1000. Thus the magnetically induced system requires a similar measurement accuracy to that of the injected current system.

The cmrr for the whole system is affected by all stages up to and including the subtractor. Each stage can convert a cm signal into a dm signal and this process is affected by the gain and phase matching of the channels feeding the subtractor. Appendix 1 defines the relationships between various mismatches in the channels feeding the subtractor and cmrr.

3.3.1 Outline of the final system designed

The instrumentation system has been constructed to give sets of high quality measurements but no attempt has been made to take them quickly. This has led to a system that is almost totally serial in that all 48 measurements are taken in sequence. It would be possible to take measurements from all 16 electrodes simultaneously to

improve the speed of the data gathering but serial measurement has the advantage that the system needs to have the separate channels matched only up to the multiplexers. This is important since poor channel matching will degrade the cmrr. For a cmrr of -70 dB, differences between channels would have to be less than 1 part in 3200.

The surface potentials are sensed by the 16 electrodes and each electrode is buffered by a high input impedance unity gain amplifier to reduce electrode loading effects. The subtractor of the new system (figure 3.3.1) which is to be described is similar to the earlier system. The buffers' outputs are multiplexed by two 16 channel multiplexers and the difference of the two outputs is found using a subtractor circuit. An HP3577 network analyser is used to measure the magnitude and phase of the subtracted signal with respect to that of the coil current, giving a measure of the transfer impedance. The network analyser also provides the signal which is amplified by a commercial power amplifier to drive the coil current. The whole system is controlled by a PC over an IEEE 488 bus.

3.3.2 Buffers

The buffers used by Purvis[17] were constructed from the TL081 op-amp and the input impedance was not sufficiently high for them to sense the electrode voltage within the specified accuracy. This will affect both the system's overall cmrr and the accuracy of measurement potentials sensed by the instrumentation. These difficulties were overcome by the construction of two types of buffer, the first mounted on a circuit board remote from the phantom and the other constructed using surface mount techniques close to the electrodes.

The sense electrodes were connected to the input buffers by 1 m of 50 Ω coaxial cable. The buffers used a bootstrapped discrete JFET front end [27] to achieve a very low input capacitance and a driven screen to reduce the effective cable capacitance. The impedance presented to the sense electrodes by the combination of the cable and

buffer amplifier was 100 MΩ in parallel with 1.5 pF, which at 50 kHz is 100 MΩ $+j2$MΩ. From Appendix 1, the relationship between the gain for two buffers and the cmrr is:-

$$\text{cmrr} \approx 20\log_{10}\left|\frac{A_1 - A_2}{A_1}\right| \text{ dB} \qquad 3.3.1$$

where A_1 and A_2 are the gains for the two buffers.

The cmrr can also be found in term of bandwidths of the two buffers assuming they show a first order frequency response:-

$$\text{cmrr} \approx 20\log_{10}\left|j\omega(\tau_1 - \tau_2)\right| \text{ dB} \qquad 3.3.2$$

where τ_1 and τ_2 are the time constants for each of the two channels.

It is also possible to find the effect of small phase errors on the cmrr:-

$$\text{cmrr} \approx 20\log_{10}\left|(\phi_1 - \phi_2)\cdot\frac{\pi}{180}\right| \text{ dB} \qquad 3.3.3$$

where ϕ_1 and ϕ_2 are the phase shift in degrees for each of the two channels.

From equation 3.3.1 it can be found that to achieve the cmrr of -70 dB the gains of the buffers must be matched to 0.03 %. Equation 3.3.3 suggests that the phase of the system must be matched to 0.02 for the system to have a cmrr of 70 dB. In order to separate conductivity and permittivity images, Scaife[28] required that the matching of the phase shifts between channels was 0.2 degrees. Thus to achieve the required cmrr, the matching of the phase shifts is a more stringent requirement than the that of Scaife's algorithm to separate conductivity and permittivity images. For small phase shifts errors in the phase shift will mainly contribute to the imaginary component of the signal and therefore the phase matching is less critical if only the real part of the signal is used.

The specification of these remote buffers designed and constructed by Tozer[27] was sufficiently good for the required conductivity measurements from the 3-D system.

3.3.3 Multiplexers

The previous system used two DG 506 analogue multiplexers to select the signal channels to be presented to the subtractor. Each switch in a DG 506 is a pair of MOSFET transistors arranged to form a standard bilateral switching element as shown in figure 3.3.2. This type of multiplexer has a number of limitations from the point of view of this application:-

- Relatively high 'on' resistance (500 Ω).
- Small bandwidth (7 MHz) which will generate significant phase shifts at 50 kHz.
- Poor matching of the 'on' resistance (manufacturer specification 50%). The interaction of this and the output capacitance of the switch would limit the system's cmrr for a pair of multiplexers to -45 dB.
- Limited 'off' isolation (-68 dB @ 500 kHz). The 'inter-channel' cross talk which is due to C is more important than the 'off' isolation but it is not specified in the data book.

Higher specification multiplexers are now available and their advantages are described below.

Video applications require analogue switches with very high bandwidth. This has led to the development of a family of analogue switches with low 'on' resistances and low levels of capacitive feed-through. Many such switches are arranged in a 'T' configuration as shown in figure 3.3.3. When the switch is 'on', the top two switches are closed and the tail switch is

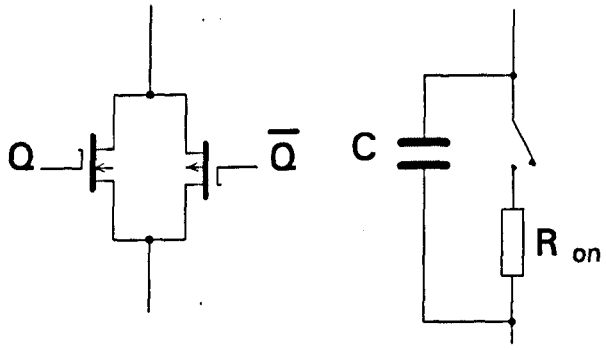

Figure 3.3.2 Bilateral switch of the DG506 multiplexer and equivalent circuit of the switch.

open, but when the switch is 'off', the top two switches are open and the tail switch is closed. Therefore any current flowing through the feed-through capacitance of the first switch is shorted to ground by the tail switch but the second switch prevents the output being shorted to ground through the tail switch. An example of such a switch is the DG535 [29] which has an 'on' resistance of about 90 Ω.

The negative analogue supply of DG535 is the same voltage as logic 0. Since the input signal could be of either polarity, the multiplexer inputs were biased to a common point whose voltage was set half way between the positive analogue supply and analogue ground. The signal was then capacitively coupled between the buffer amplifiers and the multiplexers, a strategy which has the added advantage of removing the various dc levels appearing at the buffer outputs.

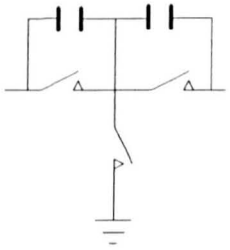

Figure 3.3.3 'T' switch used by the DG535.

Equation 3.3.2. shows that in order to minimise cmrr, it is important for the multiplexers to have a very high bandwidth or for the bandwidths of the two multiplexers to be well matched. The DG 535 addresses both these points by having a very high bandwidth of 500 MHz and the bandwidths are also well matched. The worst case for a pair of DG 535 multiplexers operating at 50 kHz is a cmrr of -80 dB. This was calculated from the largest variations in 'on' resistance and output capacitance values specified by the manufacturers[29].

3.3.4 Subtractor

Some errors in the measuring system will be introduced by the subtractor itself because:-

- It is unable to reject completely all the cm signal (a performance limit quantified by the cmrr).

- It will introduce noise.
- Its differential mode gain will be subject to drift.

Errors due to these factors must be sufficiently small for the system to make the measurements to the required accuracy.

Various subtractor circuits were considered to see whether they could meet the required system specification for making measurements to an accuracy of 1 part in 1000.

3.3.4.1 Instrumentation amplifiers

Instrumentation amplifiers are a type of subtractor and are made by various manufacturers of analogue integrated circuits. They have very high input impedances, presettable gains and low frequency cmrr of the order of -100 dB. These amplifiers are designed for, and therefore work well at, low frequencies (of the order of 100 Hz) but as frequency increases their cmrr falls with a first order frequency response. No devices were found that could meet the specification of a cmrr of -70 dB at a frequency of 50 kHz.

3.3.4.2 The long tailed pair

A simplified long tailed pair is shown in figure 3.3.5 and for simplicity no power supply or biasing circuitry has been shown. The two input signals are applied to the bases of transistors Q_1 and Q_2 and the output signal is the difference between the two collector currents. This is seen as a voltage across the two collector resistors R_1 and R_2. The two transistors are connected as emitter followers with the emitters connected by R_E. Making the

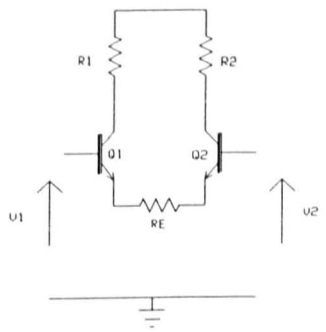

Figure 3.3.5 Simplified long tailed pair

assumption that $R_E >> 1/gm$ for both transistors, the signal voltages at the transistors' emitters will be approximately the same as those at their bases and hence the voltages v_1 and v_2 will be applied across R_E and the current in R_E will be proportional to the difference $(V_1 - V_2)$. If the current gain of the transistors is assumed to be very large, the current in the collector is approximately equal to the emitter current and the current in R_1 and R_2 will be equal to the current in R_E. Thus the current flowing in R_1 and R_2 will be proportional to the difference in the input voltages. It was found that the cmrr of a long tail pair circuit can be very good at high frequency especially if followed by an op-amp.

The circuit used, shown in figure 3.3.6, is a modified version of a design published by National Semiconductors[30]. The circuit was redesigned to optimise it for high frequency performance as follows. Transistors Q_1 and Q_2 have a similar function to Q_1 and Q_2 in figure 3.3.5. To improve the bandwidth of the circuit the input is isolated from the output by transistors Q_3 and Q_4 connected in cascode with Q_1 and Q_2. The DC bias current is supplied by the current sources constructed using Q_5 and Q_6. Ideally the subtractor will not generate any output for cm signals. One signal path for cm signals from the input to the output is through the parasitic components associated with the input transistor such as the collector base capacitance. If, assuming the transistors are matched, a cm input signal alone is applied to the bases of Q_1 and Q_2, their base voltages, and hence their emitter voltages, will be equal. Consequently there is no signal voltage across R_E and no current will flow through it. The circuit can therefore be separated into two halves which can be examined separately. Transistors Q_1, Q_3 and Q_5 make up the half circuit whose output is the current flowing through the collector of Q_3. Q_3 is connected as a common base amplifier and if the assumption is made that its current gain is high, the base current will be negligible and the collector current will equal the emitter current. The base of Q_3 is at small signal earth and therefore the emitter is also assumed to be at small signal earth. Figure 3.3.7 shows an equivalent circuit based on these assumptions. Any current

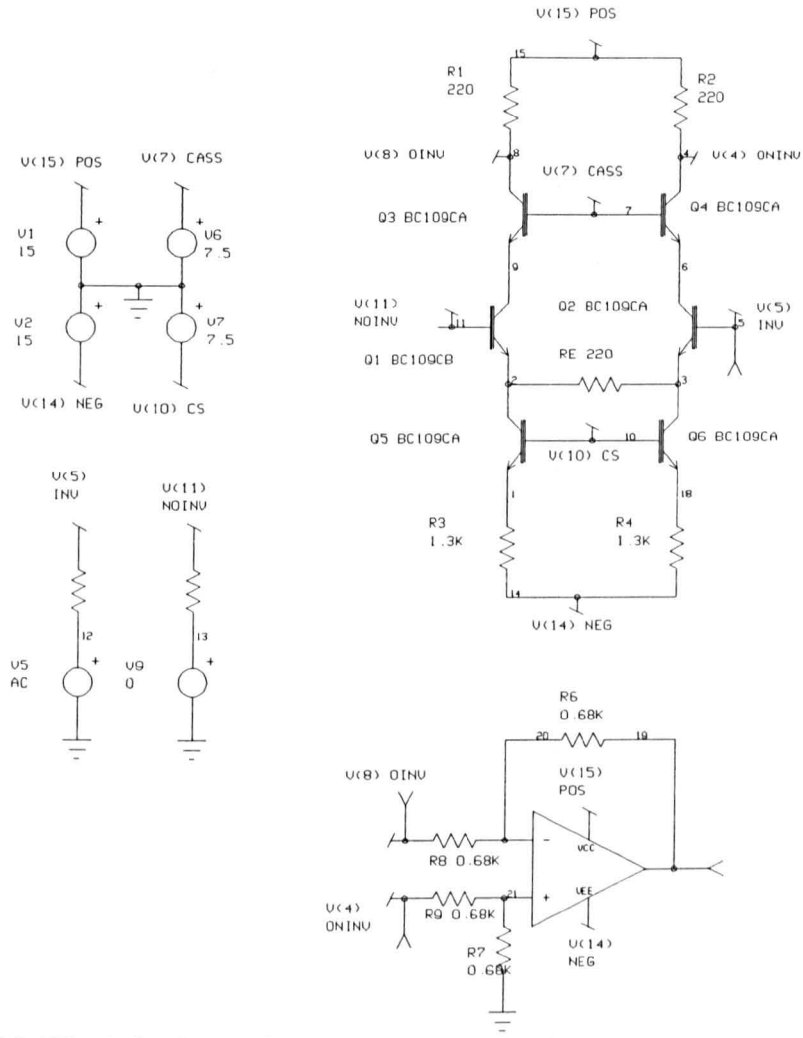

Figure 3.3.6 Final circuit used for the subtractor

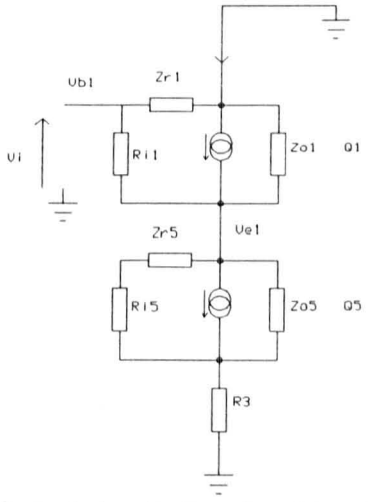

Figure 3.3.7 Equivalent circuit of one input transistor and current source transistor

which flows through Z_{r1} must contribute to the current i_{C3} and will be seen at the output. Current flowing through Z_{r5} will also contribute to i_{C3} but in the opposite direction. Q_1 behaves as a voltage follower so that v_{b1} is almost identical to v_{e1} and the currents through Z_{r1} and Z_{r5} will cancel. The effective values of Z_{o1} and Z_{o5} are not equal and do not exactly cancel but the contribution to i_C by i_{Zo1} will be reduced by i_{Zo5}. This means that the effect of the current which flows through the parasitic impedance of the input transistors can be reduced by the current which flows through the parasitic components of the current sources.

Again assuming that $R_E >> 1/gm$, the differential gain of the circuit shown in figure 3.3.6 from the input to the voltage across V(8) and V(4) is approximated by $(R_1+R_2)/R_E$ and the cm output voltage by $I_p \cdot (R_1+R_2)$, where I_p is the residual current flowing through the parasitic components. I_p is independent of the values of the resistors R_1, R_2 and R_E and hence the cmrr can be improved by reducing all the resistor values by a common factor. This will not affect the differential gain but will reduce the cm gain. The limit to this reduction in the resistor values is defined by the maximum power dissipation for the transistors and as the value of R_E is reduced the circuit's gain becomes increasingly dependent on the parameters of the input transistors. This would lead to problems of the gain stability for the circuit.

This alteration in the quiescent current for the circuit could have a detrimental effect on the noise of the subtractor and this is now examined. A source of noise for the circuit is 'shot noise' within the transistors. Davies[31] shows that the equivalent input noise voltage for a transistor is given by :-

$$\overline{v_n^2} = 4kTB[R_s + (r_b + \frac{1}{2g_m}) + (R_s + r_b)^2 \frac{g_m}{2h_{fe}}] \qquad 3.3.4$$

where

$\overline{v_n^2}$: the total mean square equivalent input noise voltage

kTB : Boltzman's constant, temperature and bandwidth

R_s and r_b : the source resistance and input resistances respectfully

g_m and h_{fe} : the mutual conductance and the current gain for the transistor.

Both g_m and r_b are a function of the collector current. Mathcad was used to plot the values of the function for noise of the input transistors shown in equation 3.3.4 against collector current. It was found that the function had a minimum at a current of about 200 mA. As referred to above, other circuit considerations set limits to the maximum current and this brief description of noise shows that the increasing of I_c to improve cmrr does not sacrifice the noise performance for the circuit. The circuit was simulated for its noise performance using the electrical circuit simulation software SPICE. The 'intusoft' version of SPICE was used which is based on Berkeley SPICE 3E.2. It was found that its equivalent input noise voltage was 15 $nVHz^{-½}$.

The output of the discrete part of the circuit of figure 3.3.6 is in a differential form *i.e.* it is the difference between the voltages across R_1 and R_2. The output could be taken as the voltage across one of the resistors but this would have several disadvantages:-

- The voltage at node V(8) is not only proportional to the current in R_E but also to the supply voltage, making the circuit very sensitive to noise on the positive supply.
- Half the potential output voltage would be discarded because the output is only taken across one of the load resistors and this lowers the gain by 6 dB and degrades the noise factor for the circuit.
- cm signals present at node V(8) and V(4) could not be rejected by only considering the voltage at V(8). Hence considering V(8) alone would degrade the overall cmrr.
- The signal will have a large DC component.
- The output impedance of the circuit will be quite high.

All these problems can be overcome by constructing a simple subtractor using an op-amp as shown in figure 3.3.6. An op-amp subtractor can be used here because the required cm rejection ratio of this op-amp subtractor is much smaller than for the whole subtractor because the cm signal has been greatly attenuated by the first stage

of the subtractor. In order to maintain a high bandwidth the op-amp used had a 50 MHz unity gain bandwidth. SPICE simulation showed that the best bandwidth could be achieved using 680 Ω resistors for R_6, R_7, R_8 and R_9. The simulation also showed that there was no overall circuit performance improvement by matching these resistors to better than 1%, thus inexpensive resistors could be used.

3.3.4.3 Results obtained from the subtractor

The complete subtractor circuit of figure 3.3.6 was modelled using SPICE. The initial simulation was with all the components matched and the frequency response of this circuit is shown in figure 3.3.8. The cm gain is shown in figure 3.3.9. The circuit has a frequency response of over 50 MHz which is useful because this implies a very low phase shift at 50 kHz of 0.06 . The circuit could be used for systems working at much higher frequencies. The cm gain is less than -130 dB up to 1 MHz but this is with perfectly matched components.

The circuit's sensitivity to the mismatching of the parameters of various components was also examined. Figure 3.3.10. shows the cm gain with a 1% variation between R_1 and R_2. The circuit still performs within specification up to 50 MHz. Figure 3.3.11 shows that the addition of a 100 fF capacitor between the base and collector of Q_1 has a large effect on the frequency response of common mode gain of the circuit although it still performs within specification up to about 2 MHz. 100 fF is a very small capacitance and the result of the simulation shown in figure 3.3.11 suggests that the physical layout of the circuit is critical since capacitive imbalances much greater than 100 fF could be introduced by poor layout of the circuit. Figure 3.3.12 shows the effect of mismatching the gain (h_{fe}) for the two transistor Q_1 and Q_2, setting Q_1 to a gain of 850 and Q_2 to a gain of 450 which is the maximum specified mismatch. With this mismatch the circuit remains within specification up to 30 MHz. This shows that close matching of the current gain of input transistors is not required and the cm gain remains less than -95 dB to over 1 MHz.

Two versions of the circuit were constructed, one using the matched transistor LM394 for (Q1 and Q2) and (Q5 and Q6), and the other using gain selected transistors BC184C. The C suffix indicates that the transistors have been selected to have a current gain between 450 and 850. The resistors used for the construction all had a tolerance of 1 %. Care was taken to maintain symmetry about Q1 and Q2 so that parasitic capacitances, formed by the wiring on the circuit board, would be well matched. Both circuits were tested using the HP3577 network analyser. Figure 3.3.13a shows the differential mode frequency response of the circuit with the matched transistors, figure 3.3.13b the cm frequency response and figure 3.3.13c the cmrr. Figures 3.3.14a to c are similar to figures 3.3.13a to c but the BC184C transistors were used. From these two sets of graphs it can be seen that the two BC184C, although poorly matched, perform better than the matched transistors. This is probably because the capacitance of the matched transistors will be greater than for the BC184C. An element of the gain of the circuit is dependent on the value of h_{fe} for the transistors which will vary from transistor to transistor and will be temperature dependent. The sensitivity of the circuit's gain to h_{fe} was modelled using SPICE. The gain was found with the h_{fe} of Q_1 and Q_2 set to 850 and then remodelled with the h_{fe} set at 450. The corresponding gain for the circuits were respectively 3.0545 dB and 3.0442 dB. Thus a full variation in h_{fe} for the input transistors only produces a 0.12% variation in gain for the circuit. This variation could be reduced by increasing the value of R_E but in the current serial system an uncertainty in the gain of 0.12% is not important. This modelling demonstrates that if multiple circuits were required, they could be constructed with very close gain matching using 0.1% resistors and BC184C and no calibration would be necessary.

The noise of the subtractor was measured approximately using a low noise amplifier connected to a digital oscilloscope. By this method a value of 30 $nVHz^{-½}$ was measured. It was not possible to make an accurate measurement of the noise because the oscilloscope does not average over a long time period and there was a

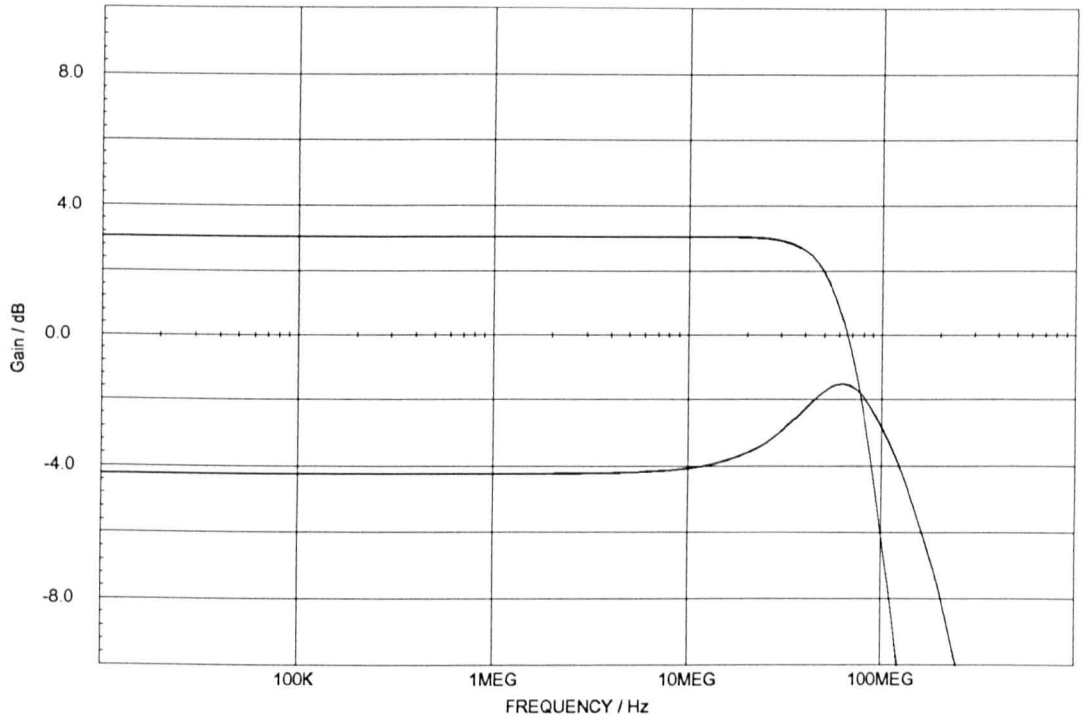

Figure 3.3.8 SPICE model of the differential mode gain of the subtractor. *The two traces show gain in dB against frequency in Hz. The top trace is the output of the whole subtractor and the bottom trace is the voltage across* R_1.

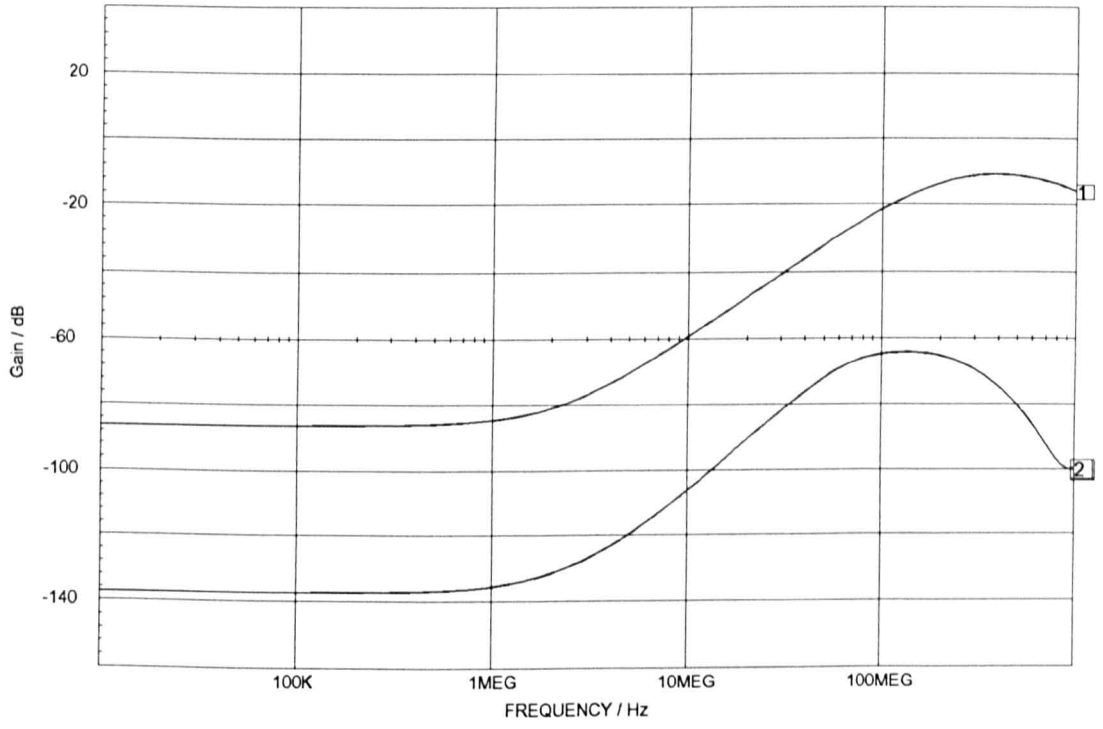

Figure 3.3.9 SPICE model of the common mode gain of the subtractor with all components matched. *The two traces show gain in dB against frequency in Hz. Trace [2] is the output of the whole subtractor and trace [1] is the voltage across* R_1.

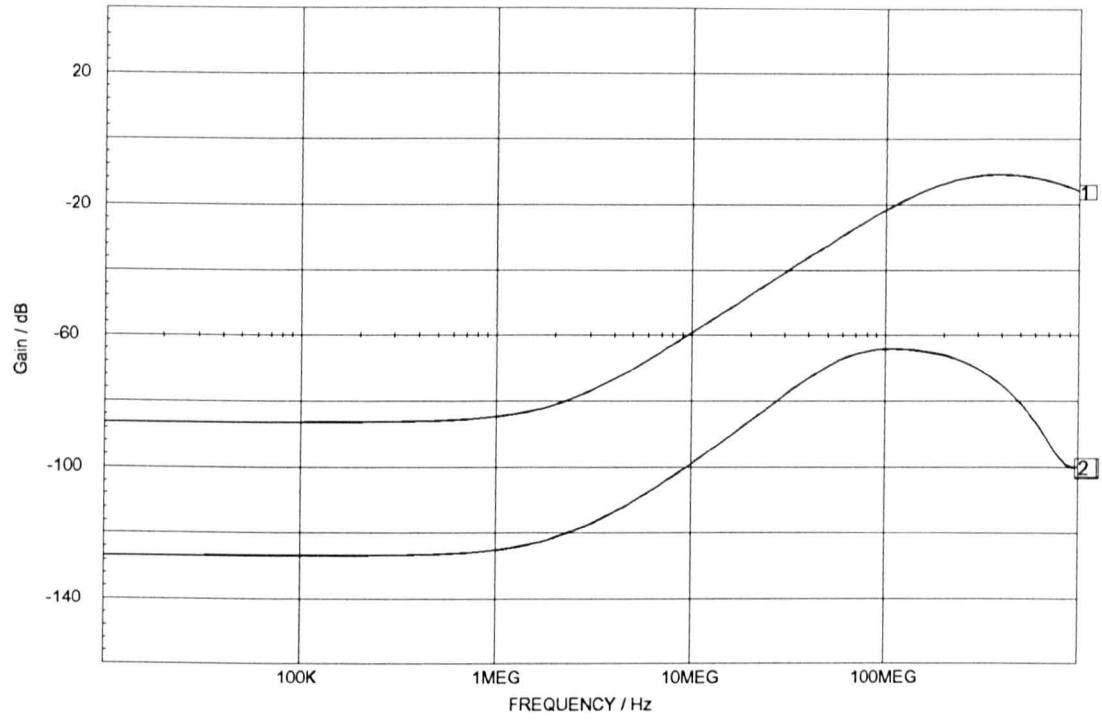

Figure 3.3.10 SPICE model of the common mode gain of the subtractor with all components matched except R_1 and R_2 which are mismatched by 1%. *Gain in dB verse frequency in Hz are shown for two traces. Trace [2] is the output of the whole subtractor and trace [1] is the voltage across* R_1.

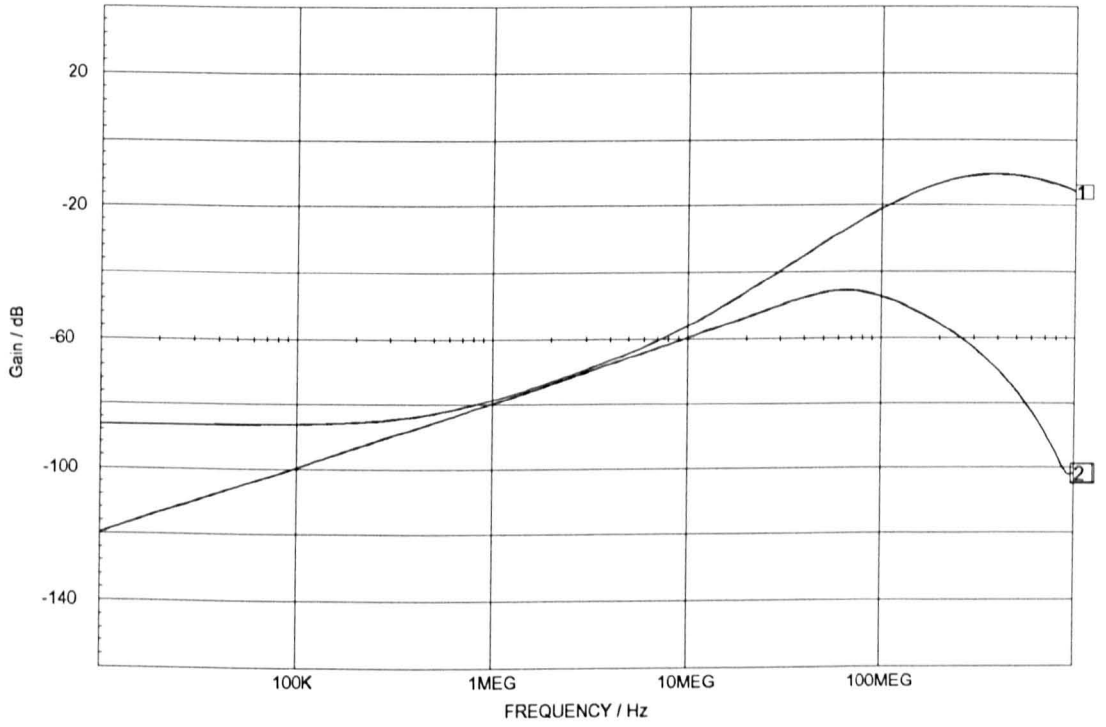

Figure 3.3.11 SPICE model of the common mode gain of the subtractor with all components but a 100 fF capacitor has been placed across the base and collector of Q_1. *The two traces show gain in dB against frequency in Hz. Trace [2] is the output of the whole subtractor and trace [1] is the voltage across* R_1.

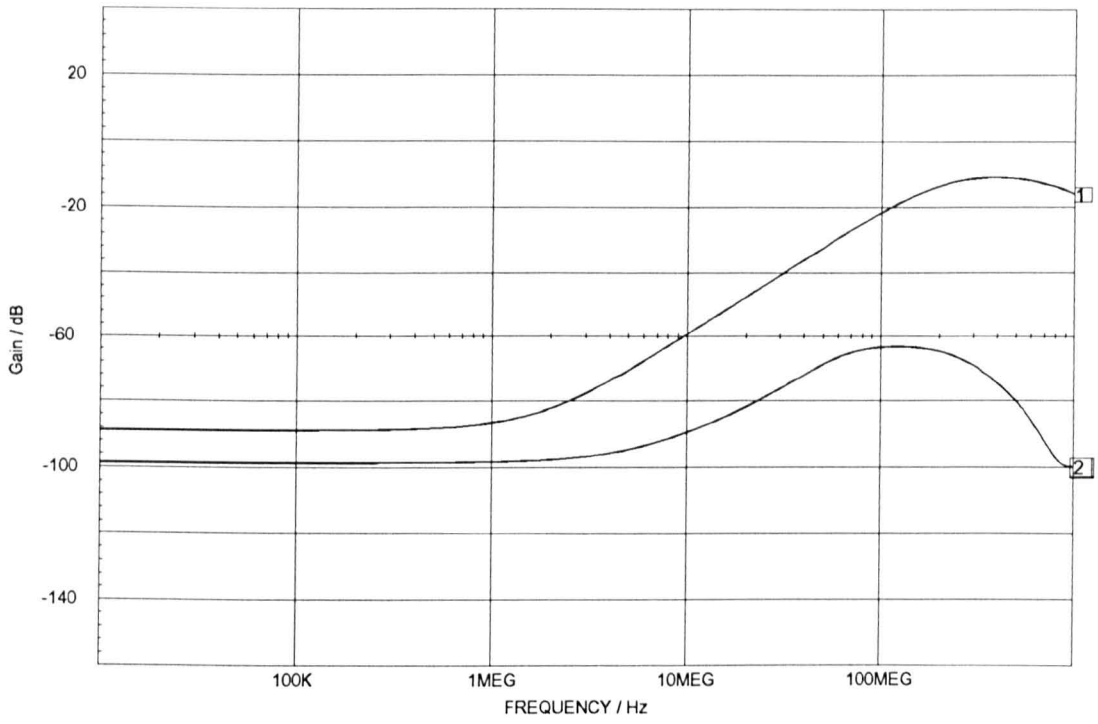

Figure 3.3.12 SPICE model of the common mode gain of the subtractor with all components matched except the Hfe of Q_1 and Q_2 which are 450 and 850 respectfully. *The two traces show gain in dB against frequency in Hz. Trace [2] is the output of the whole subtractor and trace [1] is the voltage across* R_1.

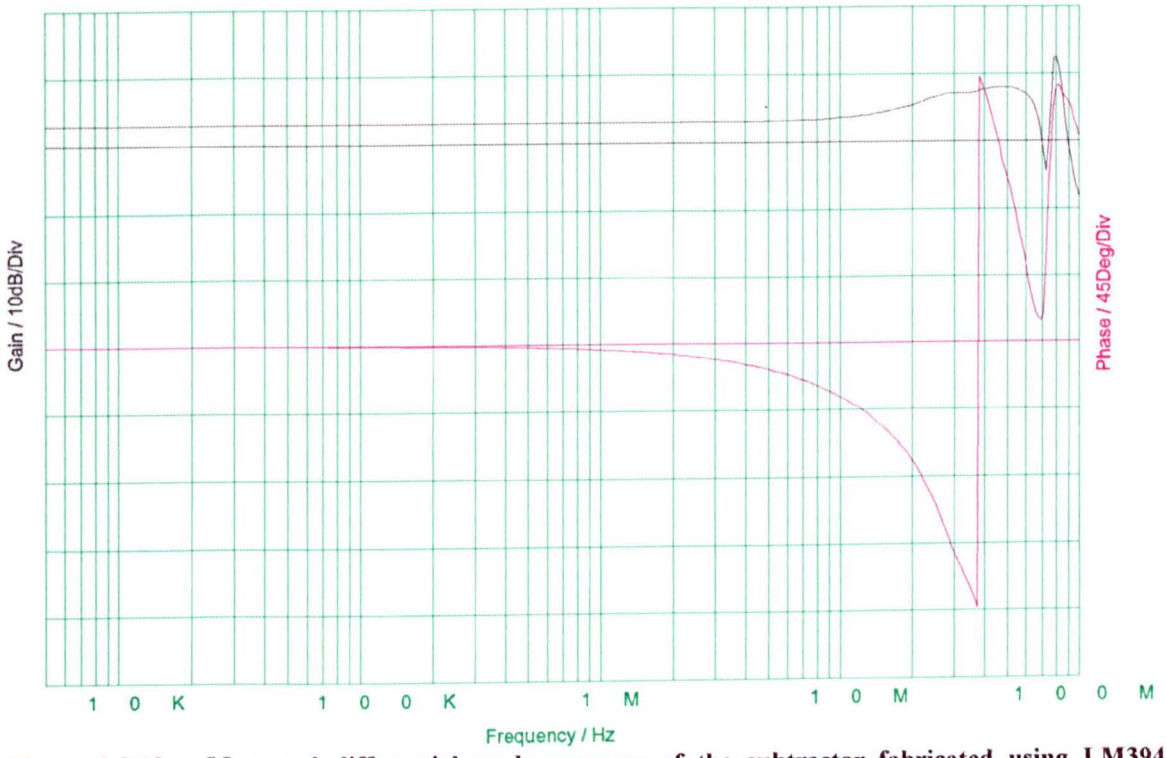

Figure 3.3.13a Measured differential mode response of the subtractor fabricated using LM394 matched transistors. *Gain shown in black and the horizontal black line represents 0 dB. Phase shown in red and the horizontal red line represents 0 degrees. Frequency is swept from 5 kHz to 100 Mhz.*

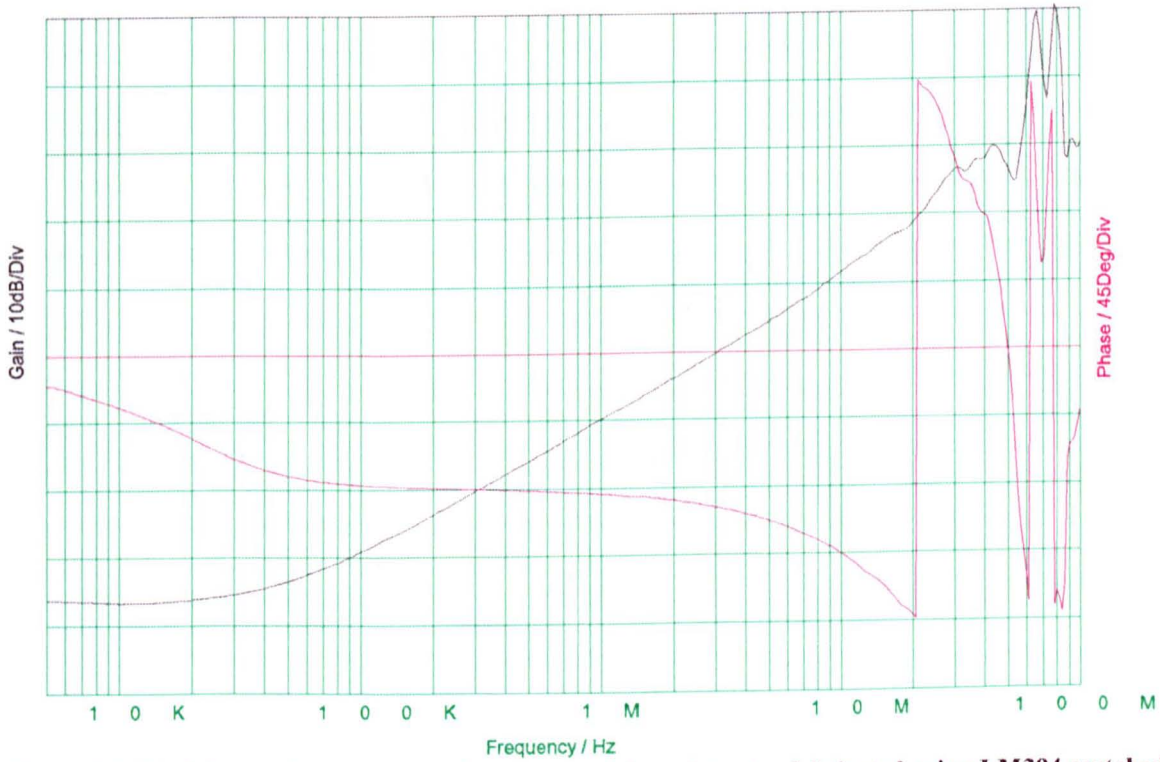

Figure 3.3.13b Measured common mode response of the subtractor fabricated using LM394 matched transistors. *Gain shown in black and the horizontal black line represents 0 dB. Phase shown in red and the horizontal red line represents 0 degrees. Frequency is swept from 5 kHz to 100 Mhz.*

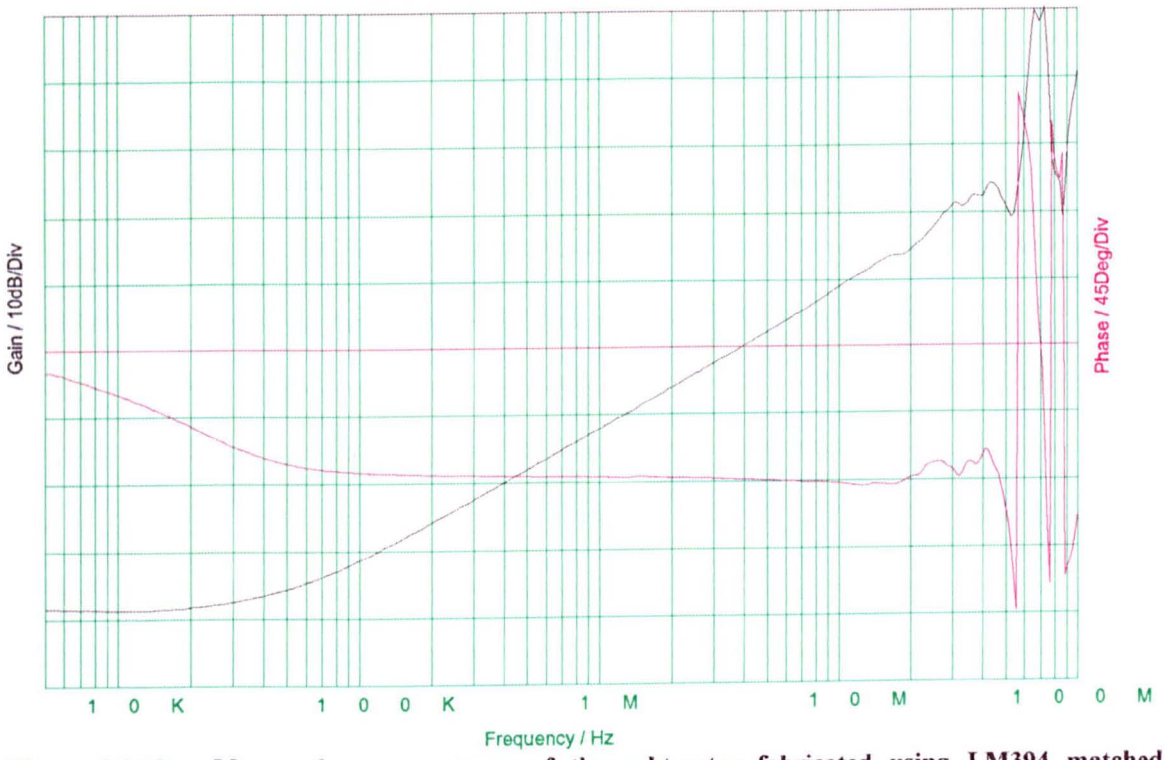

Figure 3.3.13c Measured cmrr response of the subtractor fabricated using LM394 matched transistors. *Gain shown in black and the horizontal black line represents 0 dB. Phase shown in red and the horizontal red line represents 0 degrees. Frequency is swept from 5 kHz to 100 Mhz.*

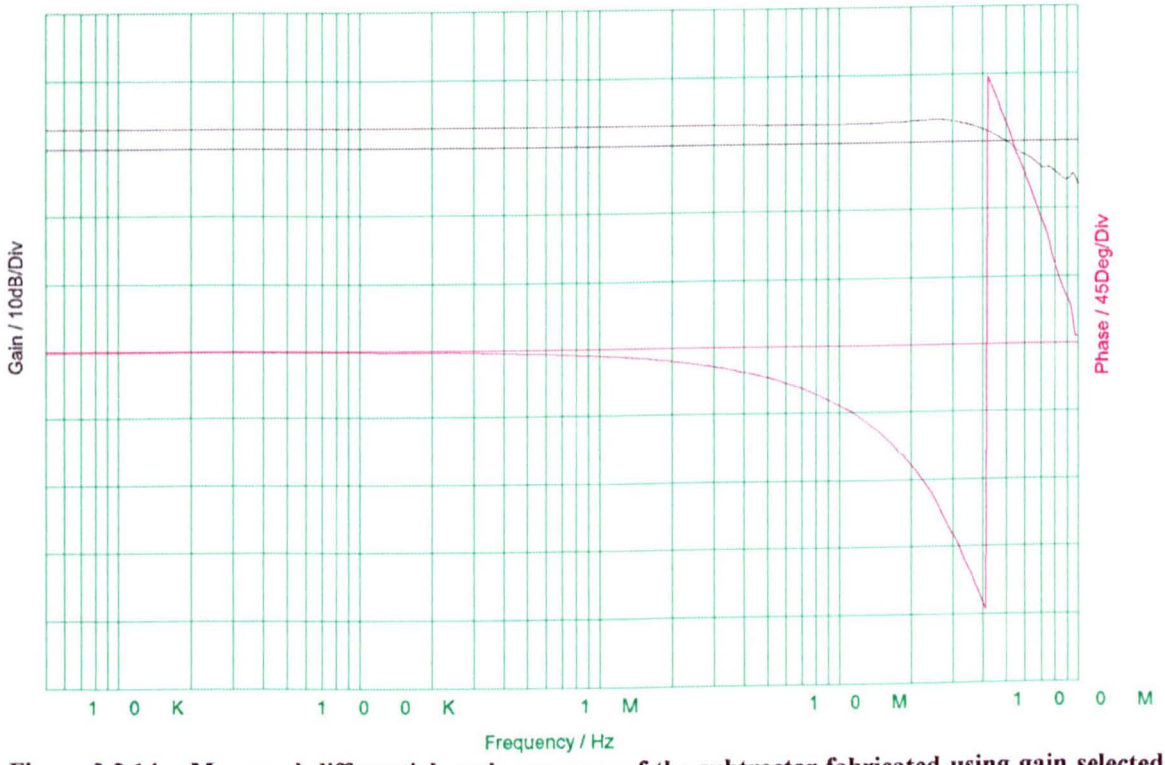

Figure 3.3.14a Measured differential mode response of the subtractor fabricated using gain selected transistors (BC184C). *Gain shown in black and the horizontal black line represents 0 dB. Phase shown in red and the horizontal red line represents 0 degrees. Frequency is swept from 5 kHz to 100 Mhz.*

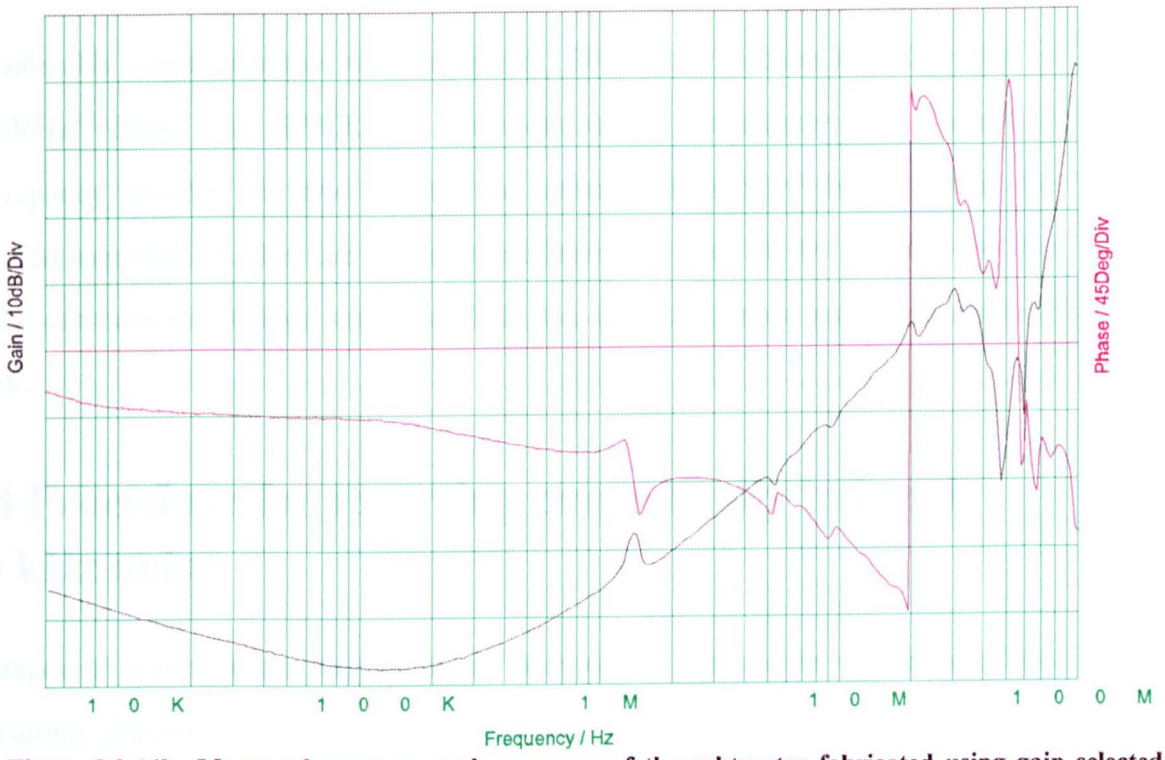

Figure 3.3.14b Measured common mode response of the subtractor fabricated using gain selected transistors (BC184C). *Gain shown in black and the horizontal black line represents 0 dB. Phase shown in red and the horizontal red line represents 0 degrees. Frequency is swept from 5 kHz to 100 Mhz.*

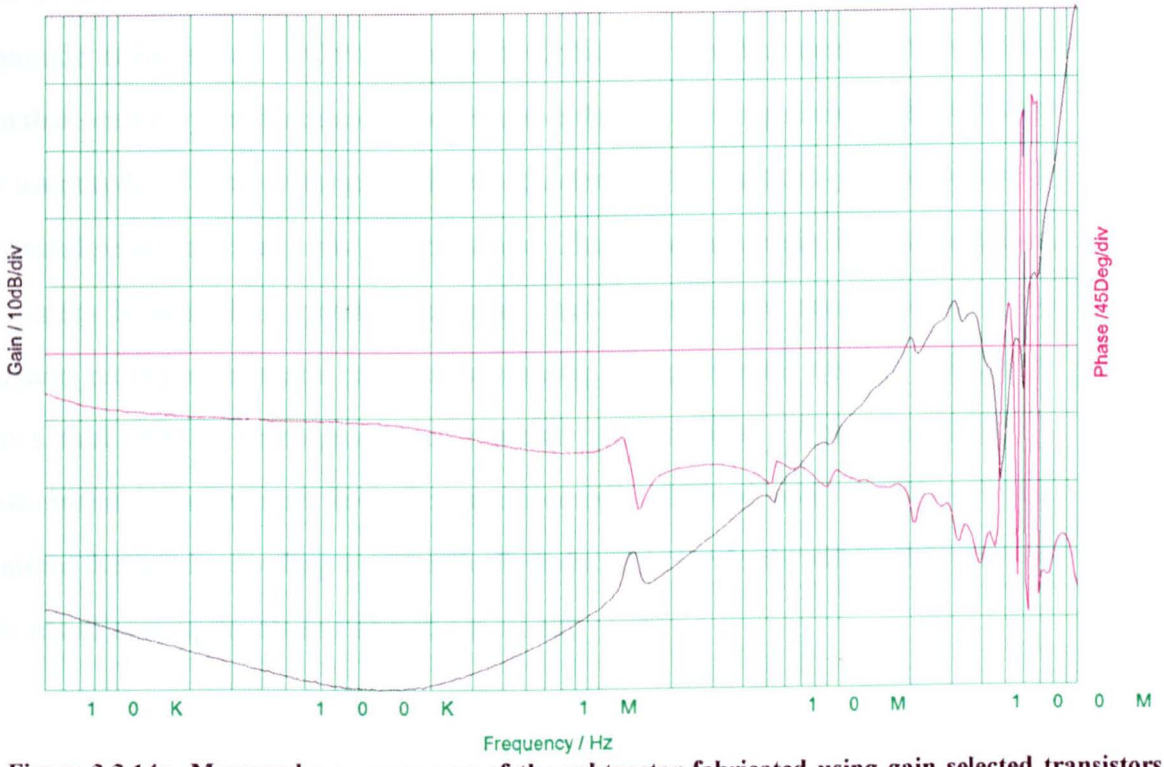

Figure 3.3.14c Measured cmrr response of the subtractor fabricated using gain selected transistors (BC184C). *Gain shown in black and the horizontal black line represents 0 dB. Phase shown in red and the horizontal red line represents 0 degrees. Frequency is swept from 5 kHz to 100 Mhz.*

considerable variation in the value measured. 30 $nVHz^{-½}$ is more than the value of 15 $nVHz^{-½}$ found using SPICE. No work was carried out to ascertain the source of discrepancy between the two because the value of 30 $nVHz^{-½}$ is still within the required specification. For the measurement bandwidth used of 100 Hz the noise due to the subtractor is 300 nV which is 80 dB less than the largest measured signal of 4 mV.

3.4 Procedure for removing magnetically induced 50 kHz noise

Voltages of an unknown magnitude are unavoidably induced in the leads of the measuring system. This is because the magnetic field induced by the coils not only couples with the body, hence inducing the desired current, but also couples with the leads of the measuring system having the effect of inducing voltages of unknown magnitude in these leads. Consequently the voltage at the electrode will be different from that sensed by the instrumentation because there is a voltage induced in the leads. The magnitude of these voltages will be dependent on the system's geometry, that is the spatial position of the coils and the leads. This effect can easily be removed from the system because it is possible to take a set of reference measurements. The reference measurements are made by measuring the peripheral voltage differences from a tank with a homogeneous conductivity distribution. When this reference measurement is subtracted from the measurements obtained with an object in the phantom, the spurious voltages magnetically induced in the leads will be the same for both sets of measurements and so will cancel out.

3.5 Conclusions

The instrumentation built was able to meet the desired specifications for the system which are that the system must be able to measure a 4 mV signal to an accuracy of 1 part in 1000 in the presence of a 10 mV cm signal. The performance of the system's components is summarised in table 3.5.

The network analyser used a bandwidth of 100 Hz which implies that the equivalent input noise of the instrumentation was 500 nV. The largest signal measured at the electrodes was 4 mV for a 19 mm insulating rod placed next to the electrodes and this implies a dynamic range of 78 dB. It would be possible to reduce the errors generated by random noise by reducing the bandwidth but the errors in the measurements would not be reduced significantly because the main source of error is the limited cmrr. The cmrr in the system described is not limited by the subtractor but by the gain errors introduced by the cables and the buffers. The results of this analysis have shown that the cable mounted buffers limit the system's performance and work by Mohd-Zainon[32] has subsequently been carried out successfully in which the buffers are mounted next to the electrodes .

Parts of the system were capable of performing in excess of the specification. The subtractor is able to function within the specification of a cmrr of better than -70 dB up to 5 MHz. Frequencies as high as 5 MHz are being used by some researchers who are building wide bandwidth impedance tomography systems in order to characterise different body tissue types [13] and this subtractor could be very useful to improve the performance of their systems. The current system has been built for evaluating the use of induced currents for impedance imaging and has not been optimised for speed of measurements. The speed of the measuring system could be greatly increased in a number of ways. For example by using 3 slightly different frequencies to drive each coil current and then simultaneously measuring all 16 electrode pair potential differences, it would be possible to make all 48 potential difference measurements in

the time it currently takes to make one measurement. The feasibility of driving simultaneously all 3 coils at different frequencies has not been investigated and there may be substantial problems to overcome, not least cross-coupling between the coils.

System Performance					
Frequency		20	50	500	kHz
subtractor	cmrr	-94	-98	-95	dB
	largest cm signal	17	17	16.5	V_{p-p}
	largest dm signal	2.9	2.9	2.7	V_{p-p}
	equivalent input noise	30			$nVHz^{-½}$
multiplexer [29]	cmrr	-102	-94	-75	dB
	cross talk	<-90	<-90	<-90	dB
buffer	input impedance	100 j7.9	100 j3.2	100 j0.32	MΩ MΩ
	equivalent input noise	25			$nVHz^{-½}$
overall (including 1 m cables)	cmrr	-70	-70	-70	dB
	cross talk	-95	-89	-71	dB
	equivalent input noise	50			$nVHz^{-½}$

Table 3.5 Performance of the modified system electronics.

Chapter 4 Validation of the Finite Element Method

4.1 Introduction

This chapter discusses the methods used to compare data measured from the experimental phantom with data from the Finite Element Method. In order to generate a reconstruction algorithm, it is necessary to have detailed knowledge of the fields within the body being investigated and the Finite Element Method (FEM) described in chapter 2 was developed in order to calculate these fields.

In producing the FEM certain approximations about the physical behaviour of the system were made, including:

- the current induced to flow within the body has no significant effect on the inducing magnetic field;
- the distribution of the fields within the body can accurately be represented by the spatially quantized mesh used by the FEM;
- any space phase effects are insignificant at 50 kHz over the dimensions of the tank.

In order to use FEM the problem must be set up in a form that can be solved by the FEM solver and the results must be processed in order to extract data in a useful form. To perform these tasks, the technique of FEM requires the production of several thousand lines of code, and as with any complex system, extensive testing is required to check that it is functioning as required. This chapter describes some of the procedures used to compare the results of the FEM program with both an analytic solution and the data obtained from the experimental phantom.

4.2 Comparison between the current patterns obtained from the 2-D analytic solution and those of the FEM

Figure 4.2.1 shows the current paths calculated for a homogenous conductivity distribution using both the FEM and the analytic method used by Anderson[21] described in chapter 2. The physical arrangement of the test phantom, coils and electrodes are as described in chapter 3. The results obtained from the analytic solution are on the right, the results from the FEM for a pseudo 2-D geometry are on the left. The top pair of figures show the current induced when only coil 1 is driven and the bottom pair show the current induced when coils 2 and 3 are driven in antiphase. The two current null pattern shown in the bottom pair is typical of the current patterns used by the reconstruction algorithm developed by Purvis[9]. Both pairs of results are very similar. The only noticeable difference is that the arrows representing the vector field of the current are centred at different locations; the arrows for the analytic solution are centred on a Cartesian grid whilst those of the FEM solution are placed at the centre of the elements used to construct the mesh.

A comparison of the peripheral profiles generated by the two methods of solution is shown in figures 4.2.2b to d in which the scale for the voltage difference is chosen arbitrarily to fit the graph. In these figures the top set of three profiles is generated by the analytic method and the bottom three profiles show the results from the FEM. These two methods were used to solve the potential distribution for the conductivity distribution of the phantom shown in figure 4.2.2a for three different target locations. Each of the three graphs below the profiles show the values of the potential differences for the two profiles plotted against each other with a false origin and demonstrate a highly linear relationship. The correspondence between the two will not be perfect because the two simulations were not for identical situations, the analytic method modelled the target as a circle and the FEM modelled the circular target using quadrilateral elements. Without detailed knowledge of the size of error that this might induce, it was not possible to quantify the quality of fit between the two but the above

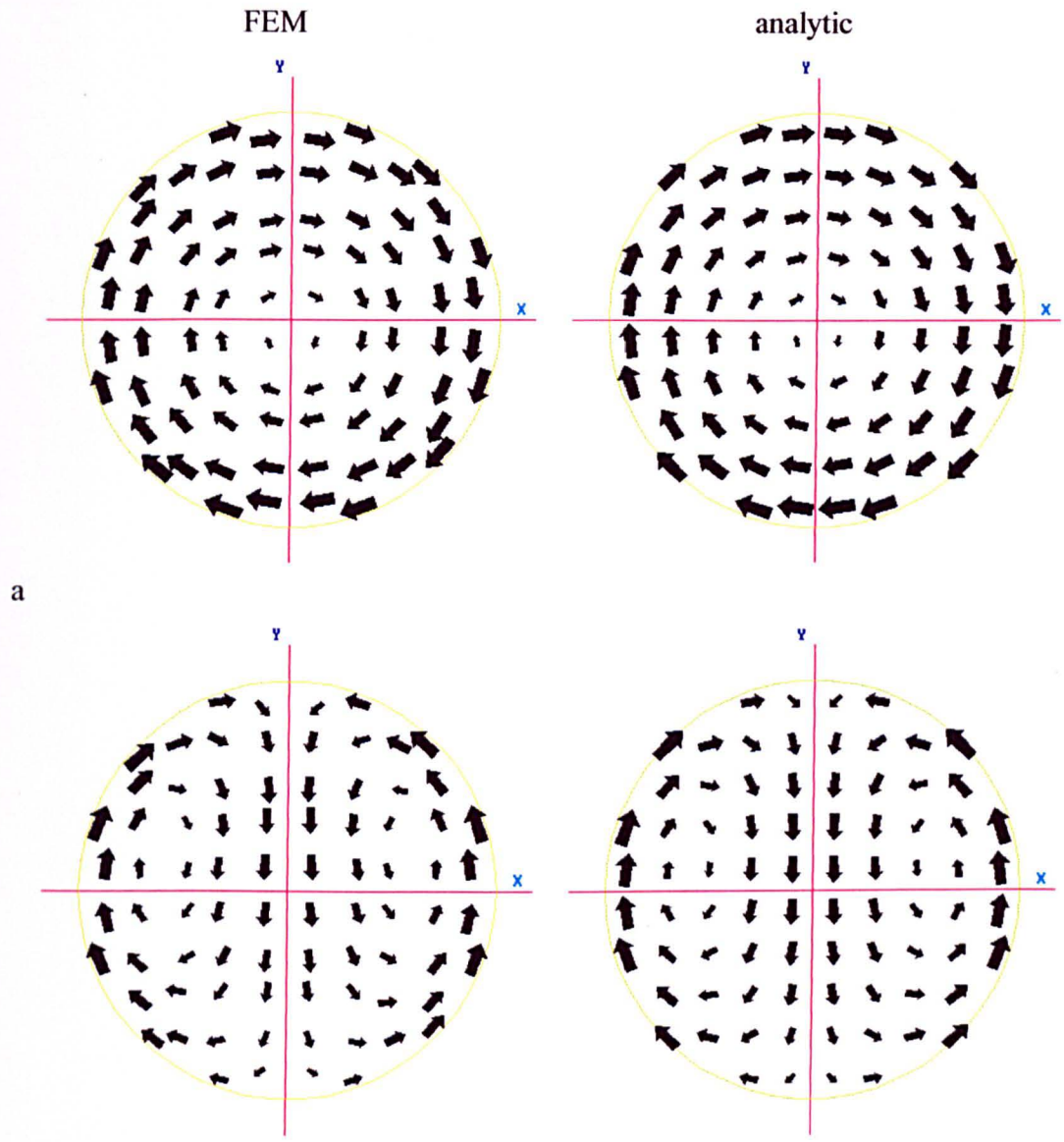

Figure 4.2.1 Maps showing the Current distribution found using the analytical method and the FEM for pseudo 2-D geometries. *Figure 4.2.1 a shows current induced by exciting coil 1 and figure 4.2.1 b shows current induced by exciting coil 2 and 3 in antiphase. Arrow area is proportional to current density.*

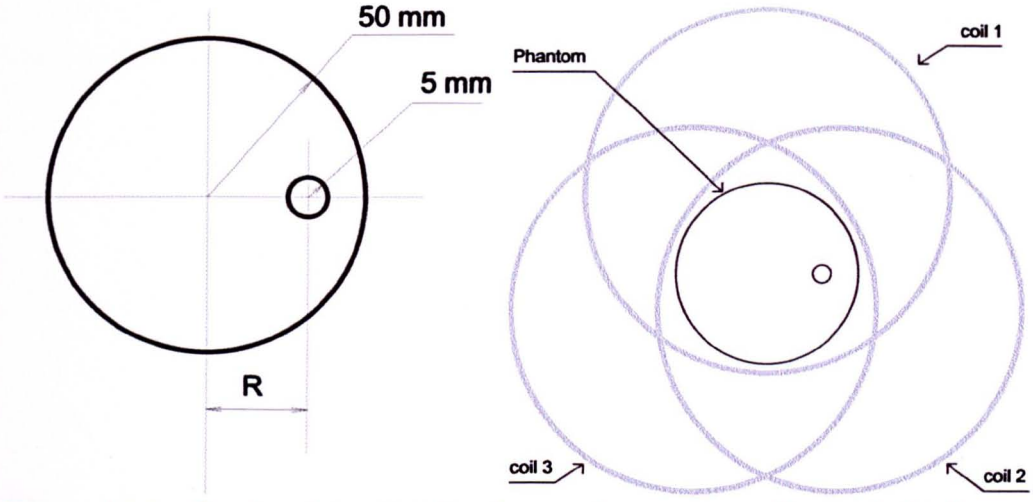

Figure 4.2.2a Conductivity distribution used to compare the analytically simulated data and that simulated by FEM for Pseudo 2-D geometries. Both sets of data are for an insulating target placed on the X axis. The results for 3 different values of R are shown in 4.2.2b..d. *The tank for the FEM simulation was set to a height of 10mm above and below the electrode plane and the target used spanned the entire length of the tank.*

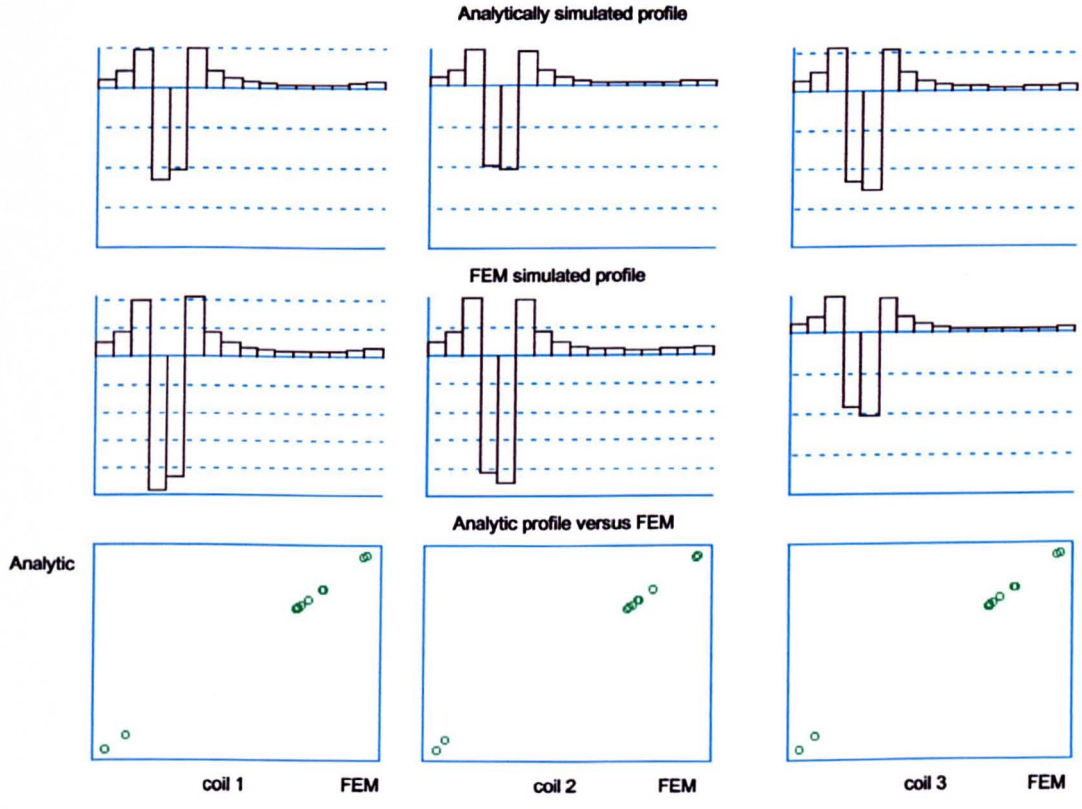

Figure 4.2.2b Target at radius R=42mm. *Each of the three sets of results are in the following form:- The top row of 3 bar graphs show peripheral voltage profiles from the analytic solution for coils 1,2 and 3. The bottom row of 3 bar graphs show the results from the FEM. The x-y graphs plot the magnitude of the voltage differences calculated using the analytic solution versus those calculated by the FEM.*

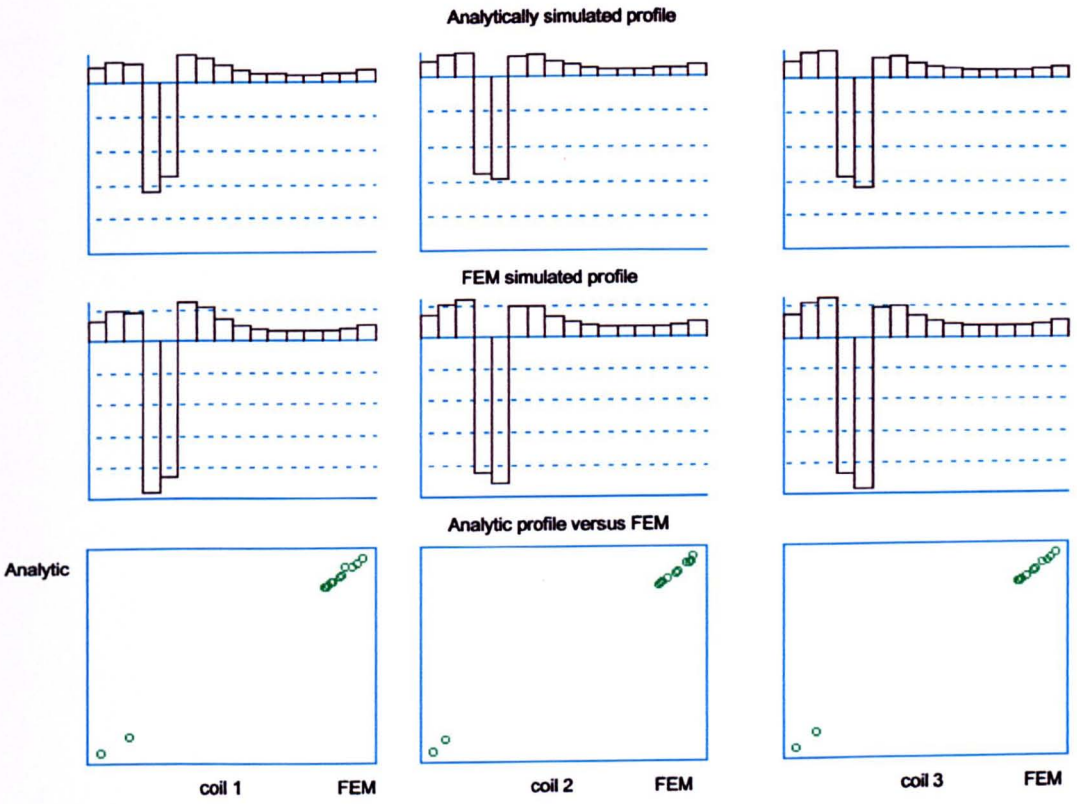

Figure 4.2.2c Showing the same graphs as 4.2.2b but R= 34 mm

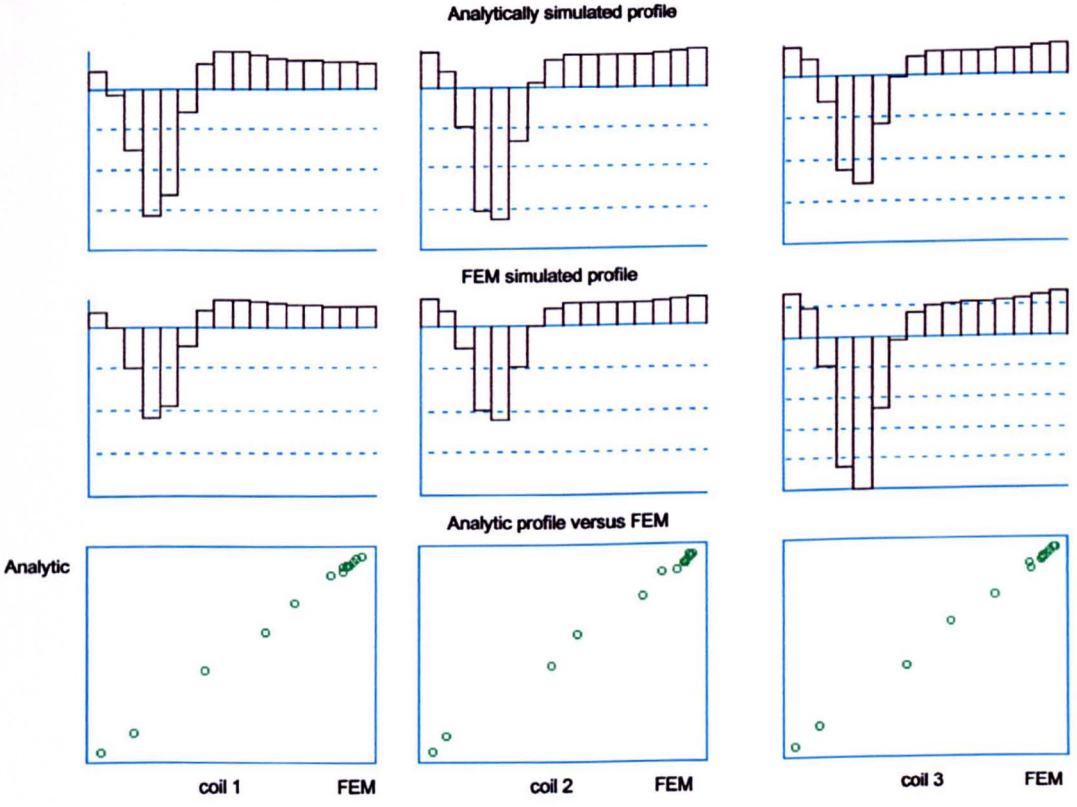

Figure 4.2.2d Showing the same graphs as 4.2.2b but R= 19 mm

results show reasonable, if unquantified, agreement between the result for the 2-D analytical method and a pseudo 2-D FEM. The agreement might be improved if a finer mesh was used.

Results obtained by the FEM and the analytical methods have been compared showing that for 2-D situations they produce similar results. Fundamental approximations of a similar nature are used in both methods. So far the FEM has not been tested against results for the more general 3-D situation.

A more rigorous and general test for the FEM was carried out by comparing the values it predicted with those measured from a phantom and an experiment aimed at quantifying the agreement between measured and simulated data for both 2-D and 3-D situations is described in the next section.

4.3 Comparison of voltage profiles obtained from measurements and FEM simulations

The instrumentation system was set up as described in chapter 3. It was connected to the experimental phantom which has adjustable depth and a fixed diameter of 103.5 mm and the tank was filled with saline. The tank was levelled by using shims under its feet.

The depth was first set to ±10 mm. This was achieved by moving the bottom plunger to 10 mm below the electrode plane and filling the phantom with saline of conductivity 1 Sm^{-1} to 10 mm above the electrode plane. Rods which were sufficiently long not to be completely submerged were placed in the tank. To improve the positional accuracy of placing the rod, the plunger was marked with lines at 5 mm intervals from the centre and 16 radial lines and the bottom of the rods were marked with 1 mm circumferential lines. The rod is made of clear polymethylmethacrylate resin, so to place it in the tank involves lining up the graduations on its underside seen through the rod and the markings on the plunger at the bottom of the phantom. This process allows the rod to be placed to an accuracy of about 0.5 mm. Once placed, two sets of measurements

were taken, first with this object in the tank and then with the object removed. These two sets of 48 measurements each correspond to the foreground and reference sets respectively.

This process was also repeated for a tank of ±200 mm. For this arrangement, two test objects were used. The first was a long rod of 19 mm diameter made of polymethylmethacrylate resin which was sufficiently long not to be completely submerged in the 400 mm total depth of the tank and the second was a short rod which was submerged.

The effect of the displacement of the saline by the rod (119 ml or a change in height of 14 mm) was checked by making a measurement and then removing 119 ml of saline and retaking the measurement. The changes in the peripheral voltage so produced were smaller than the noise of the measuring system. To quantify this, the results of this experiment were also calculated using the FEM model for both the short and long phantoms and the error induced by not maintaining the fluid level was 165 nV and 30 nV for the ±10 and ±200 mm phantoms respectively. The ratio of 2 mV, the peak simulated electrode pair difference for the homogeneous set-up, to 165 nV and 30 nV is greater than 80 dB and 95 dB respectively. Chapter 3 discussed the required specification for the dynamic range of the instrumentation which was of the order of 60 dB. Consequently an error of 80 dB smaller than the peak signal would be undetectable and it was concluded that there was no need to maintain the fluid level during the experiments with either the short or the long phantom. Because the resin is slightly opaque, it is not possible to see through a 400 mm rod and the position of the object was set by observing the graduations through the plunger in the bottom of the tank which was made of the same polymer. The positional accuracy for this experiment is in the order of 2 mm because of the difficulty in placing a rod 0.5 m long accurately on the bottom of the tank by manipulating the top of the rod.

The other test object used was a rod 20 mm high and of diameter 19 mm made of the same clear polymer. This was suspended from a plate at the top of the tank by a fine thread. It is important that the tank had been levelled in order to ensure that the top of the tank was directly above the ring of electrodes. In this way the position of the suspension would directly correspond to the position of the target with respect to the electrodes. The positional errors from this positioning method were again estimated to be about 2 mm.

A mesh editor was designed to allow any arbitrary conductivity distribution to be described in a form that the finite element program could interpret. Using this editor the desired conductivity distribution was defined. The exact shape and position of a circular rod cannot be reproduced in a finite mesh of hexahedral elements as shown in figure 2.5.1b so positions were chosen for the rod such that they would lie conveniently on the mesh. The shape of the rod was approximately reproduced using the quadrilateral elements of the mesh. The conductivity was set for the rods at 10^{-3} Sm^{-1}. A better representation for the polymethylmethacrylate resin would be to use a conductivity of zero but the FEM programme was configured such that extremely low conductivities would cause the solution to be dominated by rounding errors. This value of conductivity was chosen because for background conductivity of 1 Sm^{-1} and a target of conductivity 10^{-3} Sm^{-1}, the difference between this target and a target of conductivity 10^{-5} Sm^{-1} will only make a maximum difference to the potential distribution of 1 part in 10^4 and therefore be impossible to measure.

The method involved in obtaining a set of measurements from the experimental system was now repeated for this model. First the FEM was used to solve the field distribution for a homogeneous conductivity distribution and from the resulting array of nodal potentials, the electrodes' potentials were extracted and the electrode potential differences found. Then the process was repeated with the target in position. From these two data sets of modelled electrode potential differences, the potential change due to the introduction of the target was found by subtraction. We now have a set of

experimental data and simulated data which should, within expected experimental error, be linearly related. The constant of proportionality will depend on the gain of the instrumentation. To establish the extent to which the results of the model agree with the experimental measurements requires a statistical analysis. This is not a trivial task and it will be discussed in the next section.

4.3.1 Statistical procedures for the comparison of results obtained experimentally and from the FEM

Experimental results are subject to error which can be assessed using statistical methods. The statistical analysis allows us to examine the difference between two sets of data in terms of the estimated error in making the measurements.

In the experimental system a subtractor is used to find the difference in the potential between two electrodes. This subtractor has a gain, as do other parts of the system. This has the effect that the simulated results will not be equal to but should be linearly proportional to those measured, the constant of proportionality being the gain of the measuring system. The gain has three sources. Firstly there is the subtractor gain. Secondly there is an apparent gain because the value of the coil current is obtain by measurement of the voltage across a 0.1 Ω resistor which multiplies the transferred impedance measurement by 10. Thirdly the coils have four turns giving a reduction factor of 4. In fact we can only measure potential difference which gives information on the conductivity change between measurements. As the average conductivity is not known, reconstructed conductivity maps will not be calibrated and so the absolute system gain is not relevant. For the purpose of the validation of the FEM all that needs to be shown is that this gain is the same for all compared results. The measurements will contain errors from sources such as Johnson noise generated within the object being measured and noise within the instrumentation system. Therefore a simple comparison of the results will not show whether or not the FEM is a good simulation of the physical behaviour of the system; account must be taken of the size of the expected

errors and whether those differences can be explained by the magnitude of the system noise.

A test as to whether two sets of data are proportional to each other is to plot them graphically and draw a "best fit line" through the points. Formally the line is fitted by minimising the error between the line and the points. Different methods are available for this and the one adopted here is the least squares method. χ^2 (chi-squared) is a value which statistically quantifies the difference between two measurements, normalised with respect to the standard deviation (σ) of the measurement. The value of χ^2 in isolation has no significance but it can be used to calculate the probability that the difference in measurements is significant or could be accounted for by experimental error. The χ^2 [33] used is a function of the y axis displacement of the actual points from the best fit line and it is normalised with respect to the RMS noise. Its value describes the quality of the fit between the two data sets.

The definition of χ^2 is

$$\chi^2(a,b) = \sum_{i=1}^{N} \left(\frac{y_i - a - bx_i}{\sigma_i} \right)^2 . \qquad 4.3.1.1$$

where :-

y_i : the measured potential difference between the i^{th} pair of electrodes

x_i : the corresponding potential difference calculated using FEM

a and b : the parameters for the straight line $y = a + bx$, found by minimising $\chi^2(a,b)$

σ_i : the RMS value of the noise in the measured data y_i

χ^2 is minimised by equating its partial differentials, with respect to a and b, to zero.

It is possible to calculate χ^2 for displacement in both the y and x directions but this would require knowledge of the errors in the x values. For given sets of input data the computer will generate the same result and therefore the errors contained in the result

cannot be analysed statistically. Hence the assumption was made that the x values are noise free and equation 4.3.1.1 was used which only accounts for errors in the y (measured) values and not in the x (simulated) values. This actually makes the statistical analysis we have used more stringent than it would be if knowledge of the error in the x value was available.

From χ^2, a probability Q is calculated.[33]

$$Q = f(\chi^2, df)$$

where df is the number of degrees of freedom which relates to the number of independent measurements and f is an incomplete gamma function. This function is tabulated in statistics books but there was available an algorithm [33] to calculate the value of Q directly.

The possible range of values is $0<Q<1$. A value of 0.01 would mean that in one hundred experiments on average one would yield a value of χ^2 greater than that used to calculate Q. Large values of χ^2 (small probabilities) could arise from three possible causes. The first is that we were unfortunate enough to chance upon a set of experimental data containing errors larger than would be expected statistically from the amount of estimated experimental noise. The second is that we have underestimated the magnitude of the noise so that the differences are not significantly greater than would be expected. The third is that we have a poor model and the data is not related. Conversely small values of χ^2 (probabilities close to unity) could also have three interpretations. First is that the model is good. The second is that the estimate of the errors is so large that even for a poor model the results would come within this error. The third that although the model is poor, we happen by chance to have a set of measurements which fit. We set a null hypothesis that the straight line model fits the data. Our decision as to whether or not to accept or reject this hypotheses will be based on the value of Q. The next section describes the methods used to find the magnitude of the noise value.

4.3.2 Description of the measurement process and the measurement of the system's noise

The instrumentation has been described in detail in chapter 3 and this system was set up to take measurements from the phantom. The measurement procedure is now described in detail.

First the relay to select an individual coil is activated by computer control over the IEEE 488 bus. The electrode pair is then selected by the computer, again over the IEEE bus. Once the coil and electrode pair are selected, the signal routed through the buffers, multiplexer and subtractor will appear at the input to the network analyser in order that it may be measured. The network analyser effectively passes this signal through a narrow bandwidth filter before it is measured. This filter's output will slowly settle to its final value. The computer must wait for the network analyser to settle and in the case of the 100 Hz bandwidth used, the time allowed for settling was 55 ms [34]. The output of the analyser may now be sampled. In practice it was found that the measured data occasionally contained glitches from events such as the switching of soldering iron thermostats. These could mainly be filtered out by sampling the network analyser twice. If the signal was obtained during a glitch, the rate of change of the sampled value would probably be high and the two measurements would be significantly different. A threshold value (10^{-4}V) was chosen and if the sample varied by more than this threshold, the signal was resampled until the two successive measurements were within this threshold. This process very significantly reduces the number of unsatisfactory measurement sets.

The first method employed to quantify the system noise was with a homogeneous phantom. The system was set up to measure one electrode pair and one coil. The output from the network analyser was then repeatedly sampled for 2000 samples which were stored for later analysis to find the RMS of the values.

The second method took account of the possibility that noise is generated when switching electrode pairs, a necessary part of the process during profile measurements. To investigate this possibility, before each measurement was made, the electrode pair was switched to the preceding electrode pair and then back. This process was repeated for 500 samples which were stored for subsequent determination of the RMS.

A third method was used to ascertain the level of the noise of the system. This takes account of all possible sources of error during the measurement process and was done by taking sets of measurements with a homogeneous tank. A total of 26 sets of measurements for three coils were made. This method contains the sum of two noise measurements and comparison between the sets of measurements is made below.

The results of the three different methods is tabulated in table 4.3.1.

	method 1	method 2	method 3
number of samples	2000×16	500×16	26×48
RMS noise /μV	40	39	86

Table 4.3.1 System noise found by 3 different methods.

The value found for the noise from method one and two are very similar and it can be concluded that no extra noise is introduced by switching the electrodes.

The results of method 3 shows a level of noise considerably greater than the other two. It would be expected that this value of noise would be $\sqrt{2}$ times the noise of the measurements for one electrode pair. This is because two measurements have been made and then subtracted from each other. If two uncorrelated noise signals are added then the resultant signal can be found by finding the square root of the sum of the squares of the two noise signals. The value of 86 μV is to be compared with the

average for the electrodes individually which is approximately 40 μV. It can be concluded that during a set of measurements there is an extra source of noise of

$$\sqrt{(8.6\cdot10^{-5})^2 - 2\cdot(4.0\cdot10^{-5})^2} = 65\ \mu V$$

The source of this noise has not been investigated further.

Electrode pair 15 is more sensitive to noise than the other pairs because it is connected to the two extreme sides of the instrumentation. This has the effect of increasing the cross sectional area of the loop formed by the wires from the instrumentation to the phantom. This loop couples with the exciting magnetic field and the potential induced round the loop will be proportional to its area and so will be larger for electrode pair 15. Thus the voltage measured at pair 15 is significantly greater than that at the other electrode pairs and measurements show that the factor is typically 5.4 times as great. The expected difference in the two measured voltages at any pair of electrodes will be similar and hence the required dynamic range for electrode pairs 15 will be greater than for all other pairs. Consequently the demand made on the instrumentation for pair 15 is greater than for the other pairs and the expected noise for this pair will be greater. This has the effect of distorting the total noise statistics for the whole system because the error from pair fifteen will always be greater than for the other electrodes.

It was decided to use the values of noise obtained by taking two measurement sets from the same conductivity distribution because this would most accurately simulate the measurement process. More work is required to ascertain the source of the discrepancy between the different methods used to measure the noise. The magnitude of the noise used in the subsequent statistical analysis was 86 μV.

4.3.3 Results

Many sets of measurements were taken to compare the results obtained from the FEM and those from the experimental system for different conductivity distributions. A selection of these is shown in a graphical form with the straight line drawn through the

points. Error bars are displayed with a length of one RMS value of the noise above and below each point. Printed with each graph is the value of *b* which is the gradient of the line that corresponds to the gain of the system, together with the values of χ^2 and Q.

Figures 4.3.1b to d show a set of graphs from a simulation of a pseudo-2-D situation where the tank is ±10 mm in height containing an object of 10 mm diameter spanning the height of the tank, placed at three different radial positions as illustrated in figure 4.3.1a. For each position there are two bar graphs, the upper one showing the result of the simulation and the lower one showing measured values. Underneath each pair is a plot of the measured values on the y axis against the simulated values on the x axis. Visual inspection of each of these graphs show that the straight line fits the points quite well. Closer inspection reveals that the points have small error bars associated with them and the line does not pass through all the bars. This suggests that the fit is not quite as good as might be expected. The size of the noise is taken as constant with the value of 86 μV as calculated above. The graphs are auto-scaled so that the extreme points lie on the edges of the graph and the size of the plotted error bars are inversely proportional to the scale. Of the nine x,y graphs shown, only five have a value of Q greater than 0.001. A Q value of 0.001 implies that for the level of noise measured we would expect to find a poorer fit only 1 time in 1000. However the experimental method might introduce an extra source of error. If this error is not accounted for the statistical analysis will show a fit worse than should be expected.

It could be hypothesised that an additional source of error arises from inaccuracy in the positioning of the target within the tank. This positional inaccuracy would be described by two orthogonal components, one a radial displacement and the other circumferential. If an object is placed near to the edge, then the profile generated will show a sharp peak as illustrated in figure 4.3.1b. It will be shown in chapter 5 that the current in this region will usually be circumferential. If the current is purely circumferential in path, then the only effect of displacement of the target in a circumferential direction will be to move the peak of the profile voltage. We could test the hypothesis by not taking

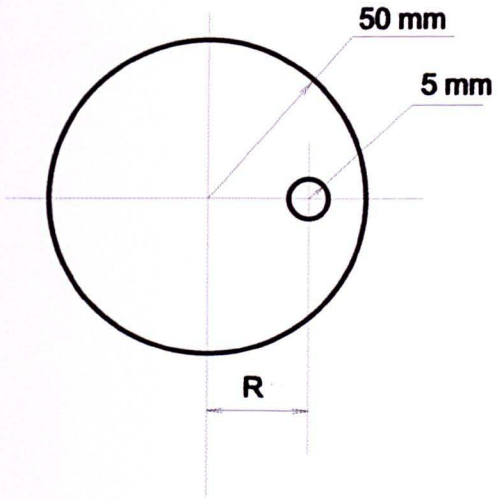

Figure 4.3.1a Conductivity distribution used to compare measured data and that simulated by FEM for Pseudo 2-D geometries. Both sets of data are for an insulating target placed on the X axis. The results for 3 different values of R are shown in 4.3.1b..d. *The tank for both the simulation and the measurements was set to a height of 10mm above and below the electrode plane and the target used spanned the entire length of the tank.*

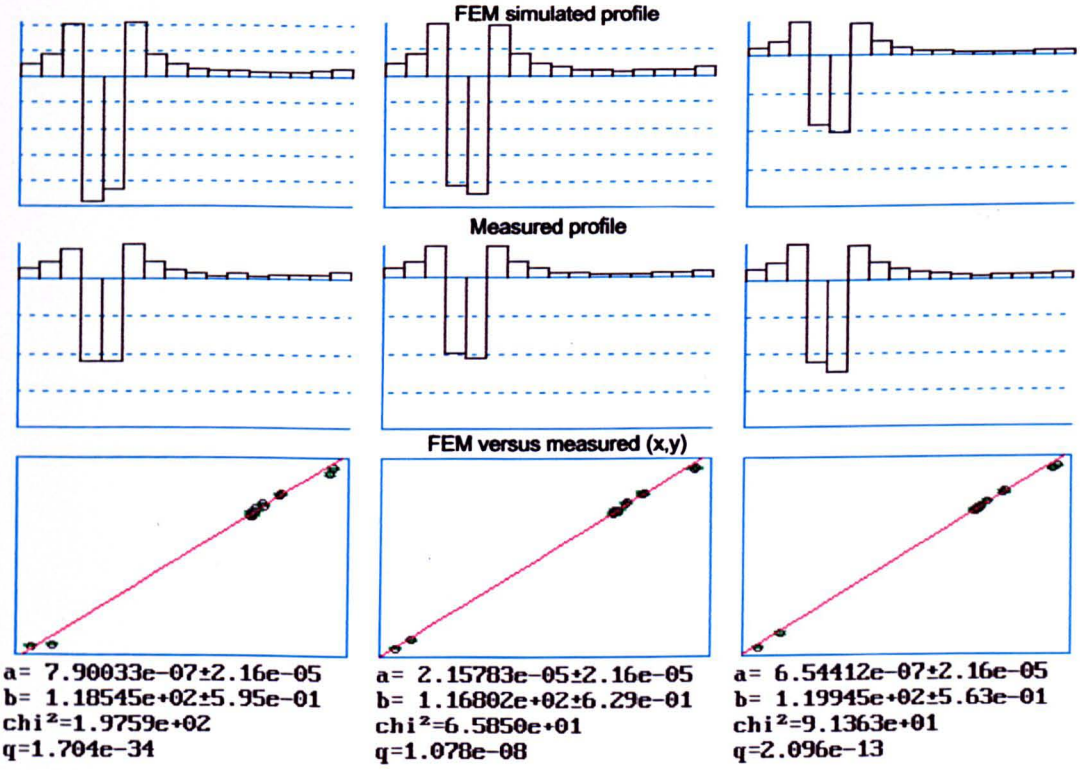

Figure 4.3.1b Target at radius R = 42 mm. *Each of the three sets of results are in the following form:- The top row of 3 bar graphs show the results from the FEM for coils 1,2 and 3. The bottom row of 3 bar graphs show the measured peripheral voltage profiles. The x-y graphs plot the magnitude of the measured voltage differences versus those calculated by the FEM.*

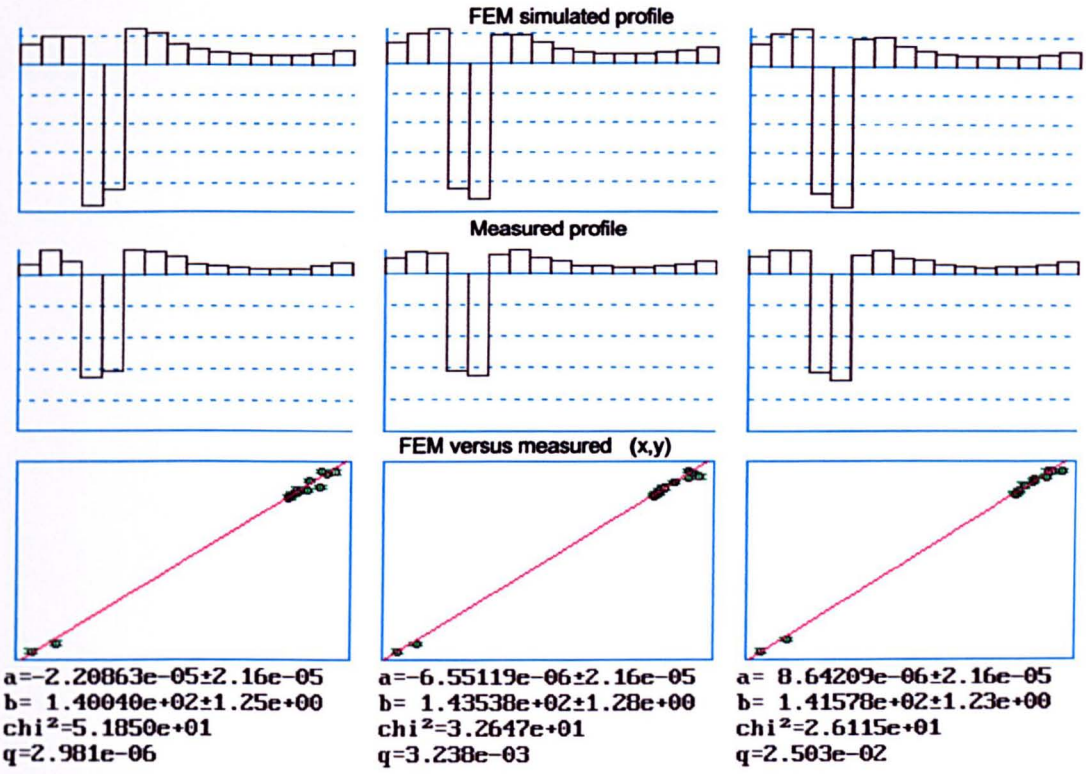

Figure 4.3.1c Showing the same graphs as 4.3.1b but R= 34 mm

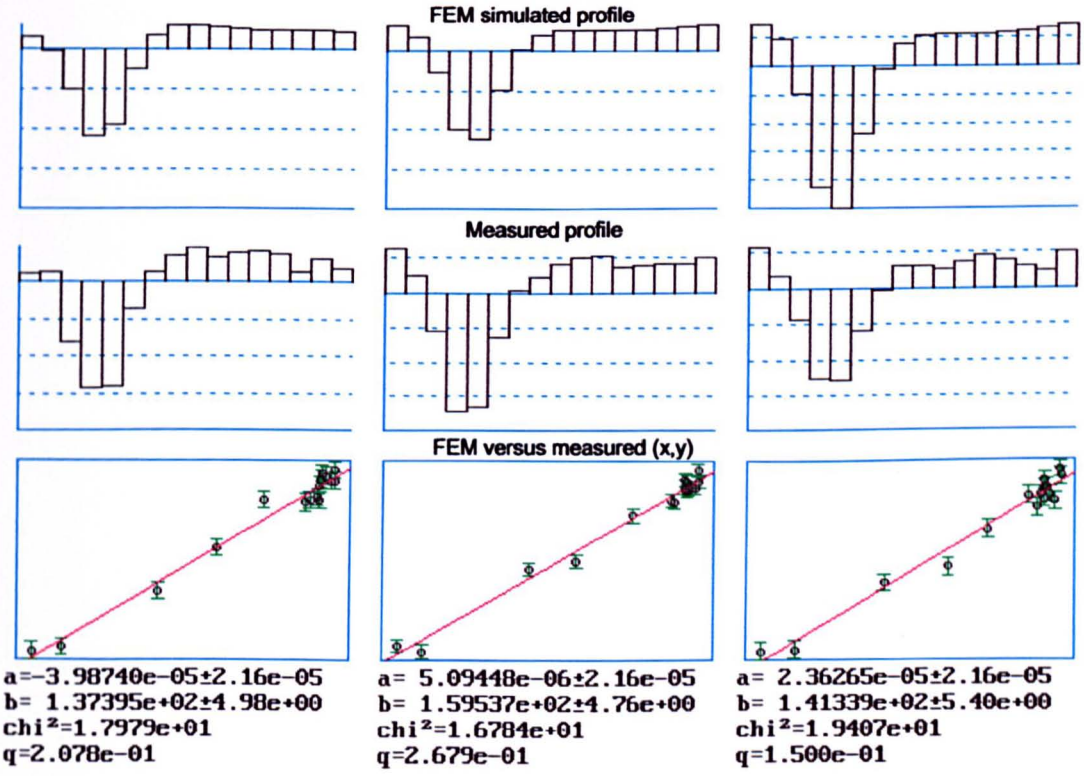

Figure 4.3.1d Showing the same graphs as 4.3.1b but R= 19 mm

account of the positional information within the profile. A possible technique to do this would be to take the Fourier transform of the two sets of data. Positional information is contained in the Fourier transform but it is in the form of the phase of the complex components and it can be ignored by using only the magnitude of the transformed data. These magnitudes of transformed data for both the measured and simulated data could be plotted against each other and if the poor fit was due to positional error of the object, we would expect the fit of the line to improve for transformed data. A condition of this argument is that the magnitude of the Fourier transform of the data will only be independent of the circumferential position of the target if the data is sampled frequently enough. The problem is that the profile is sampled at 16 points round the circumference meaning that for this set of samples to be an accurate description of the actual signal, the signal must be band limited to a maximum of 8 cycles (or two electrode spacings, which is the Nyquist sampling criterion). Our profile is clearly not band limited and so high frequency components within the profile will be aliased, and therefore the Fourier transform will not be capable of displaying complete angular invariance.

The estimate of the error and the size of the error bars will require some scaling for the graphs of the transformed data. The size of this scaling factor can be found by consideration of Parseval's theorem [33], the discrete form of which is :-

$$\sum_{k=0}^{N-1}|h_k|^2 = \frac{1}{N}\sum_{n=0}^{N-1}|H_n|^2 \qquad 4.3.3.1$$

where h_k is the raw data and H_n is the transformed data for the 16 values of n. Parseval's theorem equates the energy in the signal in both the time and frequency domains.

The variance of a signal is defined as:-

$$variance = \frac{1}{N}\sum_{k=0}^{N-1}|h_k|^2 \qquad 4.3.3.2$$

This could be substituted into the left hand side of the Parseval's theorem casting it into the form of equating variance rather than energy, i.e.

$$\frac{1}{N}\sum_{k=0}^{N-1}|h_k|^2 = \frac{1}{N^2}\sum_{n=0}^{N-1}|H_n|^2 \qquad 4.3.3.3$$

This can be rearranged to give:

$$\frac{1}{N}\sum_{k=0}^{N-1}|h_k|^2 = \frac{1}{N}\sum_{n=0}^{N-1}\frac{1}{N}|H_n|^2 \qquad 4.3.3.4$$

or

$$\frac{1}{N}\sum_{k=0}^{N-1}|h_k|^2 = \frac{1}{N}\sum_{n=0}^{N-1}\left|\frac{1}{\sqrt{N}}H_n\right|^2 \qquad 4.3.3.5$$

Hence to preserve the size of the variance, the Fourier transformed data must be divided by a factor of $\sqrt{N}$ or 4 in our case of 16 electrodes. All the data modified by the Fourier transform has been dived by this factor of 4 in order that the error bars should be of the correct magnitude and the values of χ^2 and Q correctly preserved.

Figures 4.3.2b to d show the Fourier transform plotted for the same data as in figures 4.3.1b to d, and in every case the fit is better than for the untransformed data. Of the nine values of Q six are greater than $2.0 \cdot 10^{-2}$ but in three cases they are still very small, and this implies that the fit is too poor to be explained simply by system noise. Even if the Fourier transform was capable of showing complete invariance for the position of the peak in the profile, it would still be sensitive to the radial displacement of the target and this extra unaccounted source of error would give an unsatisfactory value for Q. When the object is placed nearer to the middle, the signal seen at the periphery will be smaller and the noise will be more significant with respect to the signal. This will have the effect of making it more difficult to detect systematic errors and the statistical analysis will therefore show an improved quality of fit because of the smaller significance of these errors. Objects close to the centre show smaller signals at the periphery and small displacements will generate only small peripheral voltages. The

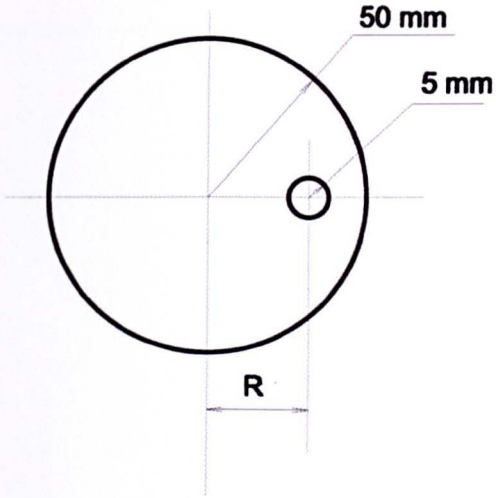

Figure 4.3.2a Conductivity distribution used to compare measured data and that simulated by FEM for Pseudo 2-D geometries. Both sets of data are for an insulating target placed on the X axis. The results for 3 different values of R are shown in 4.3.2b..d. *The tank for both the simulation and the measurements was set to a height of 10mm above and below the electrode plane and the target used spanned the entire length of the tank.*

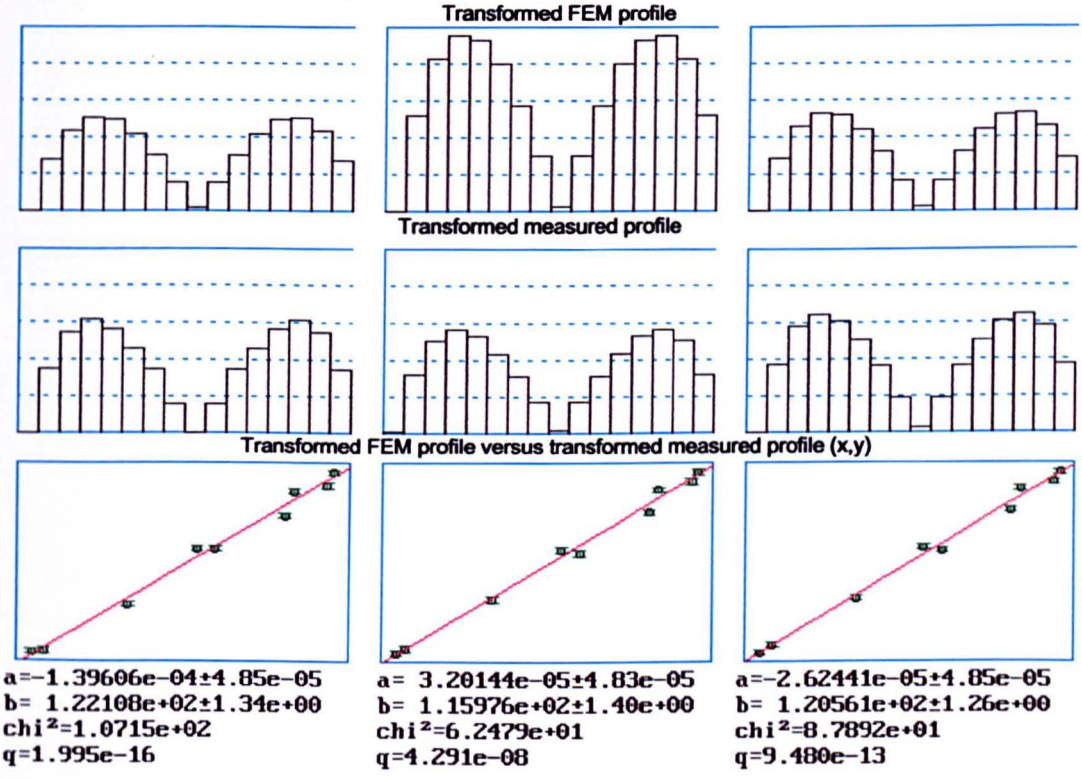

Figure 4.3.2b Target at radius R = 42 mm. *Each of the three sets of results are in the following form:- The top row of 3 bar graphs show the Fourier transform of the results from the FEM for coils 1,2 and 3. The bottom row of 3 bar graphs show the transform of the measured peripheral voltage profiles. The x-y graphs plot the magnitude of the transform of the measured voltage differences versus the magnitude of the transform of those calculated by the FEM.*

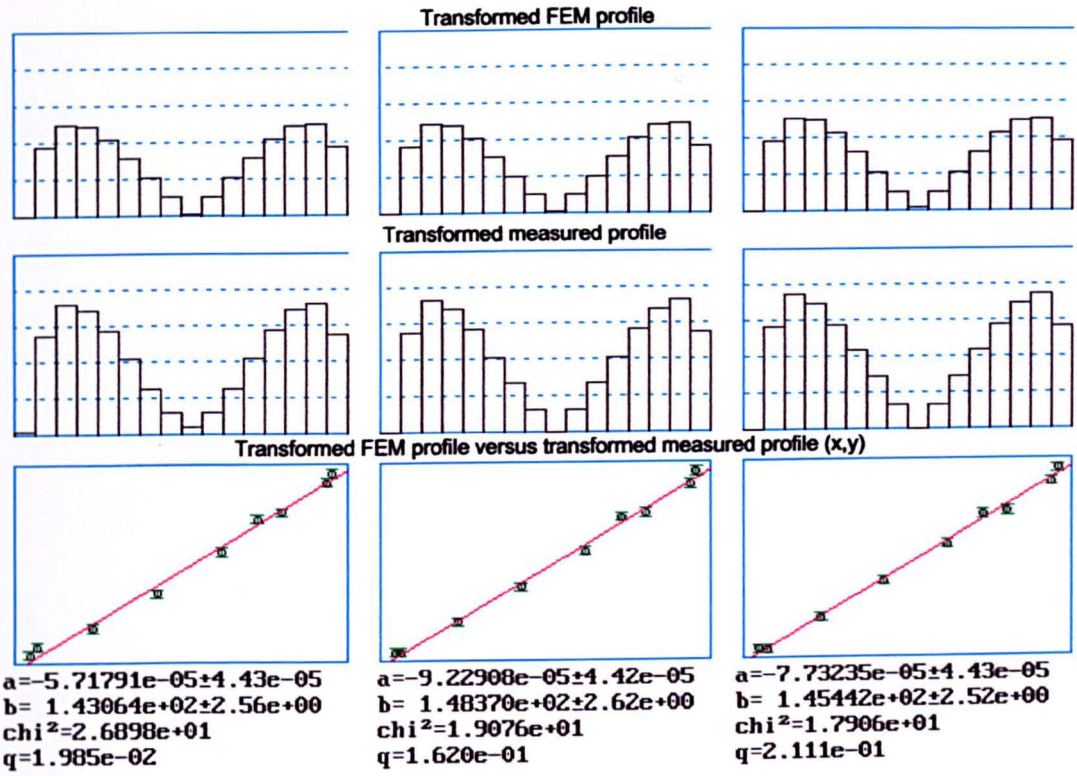

Figure 4.3.2c Showing the same graphs as 4.3.2b but R= 34 mm

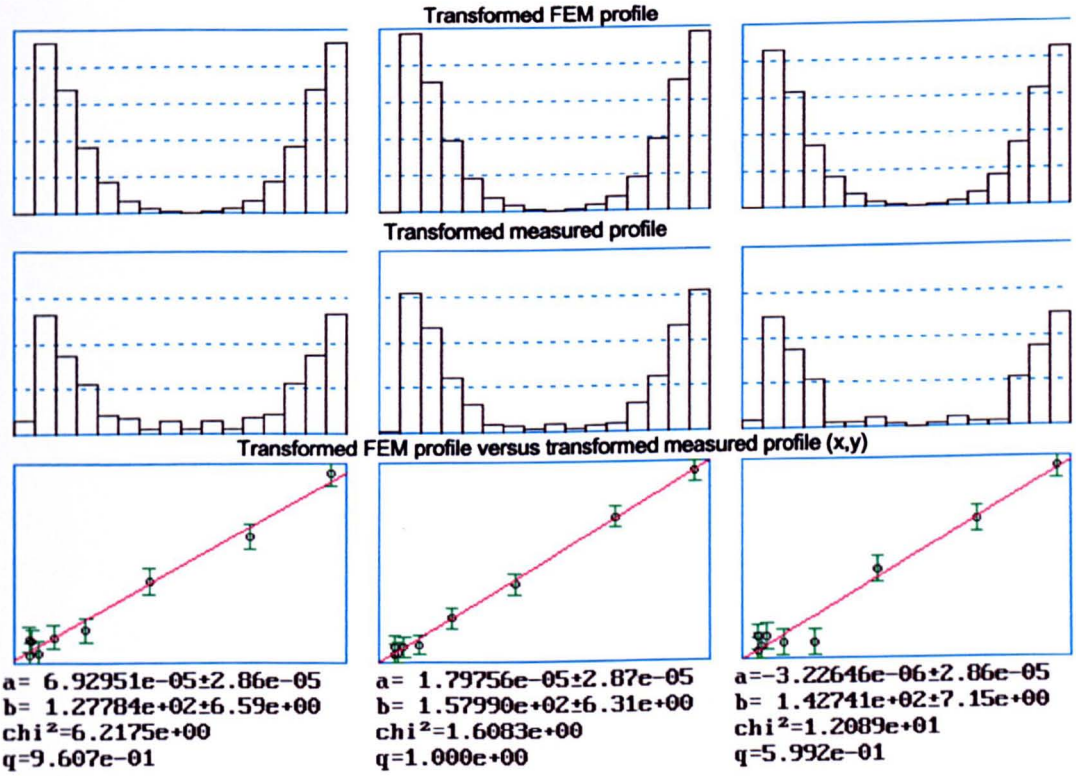

Figure 4.3.2d Showing the same graphs as 4.3.2b but R= 19 mm

estimate of the error is constant so decreasing the signal will increase the relative estimate of the error. Hence the statistical analysis will show that the recorded measurements are more likely because the measured error is bigger. When the object is near to the outside of the tank, the voltage profile will contain more high frequencies outside the bandwidth implied by the sampling at 16 electrodes and will therefore be aliased. The Fourier transform will therefore not be able to show angular invariance for these aliased frequency components. It follows that the fit of the line for targets near to the outside of the tank will not be very much better with the Fourier transform. Comparison of the graphs for the objects nearest to the outside with those for the object close to the centre show that the reduction of χ^2 is greater near the centre and these are shown in figures 4.3.2 a, b and c where the object is at different radial displacements and summarised in table 4.3.3

R /mm	Raw data		transformed data	
	χ^2	q	χ^2	q
42	$2.0 \cdot 10^{2}$	$1.7 \cdot 10^{-34}$	$1.8 \cdot 10^{2}$	$2.0 \cdot 10^{-16}$
	$6.6 \cdot 10^{1}$	$1.1 \cdot 10^{-8}$	$6.2 \cdot 10^{1}$	$4.3 \cdot 10^{-8}$
	$9.1 \cdot 10^{1}$	$2.1 \cdot 10^{-13}$	$8.8 \cdot 10^{1}$	$9.5 \cdot 10^{-13}$
34	$5.2 \cdot 10^{1}$	$3.0 \cdot 10^{-6}$	$2.7 \cdot 10^{1}$	$2.0 \cdot 10^{-2}$
	$3.3 \cdot 10^{1}$	$3.2 \cdot 10^{-3}$	$1.9 \cdot 10^{1}$	$1.6 \cdot 10^{-1}$
	$2.6 \cdot 10^{1}$	$2.5 \cdot 10^{-2}$	$1.8 \cdot 10^{1}$	$2.1 \cdot 10^{-1}$
19	$1.8 \cdot 10^{1}$	$2.1 \cdot 10^{-1}$	$6.2 \cdot 10^{0}$	$9.6 \cdot 10^{-1}$
	$1.7 \cdot 10^{1}$	$2.7 \cdot 10^{-1}$	$1.7 \cdot 10^{0}$	$1.0 \cdot 10^{-0}$
	$1.9 \cdot 10^{1}$	$1.5 \cdot 10^{-1}$	$1.2 \cdot 10^{1}$	$6.0 \cdot 10^{-1}$

Table 4.3.3 Summary of expermental results

So far the experiments have compared the FEM data with data measured on pseudo-2-D tanks; the results obtained for a similar experiment with 3-D geometries are now reviewed. The experimental arrangement and tolerances have already been described. The simplest form of a 3-D geometry is a long tank and a long target. Figures 4.3.3b to d show the results from this experiment. The results obtained for these measured and simulated data pairs shows a fit not as good as that for the 2-D situation shown in figures 4.3.1b to d, but as stated in section 4.3 the positional accuracy for 3-D is poorer

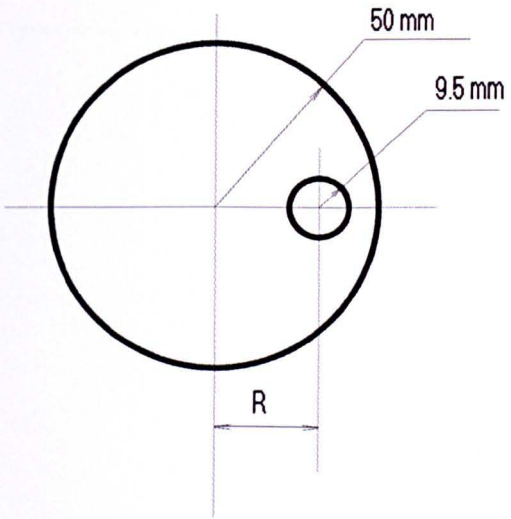

Figure 4.3.3a Conductivity distribution used to compare measured data and that simulated by FEM for 3-D geometries. Both sets of data are for a long insulating target placed on the X axis. The results for 3 different values of R are shown in 4.3.3b..d. *The tank for both the simulation and the measurements was set to a height of 200mm above and below the electrode plane and the target used spanned the entire length of the tank.*

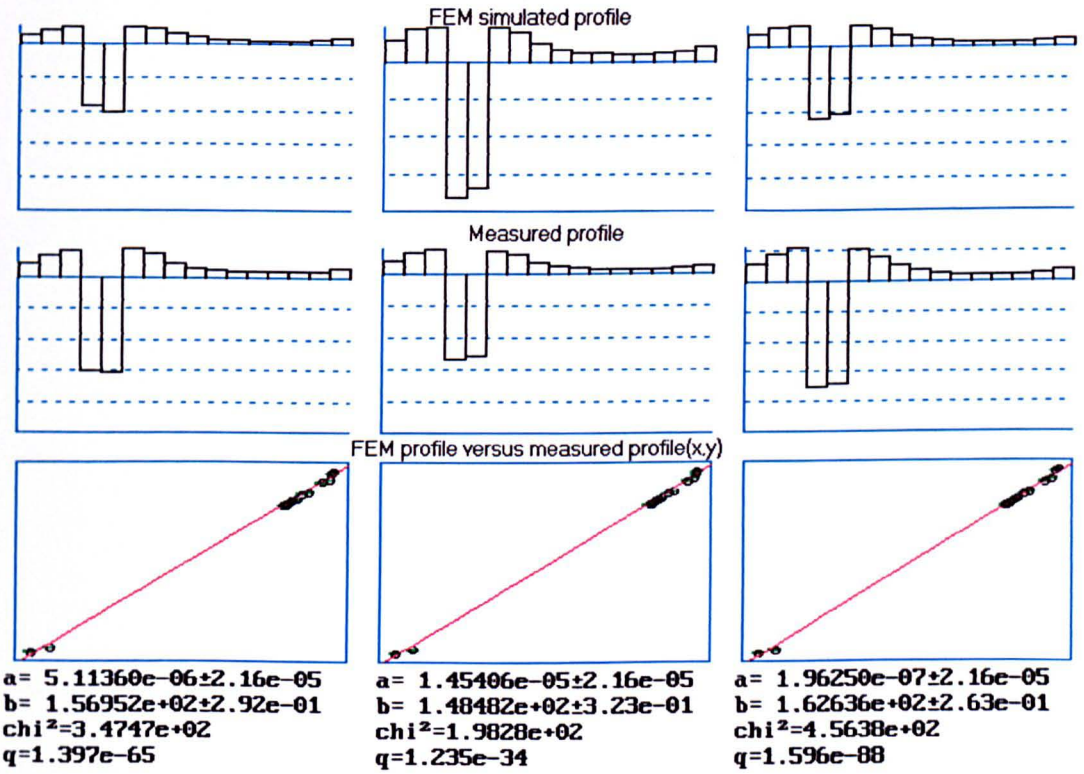

Figure 4.3.3b Target at radius R = 34 mm. *Each of the three sets of results are in the following form:- The top row of 3 bar graphs show the results from the FEM for coils 1,2 and 3. The bottom row of 3 bar graphs show the measured peripheral voltage profiles. The x-y graphs plot the magnitude of the measured voltage differences versus those calculated by the FEM.*

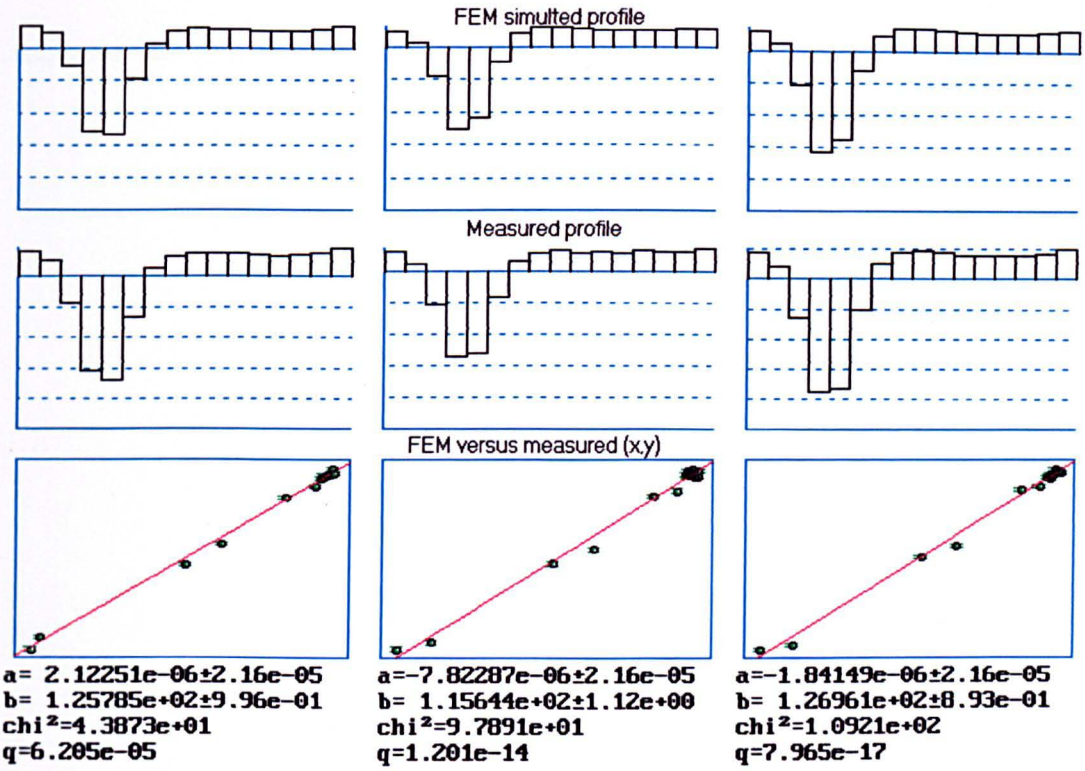

Figure 4.3.3c Showing the same graphs as 4.3.3b but R= 18 mm

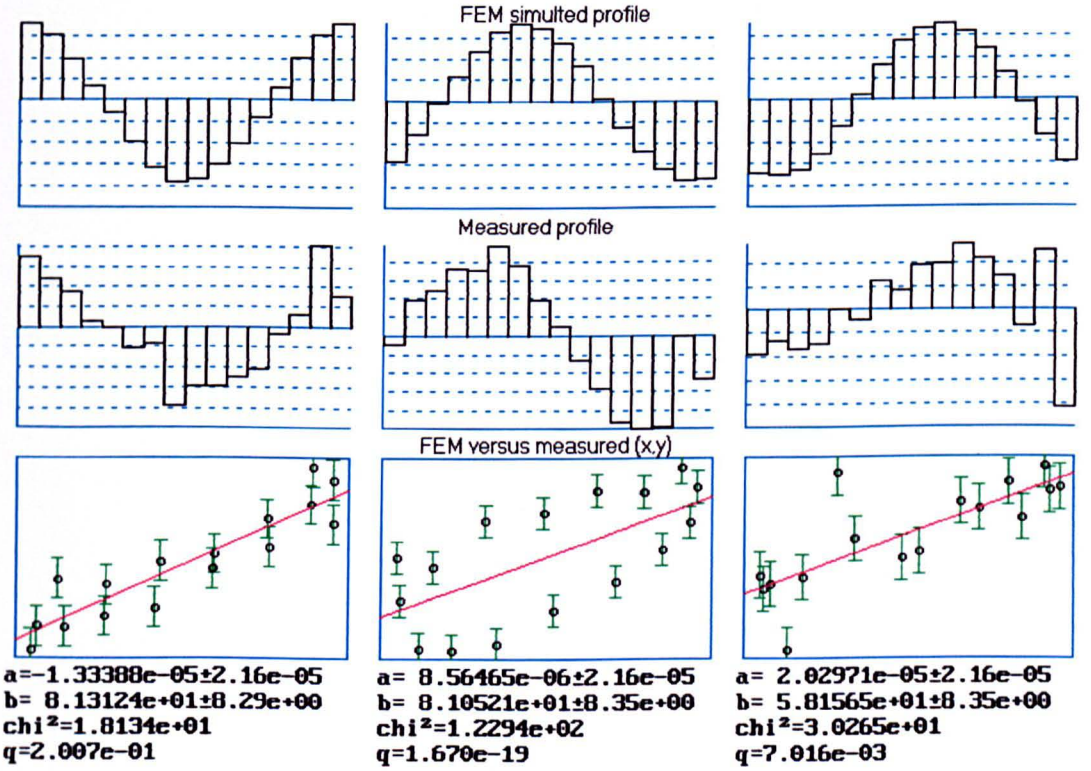

Figure 4.3.3d Showing the same graphs as 4.3.3b but R= 0 mm

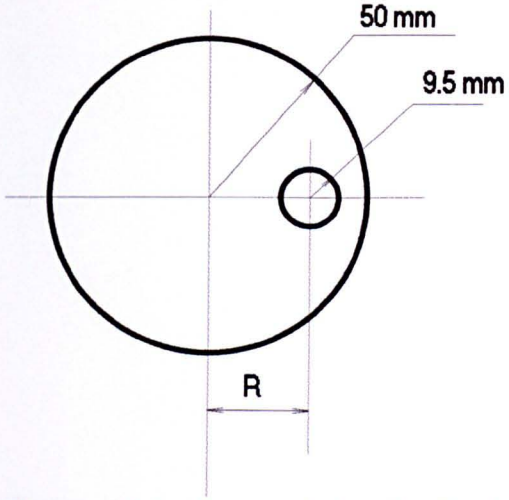

Figure 4.3.4a Conductivity distribution used to compare measured data and that simulated by FEM for 3-D geometries. Both sets of data are for a long insulating target placed on the X axis. The results for 3 different values of R are shown as shown in 4.3.4b..d. *The tank for both the simulation and the measurements was set to a height of 200mm above and below the electrode plane and the target used spanned the entire length of the tank.*

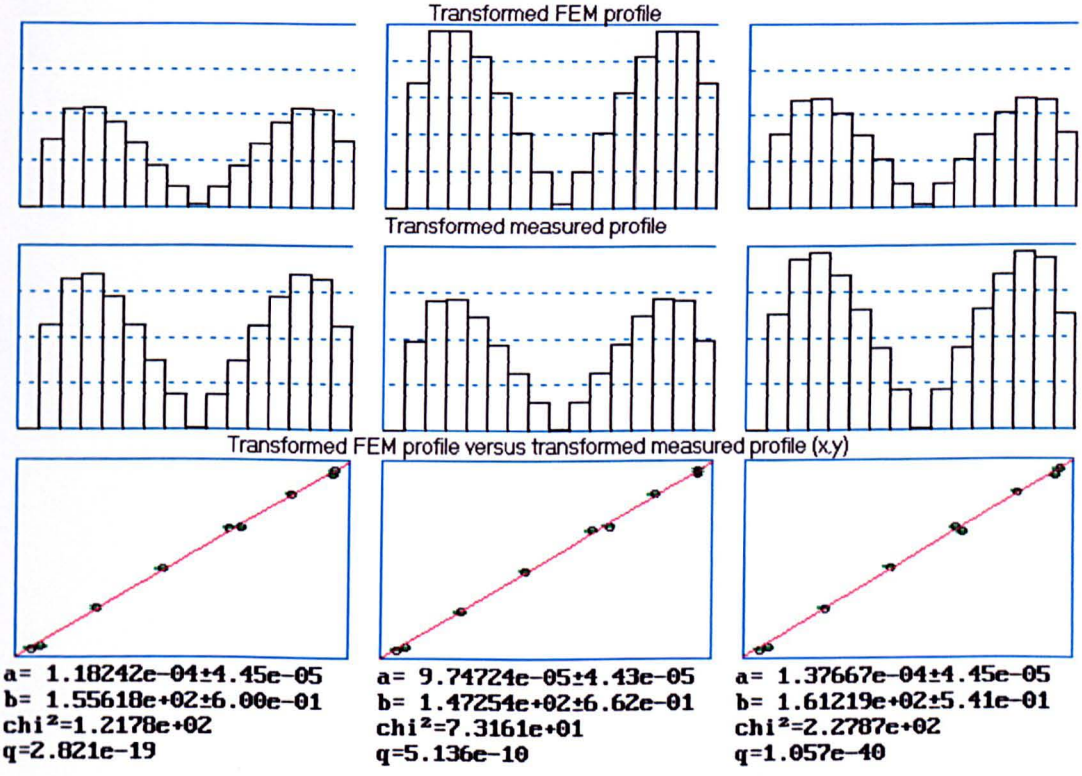

Figure 4.3.4b Target at radius R = 34 mm. *Each of the three sets of results are in the following form:- The top row of 3 bar graphs show the Fourier transform of the results from the FEM for coils 1,2 and 3. The bottom row of 3 bar graphs show the magnitude of the transform of the measured peripheral voltage profiles. The x-y graphs plot the magnitude of the transform of the measured voltage differences versus the magnitude of the transform of those calculated by the FEM.*

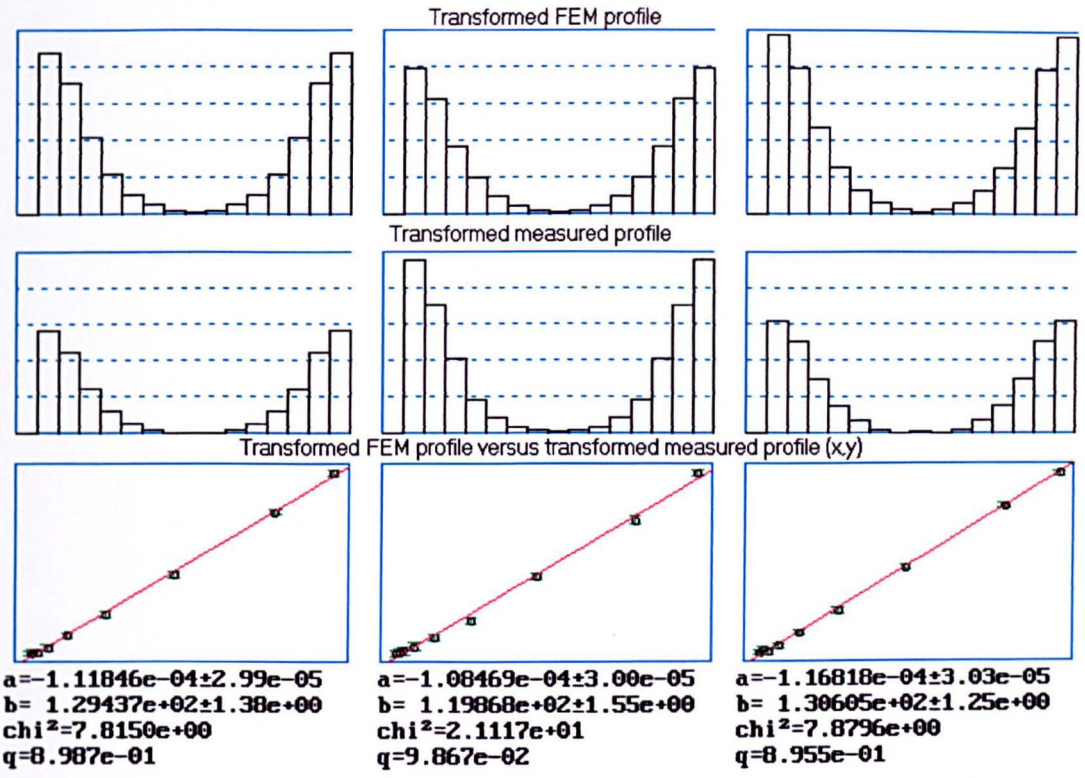

Figure 4.3.4c Showing the same graphs as 4.3.4b but R= 18 mm

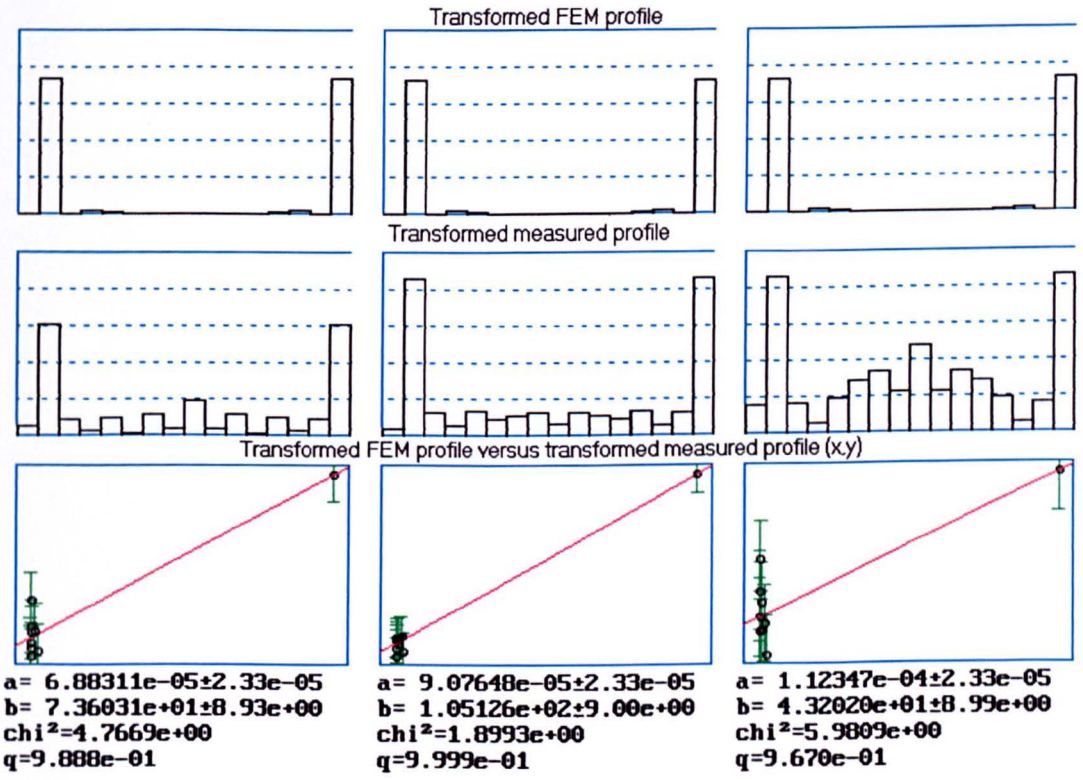

Figure 4.3.4d Showing the same graphs as 4.3.4b but R= 0 mm

than for 2-D geometries. Figures 4.3.4b to d shows the comparison for the transformed data. Again this fit is better than from raw data as would be expected for the hypothesis that the poor fit is due to inaccuracies in the positioning of the target. Figures 4.3.5b to d to 4.3.8b to d show the results of experiments with similar simulations but for small targets of height 20 mm at different levels. These targets show a poor fit if the signal is large, which is the case when the target is close to the edge and the electrode plane; the fit is good when the target is moved away from the electrodes. As the target is moved away from the electrodes the signal diminishes and so the relative error due to noise will increase. This will improve the fit not because the actual points lie closer to the straight line but because the larger error is taken into account by the statistical analysis, making it harder to reject the straight line model. In all the cases the fit of the transformed data is better than that of the raw data as would be expected if a component of error was due to circumferential displacement of the target.

The results for the 3-D experiments show a similar pattern to those of the 2-D experiments. Comparison of measured and simulated results show 17 of the 27 values for Q were greater than 10^{-3}. It might therefore be seen as dangerous to accept the null hypothesis which was that the straight line model fits the relationship between experimental and simulated data as there is also support for the second hypothesis, that the errors are due to inaccuracy in the positioning of the target, because for the Fourier transformed results 23 of the 27 values for Q are greater than 10^{-3}. On this basis it is not possible to reject the straight line model for the transformed data. In conclusion there is no evidence that the poor fit for the raw data is caused by anything other than the difficulty of accurately positioning the target.

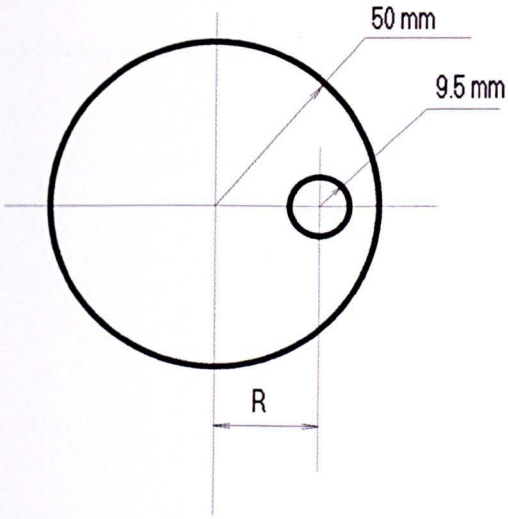

Figure 4.3.5a Conductivity distribution used to compare measured data and that simulated by FEM for 3-D geometries. Both sets of data are for a short insulating target placed on the X axis. The results for 3 different values of R are shown in 4.3.5b..d. *The tank for both the simulation and the measurements was set to a height of 200mm above and below the electrode plane and the target 20 mm high was centred about the electrode plane.*

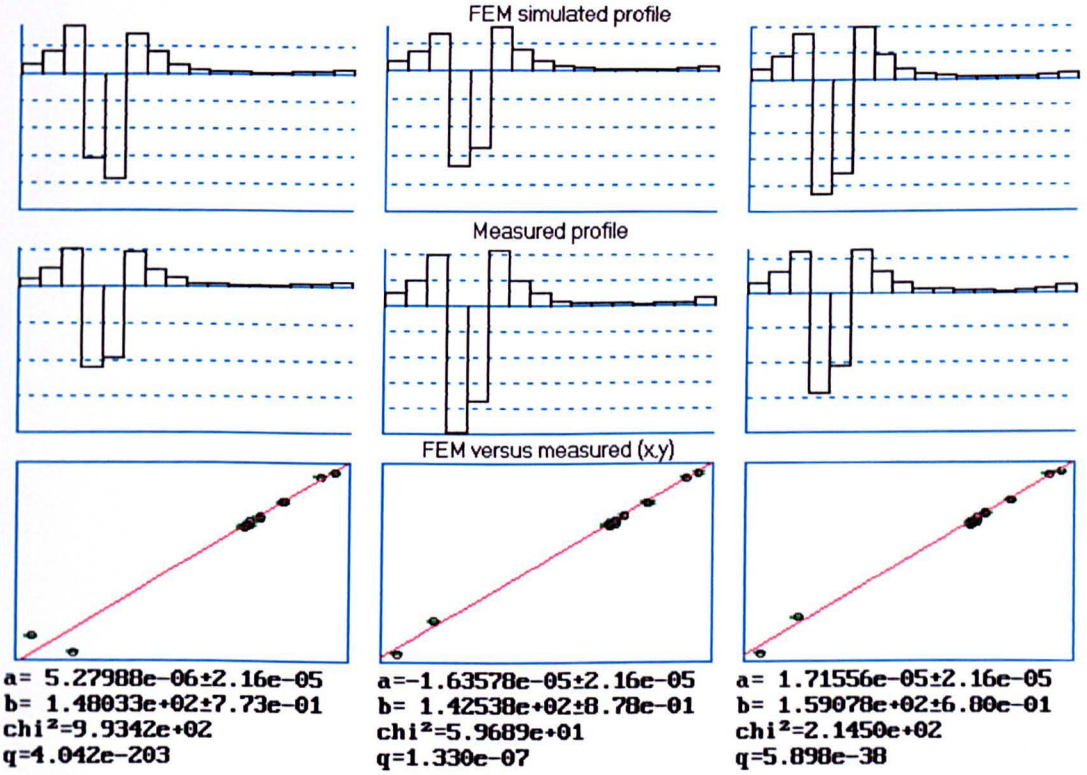

Figure 4.3.5b Target at radius R = 34 mm. *Each of the three sets of results are in the following form:- The top row of 3 bar graphs show the results from the FEM for coils 1,2 and 3. The bottom row of 3 bar graphs show the measured peripheral voltage profiles. The x-y graphs plot the magnitude of the measured voltage differences versus those calculated by the FEM.*

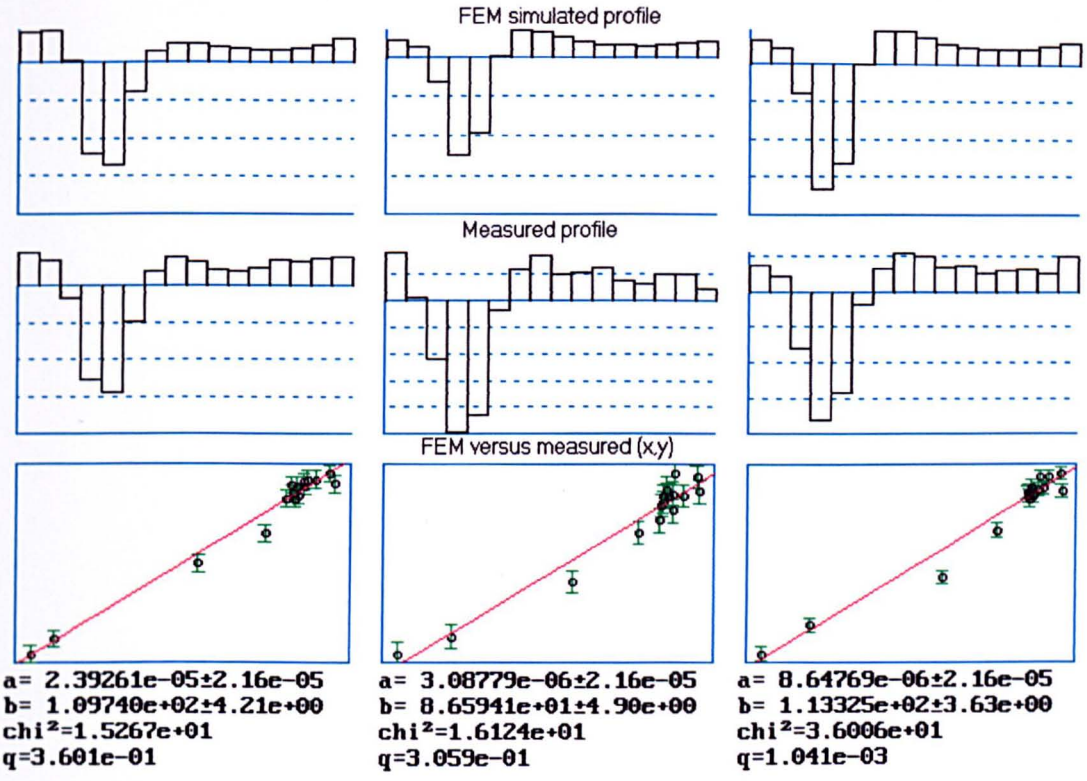

Figure 4.3.5c Showing the same graphs as 4.3.5b but R= 18 mm

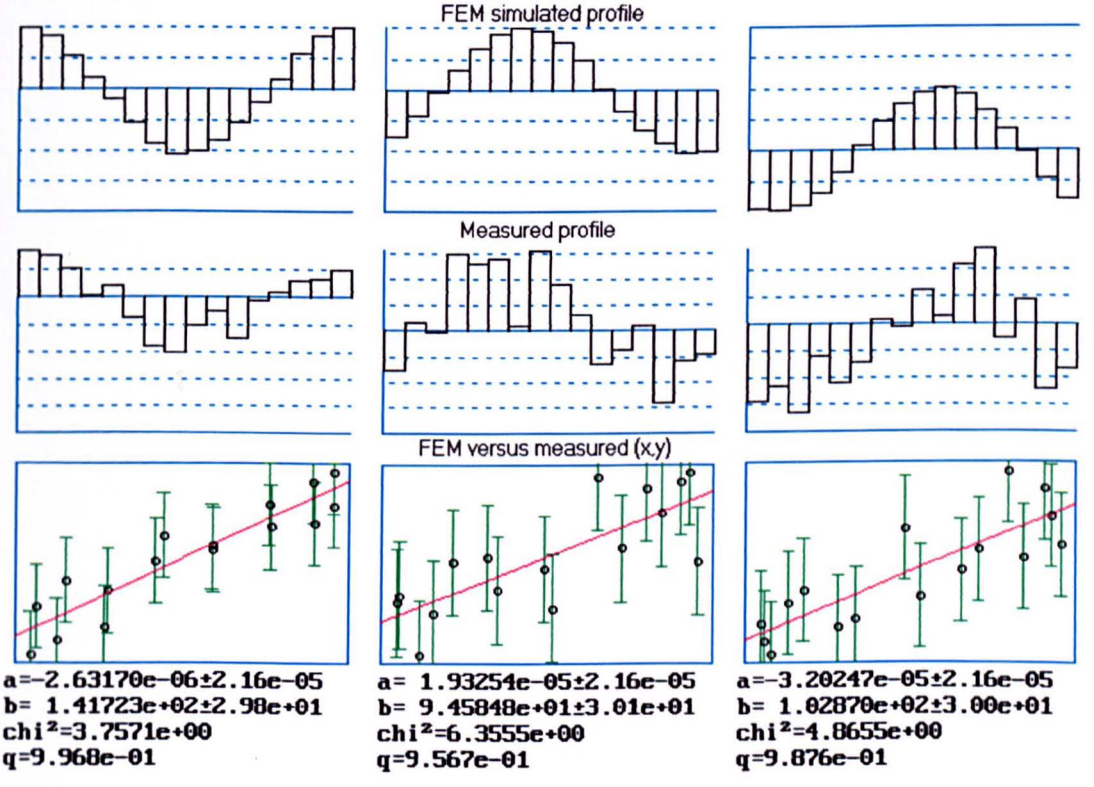

Figure 4.3.5d Showing the same graphs as 4.3.5b but R= 0 mm

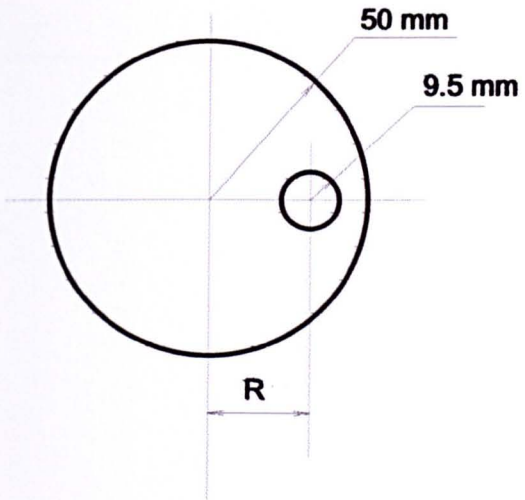

Figure 4.3.6a Conductivity distribution used to compare measured data and that simulated by FEM for 3-D geometries. Both sets of data are for a short insulating target placed on the X axis. The results for 3 different values of R are shown in 4.3.6b..d. *The tank for both the simulation and the measurements was set to a height of 200mm above and below the electrode plane and the target 20 mm high was centred about the electrode plane.*

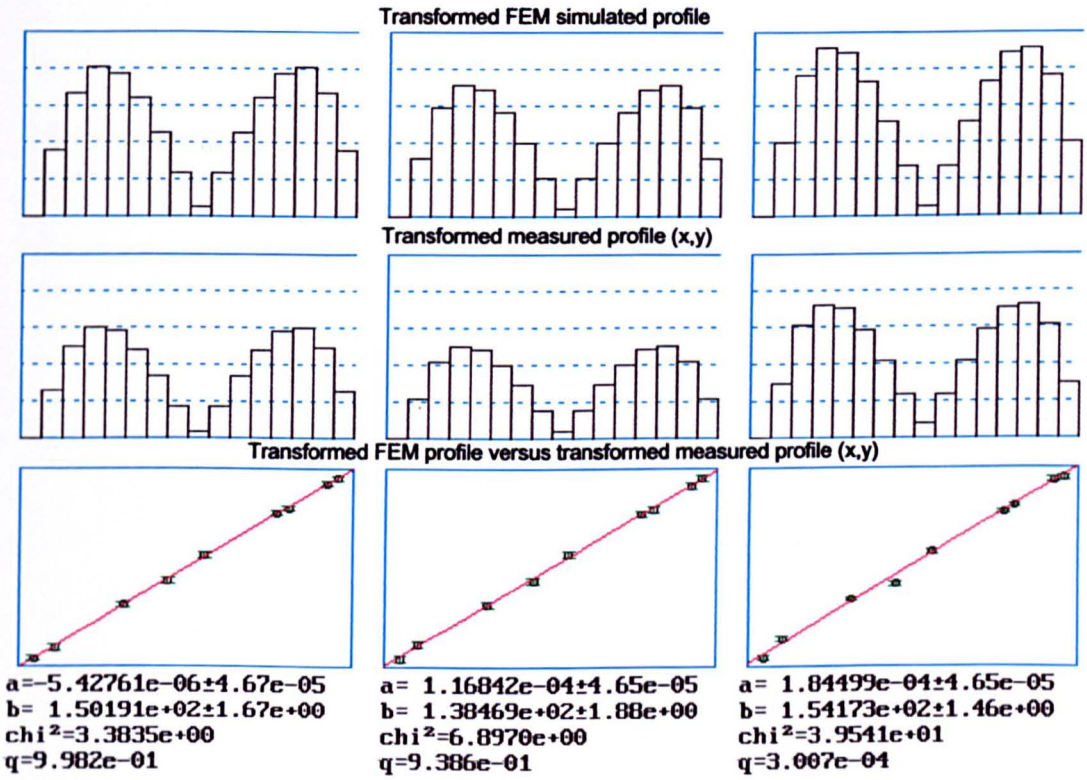

Figure 4.3.6b Target at radius R = 34 mm. *Each of the three sets of results are in the following form:- The top row of 3 bar graphs show the Fourier transform of the results from the FEM for coils 1,2 and 3. The bottom row of 3 bar graphs show the magnitude of the transform of the measured peripheral voltage profiles. The x-y graphs plot the magnitude of the transform of the measured voltage differences versus the magnitude of the transform of those calculated by the FEM*

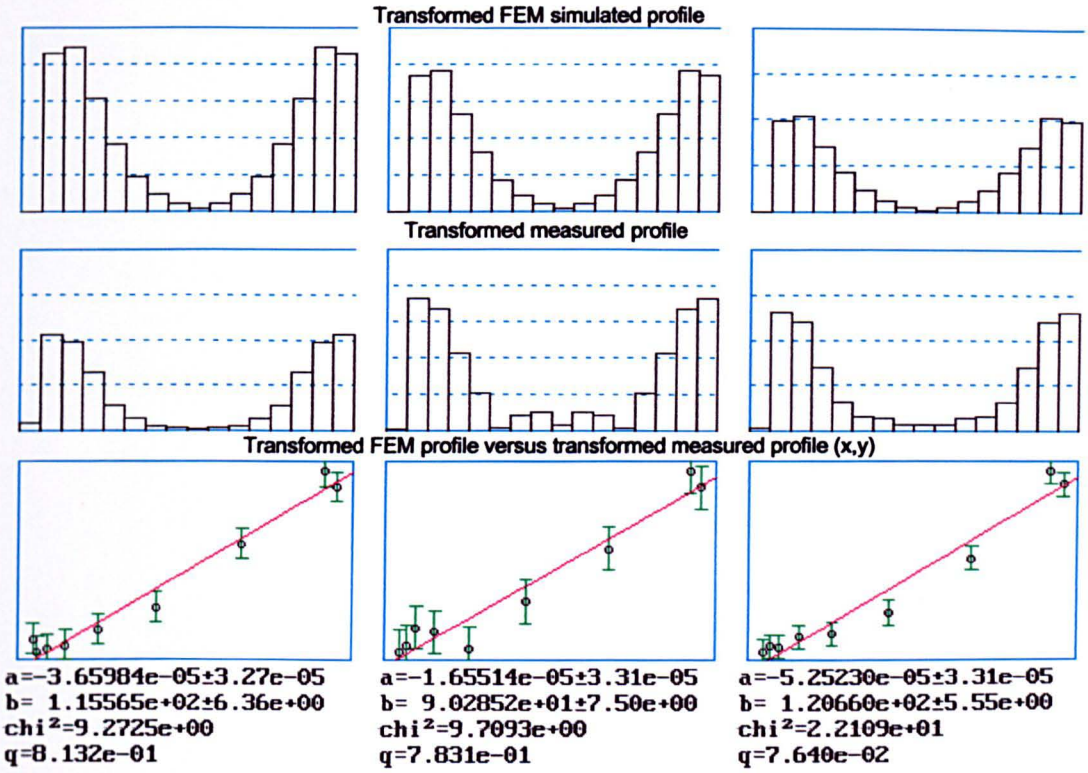

Figure 4.3.6c Showing the same graphs as 4.3.6b but R= 18 mm

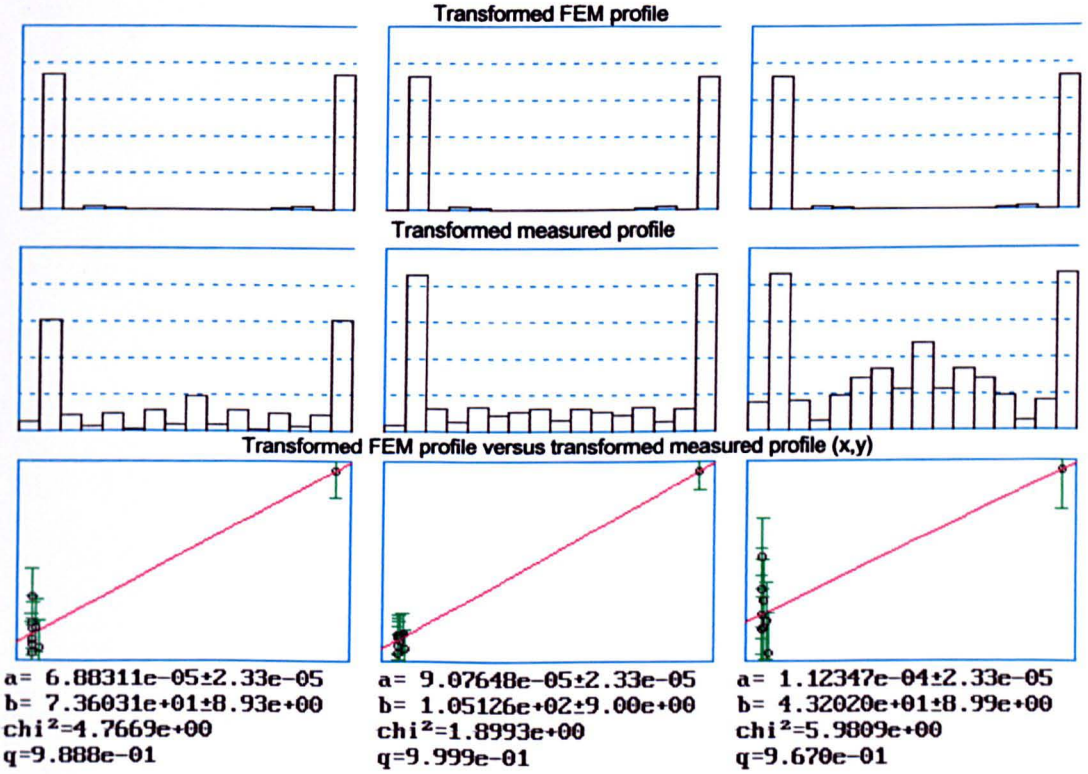

Figure 4.3.6d Showing the same graphs as 4.3.6b but R= 0 mm

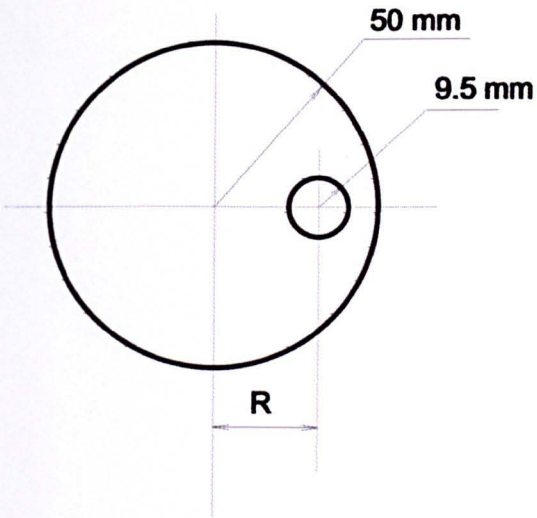

Figure 4.3.7a Conductivity distribution used to compare measured data and that simulated by FEM for 3-D geometries. Both sets of data are for a short insulating target placed on the X axis 40 mm above the electrode plane. The results for 3 different values of R are shown in 4.3.7b..d. *The tank for both the simulation and the measurements was set to a height of 200mm above and below the electrode plane and the target 20 mm high was centred 40 mm above the electrode plane.*

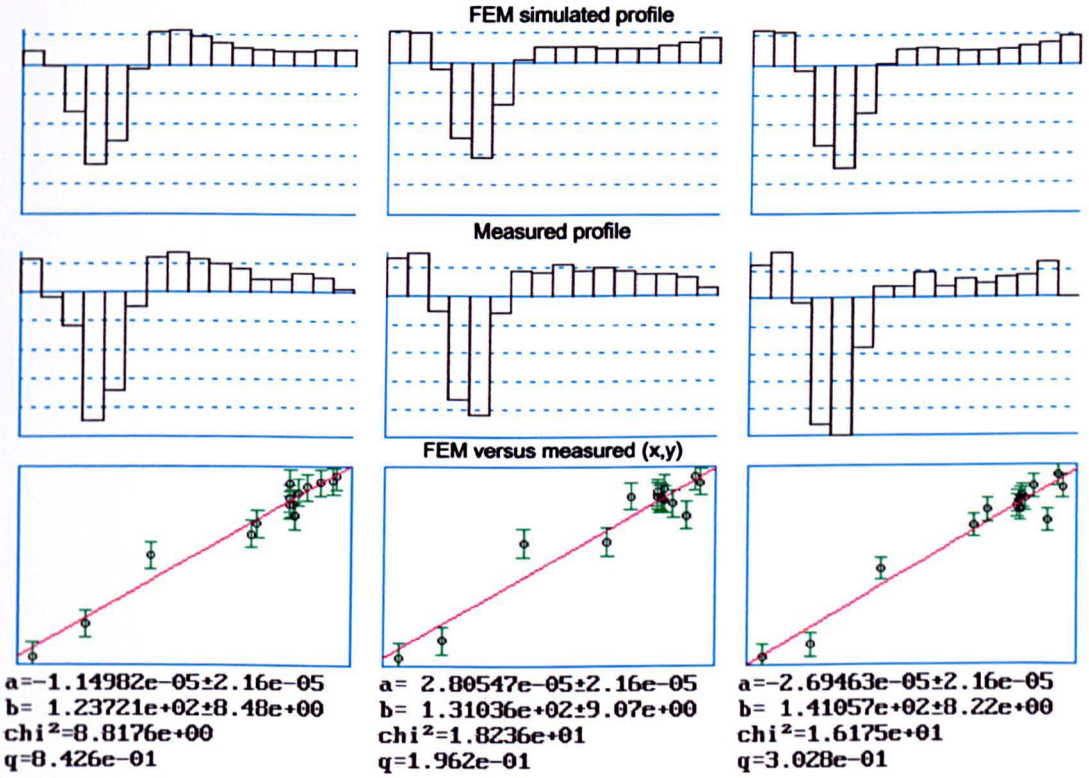

Figure 4.3.7b Target at radius R = 34 mm. *Each of the three sets of results are in the following form:- The top row of 3 bar graphs show the results from the FEM for coils 1,2 and 3. The bottom row of 3 bar graphs show the measured peripheral voltage profiles. The x-y graphs plot the magnitude of the measured voltage differences versus those calculated by the FEM.*

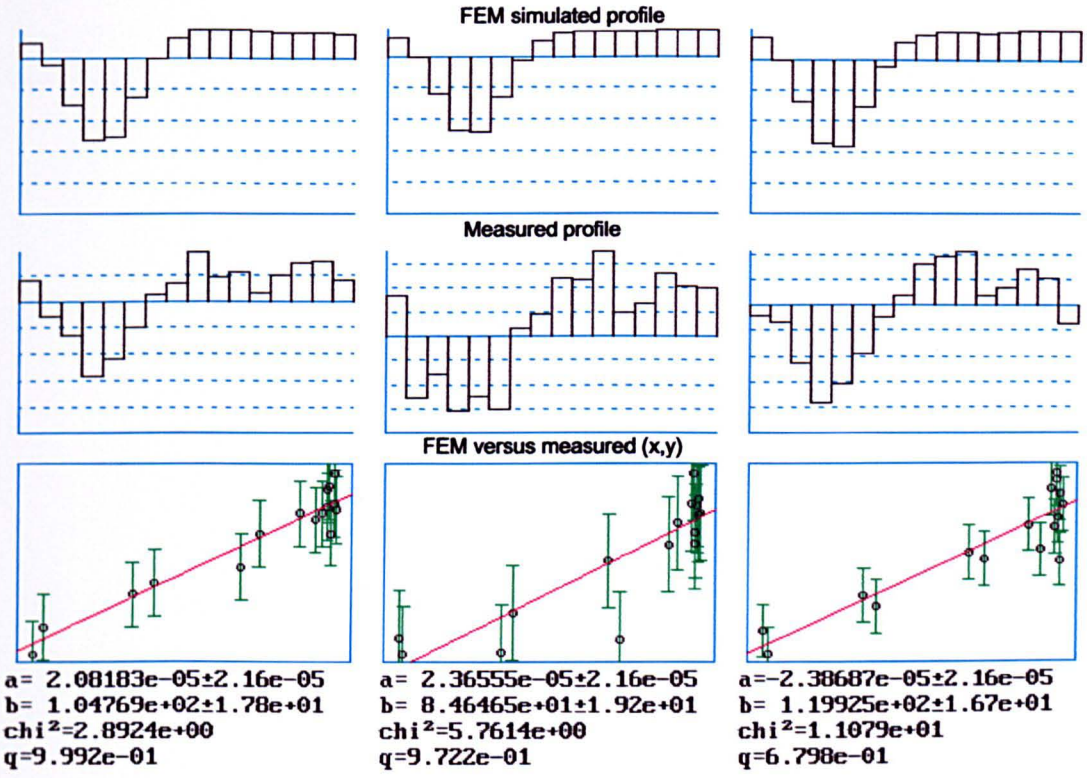

Figure 4.3.7c Showing the same graphs as 4.3.7b but R= 18 mm

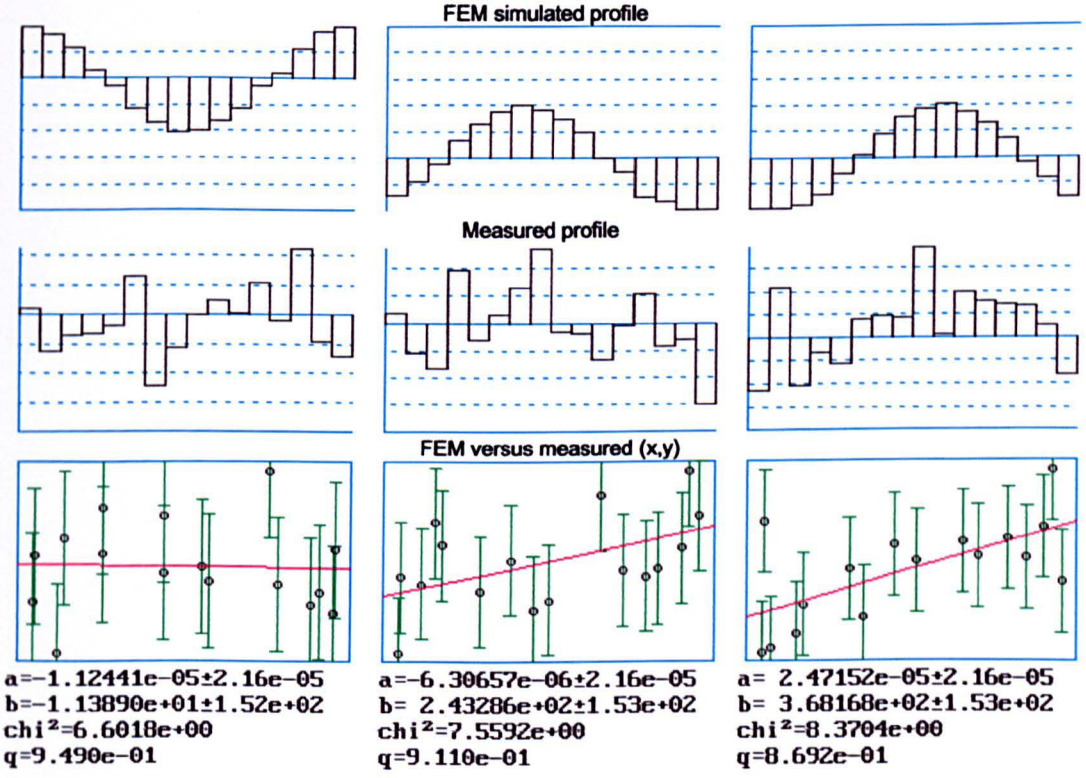

Figure 4.3.7d Showing the same graphs as 4.3.7b but R= 0 mm

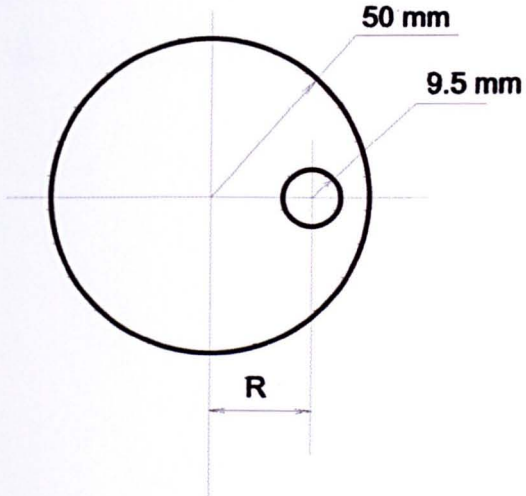

Figure 4.3.8a Conductivity distribution used to compare measured data and that simulated by FEM for 3-D geometries. Both sets of data are for a short insulating target placed on the X axis 40 mm above the electrode plane. The results for 3 different values of R are shown in 4.3.8b..d. *The tank for both the simulation and the measurements was set to a height of 200mm above and below the electrode plane and the target 20 mm high was centred 40 mm above the electrode plane.*

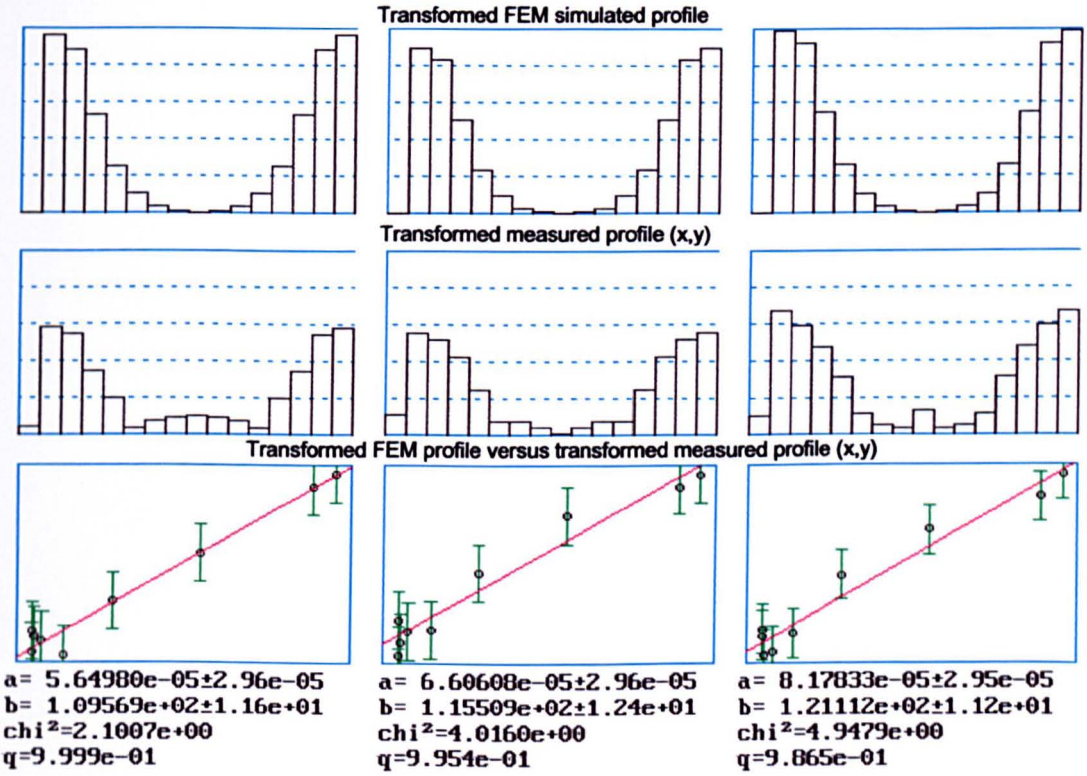

Figure 4.3.8b Target at radius R = 34 mm. *Each of the three sets of results are in the following form:- The top row of 3 bar graphs show the Fourier transform of the results from the FEM for coils 1,2 and 3. The bottom row of 3 bar graphs show the magnitude of the transform of the measured peripheral voltage profiles. The x-y graphs plot the magnitude of the transform of the measured voltage differences versus the magnitude of the transform of those calculated by the FEM.*

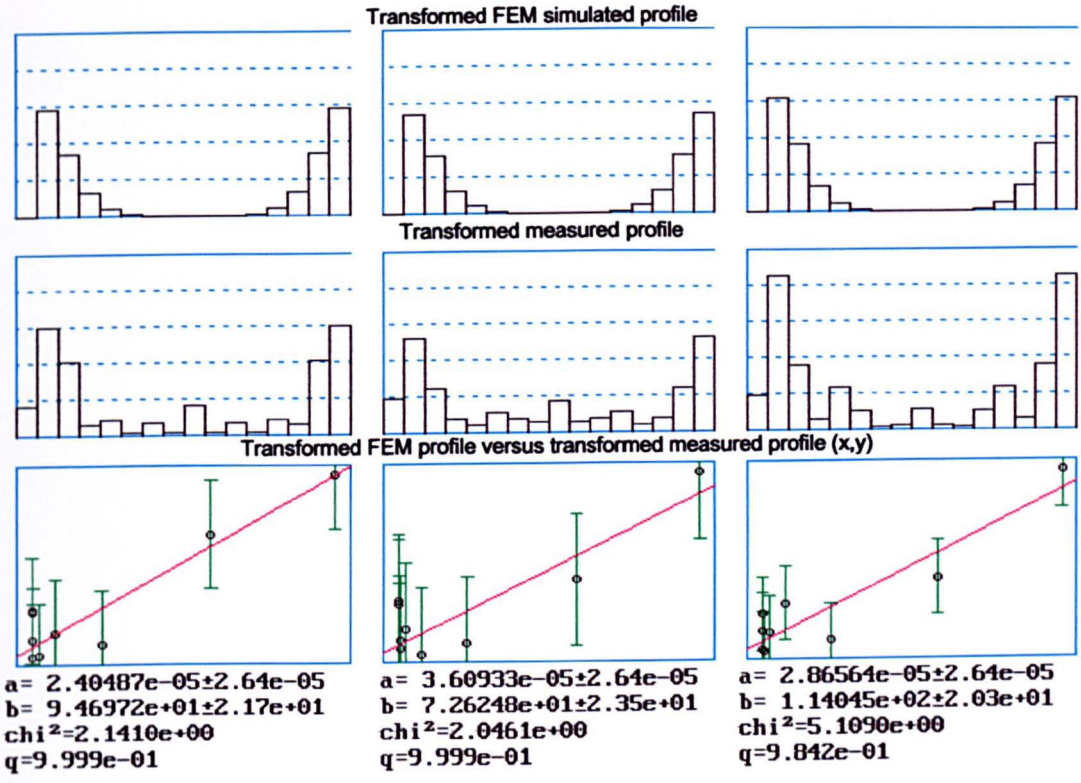

Figure 4.3.8c Showing the same graphs as 4.3.8b but R= 18 mm

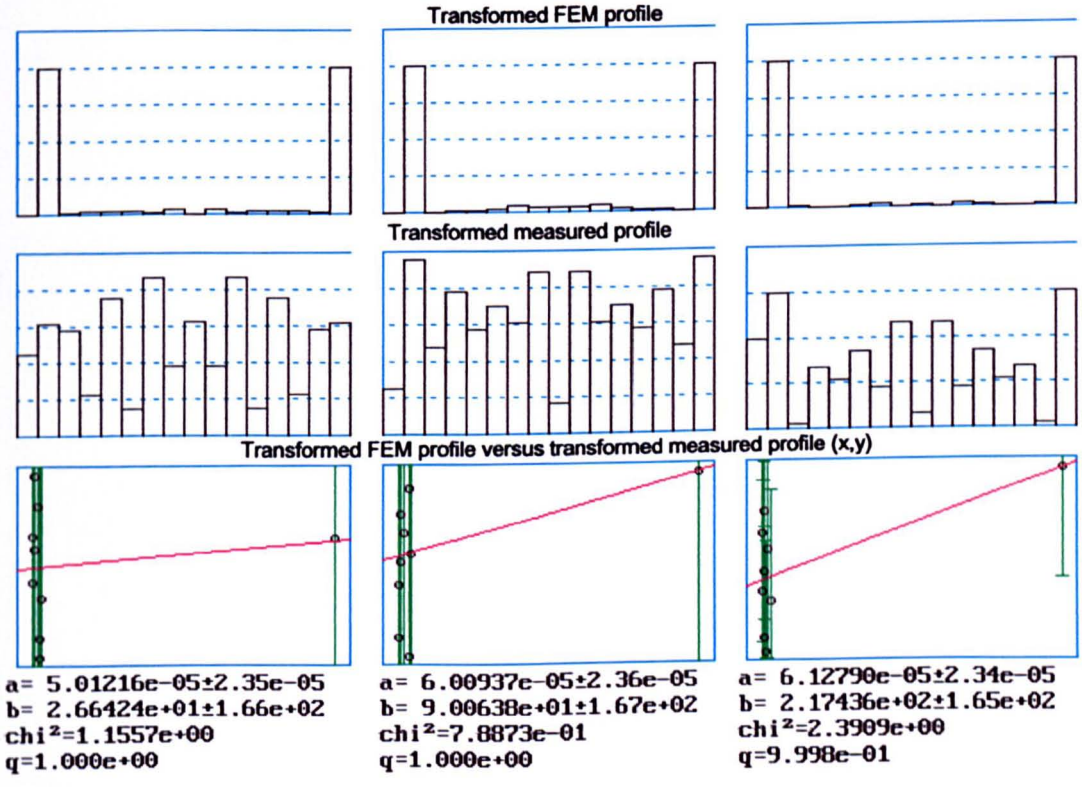

Figure 4.3.8d Showing the same graphs as 4.3.7b but R= 0 mm

4.3.4 Consideration of the value of *b* - the gradient of the graph

As described in section 4.3.1 the values of *b* should correspond to the gain of the system. In fact *b* shows considerable variation. This variation was examined statistically for the Fourier transformed data. The mean of *b* is 126 and the standard deviation 31. The bar graph is shown in figure 4.3.9. Superficially the values appear to be normally distributed and this was examined statistically by carrying out a χ^2 test between this distribution and a theoretical normal distribution with the same mean and standard deviation. The data was grouped into 6 classes to avoid there being less than 8 members in any class.

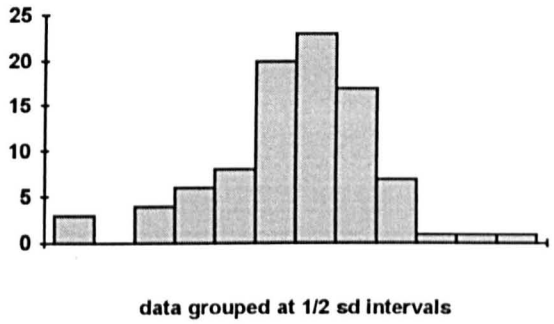

Figure 4.3.9 histogram showing spread for the value of *b*.

$n = 91$, $\chi^2 = 6.83$, $df = 5$, $p > 0.1$

where:-

n : number of values of *b*

df : number of degrees of freedom (classes -1)

p : test probability level.

With the value of $p > 0.1$ we cannot say that the distribution is anything but normal because this experimental distribution would occur by chance at least 1 in 10 times in selecting 91 values from a normally distributed parent population. Random experimental errors usually show a normal distribution leading us the possible conclusion that variation in *b* is the result of experimental error.

Drift in the gain of the system would not be sufficiently great to explain this variation in the values of *b*. The sensitivity of the system is dependent on the location of the target and this is partly due to the current density decreasing towards the centre. A simulation

was set up to investigate this sensitivity variation for change in the location of a long target . In the two separate simulations, the 19 mm target was placed at a radius of 18.5 mm and 14.75 mm. This is the smallest change in position that the mesh would allow. The peripheral profiles of the two simulations were plotted against each other and the value of the gradient calculated for a tank of vertical dimension ±200 mm. The average value of gradient for the three coils is 0.729. This was generated by a displacement of (18.5-14.75 mm) corresponding to 1.88 times the estimated error of 2 mm. By linear interpolation between this value of 0.729 and 1.00, the values for the displacement 2 mm was estimated as a 14% variation in gradient. The standard deviation of *b* found above as 31 is 25% of the mean value of 126. Although this is greater than the 14% variation for a 2 mm error in positioning, it is sufficiently close to make it not unreasonable to conclude that inaccuracy of position may be the cause of the variation in *b*. This is particularly so because the 2 mm positioning error may well be an underestimate.

4.4 Comparison of the results obtained from the 2-D analytic solution and those from the measuring system

Figures 4.4.1 and 4.4.2 show a similar set of graphs to those of figures 4.3.1 and 4.3.2 respectively except that these graphs compare the results obtained for measured data with those for the simulated data from the 2-D analytical solution [21]. As with the results for the FEM, the fit is not perfect and several of the values of Q are very much less than 0.001. The values of Q appear to be correlated with those obtained by the FEM. This would be expected if the errors were mostly in the measured data. In the majority of the cases the value of χ^2 is smaller than that obtained for the FEM. This is probably due to the unaccounted error of simulating a cylindrical object with a mesh made up of quadrilateral elements.

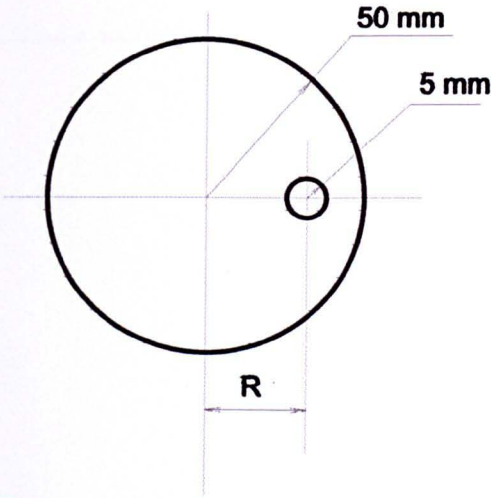

Figure 4.4.1a Conductivity distribution used to compare measured data and that for the analytically simulated data. Both sets of data are for an insulating target placed on the X axis. The results for 3 different values of R are shown in 4.4.1b..d. *The tank for the measurements was set to a height of 10mm above and below the electrode plane and the target used spanned the entire length of the tank.*

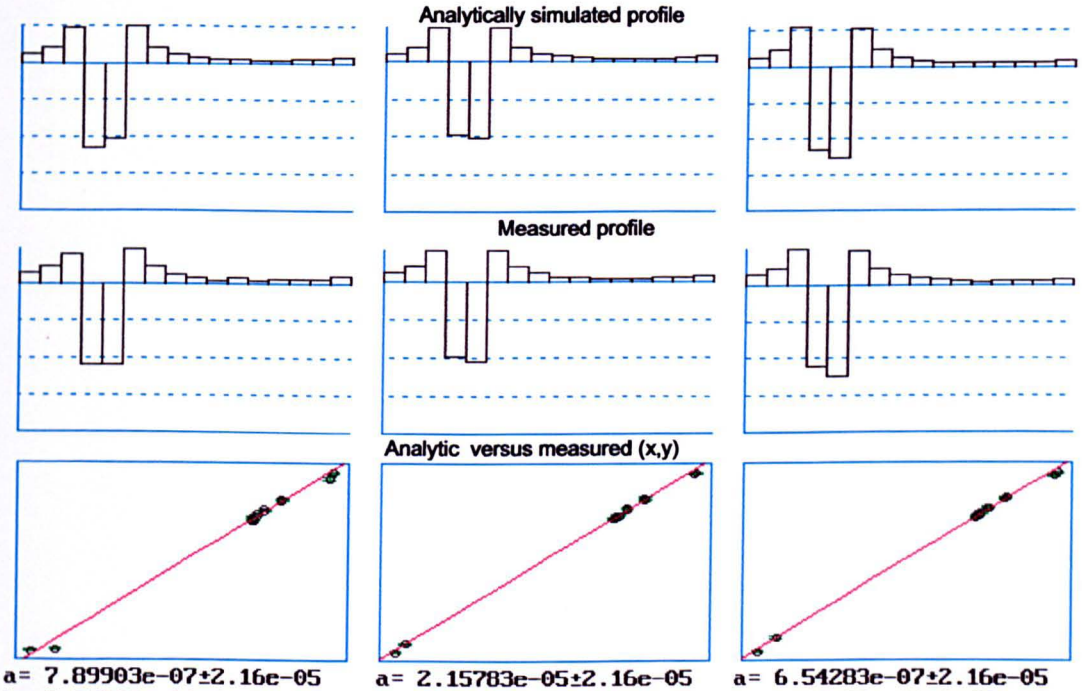

Figure 4.4.1b Target at radius R = 42 mm. *Each of the three sets of results are in the following form:- The top row of 3 bar graphs show the results from the solution for coils 1,2 and 3. The bottom row of 3 bar graphs show the measured peripheral voltage profiles. The x-y graphs plot the magnitude of the measured voltage differences versus those calculated from the analytic solution.*

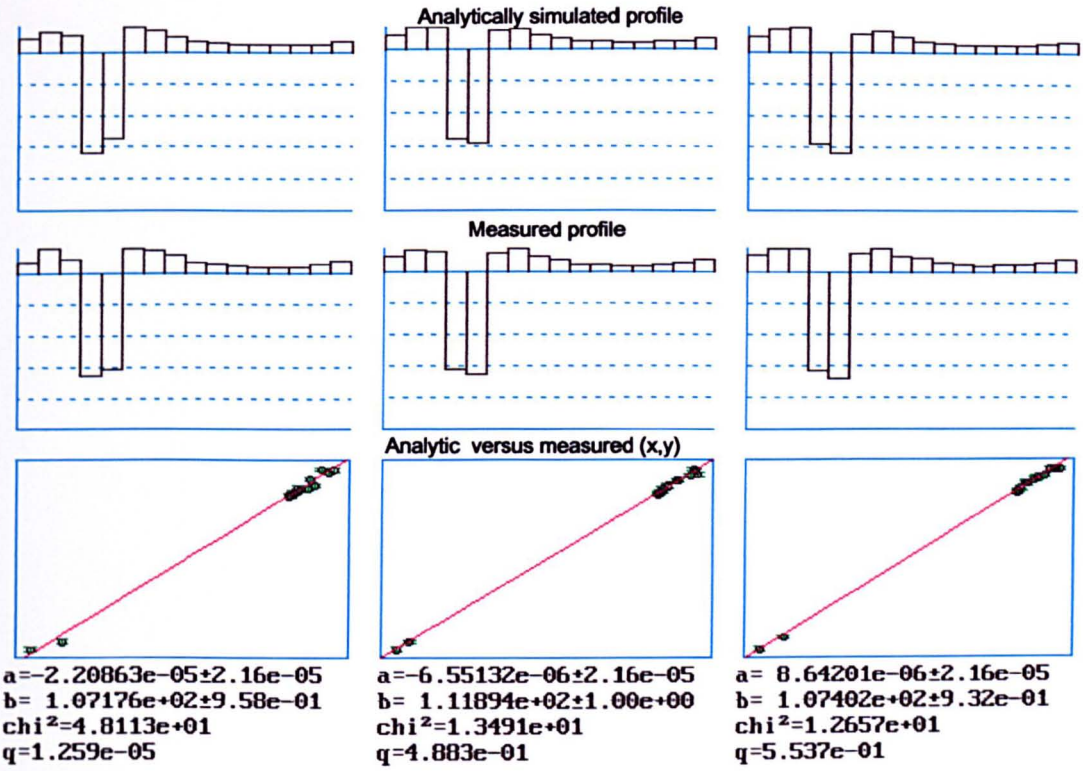

Figure 4.4.1c Showing the same graphs as 4.4.1b but R= 34 mm

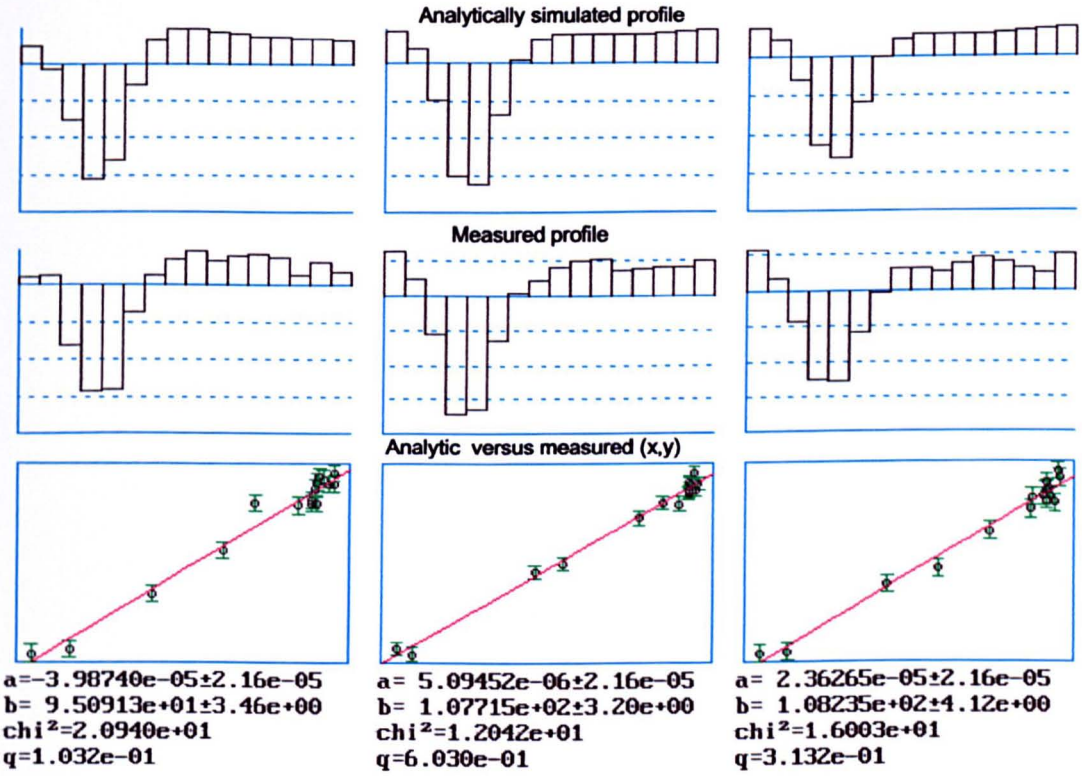

Figure 4.4.1d Showing the same graphs as 4.4.1b but R= 19 mm

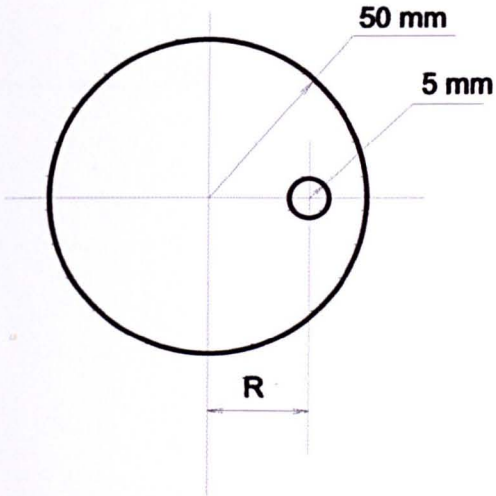

Figure 4.4.2a Conductivity distribution used to compare measured data and that simulated by FEM for Pseudo 2-D geometries. Both sets of data are for an insulating target placed on the X axis. The results for 3 different values of R are shown in 4.4.2b..d. *The tank for both the simulation and the measurements was set to a height of 10mm above and below the electrode plane and the target used spanned the entire length of the tank.*

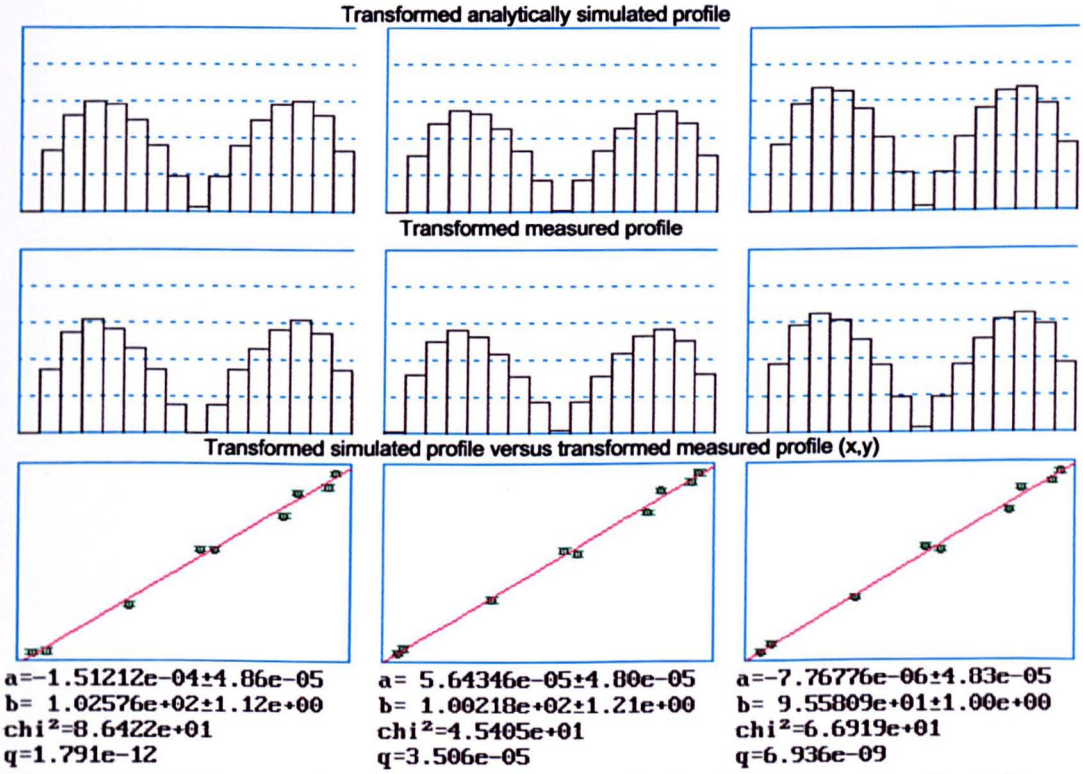

Figure 4.4.2b Target at radius R = 42 mm. *Each of the three sets of results are in the following form:- The top row of 3 bar graphs show the Fourier transform of the results from the solution for coils 1,2 and 3. The bottom row of 3 bar graphs show the magnitude of the transform of the measured peripheral voltage profiles. The x-y graphs plot the magnitude of the transform of the measured voltage differences versus the magnitude of the transform of those calculated from the analytic solution.*

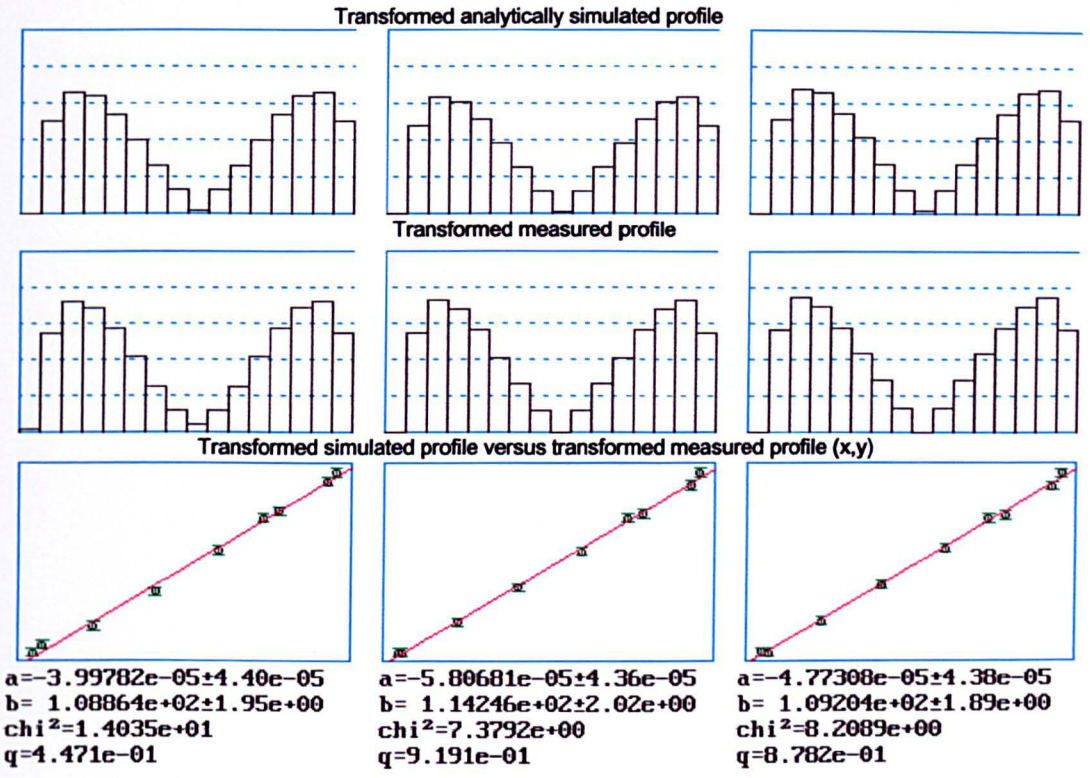

Figure 4.4.2c Showing the same graphs as 4.4.2b but R= 34 mm

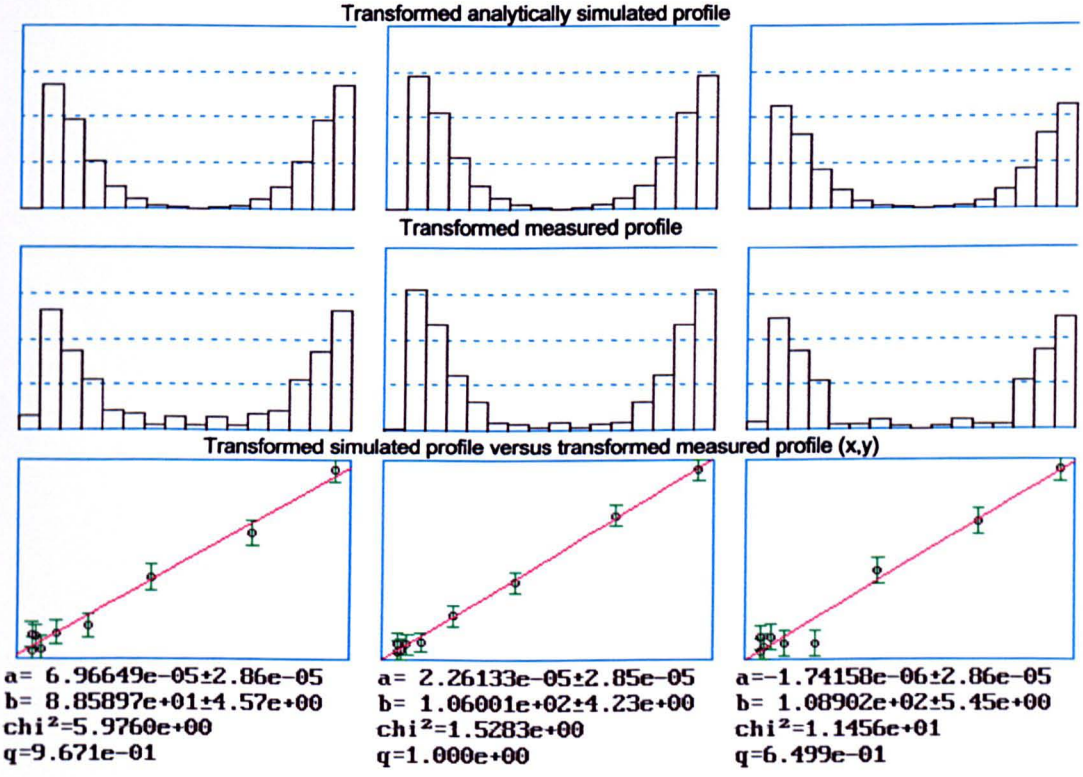

Figure 4.4.2d Showing the same graphs as 4.4.2b but R= 19 mm

4.5 Comparison of images reconstructed from data both measured from the phantom and generated by the FEM

The previous sections have shown that the data measured from the phantom is similar but not identical to that from the FEM. It has been hypothesised that the discrepancies were due mainly to the difficulty of accurately positioning the target within the phantom. The reconstruction algorithm of Purvis *et. al.* [9] is fairly insensitive to the exact position of the target so it would be expected that if the hypothesis is correct, the images produced for the measured and simulated data would be very similar. The main difference would be the addition of noise within the measuring process. Figure 4.5.1a shows a pair of images, one formed from 2-D simulated data and the other from measured data. The two images show very good correspondence. Figures 4.5.1b and 4.5.1c show similar 2-D images but the target is in different positions. Figures 4.5.2 and 4.5.3 show similar images formed by the 3-D reconstruction algorithm. The development of this algorithm will be discussed in greater detail in chapter 5. All these image pairs show very good correspondence which again demonstrates that it is not possible to find any significant errors in the simulated data. Images have not been reconstructed with the target far out of the plane of measurement because the system is not very sensitive in these positions and the images would be almost entirely corrupted by noise. The sensitivity of the system to out of plane targets is also discussed in chapter 7.

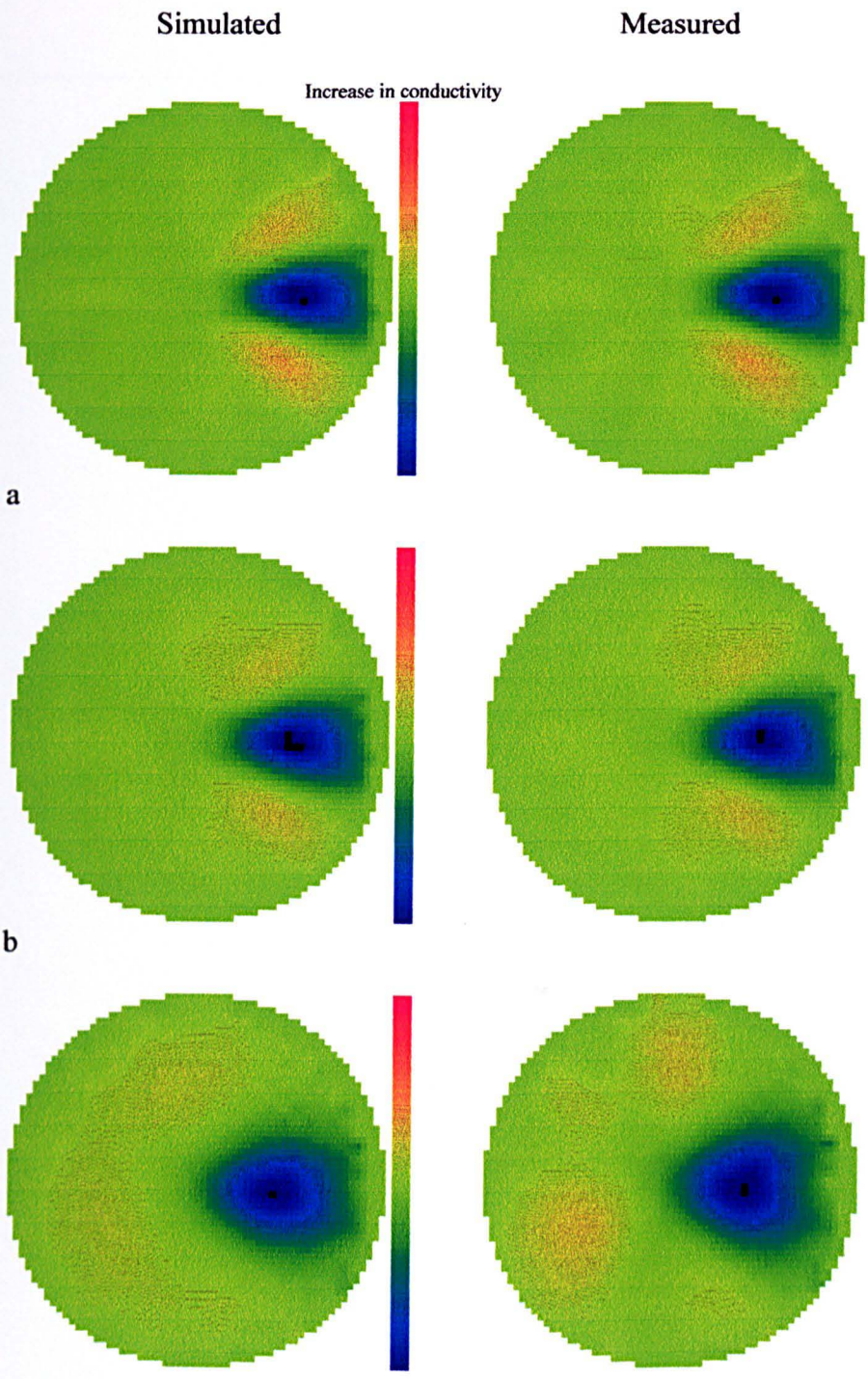

Figure 4.5.1a..c Images showing conductivity maps reconstructed from both measured and simulated data where the target is placed at R = 42 mm, R= 34 mm and R= 19 mm respectively.

The images are reconstructed from the same data as shown in figure 4.3.1.

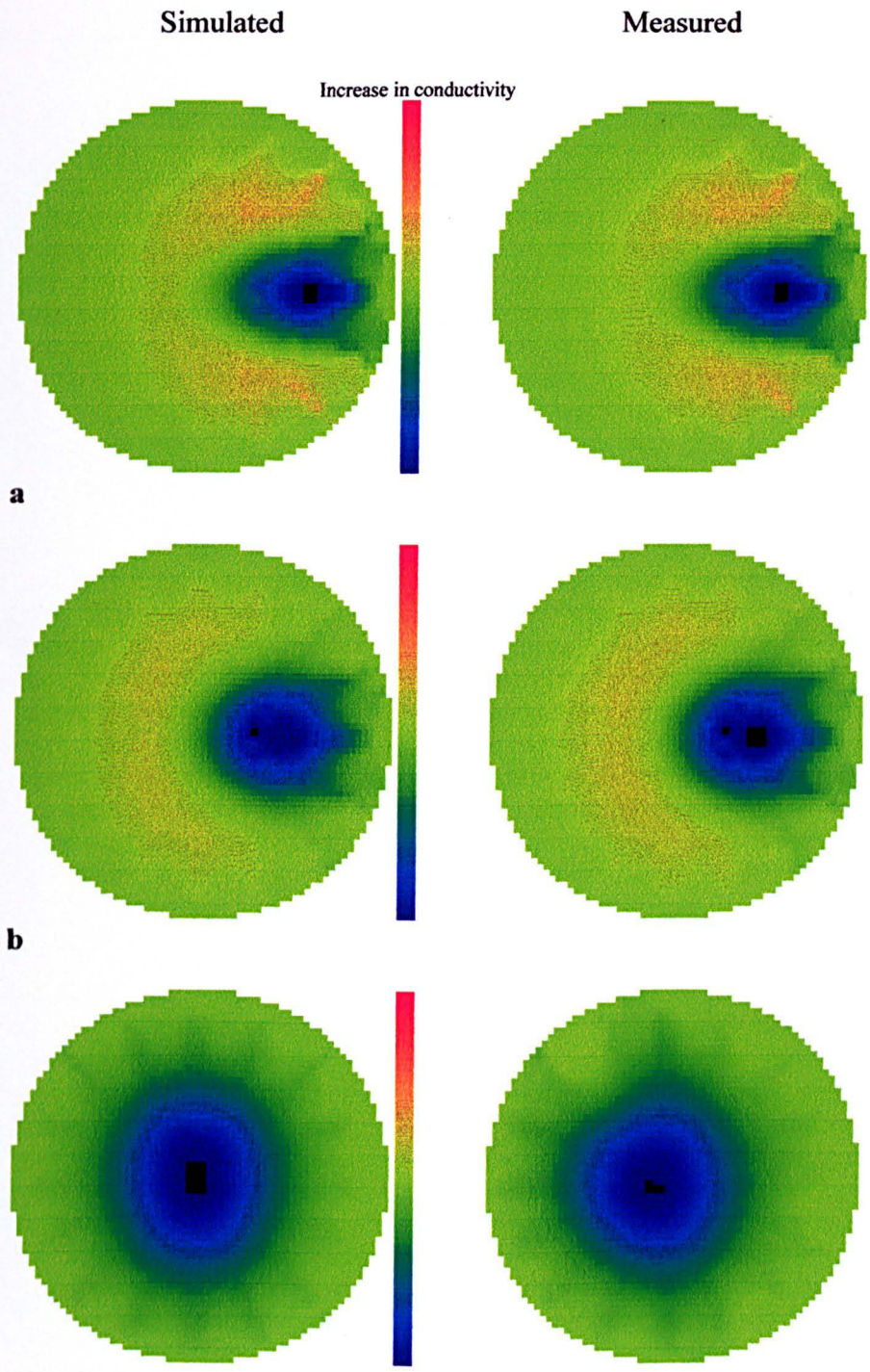

Figure 4.5.2a..c Images showing conductivity maps reconstructed from both measured and simulated data where the target is placed at R = 35 mm, R= 18 mm and R= 0 mm respectively.

The images are reconstructed from the same data as shown in figure 4.3.3.

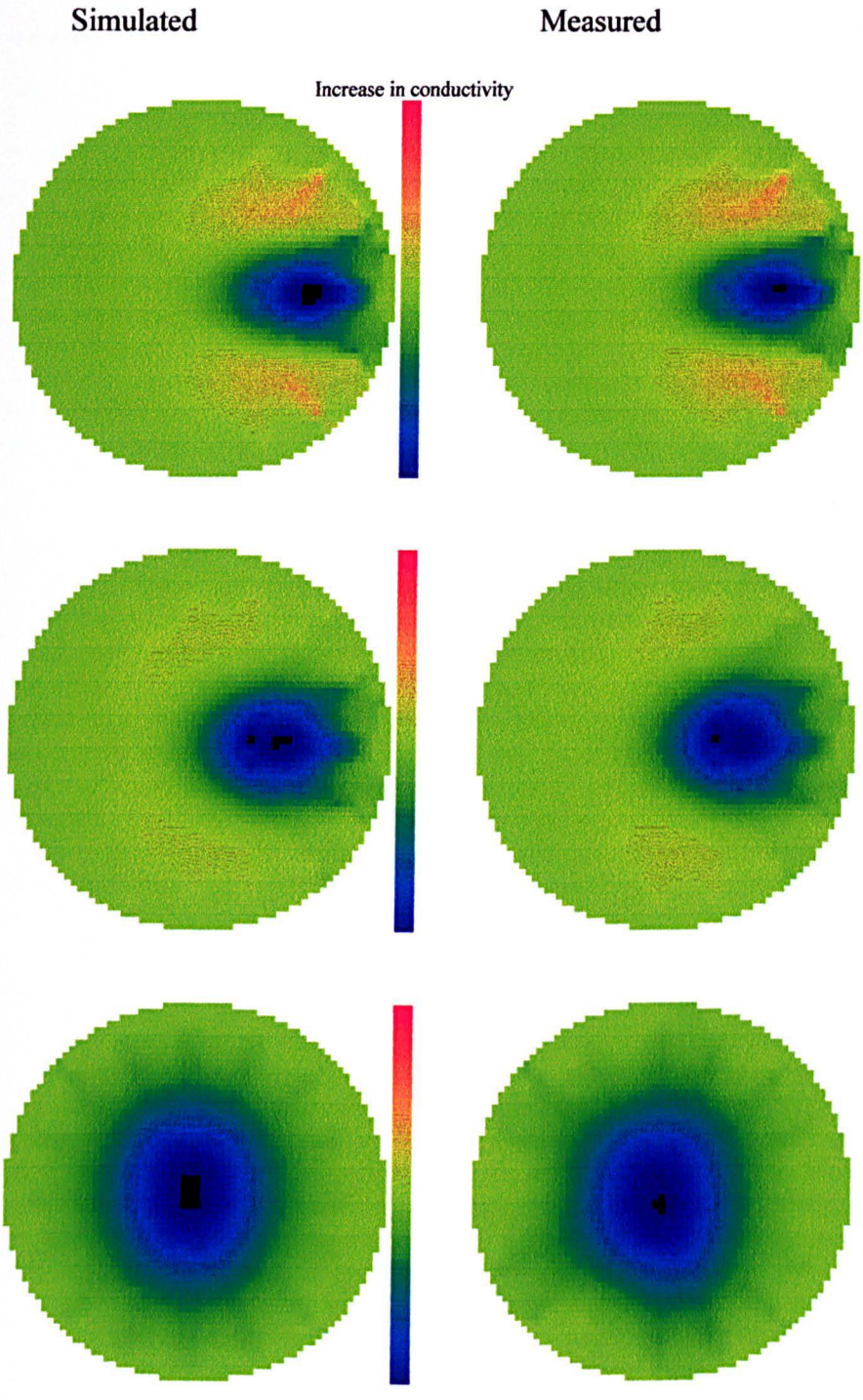

Figure 4.5.3a..c Images showing conductivity maps reconstructed from both measured and simulated data where the target is placed at R = 35 mm, R= 18 mm and R= 0 mm respectively.

The images are reconstructed from the same data as shown in figure 4.3.5.

4.6 Comparison of results obtained by FEM and measurements for axially displaced targets

A further test of the 3-D FEM programme was made for the sensitivity of the system for axially displaced targets. Figure 4.6.1 is a graph with two curves plotted on the same axes, the green curve is a normalised version of the graph, published by the author[35], which shows measured sensitivity plotted against axial positions for a small insulating target and the red curve show the results found by simulation. The overall shape of the two graphs is very similar and the variation is probably due to the positional error in the target location. From this comparison it can be inferred that the results obtained by the simulation are a useful indication of how the physical system will behave for axially displaced targets and this will be examined in further detail in chapter 7.

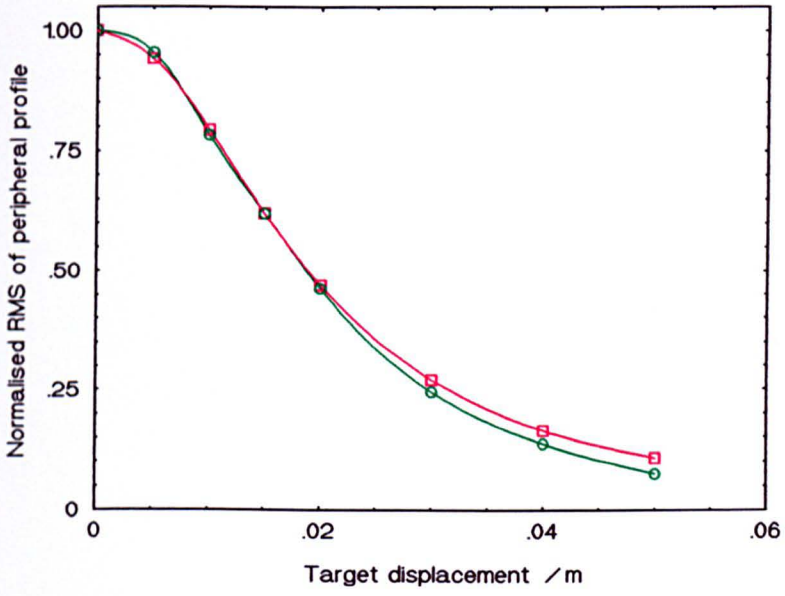

Figure 4.6.1 Normalised graph showing the sensitivity of the system to targets at different axial displacements, both simulated and measured results are plotted in red and green respectively. *The sensitivity is found from the RMS of the peripheral voltage profile for all three coils, the target was an insulator diameter 19 mm and height 20 mm placed at 60 % radius in a tank diameter 100 mm and height ±200 mm.*

4.7 Conclusions

In this chapter measurements from the physical system have been compared to values found by simulation. The statistical analysis, used to test the relationship between physical measurements and those found by simulation, was not conclusive. An important conclusion from this analysis was that there are errors made during the measurement process which were not accounted for. The method of finite elements generates data which when used to reconstruct images produces images which are virtually indistinguishable from those of the measured data.

The testing of simulated against measured results is complicated by experimental error which makes exact agreement between physical and simulated measurements impossible. It is possible to test the quality of the agreement by the use of statistics and so take account of the errors made during measurements. The results of a statistical analysis cannot be clear cut, because difference or indeed similarity between sets of measurements can be encountered by chance random error. The only answer that a statistical analysis can provide is a measure of the likelihood of false agreement or false disagreement between data sets. A statistical analysis requires an estimate of the error in the measured data. Two main types of error were identified the first was random error in the electrical system such as noise and drift, and the other was error in the spatial positioning during sets of measurements. The first is important for all further sets of measurements but the other is only important for the statistical analysis within this chapter. The positional inaccuracy was investigated by carrying out the Fourier transform of the data. If a target is displaced circumferentially, the profile will correspondingly be displaced by the same angle as long as the current pattern is also circumferential. Hence the Fourier transform with its angular invariance will remove one component of positional error because currents induced by exciting one coil are close to being circumferential. Support for the hypothesis that one of the sources of error was due to positional inaccuracy is provided by the better fit shown for the transformed data. The effect of positional errors was also investigated numerically and

it was found that the variation in the constant of proportionality between measured and simulated data could be explained by positional errors.

The extreme sensitivity of the system to the positional placement of the target could be very useful if a system was required to locate a known target within a tank. The experiments to validate the FEM program have shown that with a positional error of as little as 0.5 mm in the target placement for the pseudo 2-D case, the data did not fit well. The poorness of fit could not be explained by the measured system noise. This might suggest that a target could be located both radially and circumferentially to within 0.5% of a tank's radius.

The images reconstructed from both measured and simulated data are extremely similar and it can be concluded that simulated data is suitable for the purpose of image reconstruction. The only noticeable difference is that the measured data produces more artefact than the simulated data. This is to be expected because the noise will be greater for the measured data than for the simulated data and more noise will produce more artefact.

Chapter 5 The three dimensional problem

5.1 Introduction

It has been found [16] that for injected current impedance imaging the algorithms developed assuming a 2-D geometry would function when applied to measurements taken from a three dimensional (3-D) phantom. Although the current path spread into the third dimension in a similar fashion to that in the sketch shown in figure 5.1, the pattern of currents within the plane of interest did not change fundamentally.

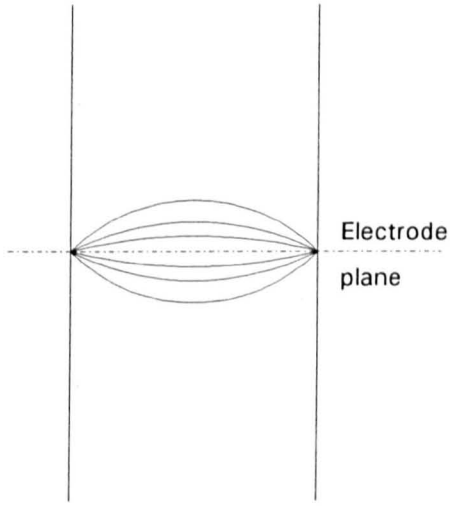

Figure 5.1 Current spreading in 3-D for the injected current system

In general the images so obtained appear to be only slightly corrupted by 3-D effects which implies that such systems are only marginally sensitive to out of plane information. The current spread in APT systems reduces the possible axial resolution but does not severely corrupt the resultant images. Conversely Purvis[17] found that when the algorithm developed for 2-D induced current impedance imaging was applied to measurements or simulations taken from systems of 3-D geometry, the images produced were severely corrupted. In certain circumstances even the polarity of the conductivity changes contained within the resultant images would be corrupted.

This result was somewhat unexpected since it has been argued that the coils would induce currents parallel to the plane of the coils. The magnetic vector potential induced

by the coil would have no axial component since the coils carry no axial component of current and the magnetic vector potential can only be parallel to the current producing it. With no axial component of the magnetic vector potential it seemed plausible that any induced axial current would be too small to have a significant effect. This assumption that there was no significant axial current would imply that all the current must flow parallel to the plane of interest, and consequently there would be very little out of plane interaction.

In this chapter the cause and the nature of the 3-D problem in induced current systems is investigated and from the results it is possible to identify particular 3-D situations where images might be reconstructed. An algorithm was then developed that was capable of reconstructing images using measurements taken from some types of 3-D geometry.

5.2 Analysis of the 3-D geometry by the method of finite elements

Using the 3-D finite element model it is possible to calculate the current paths for a 3-D homogeneous phantom. Figures 5.2.1 a and b show the paths of currents calculated in 3-D by the method of finite elements for a phantom symmetrical about the electrode plane with an aspect ratio measured as the phantom's total length to diameter ratio (l/d) of 0.125. Although for this thin phantom figures 5.2.1a and b give a good idea of the current pattern behaviour, in general current flows out of the plane of interest are best viewed on a computer screen where a model of the current paths can be rotated and a clearer appreciation of the direction of current at each individual point in the phantom attained. The magnitude of the current density at a point is indicated by the area of the arrow centred at that point and the direction by its angle. Figure 5.2.1a is the pattern predicted when coil one is driven with unit current and the second figure 5.2.1b is the pattern when coils two and three are both driven with unit current but in antiphase.

The former drive configuration produces an offset concentric current pattern and the latter a current pattern with two nulls and large radial components. These patterns can be rotated by using all three coils driven with different current weightings. The generation of radial components is important from the point of view of reconstruction because they make it possible to drive current through an image pixel at any angle.

In order to reconstruct an image using the backprojection technique used by Barber *et al* [16], an accurate estimate of the current paths is required to find the lines along which to backproject. It is usually assumed in such non-iterative schemes that impedance discontinuities in the region do not affect the paths of the current significantly. Purvis *et al* [9] used a similar assumption and generated images of reasonable quality from short phantoms for an induced current system.

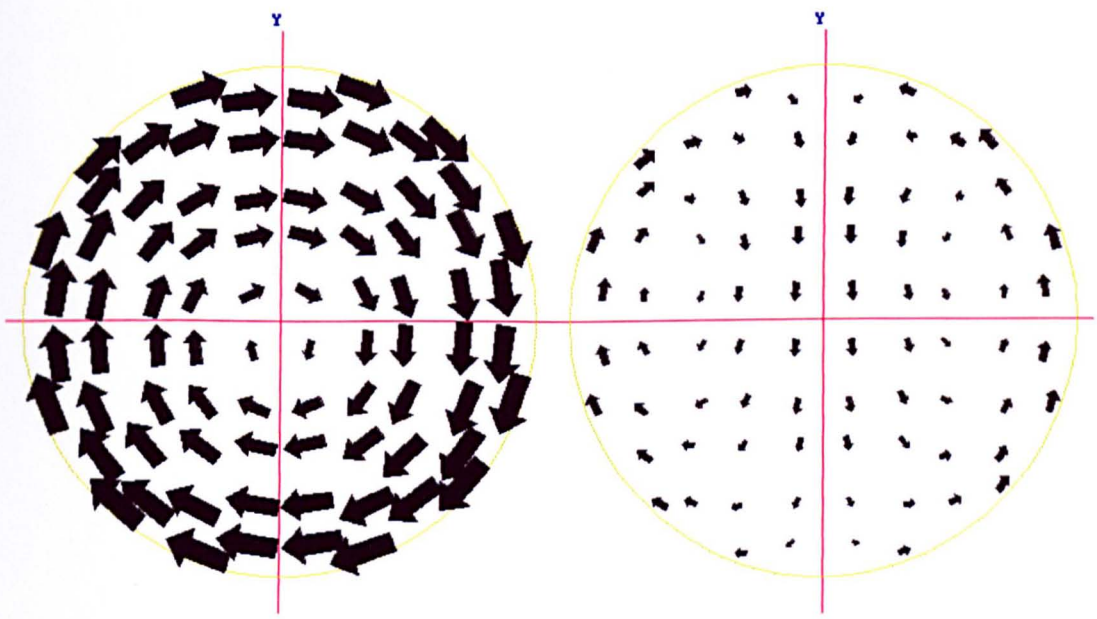

Figure 5.2.1 Plot showing the current in the plane of the coils for a short tank (l/d = 0.125), calculated by the method of finite elements.
Figure 5.2.1a: only coil 1 driven. Figure 5.2.1b: coils 2 and 3 driven in antiphase. Arrow area is proportional to current density and the scale is the same for both figures.

Figure 5.2.2 shows the effect on the paths of the currents of increasing the length of the tank. Figure 5.2.2a is for a short phantom (l/d = 0.125) and it shows patterns similar to those found by other workers using analytical methods for 2-D geometries as described in chapter 2. Figure 5.2.2b shows the effect of increasing the length by a factor of two. There is quite a noticeable change in the relative magnitudes of the currents but the basic pattern is not greatly altered except that there is a decrease in the radial component. If the tank's aspect ratio is increased so that l/d = 0.8 (figure 5.2.2c), the radial current disappears and the two nulls merge into one central null. This pattern of currents can cause serious problems for reconstruction. With no radial components of current it is only possible to drive current in one direction through any point of the tank *e.g.* in a circumferential direction. Barber[36] has shown that for injected current systems a failure to achieve angular uniformity of backprojection through each image point can produce reconstruction artefacts that are unacceptable. There is no evidence to suggest that the induced system can be exempted from this criterion. Not only is the current density at the centre very small but it changes rapidly with changes in the size of the tank.

As the current paths in the plane of interest are dependent on the axial dimensions of the tank, any attempt to use a reconstruction technique that requires the usual assumptions that the path of the currents is not affected by the exact form of the phantom are obviously inappropriate for bodies with a finite third dimension. Even if it were possible to find the exact current distribution (e.g. by precisely measuring the dimensions of the tank and solving the forward problem for a homogeneous conductivity distribution), and to use this distribution to generate a reconstruction algorithm, the current distribution would be unsuitable because it is only possible to drive current circumferentially through any part of the phantom. Furthermore towards the centre of the tank the current density would decay to zero making the sensitivity poor in this region.

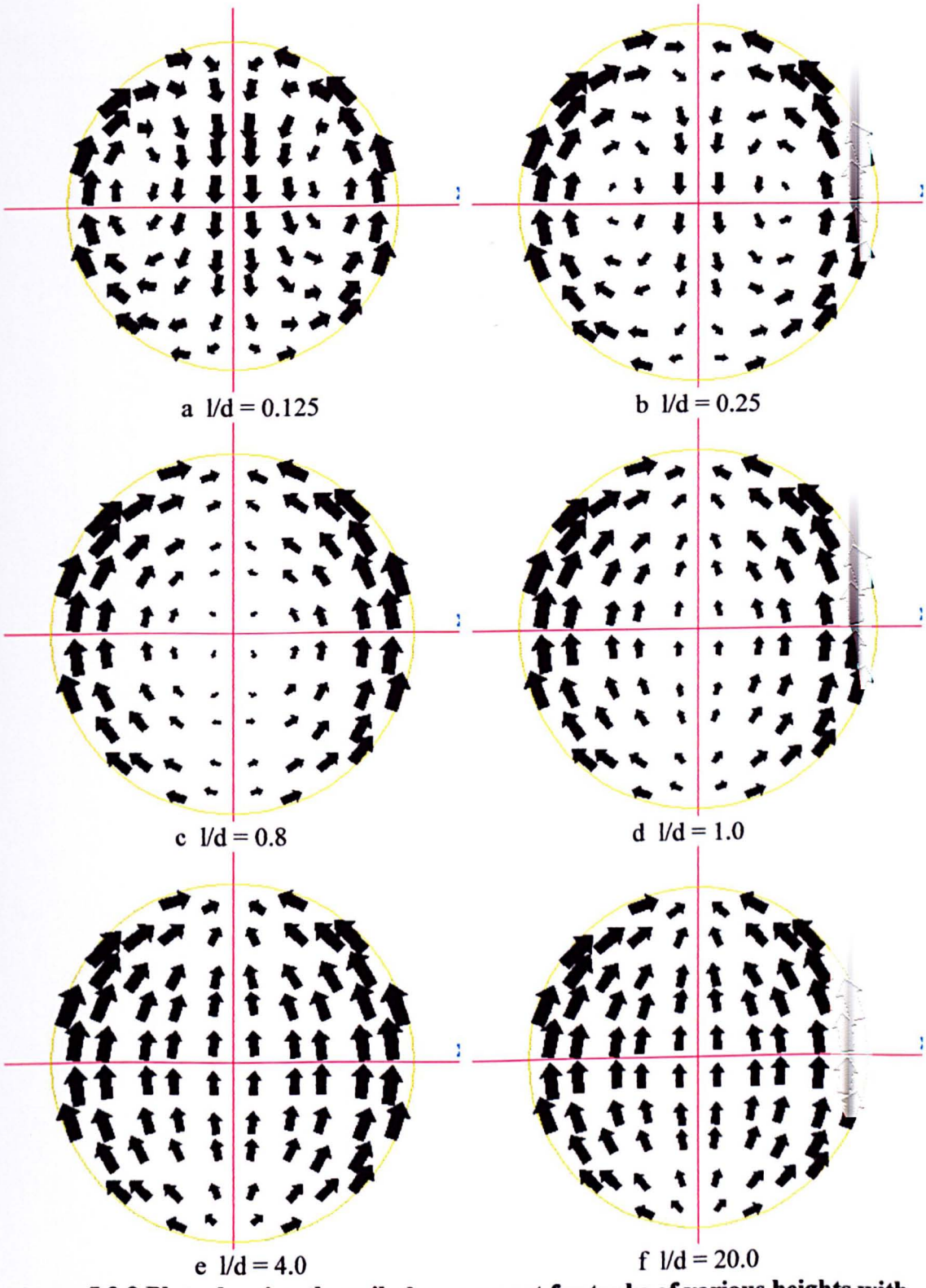

Figure 5.2.2 Plots showing the coil plane current for tanks of various heights with a diameter of 0.1 m.

The inducing field is generated by driving coils 2 and 3 in antiphase.
Arrow area is proportional to current density and the scale is the same for all 6 figures.

5.3 Dependence of the current patterns on the axial dimension

It is necessary to explain why the current pattern varies so greatly when the aspect ratio of the tank is changed. Figure 5.3 shows the inducing field due to the magnetic vector potential for two different drive configurations and at four different planes; namely the plane of interest and 0.2, 0.5 and 1 m below it. The inducing field is assumed to be the same for both 2-D and 3-D. In a 2-D system it is only the field in the plane of the coils which induces currents and it can be seen that this field is fairly uniform in one direction. At the edges normal to the direction of the vector potential, the field is slightly greater. In the 2-D case current is induced to flow in these edge regions. The only return path is through the centre even though the inducing field is opposing this path. The line integral of the magnetic vector potential from point A to point B, shown in figure 5.3c, is a function of the path from A to B. It is greater for the circumferential path than for the straight line path because of the greater magnetic vector potential in the edge regions. Hence in the loop circumferentially from A to B and back linearly from B to A there is a net field to induce current to flow in this path, and this results in the generation of a two current null pattern i.e. it has two loops of current. In the 3-D system however the current is not limited to flowing in the plane of interest but can also flow parallel to the axis of the cylindrical phantom. Although the path length, and therefore the resistance, is greater, the current induced in the plane of the coils flows in the direction of the inducing field and then returns by flowing axially crossing the phantom away from the plane of the coils where the inducing field is weaker. This means that the current pattern in the plane of interest is completely different for a short phantom than that for a long phantom.

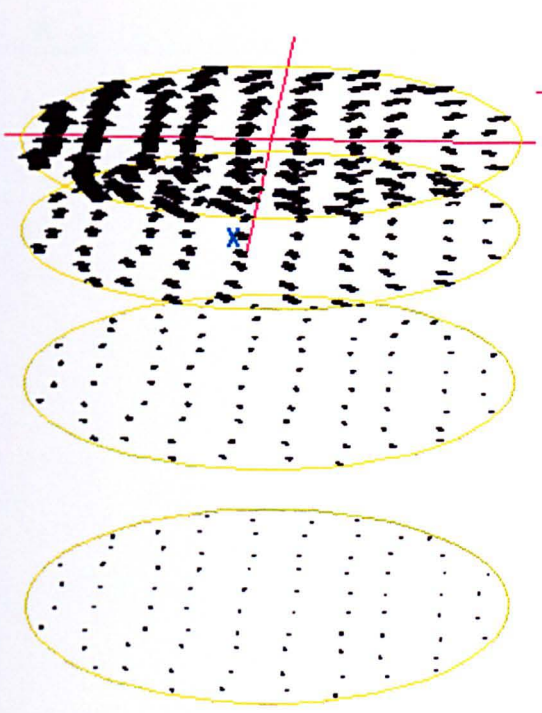

a
coil 1 driven

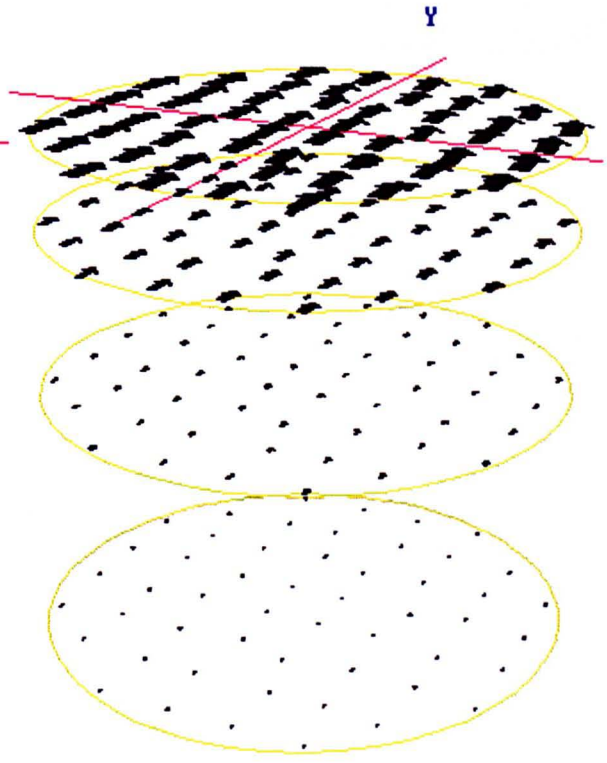

b
coils 2 and 3 driven in antiphase

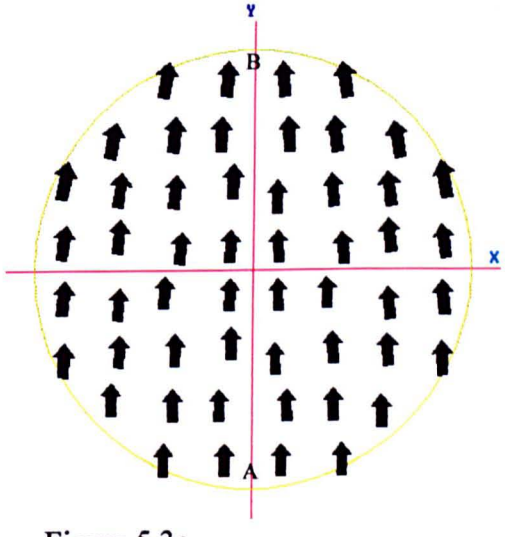

Figure 5.3c
coils 2 and 3 driven in antiphase

Figure 5.3 Plots show the induced field for two different coil drive configurations. *The induced field when coil 1 is excited is shown in figure 5.3a and when coils 2 and 3 are excited in antiphase in figures 5.3 b and c, with a perspective view and plan view respectfully. The perspective views show the fields from the coil plane to 1m below.*

5.4 3-D magnetically induced current imaging

Branston and Tofts[37] have shown analytically that it is not possible to induce radial currents within a homogeneous conducting sphere and this is true for any configuration of external drive coils. No such analytical solution has been found for cylindrical geometries but the cylindrical shape of the system has only been chosen for convenience and most practical imaging situations would be neither cylindrical nor spherical. For objects close in shape to a sphere it would be difficult to generate radial currents and any radial currents generated would be of an unpredictable nature as shown earlier. These currents would be dependent on objects that were out of the plane of interest but in general the character of these objects would not be known. Such effects limit the use of the type of reconstruction algorithms that are currently being used to reconstruct images.

This problem is fundamental and does not apply just to the algorithms generated by Purvis *et al* [9] because it is not possible to generate predictable radial currents. Hence the only current patterns in homogeneous spheres which can be used are circumferential. All other patterns have radial components rendering them unpredictable, because they are dependant on the exact axial nature of the body. Any attempt to generate radial current patterns for arbitrary structures close to spherical will produce unpredictable results unless the axial nature of the body is known. With only one predictable current pattern it is only possible to take one measurement from each electrode. The current system has 16 electrodes and therefore only 15 independent measurements can be made. Seagar *et al* [38] suggest that it would be possible to reconstruct an image with a number of pixels equal only to the number of independent measurements, giving in this case an image of approximately 4 by 4 pixels. Images of this type would have limited use and the generation of a reconstruction algorithm for this situation has not been attempted. These problems are fundamental to any reconstruction technique having the effect of limiting the method of induced current imaging for structures unless they are short enough to be considered 2-D. The method

of injected currents does not suffer from problems of this nature because the planar shape of the currents is not fundamentally altered in the plane of interest by the spread of currents in the axial direction. The method of injected currents can be applied to virtually any geometry with only slight distortion to the resulting images. [39]

However, it may be possible to image a spherical, or almost spherical, inhomogeneous region by an alternative arrangement. For a uniform spherical region the measurements are deferent, and so any departure of the measurements from that expected, is due either to a non-spherical shape or to a non-uniform distribution. Another approach could be adopted where the background conductivity distribution is both known and non-uniform, and in this situation it may be possible to generate a desirable selection of current patterns. An example of this is the head which has a known conductivity distribution that is highly divergent from uniform. For both these methods a different reconstruction algorithm would be needed, and this has not been pursued in this thesis.

5.4.1 General 3-D reconstruction algorithms

The current 2-D reconstruction algorithm is capable of reconstructing images from 2-D structures which conform to certain assumptions, such as the conductivity distribution must be sufficiently uniform so that the current pattern is not significantly disturbed from that of a homogeneous conductivity distribution, and that the structures must be sufficiently thin for the region to be considered 2-D. In this thesis an algorithm of the general type has been developed for imaging a group of 3-D structures. The algorithm is outlined and its limitations are discussed in the section 5.5. Section 5.4.2 describes some of the possible techniques that could be used for application specific algorithms.

5.4.2 Application specific algorithms

For structures where the path of the current is critically sensitive to the axial extent of the structure being imaged, a general algorithm would not be well suited to reconstructing images. In some situations a great deal is known about the conductivity distribution and therefore a prediction of the current paths could be made and then used to develop an algorithm. The head is a good example of such an imaging situation. Although the head is quite close to spherical the non-uniform conductivity distribution would enable the possibility of inducing currents with radial paths. It would also be possible to use electrodes and coils which are at different orientations to horizontal as shown in figure 5.4.1. This would allow the use of many other types of current pattern, such as circumferential at non-horizontal orientations, and so many more independent measurements would be possible. However in this thesis there has been no attempt to develop these ideas further.

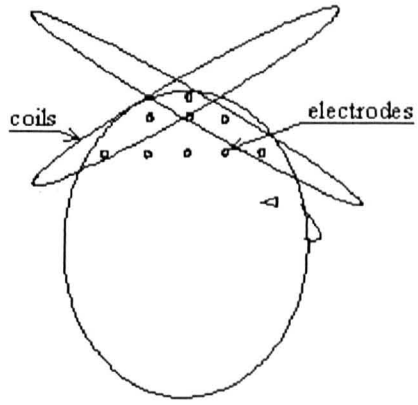

Figure 5.4.1 Possible alternative arrangement of electrodes and coils for imaging the head.

5.5 Generation of a 3-D reconstruction algorithm

The images shown in figures 5.5.1 demonstrate how the 2-D reconstruction algorithm of Purvis behaves for phantoms of varying aspect ratios. Figure 5.5.1a shows the cross section of the conductivity distribution which was uniform over the entire length of the phantom. The peripheral potentials were calculated using FEM and then used to reconstruct the images shown in figures 5.5.1b to f. For objects close to the edge the

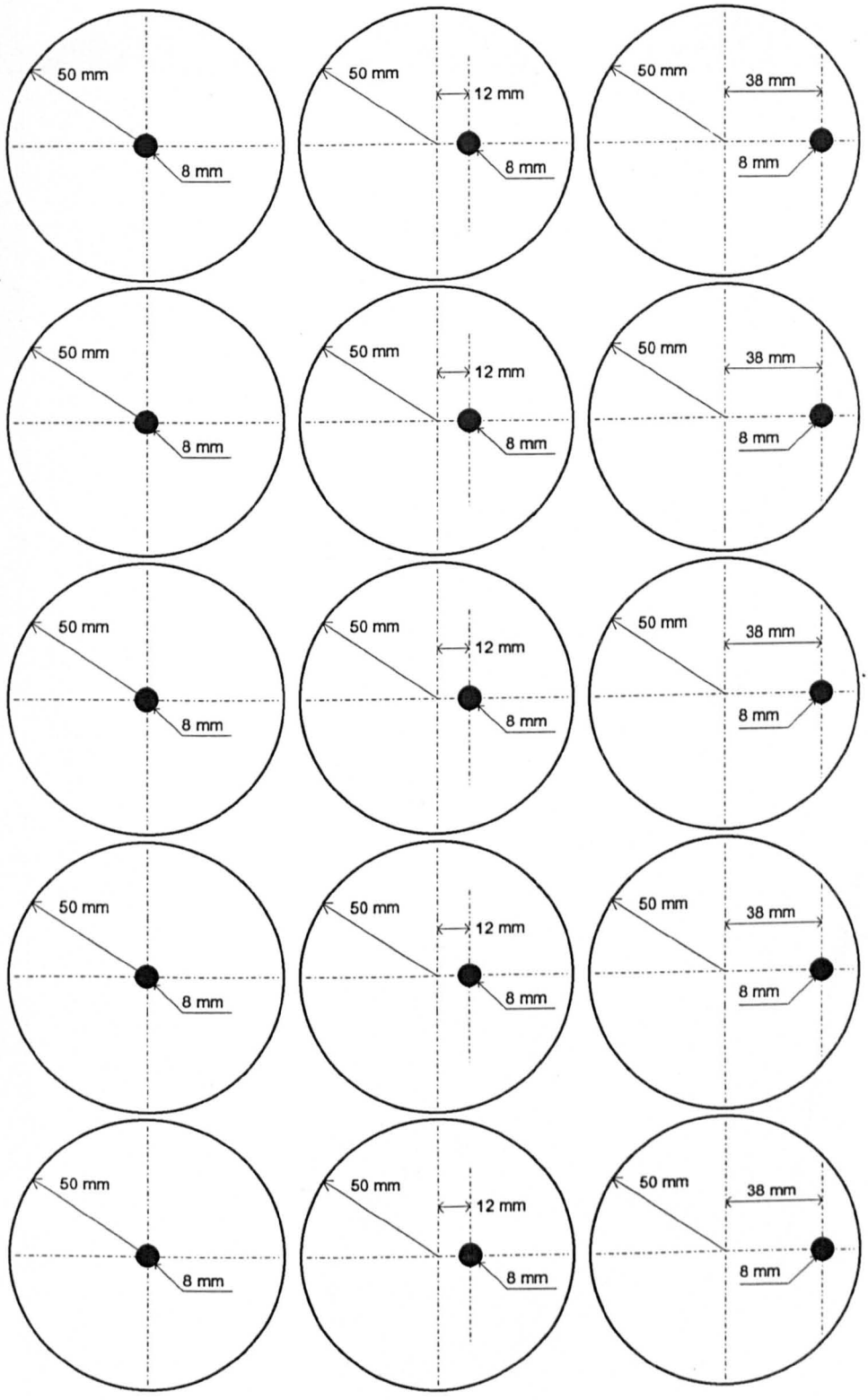

Figure 5 5 1a Overlay showing the position of the insulating target

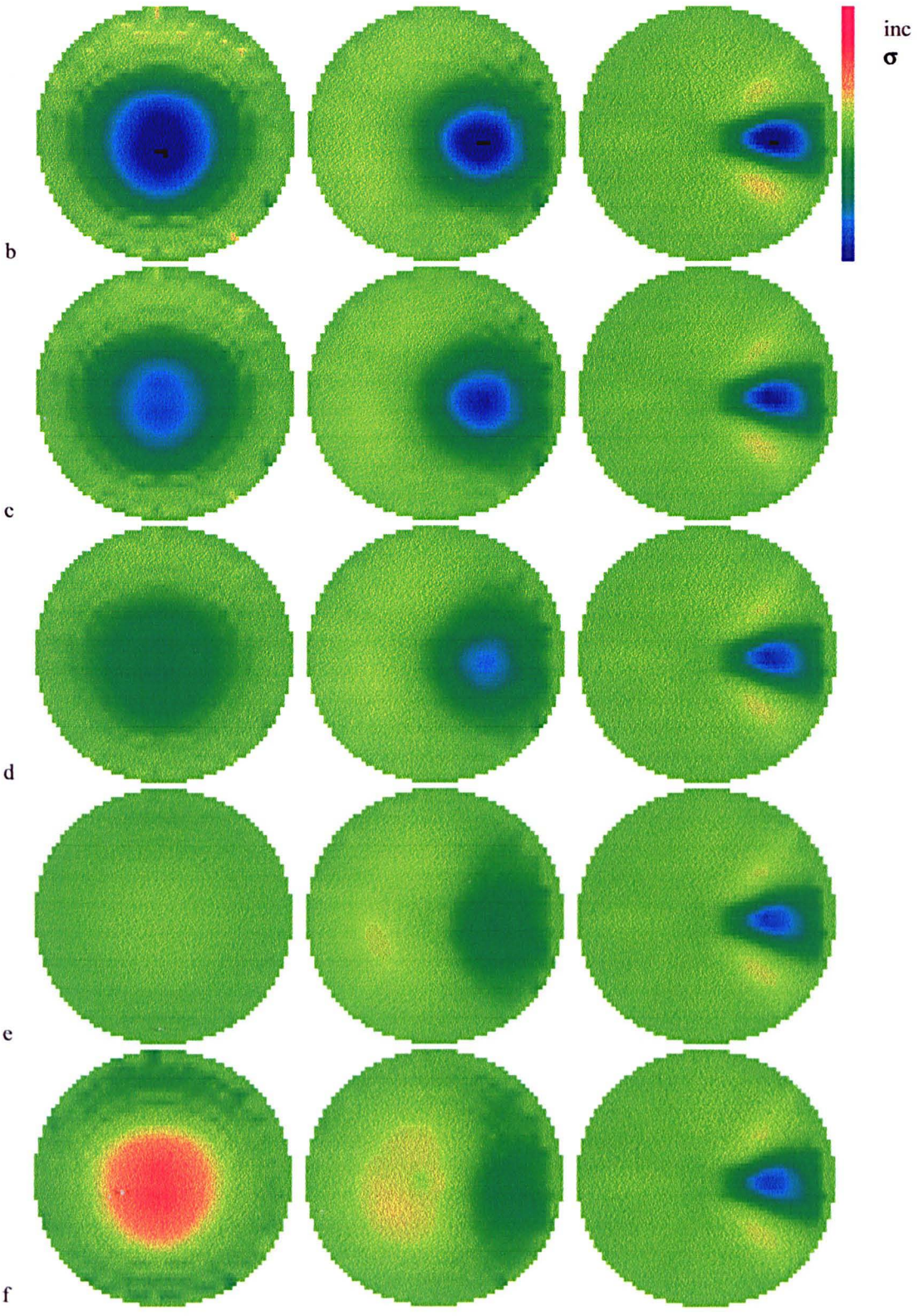

Figure 5.5.1 b..f Images reconstructed using the 2-D reconstruction algorithm from data calculated for phantoms with various length to diameter ratios. *Each column of images is displayed to the same scale and reconstructed from a phantom with the conductivity distribution shown on the overlay. The length to diameter ratios are b = 0.1, c = 0.63, d = 1, e = 1.6, f = 10*

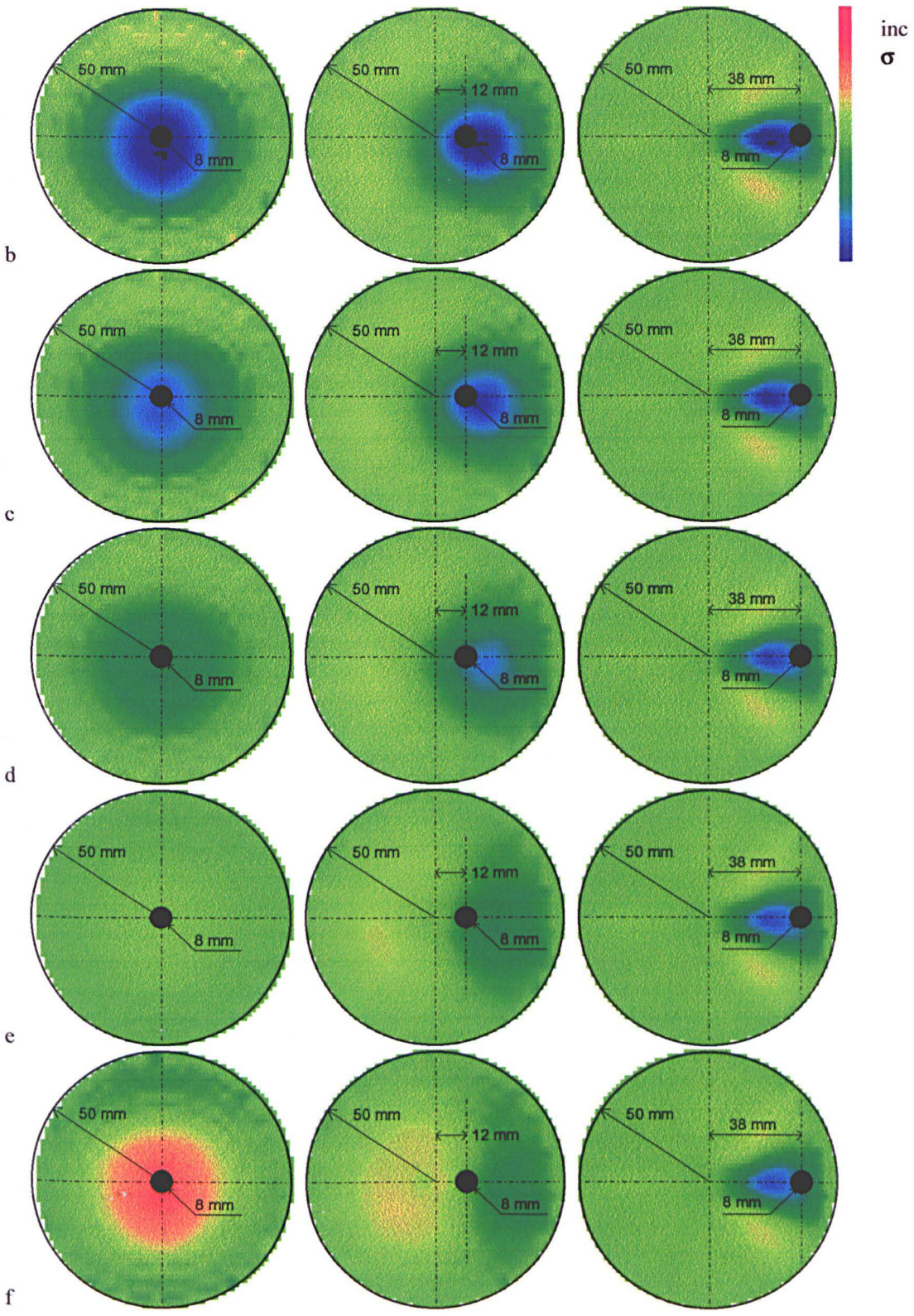

Figure 5 5 1a Overlay showing the position of the insulating target

Figure 5.5.1 b..f Images reconstructed using the 2-D reconstruction algorithm from data calculated for phantoms with various length to diameter ratios. *Each column of images is displayed to the same scale and reconstructed from a phantom with the conductivity distribution shown on the overlay. The length to diameter ratios are b = 0.1, c = 0.63, d = 1, e = 1.6, f = 10*

images can be reconstructed for any aspect ratio but for objects close to the centre the algorithm is only capable of reproducing images from data with an aspect ratio l/d << 1.

Figures 5.2.2d to f show the effect on the current paths when the aspect ratio is altered. Figures 5.2.2e and f show long tanks with l/d = 4 and l/d = 20 respectively. The currents of both are drawn to the same scale. These two figures clearly show that there is little difference both in the pattern and also in the magnitude of the currents even though there is a five fold change in the aspect ratio. There appears to be a limit above which the magnitude of the l/d has no significant effect on the pattern of currents. The graph in figure 5.5.2 shows the magnitude of the current at the centre of the plane of interest with coils two and three driven in antiphase plotted against the length of phantom. It clearly shows that the current goes through a null when l/d equals approximately 0.8. This is the point at which the sign of the current changes. For phantoms with both very small and very large values of l/d the rate of change of current associated with a change in l/d for the phantom is small. With l/d values from 0.2 to 2.0 the current varies from one extreme to another. This result, which shows that the current has two stable regions is useful because it means that for a tank with a high value of l/d (> 2) the current pattern is predictable and not only predictable but independent of the ratio of the tank dimensions.

5.5.1 Limits to the use of the 3-D algorithm

If current patterns for a phantom with l/d > 2 were used to generate a reconstruction algorithm, it would be possible to generate images from a range of phantoms, the only restriction being that they would have to conform to the criterion of having a large l/d i.e. l/d ≥ 2. An algorithm already exists for the 2-D case Purvis *et al* [9] so short phantoms i.e. l/d ≤ 0.2 can also be imaged. This does exclude phantoms that are neither short nor long because as explained above it becomes difficult to generate predictable radial currents for structures that tend to the spherical. Without radial currents a very limited number of independent measurements can be made and so only extremely crude images could be generated.

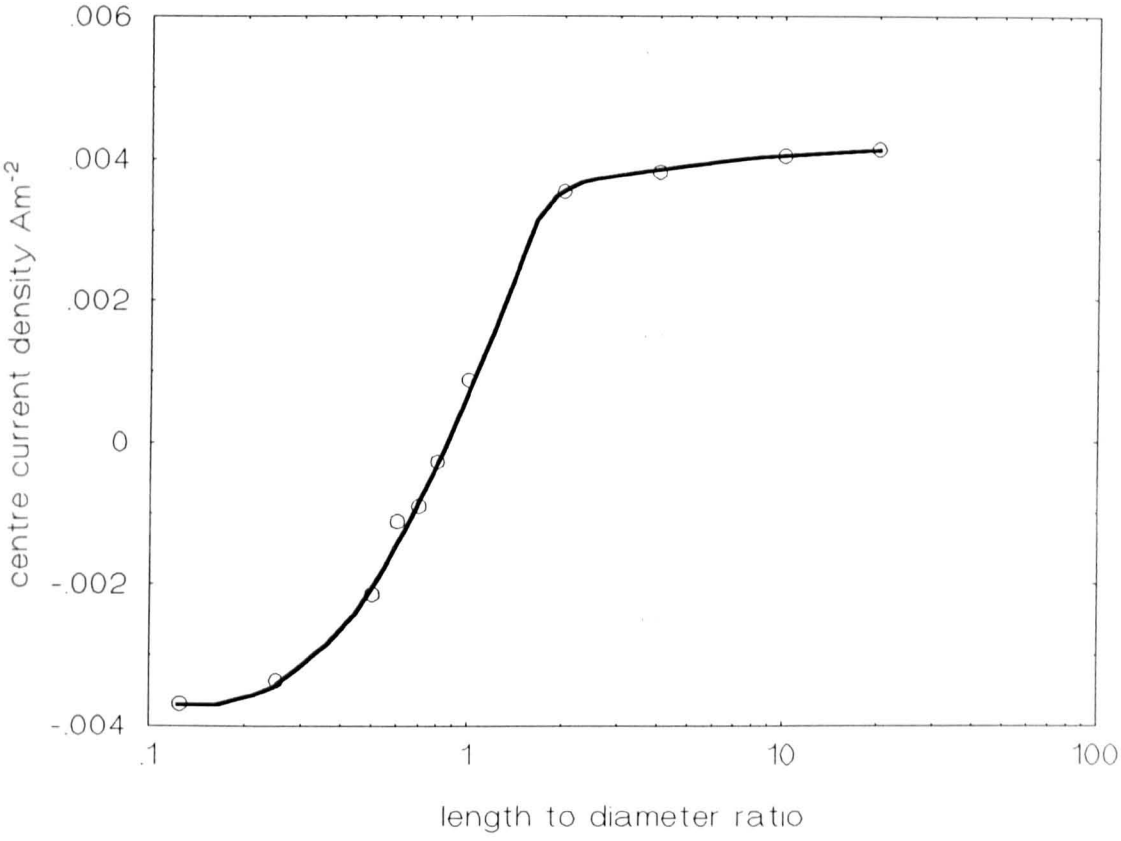

Figure 5.5.2 The relationship between the length to diameter ratio of the phantom and the current density at its centre.

5.5.2 Calculation of a 3-D reconstruction algorithm

Figure 5.5.2 shows how current at the centre of the phantom (calculated using FEM) varies as the aspect ratio of the tank is changed. It will be seen that in a tank of $l/d > 2$, the rate of change of centre current is small and therefore is quite a good approximation to a long tank. In order to generate a backprojection algorithm the path of the currents was found using the 3-D finite element program. The current distribution was found using a tank with an l/d value of 20 and from this distribution the plane of interest current patterns were extracted for each coil. Using these current patterns a set of reconstruction matrices was generated using exactly the same process as for the 2-D case.

This process was developed by Purvis[9] who uses a type of sensitivity matrix to form images and a detailed description of this is given in appendix 2. Reconstruction matrices for a long tank were generated by directly applying the method discussed in appendix 2 to generate a 2-D reconstruction matrix but using the currents calculated in the plane of interest for a tank with a l/d of 20.

Figure 5.5.3 shows the images obtained using this new algorithm for the three different conductivity distributions shown in figure 5.5.3a. Figures 5.5.3b to f show the images reconstructed from the same data as those in figures 5.5.1b to f. The images shown in figure 5.5.3f are reconstructed using the new algorithm from data calculated for the long phantom and are of similar quality to those reconstructed from data calculated for a 2-D phantom using the 2-D reconstruction algorithm (figure 5.5.1b). Figures 5.5.3b to e show that the 3-D reconstruction algorithm suffers problems when data is taken from phantoms which are not sufficiently long in the same way that the 2-D algorithm suffers problems when data is taken from phantoms which are not sufficiently short. With very short phantoms the system is sensitive to objects at the centre but the 3-D algorithm corrupts the sign of the reconstructed image and also generates increased reconstruction artefact. When the length to diameter ratio for the phantom approaches unity the sensitivity to objects close to the centre falls and neither the 2-D nor the 3-D algorithms produce satisfactory results.

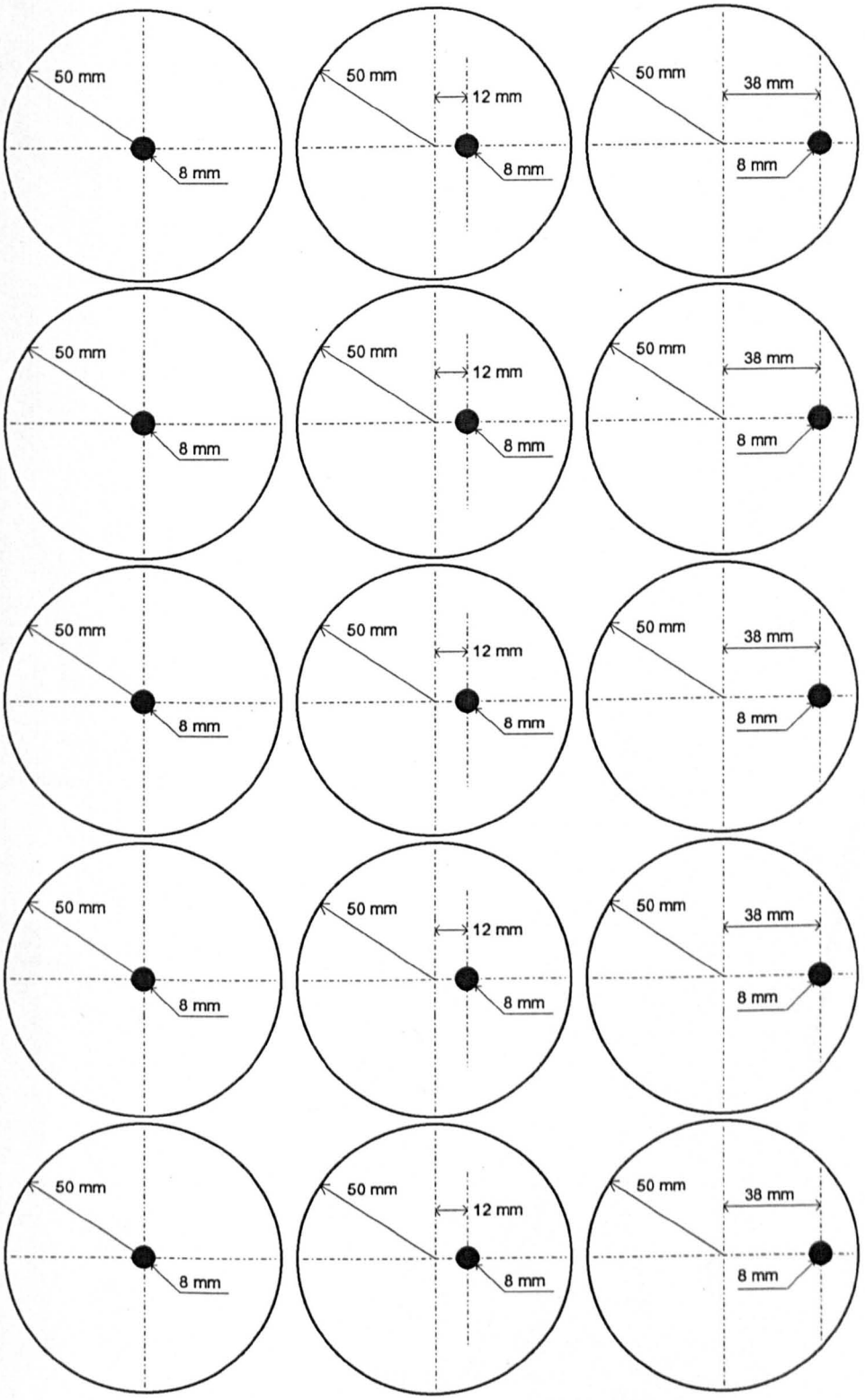

Figure 5 5 3a Overlay showing the position of the insulating target

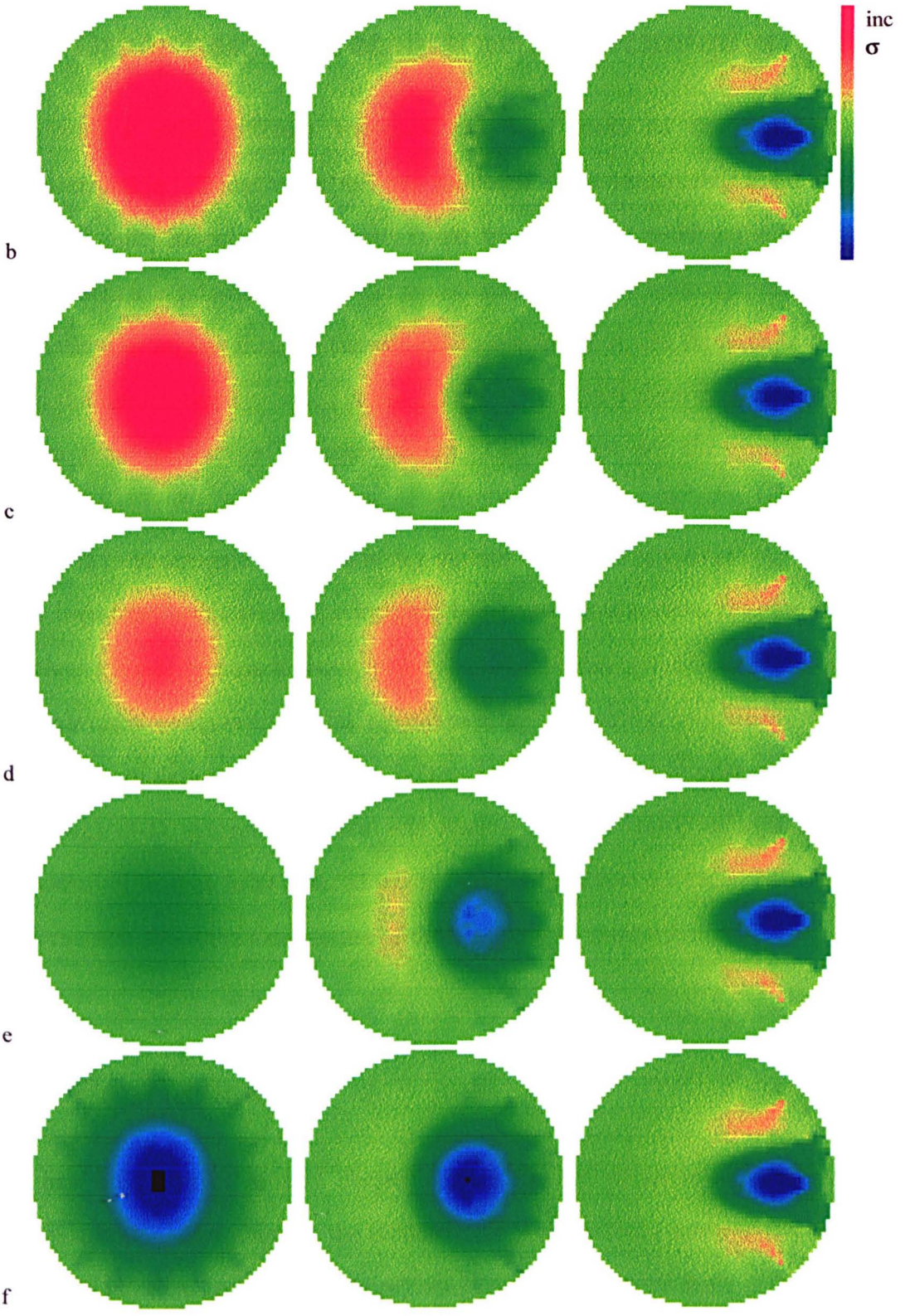

Figure 5.5.3 b..f Images reconstructed using the 3-D reconstruction algorithm from data calculated for phantoms with various length to diameter ratios. *Each column of images is displayed to the same scale and reconstructed from a phantom with the conductivity distribution shown on the overlay. The length to diameter ratios are b = 0.1, c = 0.63, d = 1, e = 1.6 , f = 10*

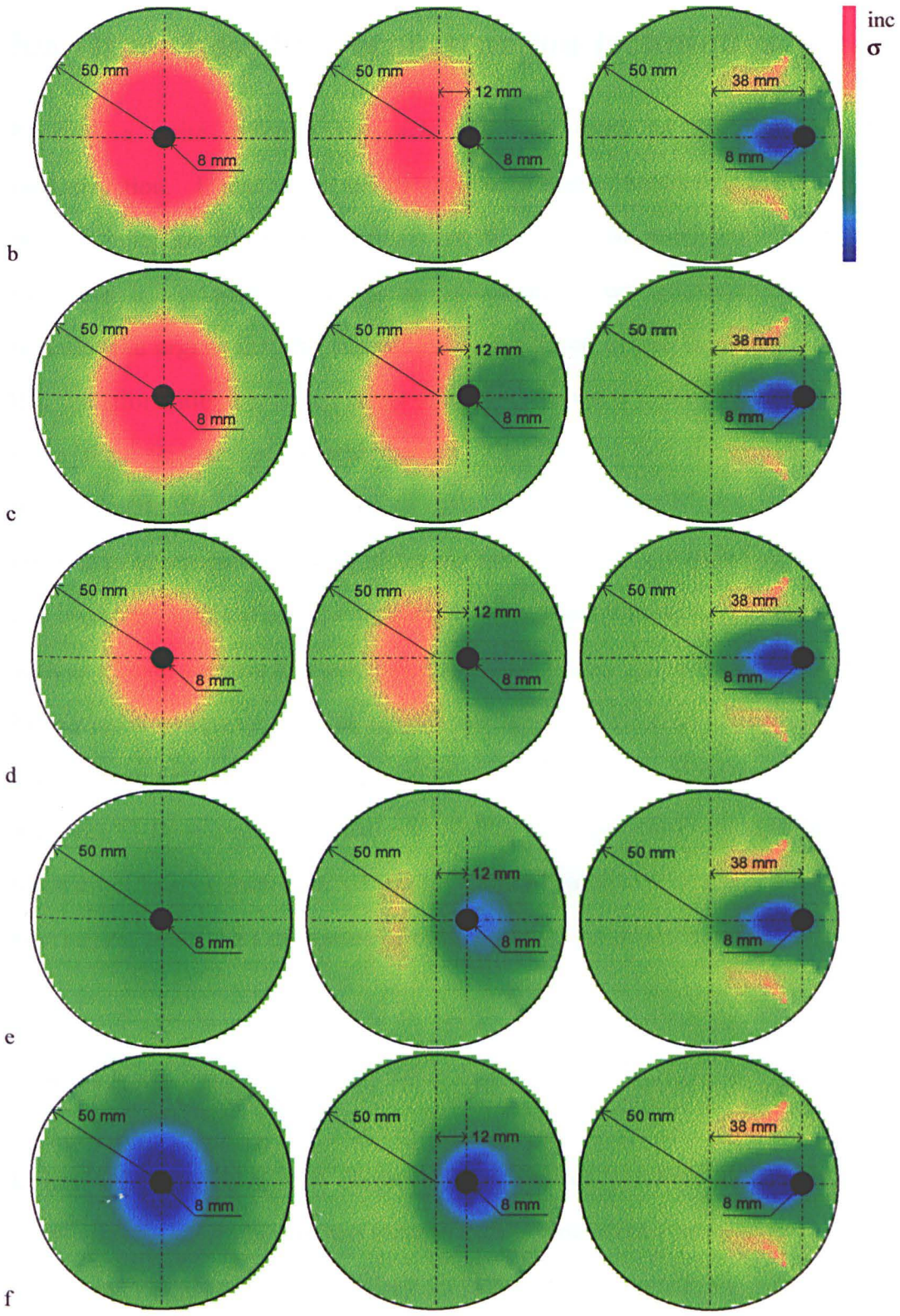

Figure 5 5 3a Overlay showing the position of the insulating target

Figure 5.5.3 b..f Images reconstructed using the 3-D reconstruction algorithm from data calculated for phantoms with various length to diameter ratios. *Each column of images is displayed to the same scale and reconstructed from a phantom with the conductivity distribution shown on the overlay. The length to diameter ratios are b = 0.1, c = 0.63, d = 1, e = 1.6 , f = 10*

5.6 Other possible reconstruction techniques

Recently a quite different approach has been made to the problem of image reconstruction. Bouallouche[40] has produced some remarkably good images using only 15 independent measurements taken from one coil making the assumption that from them it is possible to infer the measurements for any arbitrary pattern of currents. Bouallouche argues that the current patterns induced by the three coils are so similar that the information contained in the differences between them does not warrant taking more than one set of measurements. Calculations are then made to find the measurements that would have been taken from any pattern of currents. Thus it is possible to interrogate any pixel with a current flowing in any direction. This technique has important implications for imaging bodies which are close to spherical in shape, such as a head, because it is only possible to induce one type of current pattern and this has no radial components. This algorithm is only suitable at present for reconstructing images from data gathered from a 2-D system and work is in progress to adapt it for use with 3-D systems. There will always be limitations to algorithms used to reconstruct images from induced current systems because a certain amount of *a priori* information about the axial nature of the body will be required.

5.7 Conclusions

It has been shown in this chapter that it is not possible to create a universal reconstruction algorithm for the induced current impedance tomography system. It is possible to reconstruct images from data gathered from both short and long phantoms. The images reproduced will be of reasonable quality as long as the appropriate reconstruction algorithm is used. Neither of the two algorithms is capable of forming images with data taken for phantoms which have an aspect ratio (l/d) close to unity. For this case it is not possible to induce substantial radial currents, and hence effectively only one current pattern can be used, yielding only 15 independent measurements. The

current density near the centre is close to zero so that the sensitivity for objects near to the centre is very small.

Chapter 6 Image Filtering

6.1 Introduction

Chapter 5 outlined the algorithm which was used to generate a matrix to reconstruct images from measurements taken from a 3-D phantom. The algorithm used was restricted in the range of l/d for which it could be used, and the images generated showed a limited spatial resolution and some reconstruction artefact. The reconstructed images are also distorted in that the reconstructed target is moved towards the centre of the region. This chapter discusses an approach used to improve this limited resolution, in which the data is filtered before it is used to form an image.

6.2 The principle of the filter

This filter uses the method of Barber *et al* [18], but applies it to forming 2-D images of the cross section of 3-D regions. The images are formed using the difference between two sets of measurements yielded by the change in conductivity distribution from that of a uniform region. The process by which the conductivity distribution is transformed to boundary measurements can be described by the equation:-

$$\Delta \mathbf{g} = \mathbf{F}\Delta \mathbf{c} \qquad 6.2.1$$

where **F** is the forward matrix which, when it operates on the column vector $\Delta \mathbf{c}$ of conductivity change, produces the row vector $\Delta \mathbf{g}$ of changes in the boundary measurements . If the backprojection operator **B** is exact, it would be the inverse of **F**, but it is clear from the images produced so far that this is not the case. The question is whether it is possible to modify the backprojection operator **B** so that it is a better approximation to $\mathbf{F}^{-1}$. The method of Barber *et al* is to determine a set of peripheral voltages $\Delta \mathbf{g}'$ such that back-projecting using **B** gives the correct image $\Delta \mathbf{c}$, *i.e.*:-

$$\Delta \mathbf{c} = \mathbf{B}\Delta \mathbf{g}' \qquad 6.2.2$$

Then from equations 6.2.1 and 6.2.2

$$\Delta \mathbf{g} = \mathbf{FB}\Delta \mathbf{g}' \qquad 6.2.3$$

or

$$\Delta \mathbf{g}' = (\mathbf{FB})^{-1}\Delta \mathbf{g} \qquad 6.2.4$$

The term $(\mathbf{FB})^{-1}$ is a filter operating on the measured data $\Delta \mathbf{g}$ to form a new set of data $\Delta \mathbf{g}'$ such that backprojection will form the correct image. In fact it is not necessary to calculate $\Delta \mathbf{g}'$ explicitly because putting 6.2.4 into 6.2.2 gives:-

$$\Delta \mathbf{c} = \mathbf{B}(\mathbf{FB})^{-1}\Delta \mathbf{g} \qquad 6.2.5$$

The whole of operator $\mathbf{B}(\mathbf{FB})^{-1}$ can be found in advance of the reconstruction and it simply reduces to a new reconstruction matrix so that no extra computation is required at the time of the reconstruction.

If **F** and **B** were square matrixes then $\mathbf{B}(\mathbf{FB})^{-1}$ will simply reduce to $\mathbf{F}^{-1}$ and it would seem possible to find the reconstruction matrix by inverting **F**. However the direct inversion of **F** would not be easy because **F** is not a square matrix having more image pixels than there are independent measurements, and consequently **F** does not have a unique inverse. The matrix **(FB)** is square which greatly simplifies its inversion compared with the inversion of **F**, and it should be close to diagonal (depending on how accurate **B** is). The Barber filter has been used mainly on 2-D problems, that is to say **F** and **B** were calculated for 2-D models, although the filter has been applied to data measured on 3-D structures. The adaptation to be described here extends this idea to 3-D because **F** is found from 3-D conductivity distributions which are made up of long rods which span the length of the phantom, but **B** is still a reconstruction matrix for a 2-D image.

6.3 Calculation of the filter

To generate the filter it is first necessary to find the forward matrix **F**. The **F** matrix contains information about the peripheral voltage profiles for conductivity discontinuities placed at the location of each of the pixels in the image. To find the **F** matrix the FEM was used where the conductivity distribution was defined as a vertical column of elements of conductivity 10^{-3} S m^{-1} in a tank of height ±500 mm. The **F** matrix was constructed from the results of the FEM which was used to find the potential distribution of the region and then the peripheral voltage differences were extracted. As all the elements of the finite element mesh do not have the same cross sectional area, this could lead to some pixels showing a higher sensitivity than others. To reduce this effect the assumption was made that there would be a linear change in the sensitivity for small changes in cross sectional area. Anderson *et al* [21] has shown that for all but large discontinuities the change in the area of a discontinuity has only a very small effect on the shape of the profile, and that the magnitude of the profile is almost proportional to the change in area. The voltage profiles were normalised with respect to the cross sectional area of the column of elements. This calculation was repeated for each of the 716 pixels for excitation by each of the three coils in turn.

The **F** matrix, which has 716×45 elements, is multiplied by the 3-D reconstruction matrix **B** described in chapter 5, thus giving (**FB**), with 45×45 elements, which needs to be inverted in order to produce the filter. This is a difficult inversion to perform because the matrix is ill-conditioned. An ill-conditioned matrix is one that is numerically close to being singular, and such a matrix does not have a unique inverse. This situation is similar to attempting to find the solution to a set of simultaneous equations where two or more equations are linear combinations. A singular matrix has at least one pair of rows or pair of columns which have members which are a linear combination, and an ill-conditioned matrix will have one or more pairs which are numerically close to this condition.

Ill-conditioned matrices can be inverted by direct methods such as 'Gaussian elimination' but the problem with these methods is that the solution places excessive weight on slight differences in the linear combination of two rows or columns. This can result in the inverse being pulled away from a more appropriate result. At the same time the numerical precision of the computation becomes increasingly important and the inverse can be dominated by rounding errors.

There are alternative methods for inverting matrices that avoid this problem and can in fact generate solutions to singular matrices. One such method is called singular value decomposition (SVD) [33] and the solution found, although not unique, is the minimum energy solution for the set of all possible solutions.

6.3.1 Singular value decomposition

A detailed description of the method of singular value decomposition [33] is beyond the scope of this thesis but a brief outline of the method is described here.

Any matrix A can be split into three square matrices as shown:-

$$\mathbf{A} = \mathbf{U}.\begin{pmatrix} w_1 & 0 & 0 & 0 \\ 0 & w_2 & 0 & 0 \\ 0 & 0 & \dots & 0 \\ 0 & 0 & 0 & w_n \end{pmatrix}.\mathbf{V}^T \qquad 6.3.1.1$$

U and V are matrices with the property that their inverse is equal to their transpose so that the calculation of the transpose of both U and V is trivial and the W is a diagonal matrix as shown. The calculation of its inverse involves finding the reciprocal of each element. The matrices U, W and $\mathbf{V}^T$ can always be found for any A however ill-conditioned.

rearranging 6.3.1.1

$$\mathbf{A}^{-1} = \mathbf{V}.\begin{pmatrix} \frac{1}{w_1} & & & \\ & \frac{1}{w_2} & & \\ & & \cdots & \\ & & & \frac{1}{w_n} \end{pmatrix}.\mathbf{U}^T \qquad 6.3.1.2$$

The matrix **W** holds the key to the method of SVD. The ratio of the largest to the smallest values of w_i is called the "condition number" for the matrix and is a quantitative measure of how close to singular the matrix is. If the condition number for the matrix is infinity, which would be caused by one of the w_i values being 0, then the matrix is singular as this value of $1/w_i$ cannot be determined. In the method of singular value decomposition the value 1/0 is replaced by 0 or, in the case of an ill-conditioned matrix, values of w which are less than a predetermined minimum threshold $1/w_i$ are replaced by zero. This action discards information to which a direct method would have paid excessive attention and so would drag the solution away from an appropriate inverse. Once the value of $\mathbf{W}^{-1}$ has been found, 6.3.1.2 is used to evaluate $\mathbf{A}^{-1}$. This solution will be the minimum energy solution of the possible set of solutions for $\mathbf{A}^{-1}$.

6.4 The inversion of (FB)

The matrix **(FB)** to be inverted, obtained as described in section 6.2, has a condition number of $1.4 \cdot 10^5$ which is sufficiently large for direct methods of inversion to produce completely inappropriate results. In chapter 4 methods were described by which the accuracy of the forward problem was tested but it was not possible to test this to an accuracy of 1 part in $1.4 \cdot 10^5$. It is unreasonable to assume that with 22000 nodes it is possible to model the system to within one part in $1.4 \cdot 10^5$, and therefore attempting to invert this matrix directly with such a condition number is likely to lead to a solution that is totally dominated by errors in **F**, and for this reason the method of SVD was used to invert **(FB)**. The method of SVD for the generation of the filter needs to be

supplied with a minimum value as a threshold for the w matrix. In the absence of an analytical method of finding this value, an iterative method was used. The filter was generated with a particular threshold value and was used to reconstruct a range of images. These images were compared with each other and on this basis a threshold value was chosen. Figure 6.4.1a. shows a range of three test conductivity distributions from which the FEM was used to calculate the peripheral potential distribution. Figure 6.4.1b shows images reconstructed by the unfiltered matrix and figures 6.4.1c, d, e, and f show images reconstructed using the filtered matrix at threshold values of $1/w_i<(100, 10^3, 2\cdot10^3$ and $5\cdot10^3)$ respectively. Values of $1/w_i$ in excess of this threshold are decomposed to zero. These images show that for low threshold values the filtering does not make very much difference except an increase in the blurring of the image accompanied by a decrease in the artefact associated with the image. The locations of the reconstructed targets are still displaced. As the threshold value is increased the artefact is increased but the blurring is decreased. At the same time the reconstructed object is moved closer to the correct location. For very high values of the threshold the filtered image completely decomposes and appears to be meaningless as shown in figure 6.4.1g which is generated by a direct inversion of the **(FB)** matrix.

A method that could preserve both the low artefact of the filtered image and the better resolution of the unfiltered images is to multiply the images together: *i.e.* each pixel value is set to the product of that pixel in the filtered and unfiltered image. In order to preserve the sign of the images the unfiltered images are multiplied by the modulus of the filtered image. Figures 6.4.2 c to f show similar images to those of figure 6.4.1 c to f but they are multiplied as described. By multiplying the images together the resulting image will have square law characteristics and the question arises as to whether or not this is an acceptable procedure.

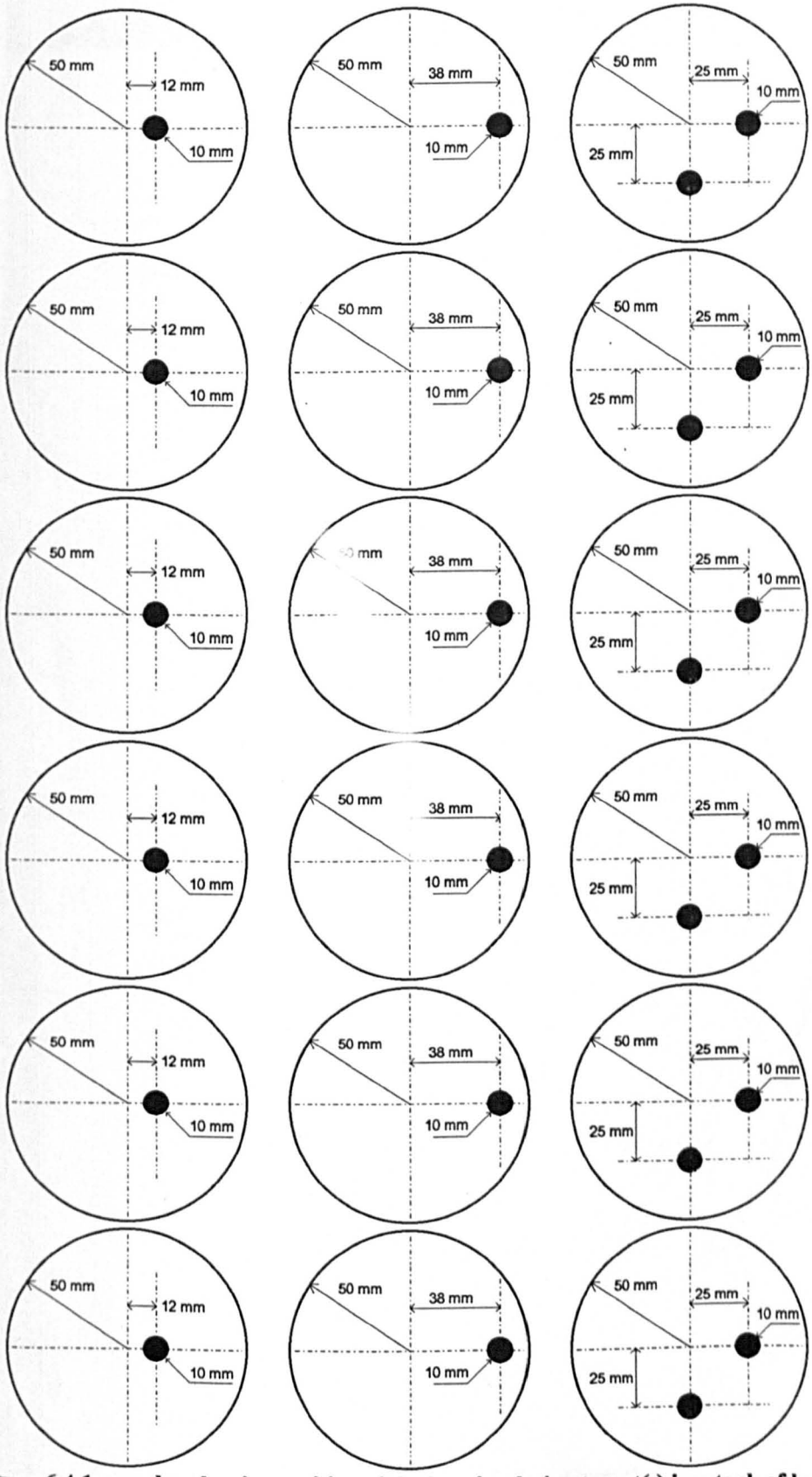

Figure 6.4.1a overlay showing position of the long insulating target(s) in a tank of height ±500mm

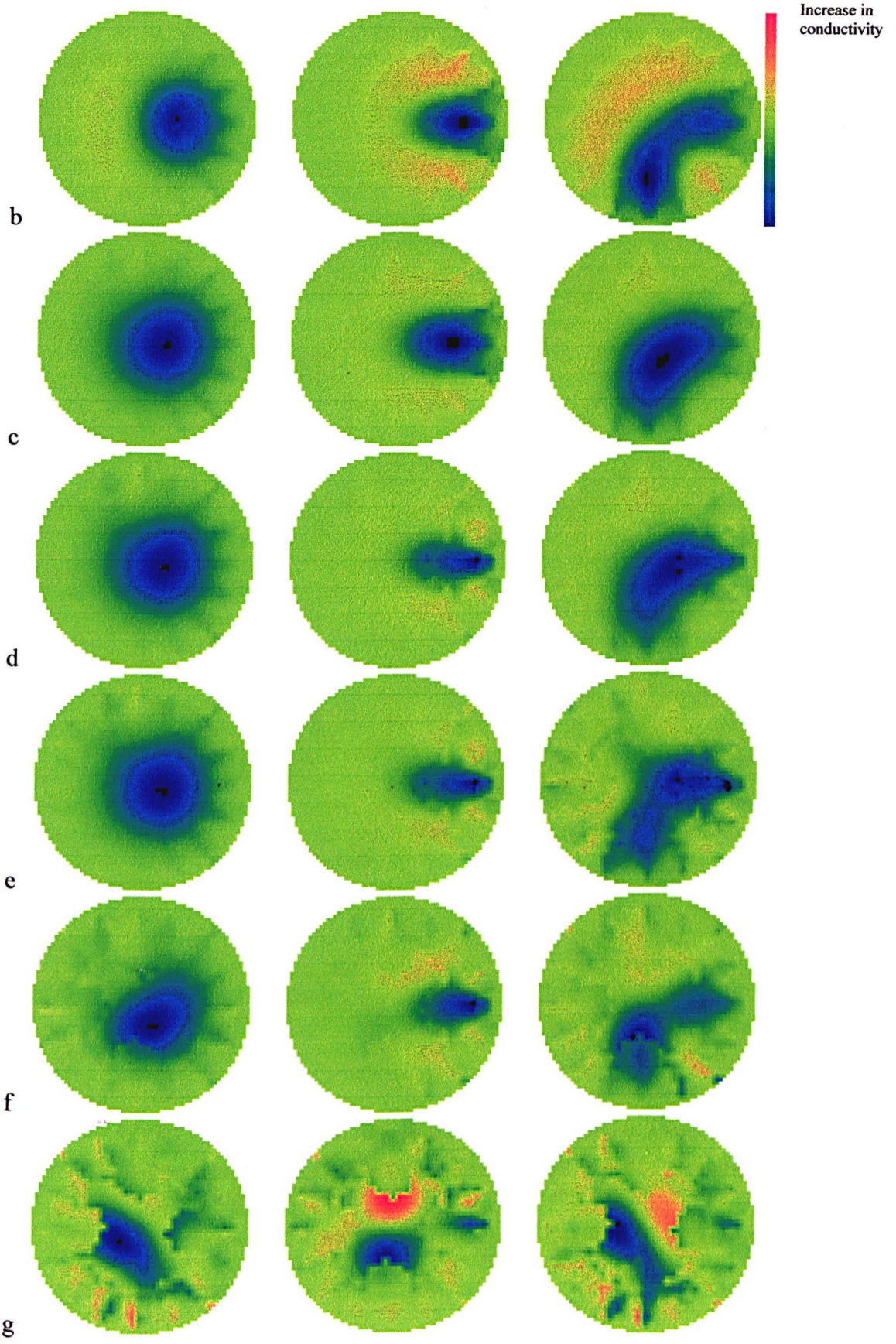

Figure 6.4.1 Images reconstructed using different filters

Conductivity images reconstructed from data found using the test distributions shown on overlay. b {no filter}; c {threshold $1/w_i<100$}; d {threshold $1/w_i<10^3$}e {threshold $1/w_i<2\cdot10^3$}; f {threshold $1/w_i<5\cdot10^3$}; g {direct inversion}

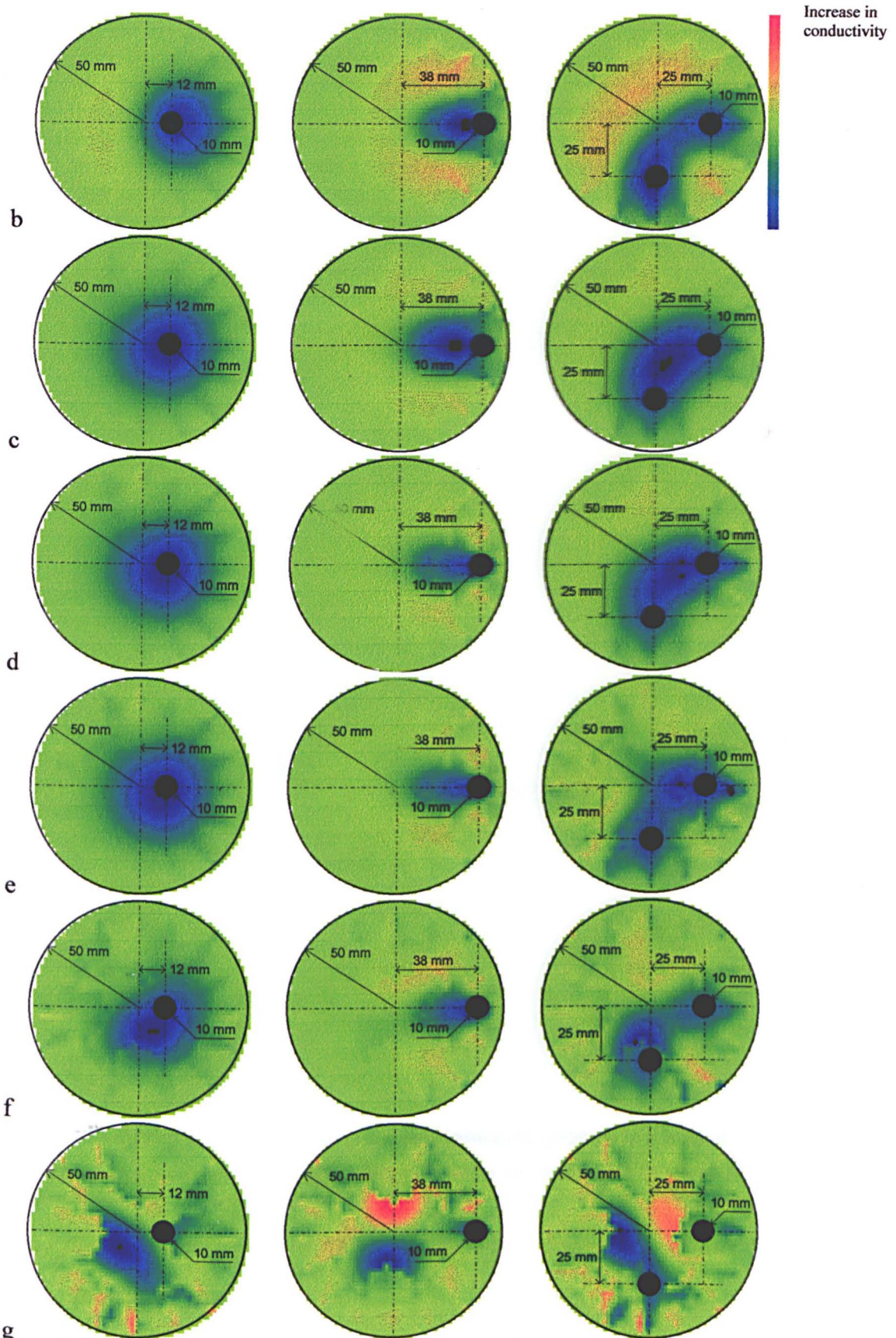

Figure 6.4.1a overlay showing position of the long insulating target(s) in a tank of height ±500mm

Figure 6.4.1 Images reconstructed using different filters

Conductivity images reconstructed from data found using the test distributions shown on overlay.
b {no filter}; c {threshold $1/w_i<100$}; d {threshold $1/w_i<10^3$}e {threshold $1/w_i<2\cdot10^3$}; f {threshold $1/w_i<5\cdot10^3$}; g {direct inversion}

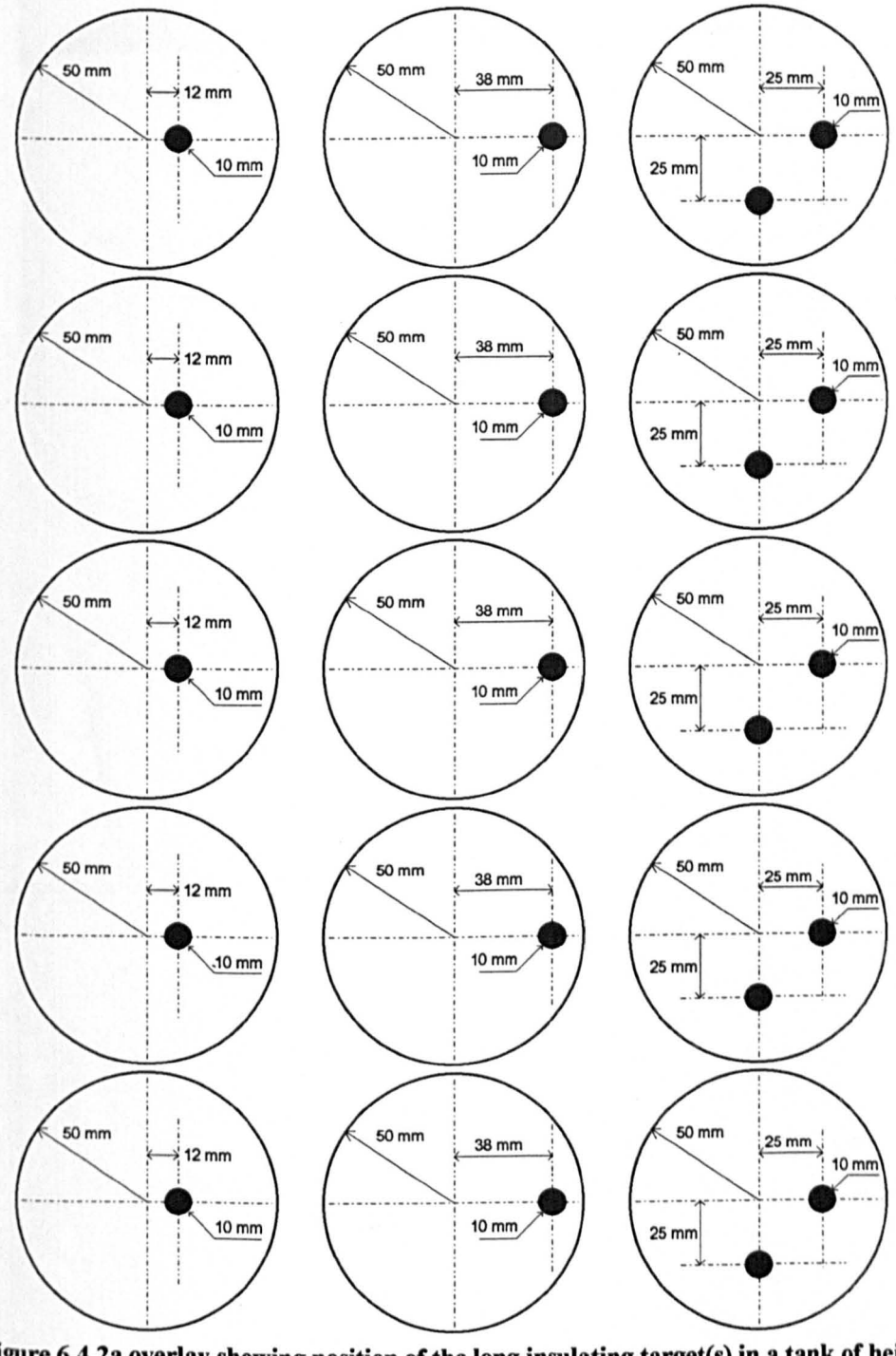

Figure 6.4.2a overlay showing position of the long insulating target(s) in a tank of height ±500mm

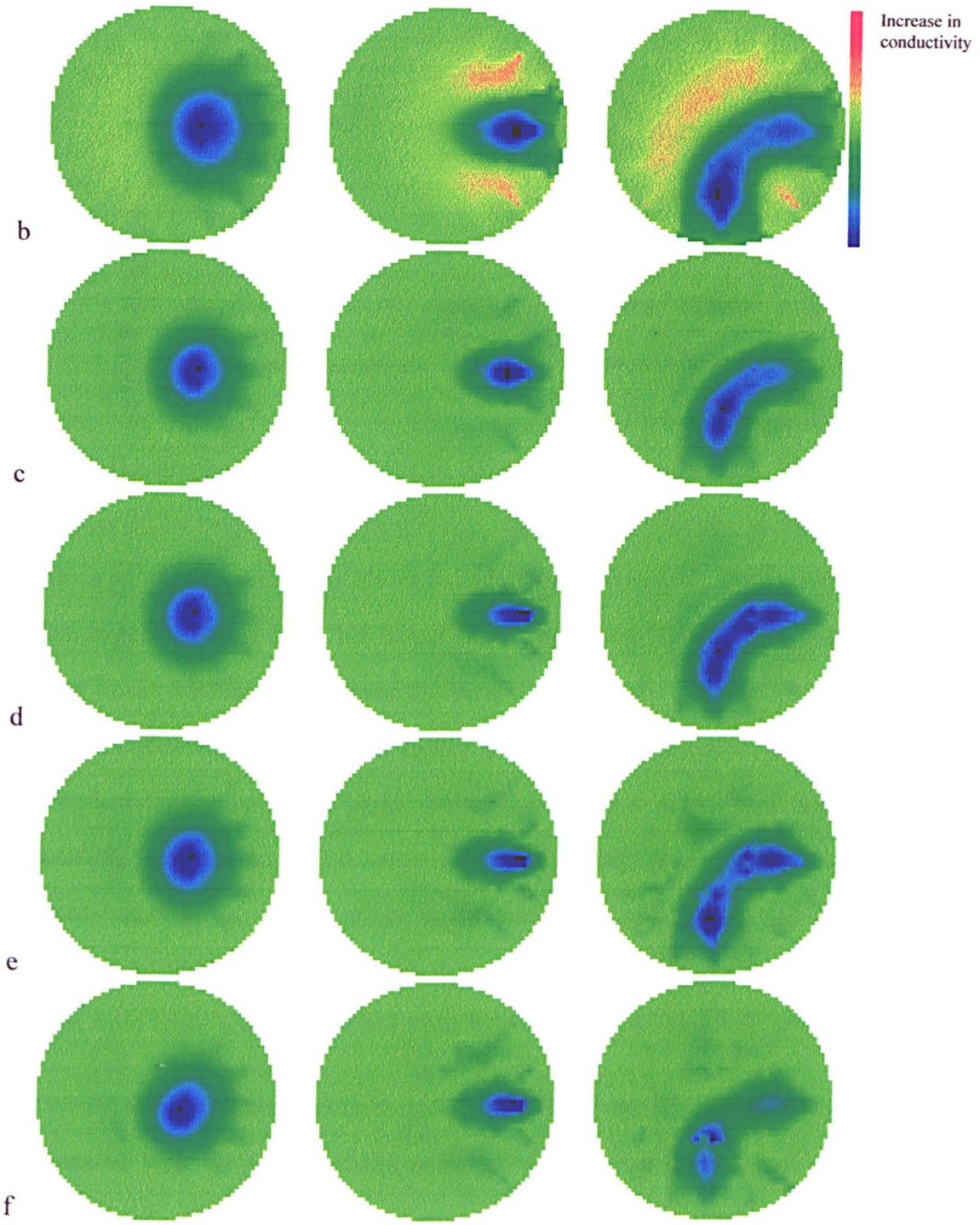

Figure 6.4.2 Images reconstructed using different filters and multiplied by the unfiltered image
Conductivity images reconstructed from data found using the test distributions shown on overlay.

b {no filter}; c {threshold $1/w_i<100$}; d {threshold $1/w_i<10^3$}; e {threshold $1/w_i<2\cdot10^3$}; f {threshold $1/w_i<5\cdot10^3$}

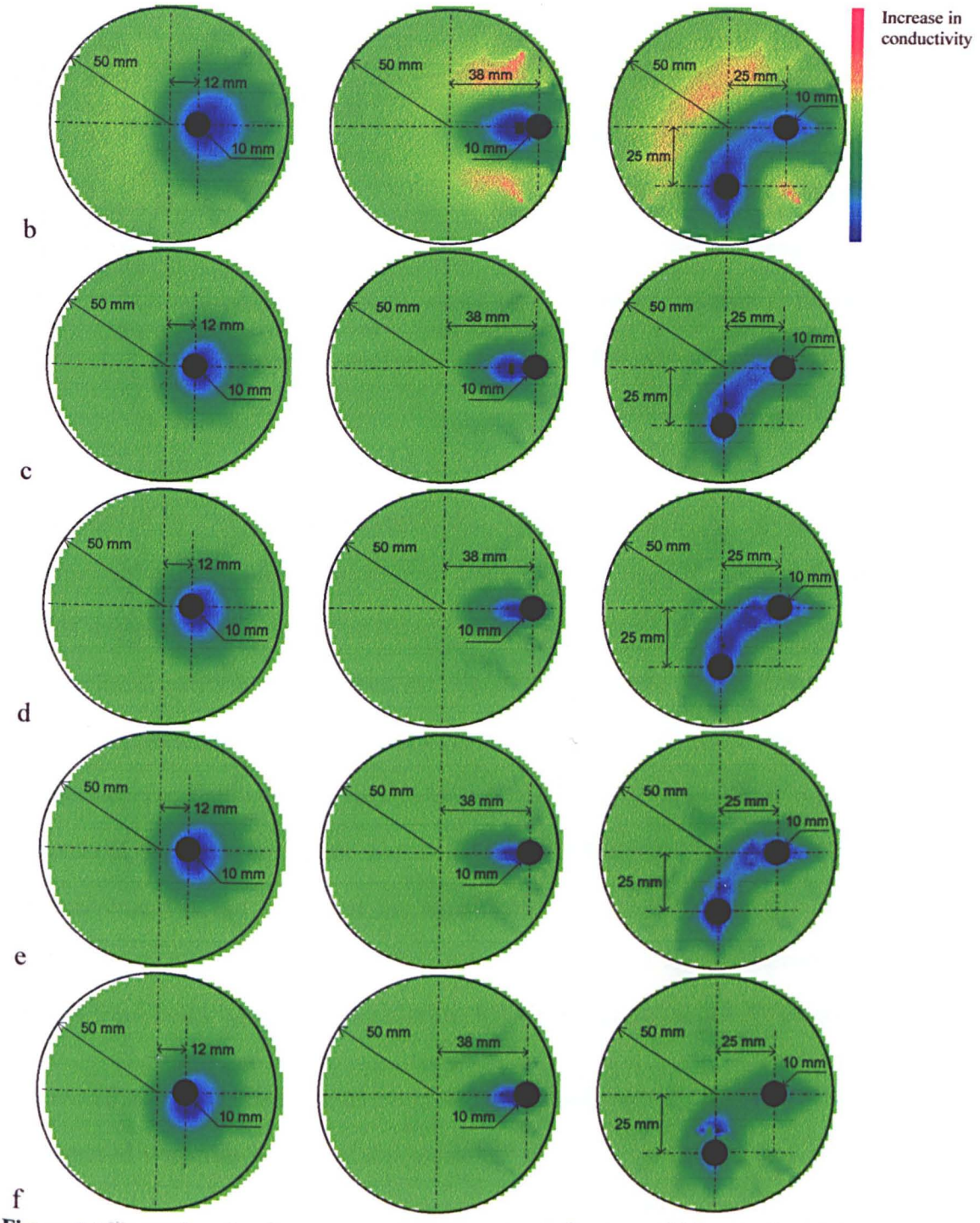

Figure 6.4.2a overlay showing position of the long insulating target(s) in a tank of height ±500mm

Figure 6.4.2 Images reconstructed using different filters and multiplied by the unfiltered image
Conductivity images reconstructed from data found using the test distributions shown on overlay.

b {no filter}; c {threshold $1/w_i<100$*}; d {threshold* $1/w_i<10^3$*}; e {threshold* $1/w_i<2\cdot 10^3$*}; f {threshold* $1/w_i<5\cdot 10^3$*}*

Figure 6.4.3

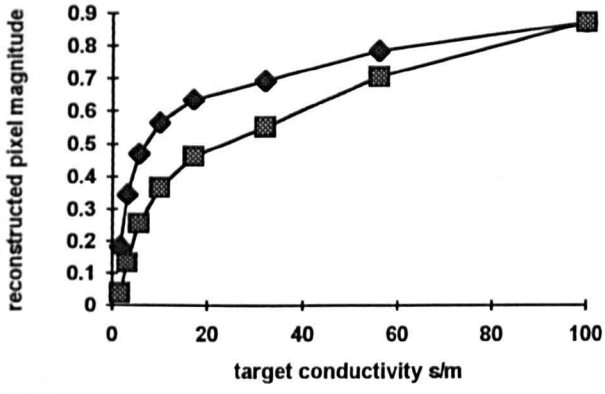

Figure 6.4.3 shows the values of the pixels with the greatest magnitudes for reconstructed images for different conductivity changes placed at the central location in the phantom. The diamonds are the raw data and the squares are the square of the same data. The graphs were normalised to have a maximum value of 1 and the conductivity was varied by two orders of magnitude. The transfer function shown for the squared values although not linear is closer to linear than the transfer function for the raw data. This suggests that it is in fact beneficial to square the image because it will lead to a more linear relationship between the image intensity and conductivity. The results of this multiplication are shown in figures 6.4.2c to f for the same sets of conditions as described for figure 6.4.1c to f. As with the filtered images the best value for the threshold appears to be at about 2000 for which there appears to be a great improvement in the quality of the image compared with that shown in figure 6.4.2b, which is an unfiltered image. The next section shows images reproduced from data taken from tanks with dimensions other than those for which the filter was optimised.

It would also be argued that to evaluate this procedure, the multiplied images should be compared with the square of the unfiltered and filtered images, and this is shown in Figure 6.4.4. The first two sets of images (b) and (c) show (unfiltered $\times$ |unfiltered|) and (filtered $\times$ |filtered|) respectively. Neither the unfiltered nor the filtered images are improved by the multiplication process. The unfiltered (figure 6.4.4b) images show a certain amount of sharpening but the location of the targets is corrupted and the filtered images (figure 6.4.4c) are not capable of displaying two targets. In contrast, when the filtered is multiplied by the unfiltered (figure 6.4.4d) the reconstructed position of the targets is improved, the system is capable of displaying two targets and the images are sharper.

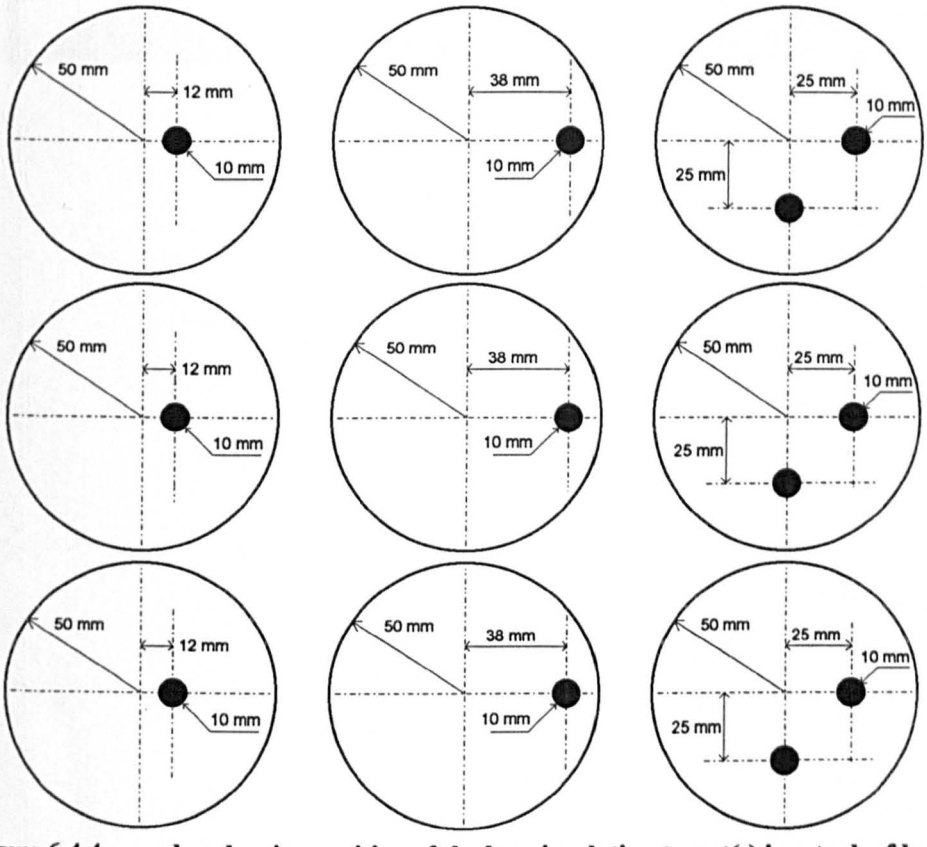

Figure 6.4.4a overlay showing position of the long insulating target(s) in a tank of height ±500mm

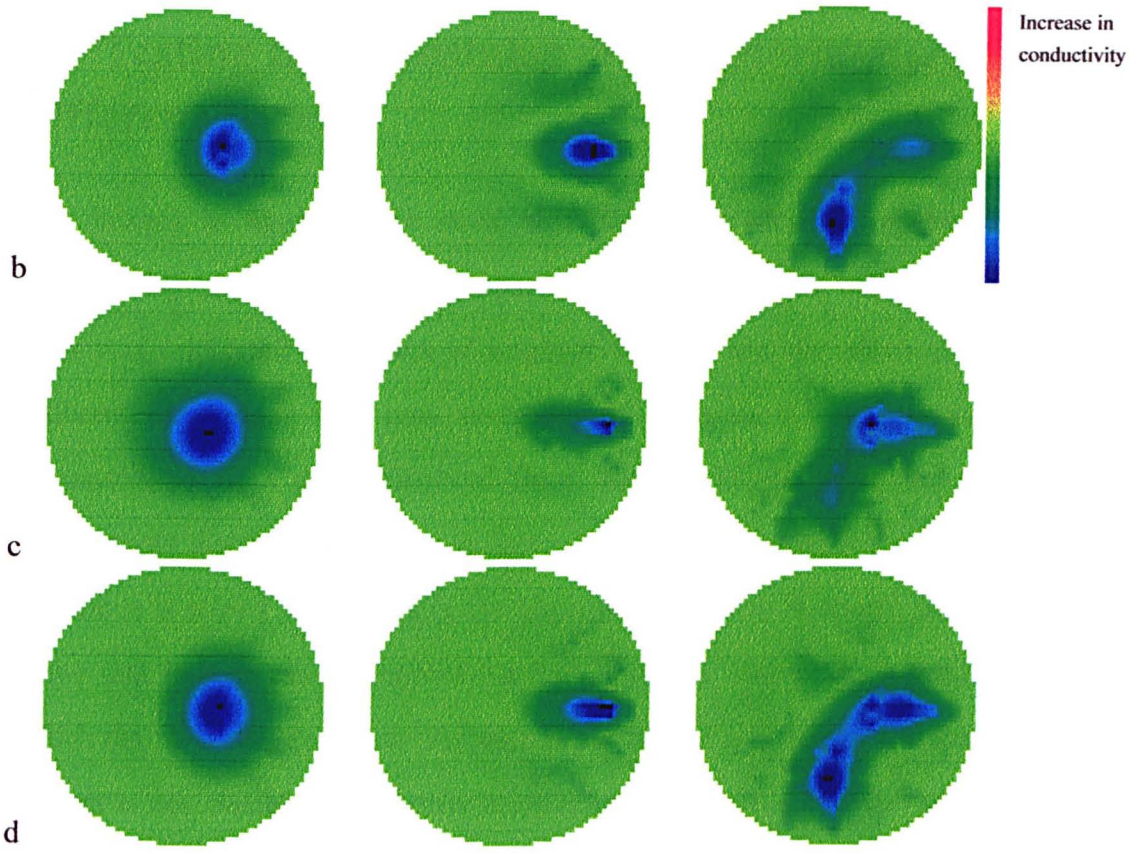

Figure 6.4.4 Images showing the effect of multiplying images by themselves
Conductivity images reconstructed from data found using the test distributions shown on overlay. b unfilter × |unfilter|; c filter × |filter|; d unfilter × |filter|; {threshold $1/w_i < 2 \cdot 10^{-3}$}

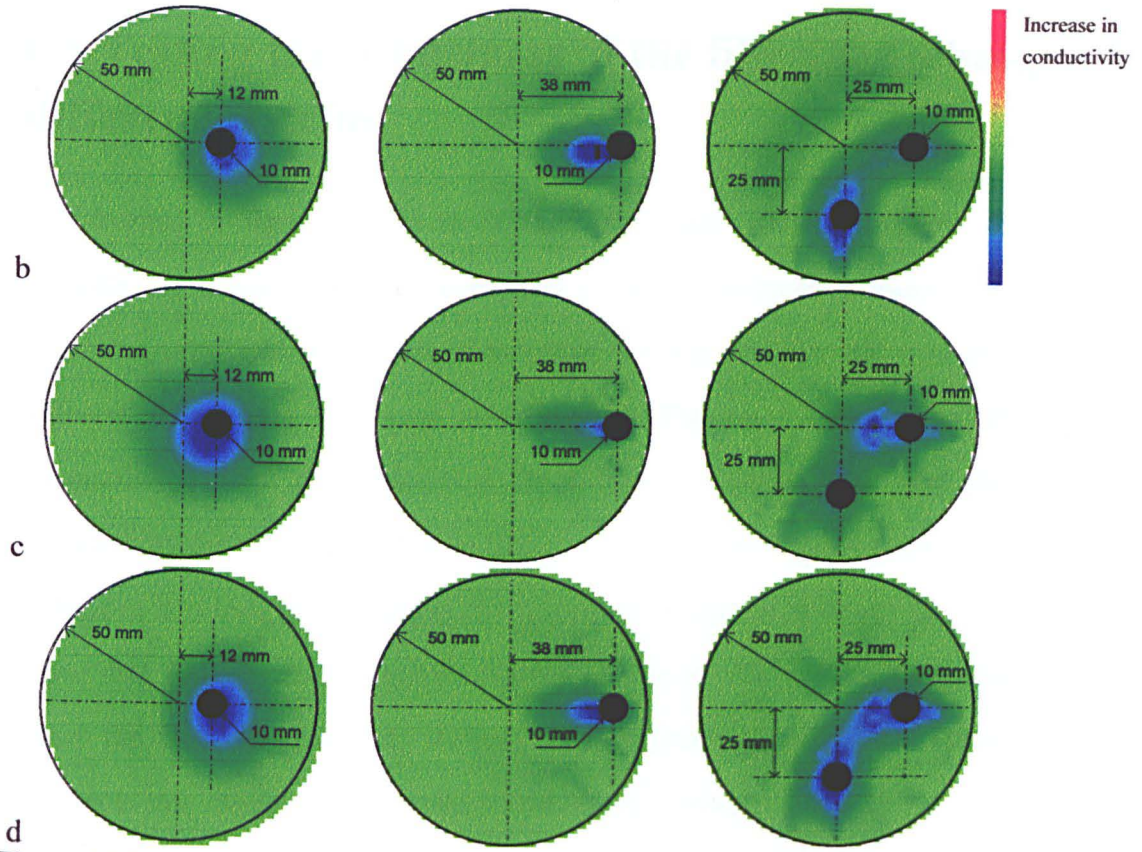

Figure 6.4.4a overlay showing position of the long insulating target(s) in a tank of height ±500mm

Figure 6.4.4 Images showing the effect of multiplying images by themselves
Conductivity images reconstructed from data found using the test distributions shown on overlay.
b unfilter × |unfilter|; c filter × |filter|; d unfilter × |filter|; {threshold $1/w_i < 2 \cdot 10^3$*}*

6.5 Testing the robustness of the filtering technique for different systems

The images in figure 6.5.1c show that the image filter is capable of producing considerably improved images compared to those produced without the filter. This filter was calculated for a tank of height ± 500 mm and the effect of phantoms with different dimensions was now investigated. Figures 6.5.1b and d show images reconstructed from data calculated for a tank of height ±1 m and ±200 mm with conductivity distributions shown in figure 6.5.1a. These images show that the filtering technique is robust to changes in the phantom's length to diameter ratio and they also show that images can be reproduced from tanks of dimensions other than those for which the filter was designed. As with the unfiltered 3-D reconstruction algorithm the system is not capable of correctly reconstructing images with l/d < 2. Figure 6.5.1e shows slight corruption with l/d = 2 and in figures 6.5.1 f and g there is severe corruption where l/d is 1 and 0.5 respectively.

The reconstruction process has been designed using small targets and the filter performs relatively well at reconstructing images with a limited number of small objects. To test the reconstruction process for conductivity distributions other than small objects the conductivity distribution shown in figure 6.5.2a was used to generate data for the reconstruction algorithm. Figures 6.5.2b to d show images reconstructed with; a, no filter; b, filtered; c, filtered multiplied by unfiltered. The images show very little resemblance to the conductivity distribution of figure 6.5.2a and the filtered image is very poor. This is probably because we have approximated the operator F by a linear function which it is not. Summing the results of changing the conductivity of each pixel separately will not produce the same result as changing all the pixels simultaneously: because the current pattern will be significantly altered when large areas are changed. A possible solution to this problem, which has not been pursued, could be to generate the matrix F not on an individual pixel basis but on an area basis, consequently the filter would be optimised to conductivity distributions with area changes in conductivity.

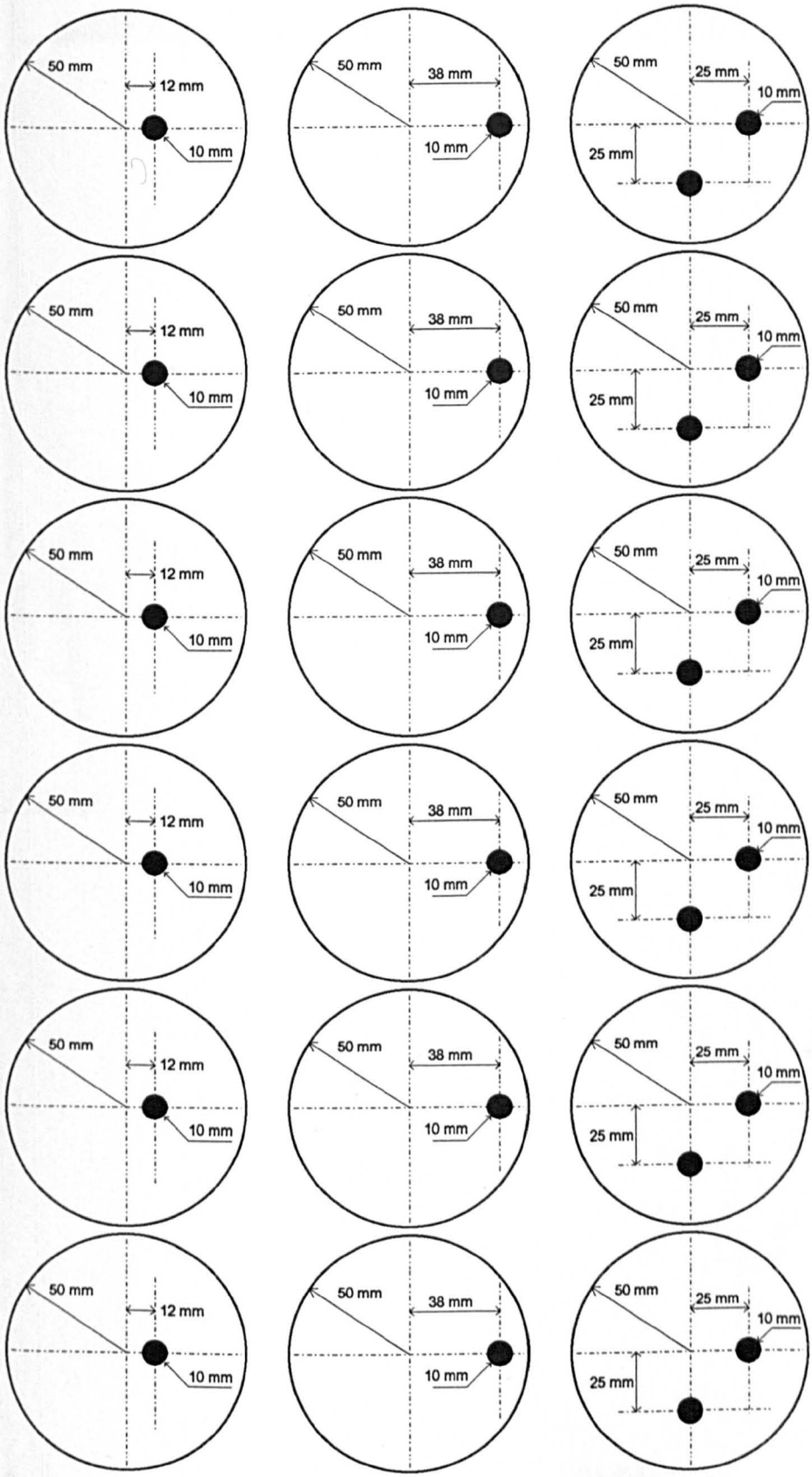

Figure 6.5.1a overlay showing position of the long insulating target(s) in a tank of variable height

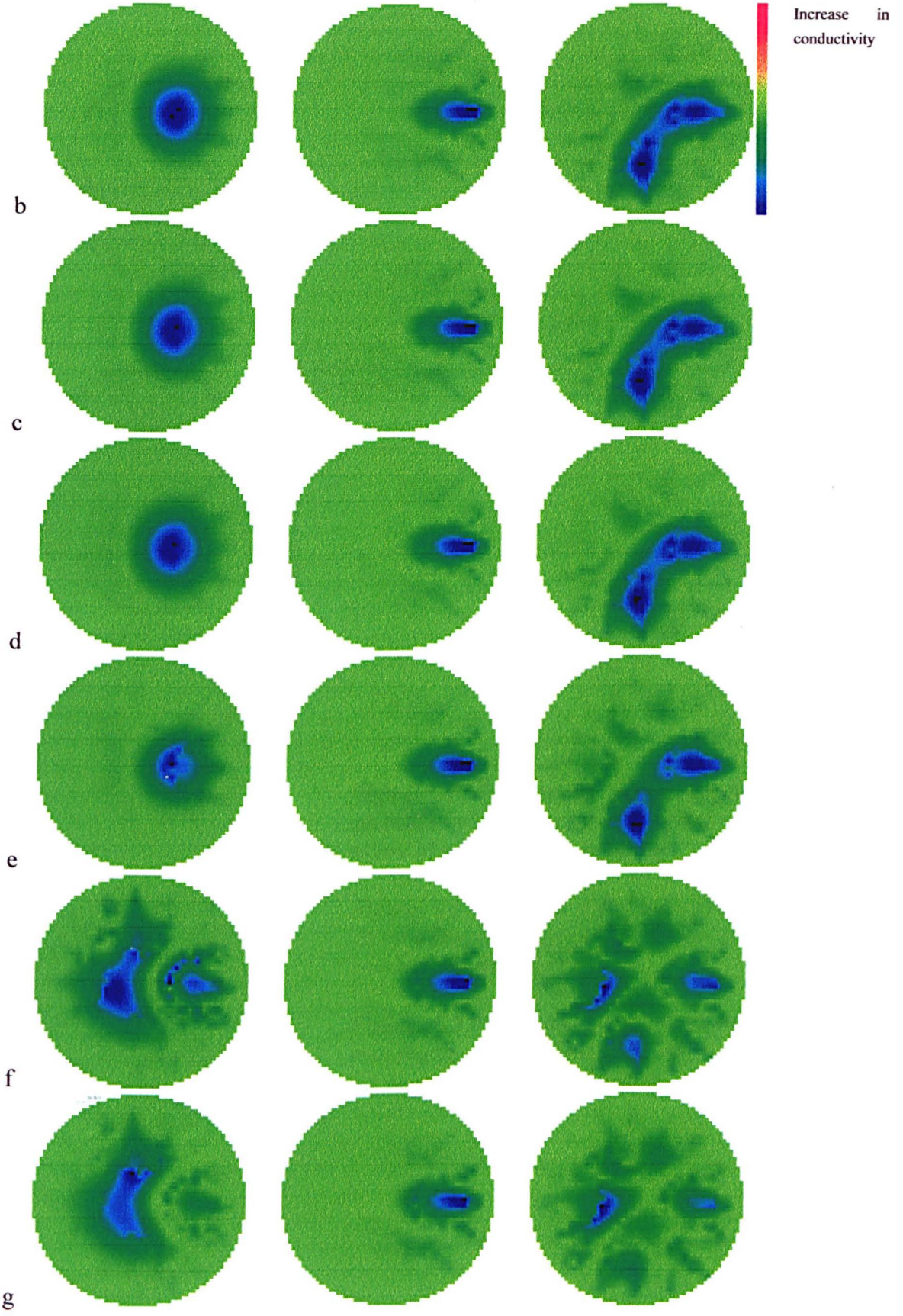

Figure 6.5.1 Image reconstructed by multiplying the filtered {threshold $1/w_i < 2 \cdot 10^{-3}$} by unfiltered images for data taken from different tanks of different height.
Conductivity images reconstructed from data found using the test distributions shown on overlay. b {±1 m}; c {±500 mm}; d {±200 mm};.e {±100 mm}; f {±50 mm}; g {±25 mm}

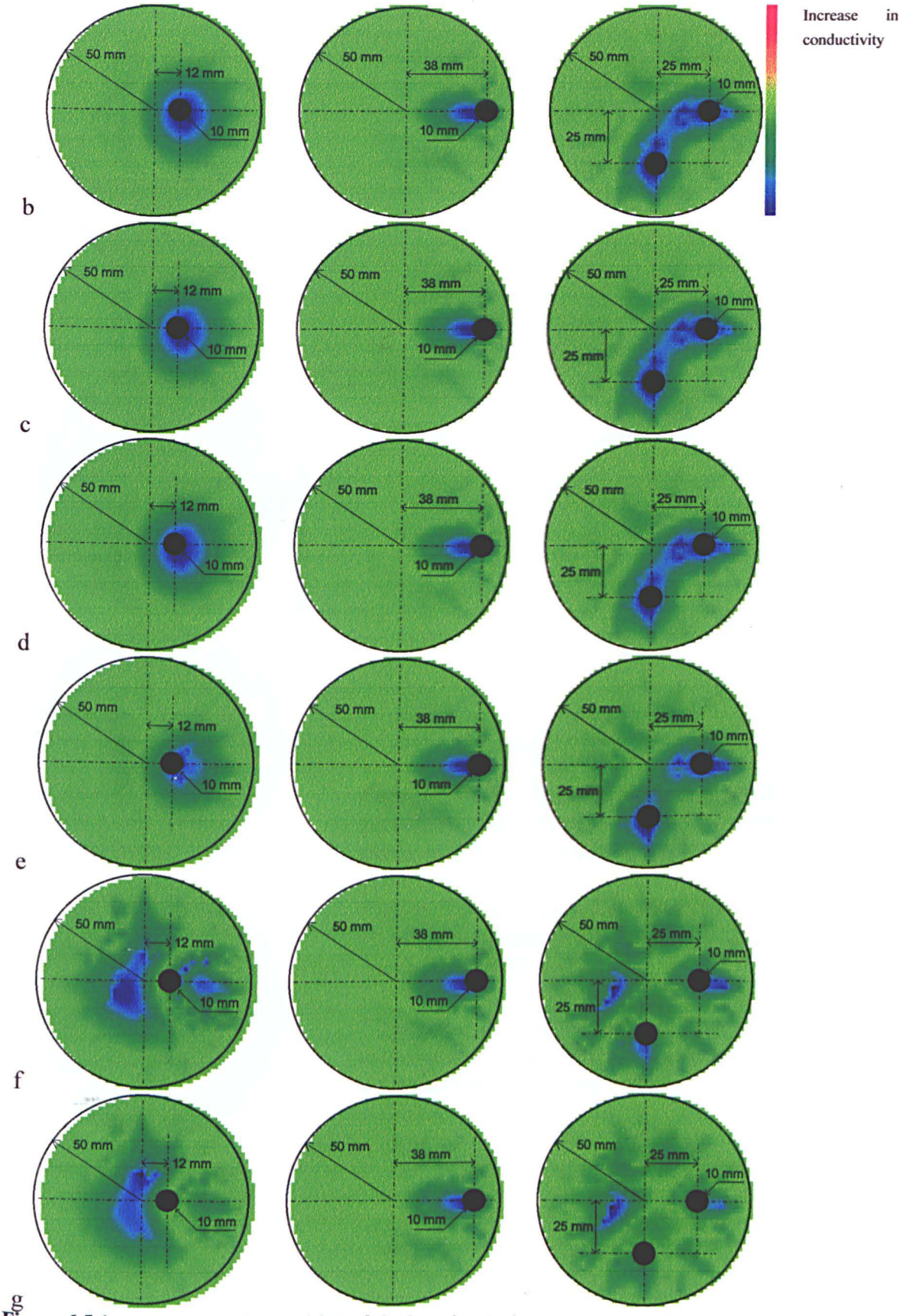

Figure 6.5.1a overlay showing position of the long insulating target(s) in a tank of variable height

Figure 6.5.1 Image reconstructed by multiplying the filtered {threshold $1/w_i < 2 \cdot 10^3$} by unfiltered images for data taken from different tanks of different height.
Conductivity images reconstructed from data found using the test distributions shown on overlay.
b {±1 m}; c {±500 mm}; d {±200 mm};.e {±100 mm}; f {±50 mm}; g {±25 mm}

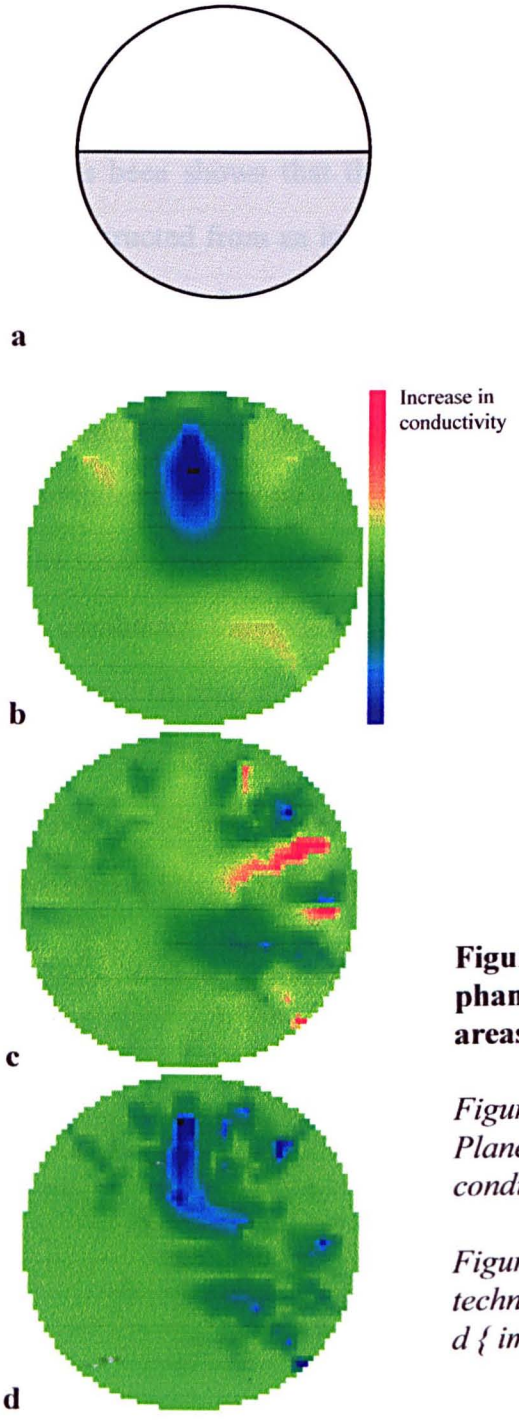

Figure 6.5.2. Images reconstructed from a phantom with a region of interest with two large areas of differing conductivity.

Figure 6.5.2a shows the conductivity distribution. Plane area conductivity 1 Sm^{-1} and the shaded area conductivity 0.95 Sm^{-1}.

Figures 6.5.2b..c show various image reconstruction techniques b {no filter}; c {filter (1/w<2000)}; d { images multiplied together}

6.6 Conclusions

It has been shown that the filter described by Barber *et al* [18] for filtering images reconstructed from an injected current electrical impedance tomography system can be applied to the 3-D induced current tomography system. Although the results of this method only give a slight improvement in quality, the location of features, within the reconstructed image, is less distorted. If the filtered and unfiltered images are multiplied together on a pixel by pixel basis the quality of the image is greatly improved. The multiplying of the filtered image by the unfiltered image has the added advantages of combining the improved target locations of the filtered with the ability of the unfiltered to reconstruct images with two targets and also of improving the linearity of the transfer function between conductivity and pixel intensity. The technique is also shown to be robust to changes in the length of the tank, but it is not capable of generating images from large area changes in conductivity without further modification.

Chapter 7 Quantifying the effect of structures out of the plane of interest

7.1 Introduction

Planar X-rays are difficult to interpret because information from the whole structure is collapsed on to a single 2-D plane. To aid the interpretation of X-ray images tomographic systems were developed. The corollary to this for impedance imaging is that an image will be difficult to interpret because information from cross sections close to the plane of interest are all collapsed on to the 2-D image. It is therefore important that the systems should be sensitive to only a thin band of the structure, and this chapter investigates firstly the sensitivity to out of plane structures and secondly strategies that could be employed to reduce the width of the band.

In chapter 5 the problem of imaging 3-D subjects was investigated and resulted in the generation of an algorithm that was capable of reconstructing images from data taken from 3-D phantoms. The reason that it required a different reconstruction algorithm is that current paths in the plane of measurement are different in 3-D structures from those in 2-D structures. Figure 7.1.1 shows the current paths for both a long and a short phantom when excited by two different coil arrangements. The current paths differ because the current can and does flow out of the plane of interest. If any of the current which flows out of the plane is disturbed by impedance variations, then the potential distribution will be affected by these disturbances and it would be reasonable to conclude that the potentials sensed by the electrodes will be affected. This chapter describes how the FEM was used to simulate the disturbance caused by out of plane structures and to investigate and quantify their effect on reconstructed images. Experiments are described in which the FEM is used to find the sensitivity of the system to small objects out of the plane of measurement. Also investigated are some methods that could be used to gain information about planes other than the one containing the electrodes.

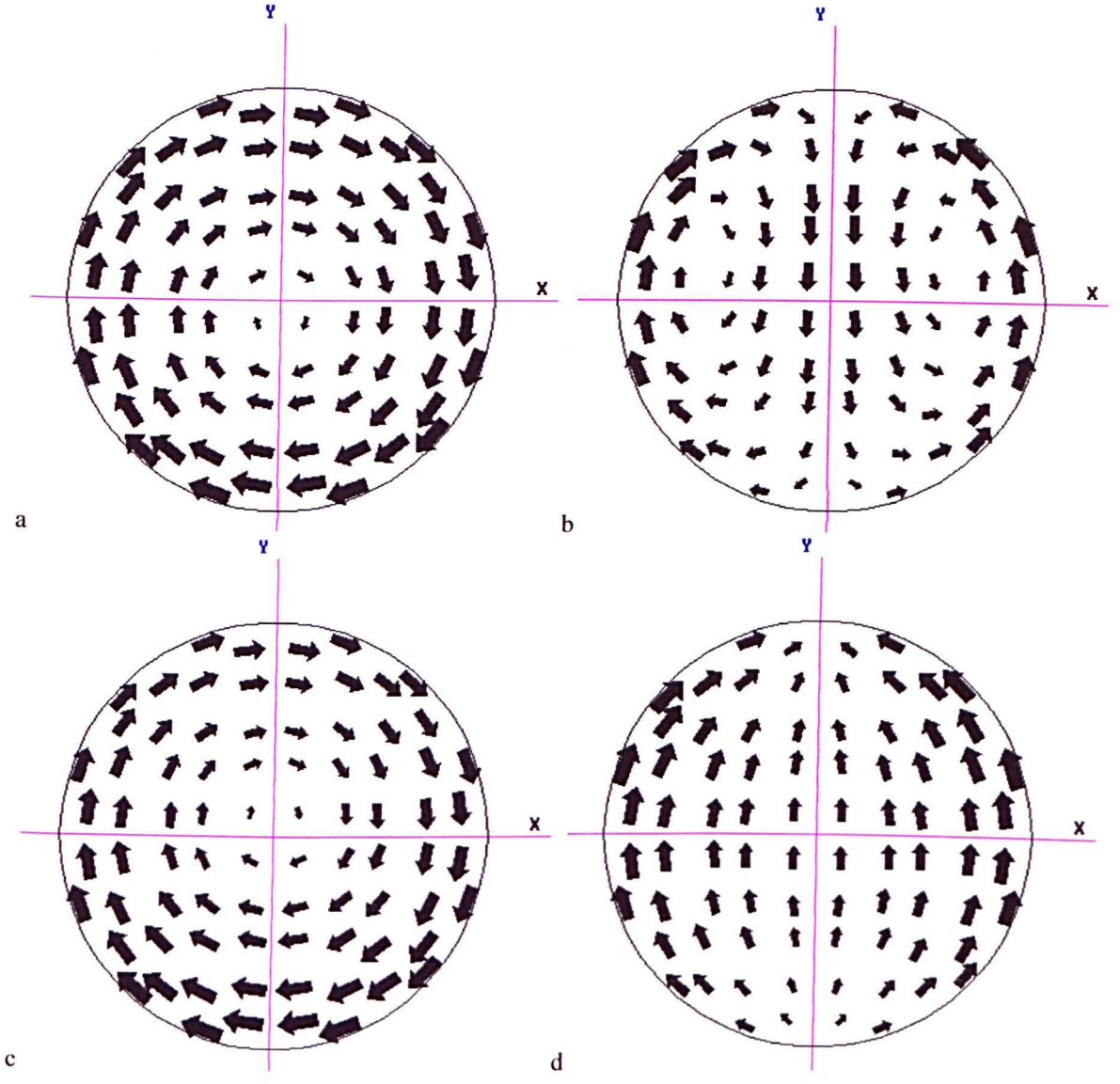

Figure 7.1.1 typical current patterns induced in the plane of measurement for two coil drive configurations for both a long and short phantom.

Figures 7.1.1a and b are a short phantom ±6 mm and figures 7.1.1 c and d are a long phantom ±1 m.

Figures 7.1.1 a and c are excited by coil 1 and figures 7.1.1 b and d are exited by coils 2 and 3 antiphase.

7.2 The effect of out plane structures

Figures 7.2.1b to d show the images reconstructed from simulated data with targets at various positions in the phantom. The conductivity distribution is shown in figure 7.2.1a where the target was a cylindrical insulator of 8 mm diameter which spanned from a point above the plane of measurement to the top of the phantom. Each column of images is plotted using the same conductivity scale. They show that as the structure is moved from the plane of measurement, the sensitivity is reduced. As predicted these images show that the reconstructions are sensitive to structures out of the plane of measurement.

To investigate how an image would be corrupted by an out of plane structure a long thin rod, which spanned the entire length of the tank, was used as a target and images were reconstructed with only this target. Next a second target of the form used in the previous experiment was added at various locations above the plane; the detail of this arrangement is shown in figures 7.2.2a and 7.2.3a. From the images shown in figures 7.2.2b to d and 7.2.3b to d it can be seen that as the out of plane target is moved away from the plane of measurement, the image becomes less corrupt and a structure, close to the periphery but still out of the plane of measurement, corrupts the image so badly that it completely masks an object placed close to the centre and on the plane of interest. The disturbance caused by targets close to the centre is so small that even with the target only 20 mm from the plane of measurement there is negligible effect on the images.

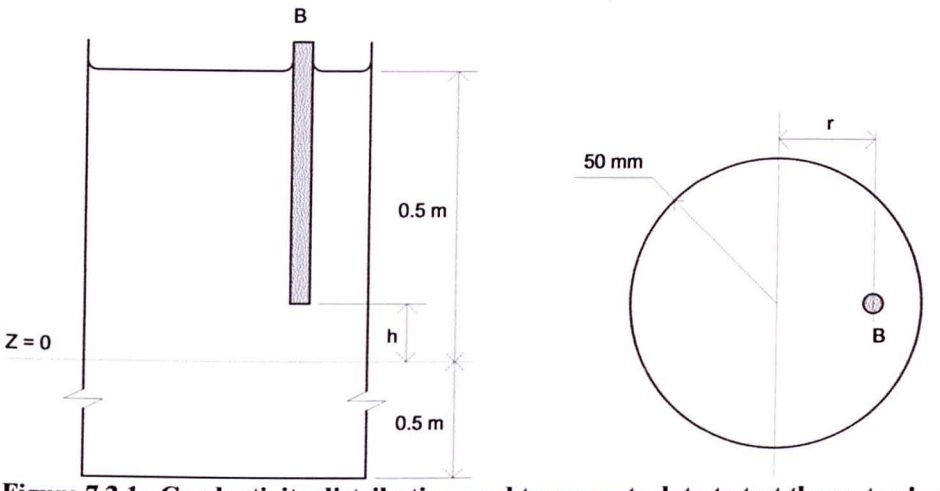

Figure 7.2.1a Conductivity distribution used to generate data to test the system's sensitivity to out of plane structures. *A long insulating rod 'B' of diameter 8 mm is placed at a radius r which is expressed as a percentage of the total radius a height h above the plane of measurement. The system was simulated using the FEM for various values of h.*

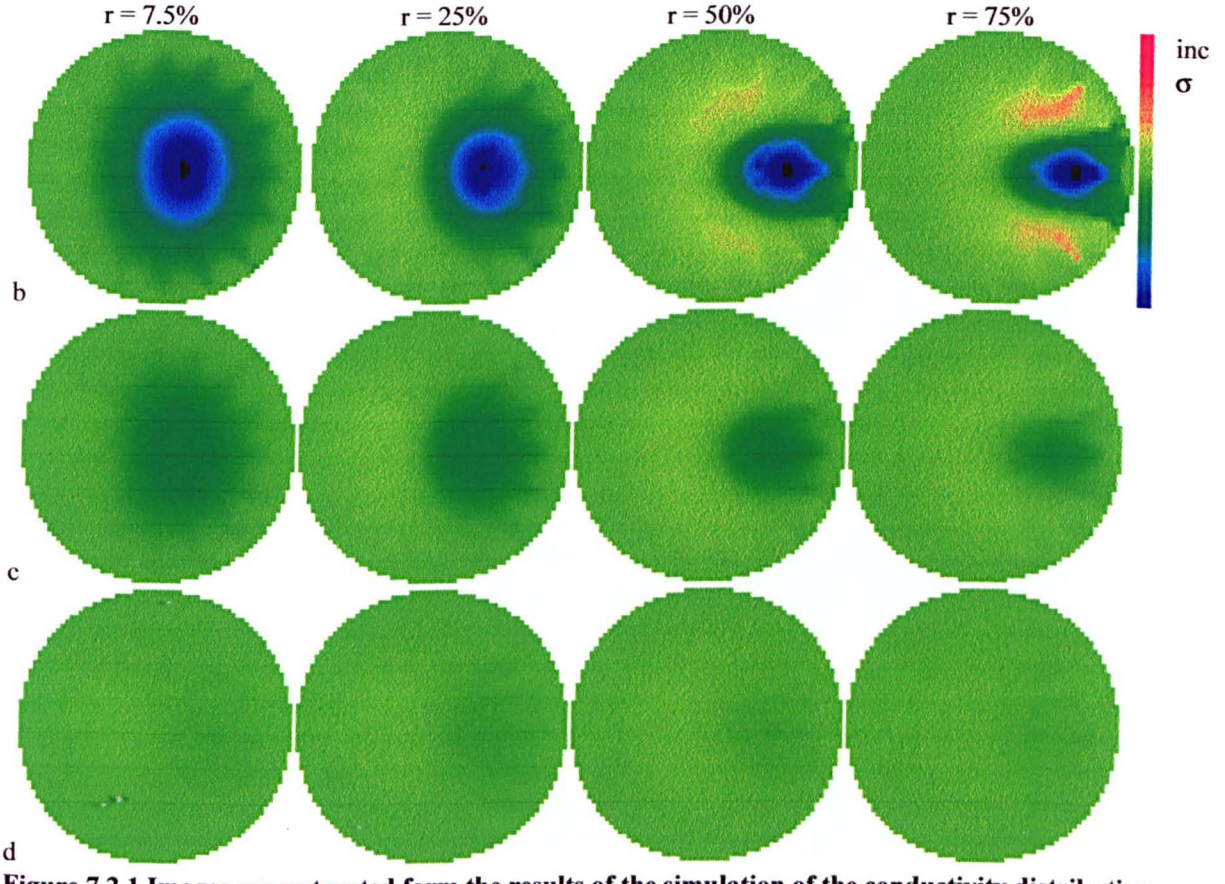

Figure 7.2.1 Images reconstructed form the results of the simulation of the conductivity distribution shown in figure 7.2.1a.

Figure 7.2.1b, 7.2.1c and 7.2.1d show the images reconstructed when h = 0, h = 20 mm and h = 45 mm respectively. Each column of images has one value of r and is plotted with the same conductivity scale.

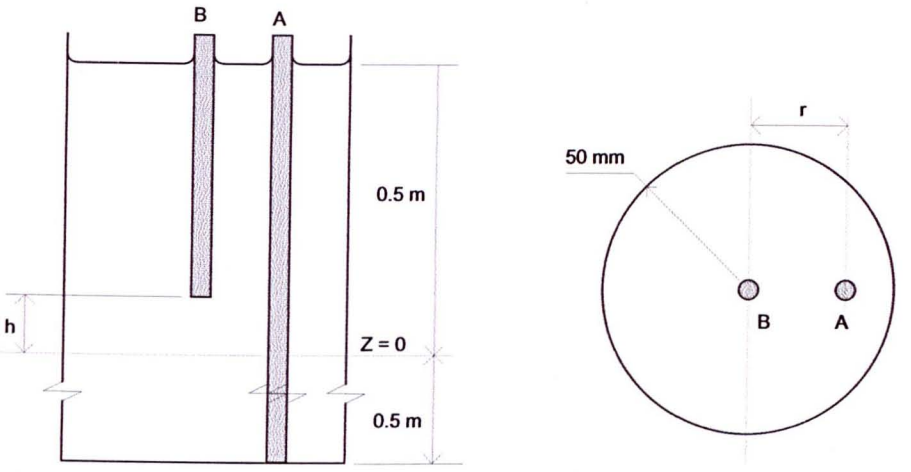

Figure 7.2.2a Conductivity distribution used to generate data to test the system's sensitivity to out of plane structures. *A long resistive rod 'A' with a diameter of 8 mm that spanned the entire length of the phantom was placed at a radius r which is expressed as a percentage of the total radius. A second conductive rod 'B' was placed at centre of the phantom at a height h above the plane of measurement. The rod 'A', the rod 'B' and background had conductivities of 0.9sm^{-1}, 1.1sm^{-1} and 1.0sm^{-1} respectively. The system was simulated using the FEM for the two values of h.*

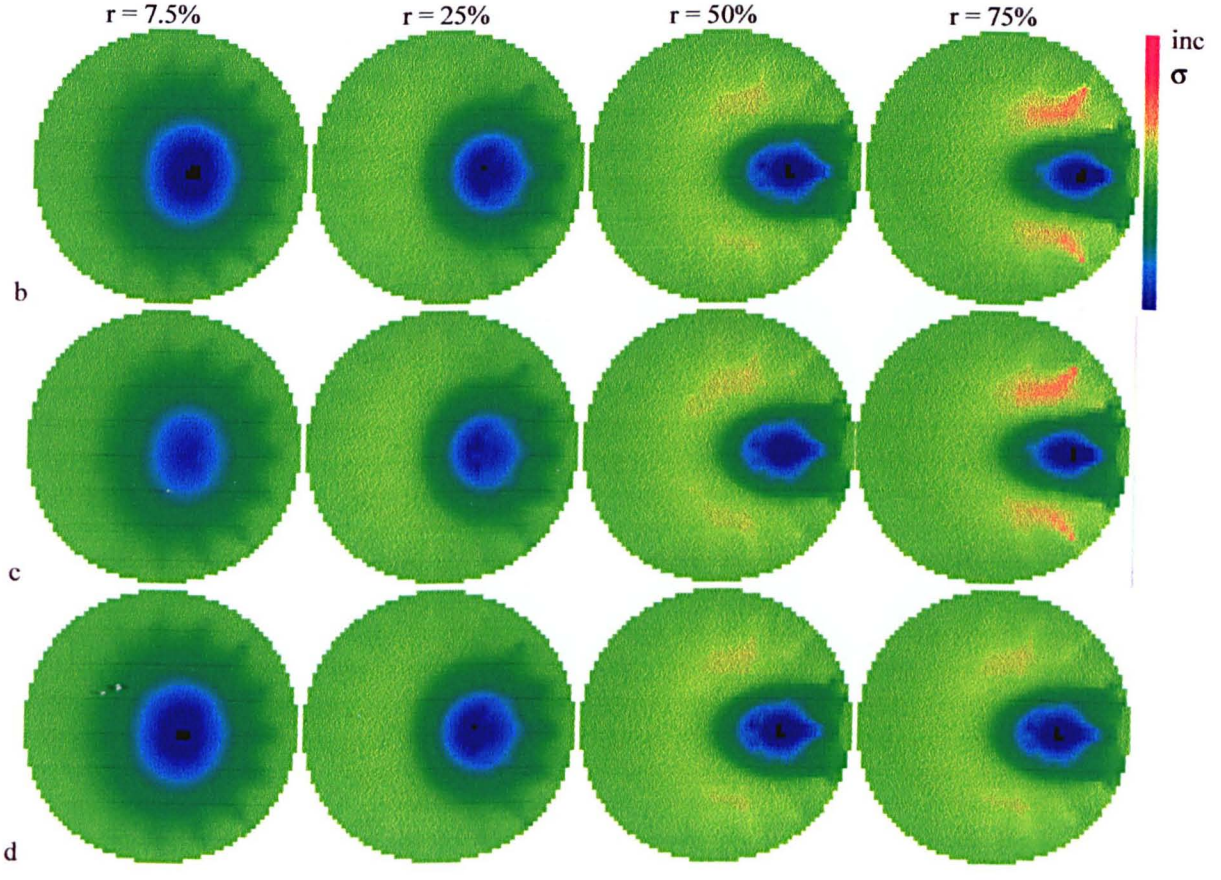

Figure 7.2.2 Images reconstructed form the results of the simulation of the conductivity distribution shown in figure 7.2.2a.
Figure 7.2.2b, 7.2.2.c and figure 7.2.2d show the images reconstructed without 'B' and when h = 20 mm and h = 45 mm respectively. Each column of images has one value of r and is plotted with the same conductivity scale.

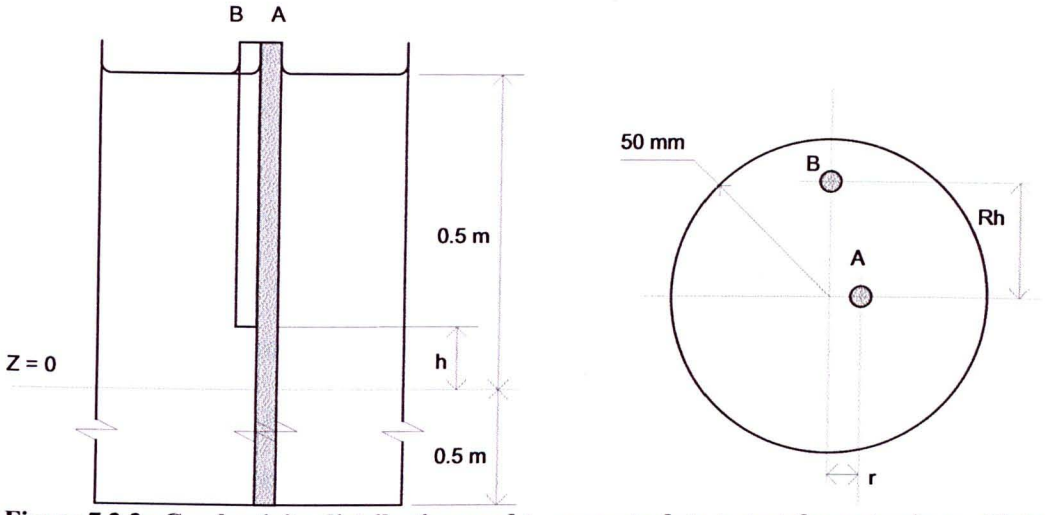

Figure 7.2.3a Conductivity distribution used to generate data to test the system's sensitivity to out of plane structures. *A long resistive rod 'A' with a diameter of 8 mm that spanned the entire length of the phantom was placed at a radius r which is expressed as a percentage of the total radius. A second conductive rod 'B' was placed at a radius Rh = 75 % at a height h above the plane of measurement. The rod 'A', the rod 'B' and background had conductivities of 0.9sm^{-1}, 1.1sm^{-1} and 1.0sm^{-1} respectively. The system was simulated using the FEM for the two values of h.*

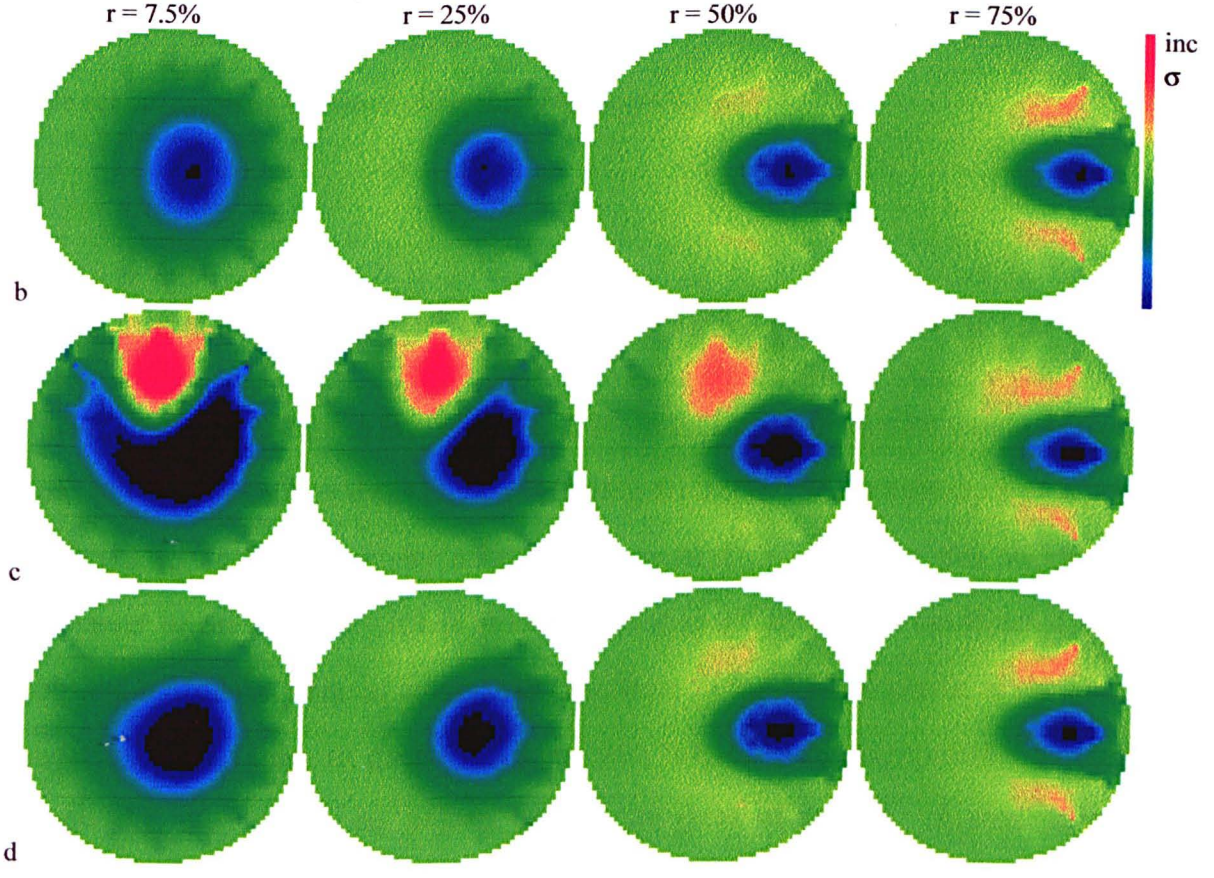

Figure 7.2.3 Images reconstructed form the results of the simulation of the conductivity distribution shown in figure 7.2.3a.
Figure 7.2.3b, 7.2.3c and 7.2.3d show the images reconstructed without 'B', when h = 20 mm and h = 45 mm respectively. Each column of images has one value of r and is plotted with the same conductivity scale.

7.3 Sensitivity of the injected current technique to objects out of the measurement plane

There is evidence that the injected current technique suffers from similar problems of sensitivity to out of plane structures. Jossinet[41] presented experimental results for two different current injections and potential sensing configurations. He plotted graphs of the sensitivity against the axial position of a small target. These graphs had a bell shape with the peak occurring in the plane of measurement. The bell shaped curve was measured and found to have a half height width of approximately 75 mm for a target on the axis of the cylindrical tank, diameter 192 mm. Thus the sensitivity falls by a half with an axial displacement of approximately 38 mm and this corresponds to a half sensitivity width of 0.4 diameters. Quoting the sensitivity in term of diameters makes direct comparison between different systems possible.

7.4 Quantifying the effect of out of plane structures

Simulated experiments to investigate how the induced current system would respond to out of plane structures were carried out using the FEM. The sensitivity region will be referred to as half sensitivity width and expressed as a ratio of this width to the diameter of the cylinder. It has already been shown that as with the injected system, objects out of the plane of interest do contribute to the voltage profile at the plane of interest and in order to quantify this problem the following experiment was used to show the effect of placing objects outside the plane of interest. A small insulating object 20 mm long with a diameter of approximately 8 mm was placed at different points in the tank, and for each position, the finite element model was used to find the change from reference of the peripheral profile voltage. The root mean square of the peripheral voltages, taken from the 16 electrodes, was calculated as a measure of total signal power in order to quantify a set of peripheral voltage profiles for small objects

placed in different positions in the phantom. This total power was used because it was considered to be an indication of the system's sensitivity in the presence of noise. The noise could be either random electrical noise or coherent noise from other objects outside the plane of interest. The back projection algorithm discussed in chapter 5 uses the weighted sum of many different coil excitations in order to generate an image. There are two typical forms that the current will take, one with the current flowing in concentric rings and the other where it flows predominately in one direction as shown in figures 7.4.1a, b and c. For the purposes of testing the sensitivity of the system to objects out of the plane of measurement 3 main current patterns will be used, where the plane of measurement current flows in :-

- concentric rings excited by a single concentric coil,
- predominately in the y direction, excited by drive coils 2 and 3 in antiphase,
- predominantly in the x direction, excited by driving the coils with weighted currents of 1.155, -0.5775 and -0.5775 for coils 1, 2 and 3 respectively.

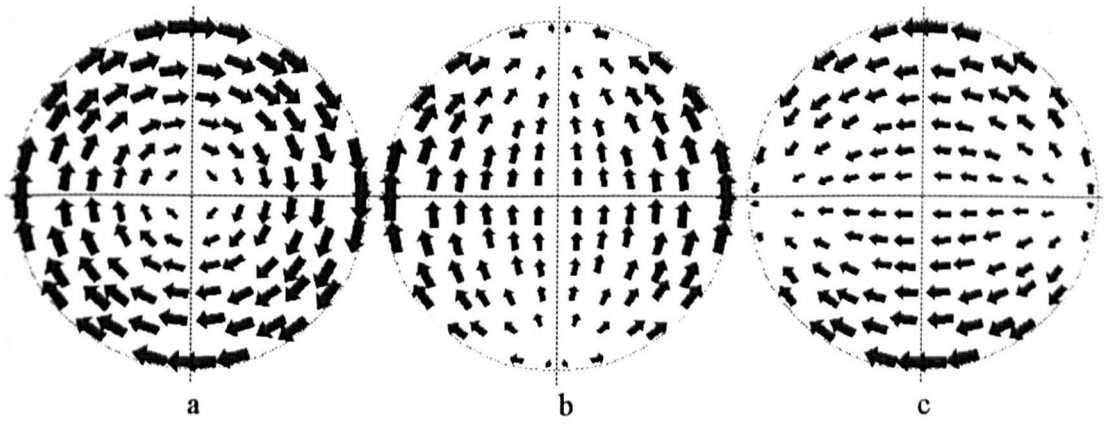

Figure 7.4.1 Plots showing the electrode plane current for different coil excitations.
The current patterns shown are for the following coil excitations; a, 1·(coil 1); b, 1·(coil 2)-1·(coil 3) and c, 1.155·(coil 1)-0.5775·(coil 2)-0.5775·(coil 3)

Figures 7.4.2a, b and c are pseudo-3-D diagrams of the phantom laid on its side. The vertical axis shows the sensitivity resulting from the disturbance for various positions of a small object in the phantom shown in the horizontal plane. The sensitivity is defined as the RMS of the peripheral voltage differences for 1 amp turn of excitation current for an small insulating object diameter 10 mm and length 20 mm. The horizontal plane represents a plane through the phantom which contains both the x and z axes of the phantom. The x axis is plotted diagonally downward and towards the right and the z axis is plotted diagonally downward and towards the left. The plane of the coils is parallel to the section through the phantom and shown at the back (B). This is the position which is closest to the coils and to the electrodes and so has the greatest sensitivity. Figure 7.4.2a shows the sensitivity distribution when the system is excited by a single concentric coil. With this drive configuration the current flows in concentric rings and the current density is low at the centre of the plane of measurement. Consequently the sensitivity is low here. When the current is excited by a single concentric coil, the current flows parallel to the plane of the coils and the system's sensitivity falls quite rapidly with increased displacement from the plane of measurement. Figure 7.4.2b shows the sensitivity for a coil excitation which induces current to flow in the 'y' direction in the plane of interest. The axial current flows along the edges where $x = 0$ so that at the edges where the objects were placed ($y = 0$), the current density is low and there is little sensitivity. Figure 7.4.2c shows the situation where the current is excited to flow in the 'x' direction in the plane of the coils and therefore axially, close to the edge where $y = 0$. In this region the current density is large so that the voltage profile is sensitive to an object at the edge where $y = 0$. From this diagram it can be seen that the system is sensitive to objects close to the boundary and separated from the plane of the coils. Further examination of the figure 7.4.2c shows that the sensitivity in the centre region (P) is of equal magnitude to the sensitivity in the region displaced axially by 120 mm (Q). Hence for this drive configuration the system will be equally sensitive to objects at the centre and on the boundary but displaced by over one diameter.

a

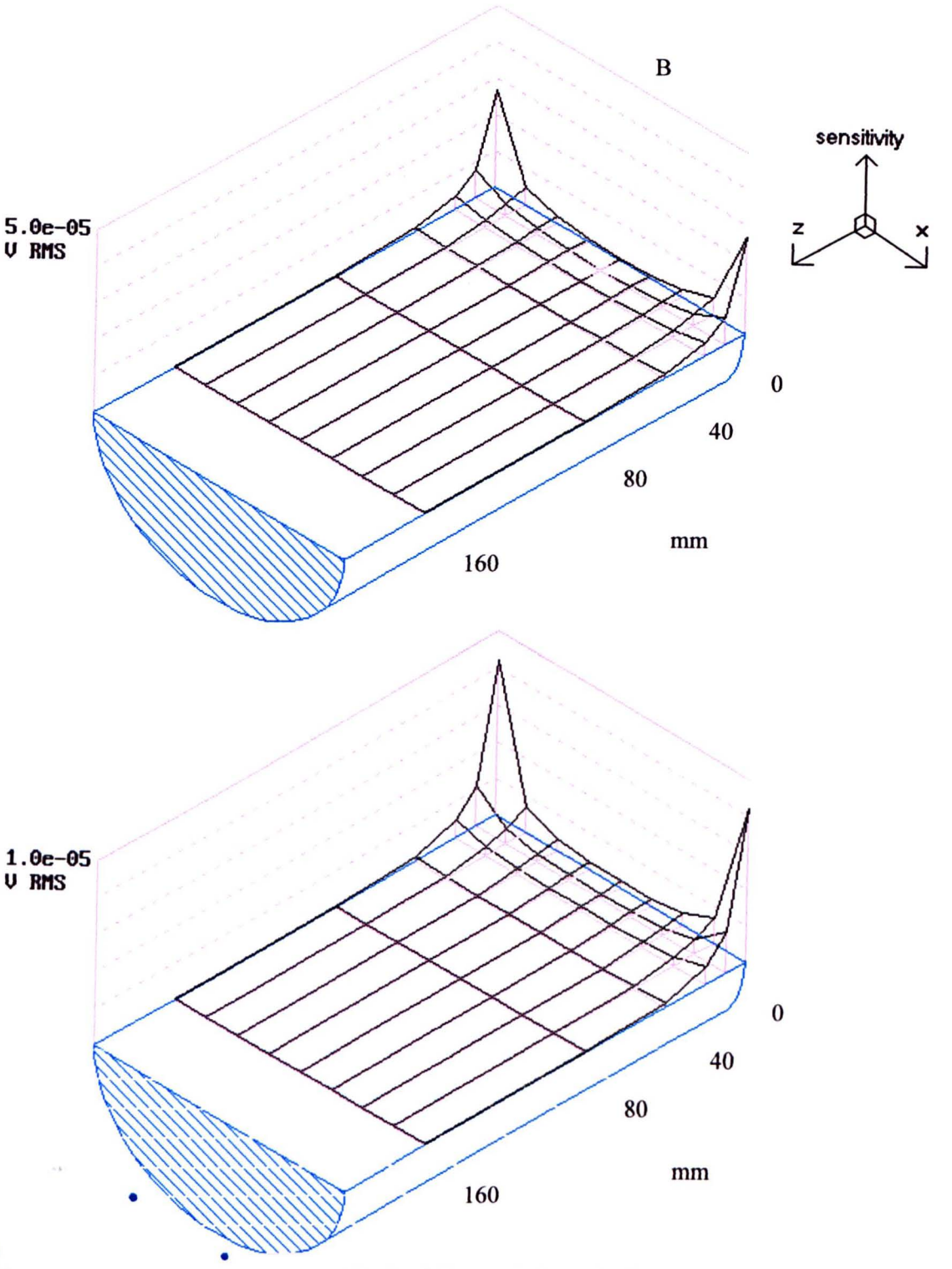

b

Figure 7.4.2 plots showing the RMS of the peripheral voltage profile for a small object placed at different locations in a phantom 1m long and of diameter 100 mm. *Figure 7.4.2a shows current excited by a single concentric coil; figure 7.4.2b shows current induced to flow in the 'y' direction; figure 7.4.2c shows current induced to flow in the 'x' direction.*

continued over page

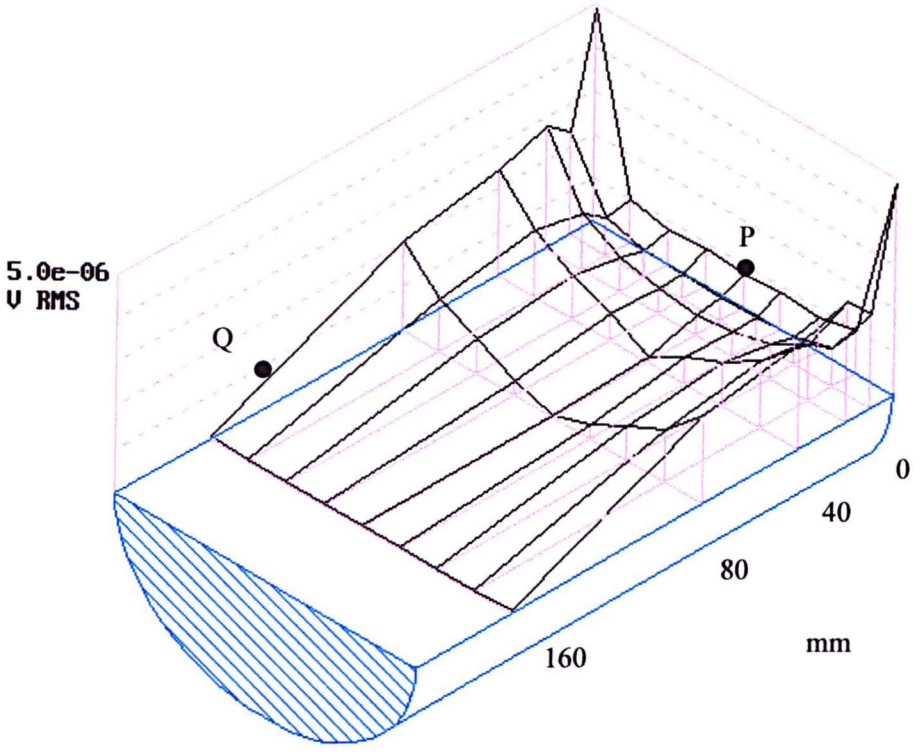

c

Figure 7.4.2 plots showing the RMS of the peripheral voltage profile for a small object placed at different locations in a phantom 1m long and of diameter 100 mm. *Figure 7.4.2c shows current induced to flow in the 'x' direction.*

Figures 7.4.2a, b and c show graphs for the sensitivity of the profile for various coil drive configurations. These should give an indication of how sensitive the reconstruction algorithm will be to objects out of the plane of interest. However the figures show that the sensitivity of the peripheral measurements is dependent on the coil drive used to excite the current in the phantom. The reconstruction algorithm is effectively based on a weighted sum of many different configurations of coil drive. To quantify the sensitivity of our reconstruction algorithm to objects out of the plane of interest a similar set of simulations was set up as before but these simulations were used to reconstruct images. A graph was plotted of the sensitivity of the image against the target location (figure 7.4.3) where the image sensitivity is found from the magnitude of the largest reconstructed conductivity change. The graph shows that the reconstruction algorithm has equal sensitivity for objects in the centre region and for those axially displaced by about 0.06 m and on the edge (Q). The graph shown in figure 7.4.2c shows that for certain drive configurations the profile is very sensitive to out of plane structures over a large distance.

Fortunately the reconstruction algorithm does not strongly weight the drive configuration used for figure 7.4.2c, so that the sensitivity of reconstructed images falls rapidly with increased displacement.

The plot shown in figure 7.4.3 shows one of the problems of the reconstruction algorithm which is that it is much more sensitive to objects near to the edge than close to the centre. This is a problem of the reconstruction algorithm currently in use and it could be reduced by weighting the pixels at the centre more than those at the edge. The graphs shown in figures 7.4.2 and 7.4.3 were replotted in figures 7.4.4 and 7.4.5 with the sensitivity in the plane of measurements normalised to one. The graph in figure 7.4.5 shows half a bell shape in the axial direction in that there is a peak on the plane of measurement and the sensitivity falls rapidly with a pronounced tail further away from the measurement plane, and is similar to those observed by Jossinet using injected current. The sensitivity falls to half height with an axial displacement of

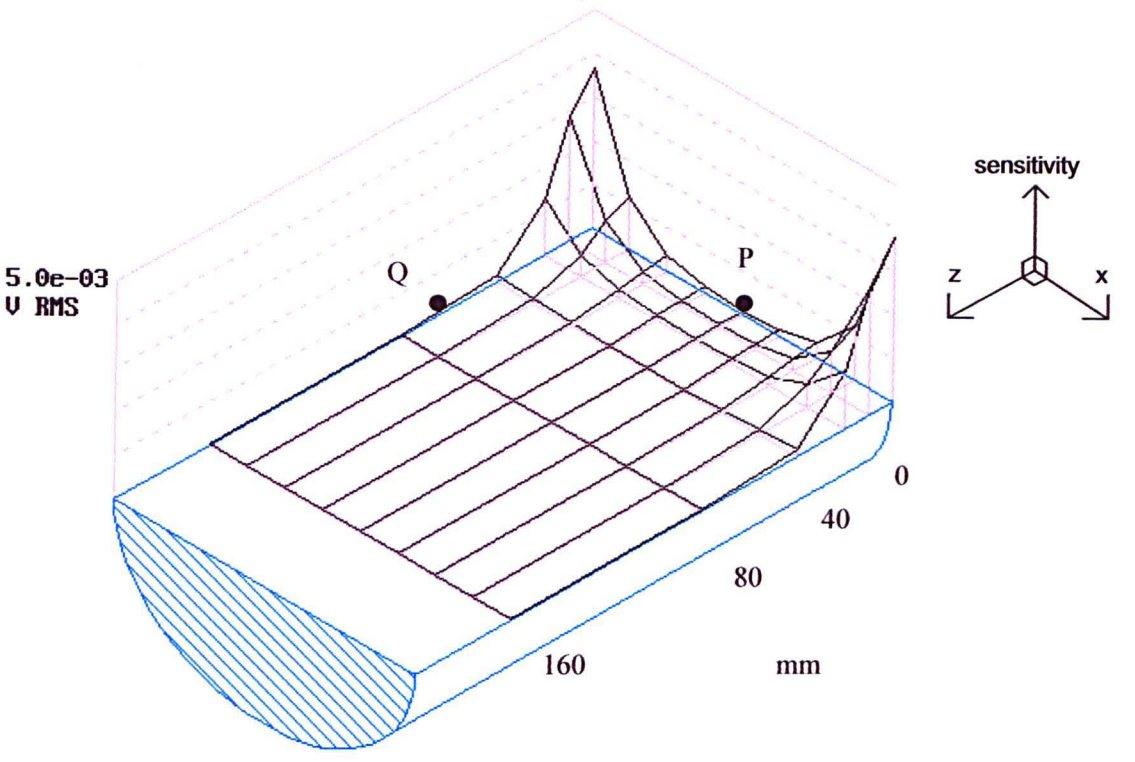

Figure 7.4.3 plot showing the image sensitivity to a small object placed at different locations in a phantom 1m long and of diameter 100 mm. *The image sensitivity is defined as the magnitude of the largest reconstructed pixel.*

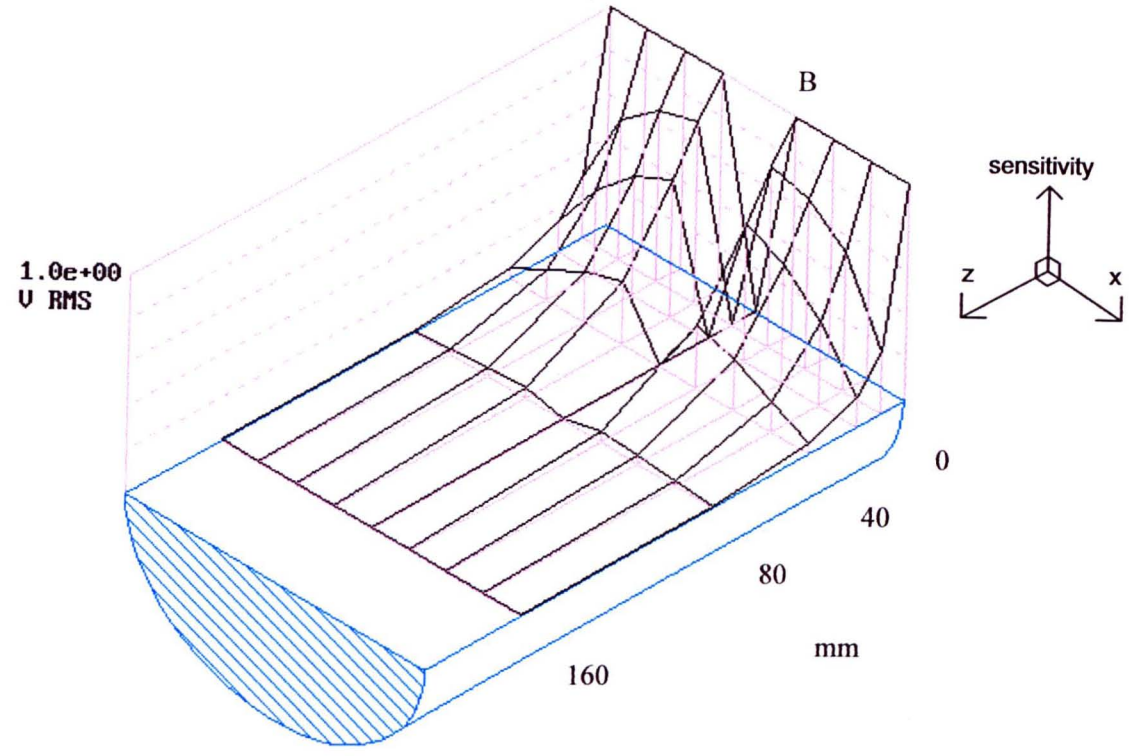

a

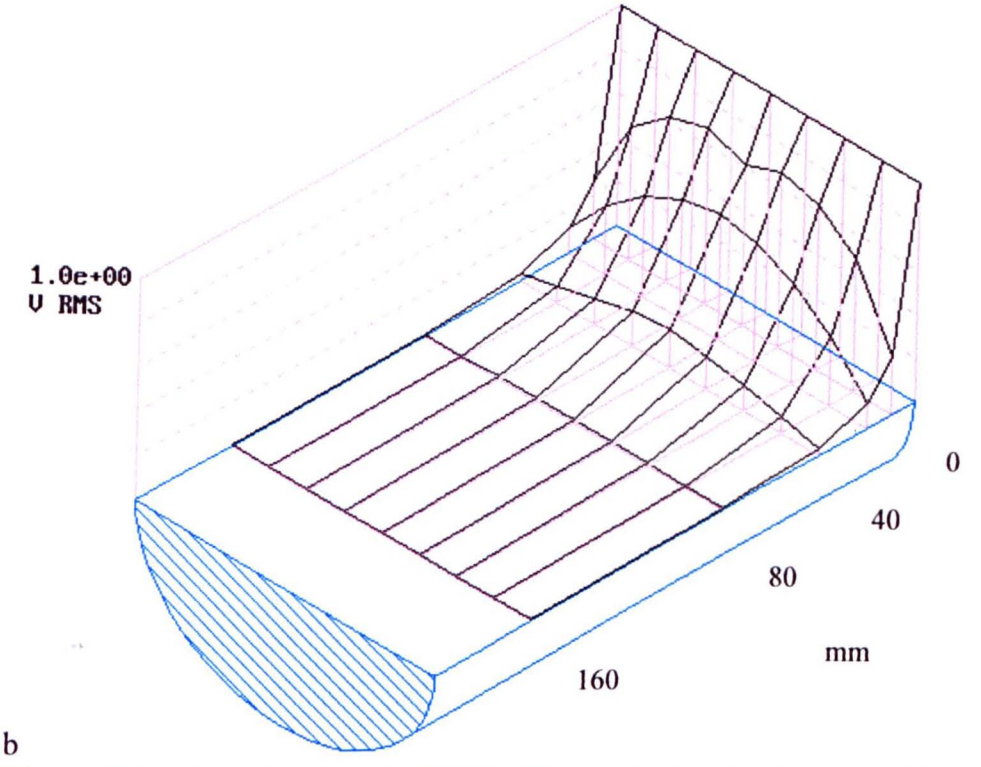

b

Figure 7.4.4 plots showing the RMS of the peripheral voltage profile for a small object placed at different locations in a phantom 1m long. The plots were normalised so that the plane of electrode values are 1. *Figure 7.4.4a shows current excited by a single concentric coil; figure 7.4.4b shows current induced to flow in the 'y' direction; figure 7.4.4c shows current induced to flow in the 'x' direction.*

continued over page

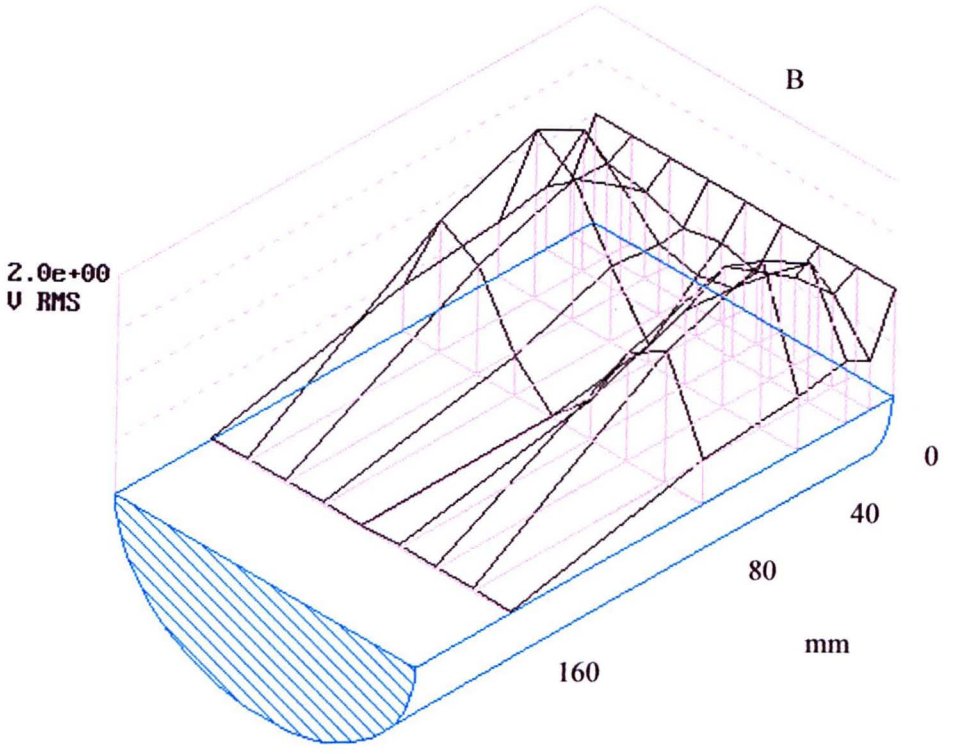

c

Figure 7.4.4 plots showing the RMS of the peripheral voltage profile for a small object placed at different locations in a phantom 1m long. The plots were normalised so that the plane of electrode values are 1. *Figure 7.4.4c shows current induced to flow in the 'x' direction.*

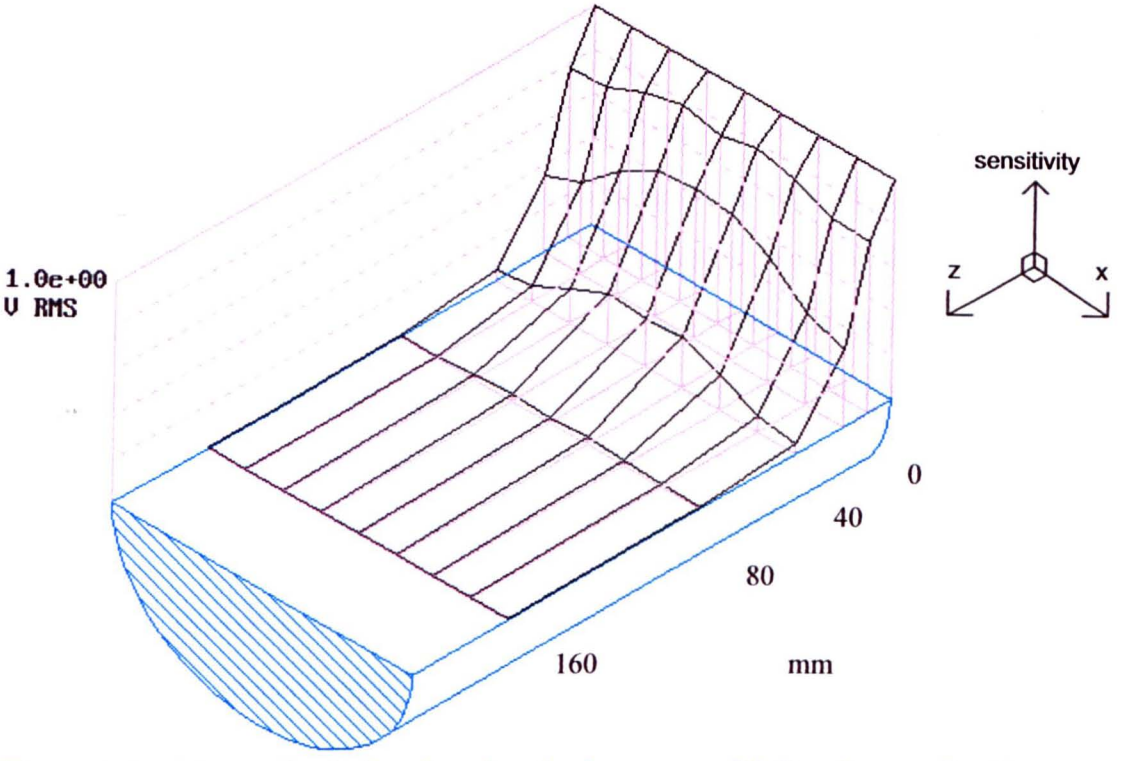

Figure 7.4.5 Normalised plot showing the image sensitivity of a small object placed at different locations in a phantom 1m long. *The plot was normalised so that the plane of electrode values are 1.*

approximately 20 mm giving a half sensitivity width of 0.4 diameters. This is of a similar magnitude to that of the injected current system. These graphs could, with a considerable cost in time, be recalculated using more points, a finer mesh and shorter targets to get a better estimate of the half sensitivity width but these preliminary results do suggest that a 3-D system using induced current will show similar behaviour to that of the injected current system.

7.5 Methods to improve the axial resolution for the system

It has been shown that the induced current system shows similar sensitivity to out of plane structures as the injected current system. Some methods that could be employed to improve the axial resolution are now discussed.

The graphs in figures 7.4.2a, b and c have shown that the peripheral voltage profiles are sensitive to structures out of the plane of measurement and some of the possible coil drive configurations are much more sensitive to out of plane targets. None of the coil drive configurations show a good sensitivity near to the centre on the plane of interest, associated with a sensitivity which falls rapidly away from the plane of measurement. By using only coil weightings which are less sensitive to structures out of the plane of measurement, it is possible that a back projection algorithm could have low sensitivity to out of the plane of structures, but such an algorithm could not use current paths which efficiently interrogate structures within the plane of measurement. This would almost certainly compromise the already limited resolution of the algorithm and therefore no attempt has been made to find an algorithm with low off-plane sensitivity.

The results shown in figures 7.4.4 and 7.4.5 are for the coil configuration used by Purvis *et al* [9]. Anderson[42] is developing an imaging system which uses a number of small coils placed externally to the phantom. This allows greater flexibility for the possible induced current paths and also a greater number of independent measurements. Investigations are required to find out whether the current induced to flow by these

Investigations are required to find out whether the current induced to flow by these coils in 3-D systems would be suitable for image reconstruction. It is possible, but by no means confirmed, that because the fields induced by these coils will decrease away from the plane of measurement more rapidly than for the encircling coils considered so far, that the sensitivity will fall more rapidly as structures move away from the plane of measurement. It is also possible to argue that this system will be no better that the system using the encircling larger coils because the inducing electric field falls more rapidly with displacement from the plane of measurement and therefore a large axial current will be induced.

Other techniques to increase the axial resolution of the system could involve obtaining measurements about structures in planes other than the current plane of measurement. There are several techniques that could be employed to obtain information about regions other than that of the plane of interest. These include:-

- more than one set of coils displaced axially from each other (figure 7.5.1a);
- coils at different orientations (figure 7.5.1b);
- extra layers of electrodes(figure 7.5.1c);
- combinations of the above.

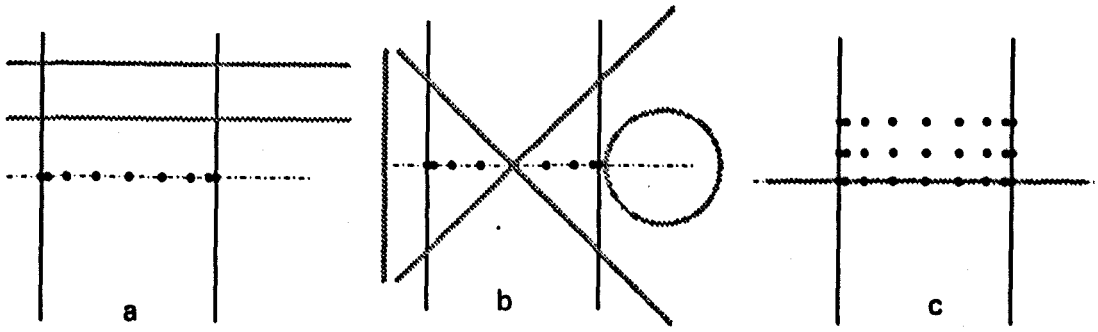

Figure 7.5.1 showing possible arrangements of coils and electrodes
The coils are shown in grey and the electrodes as black dots

From the perspective of the hardware implementation, extra coils would be more attractive as it is easier to add a coil and drive, than to add electrodes with all the associated cables and sense electronics. In medical imaging systems it would be preferable to keep the number of electrodes as small as possible because of the

difficulties of placing large numbers of electrodes. Electrode placement schemes which use belts of electrodes have been investigated [43] in order to ease the placement of large number of electrodes but it becomes difficult to use very many rows of electrodes because the human body is not regular in shape. In an injected current system the only possible way of making the system sensitive to different axial layers would be to add extra electrodes acting as either current injection or potential sense or both. The only one of these possible methods to be investigated further was that using axially displaced coils and this is discussed in the next section

7.5.1 Axially displaced coils

A multi-coiled approach would alter the current paths and would increase the sensitivity of the algorithm to structures away from the plane of the electrodes and so provide voltage profiles which contain information about out of plane structures. There would therefore be advantage to be gained by constructing a system which could obtain information about layers other than that where the electrodes were placed. This was investigated by FEM using coils out of the plane of the electrodes in the same way as the simulation which produced the results shown in figures 7.4.4a, b and c. Figures 7.5.2 and 7.5.3 show the effect of different axial coil positions. Figure 7.5.2a, b and c shows the situation where the current is induced to flow in the y direction and figure 7.5.3a, b and c in the x direction. When the coils are displaced by 50 mm, corresponding to a displacement of a full radius of the phantom, the peak sensitivity moved to a position approximately 20 mm from the plane of measurement. When the coils are moved further away from the plane of measurement, the sensitivity has two peaks, one on the plane of measurement and the other on the plane of the coils. The peak at the plane of the measurement is much larger than the one on the plane of the coils. As the coils are moved a long way from the plane of the electrodes the displaced sensitivity peak falls. Consequently it would be difficult to take measurements a long way from the electrodes using the multi-coil technique but it would be possible to gain information from a set of planes close to the measuring electrodes.

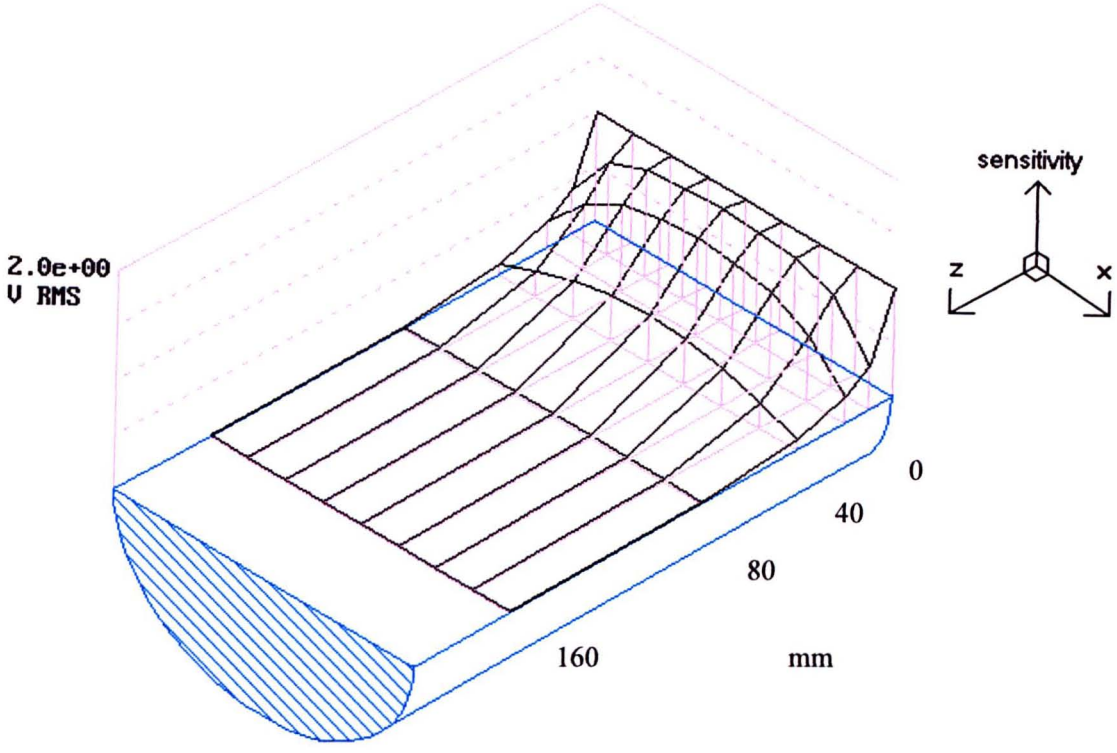

a

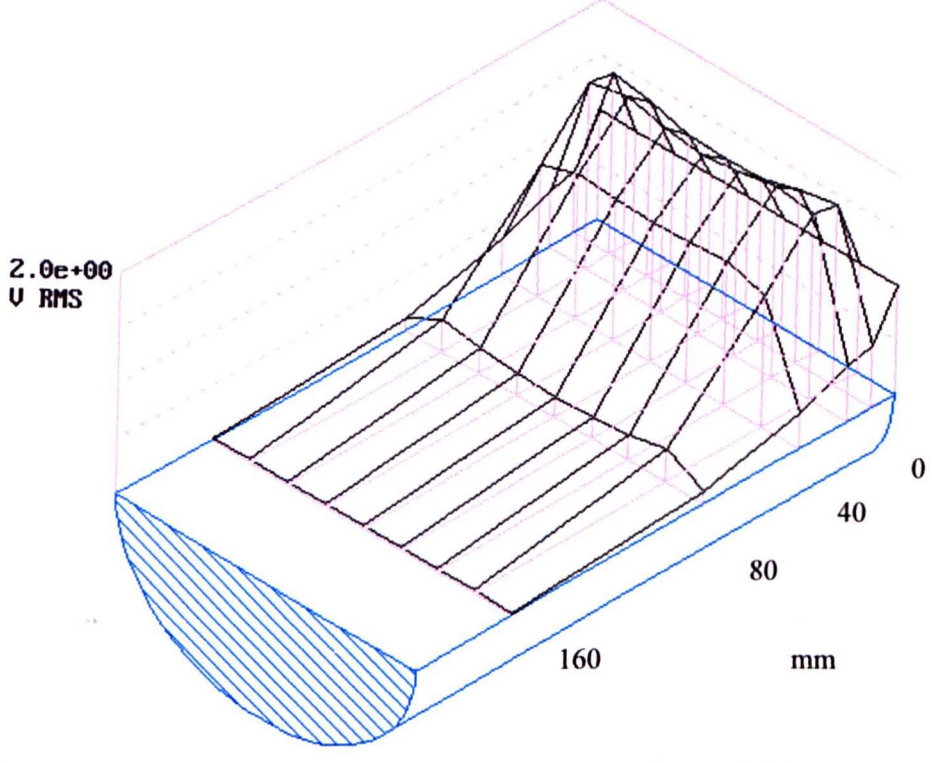

b

Figure 7.5.2 Normalised plots showing the system's sensitivity to a small object placed at different locations in the phantom when the coils are axially displaced. The coils are excited such as to induce the current to flow in the x direction in the plane of the coils. Figures 7.5.2a, b and c show the sensitivity for the coils displaced by 25 mm, 50 mm and 100 mm respectively. *The sensitivity is defined as the RMS of the voltage profile measured at z = 0.*

continued over page

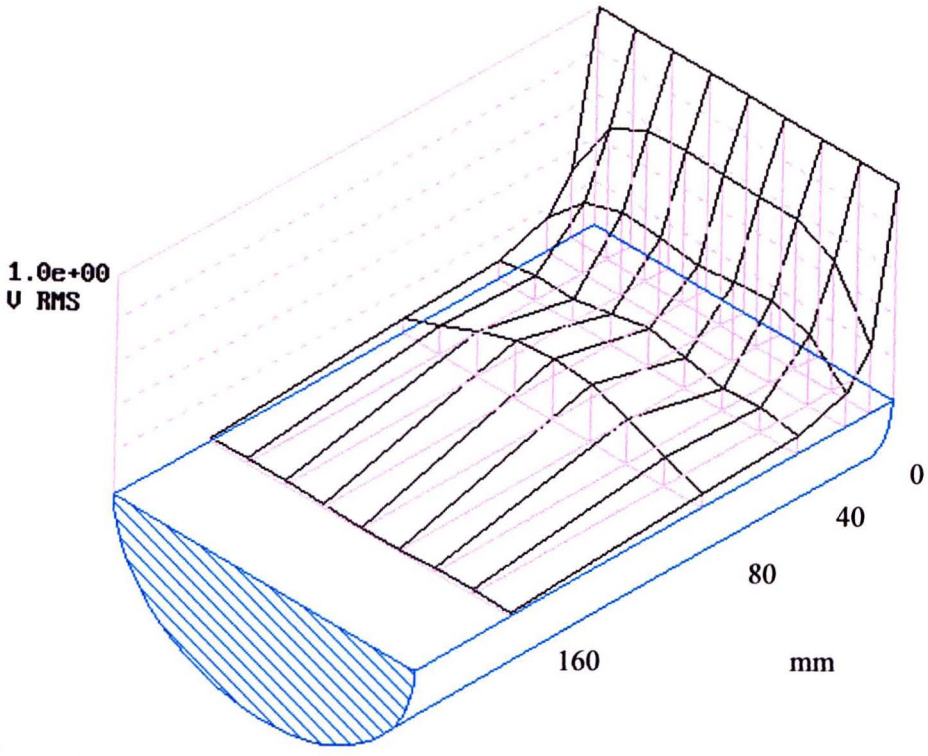

c..

Figure 7.5.2 Normalised plots showing the system's sensitivity to a small object placed at different locations in the phantom when the coils are axially displaced. The coils are excited such as to induce the current to flow in the x direction in the plane of the coils. Figure 7.5.2c shows the sensitivity for the coils displaced by 100 mm. *The sensitivity is defined as the RMS of the voltage profile measured at* $z = 0$.

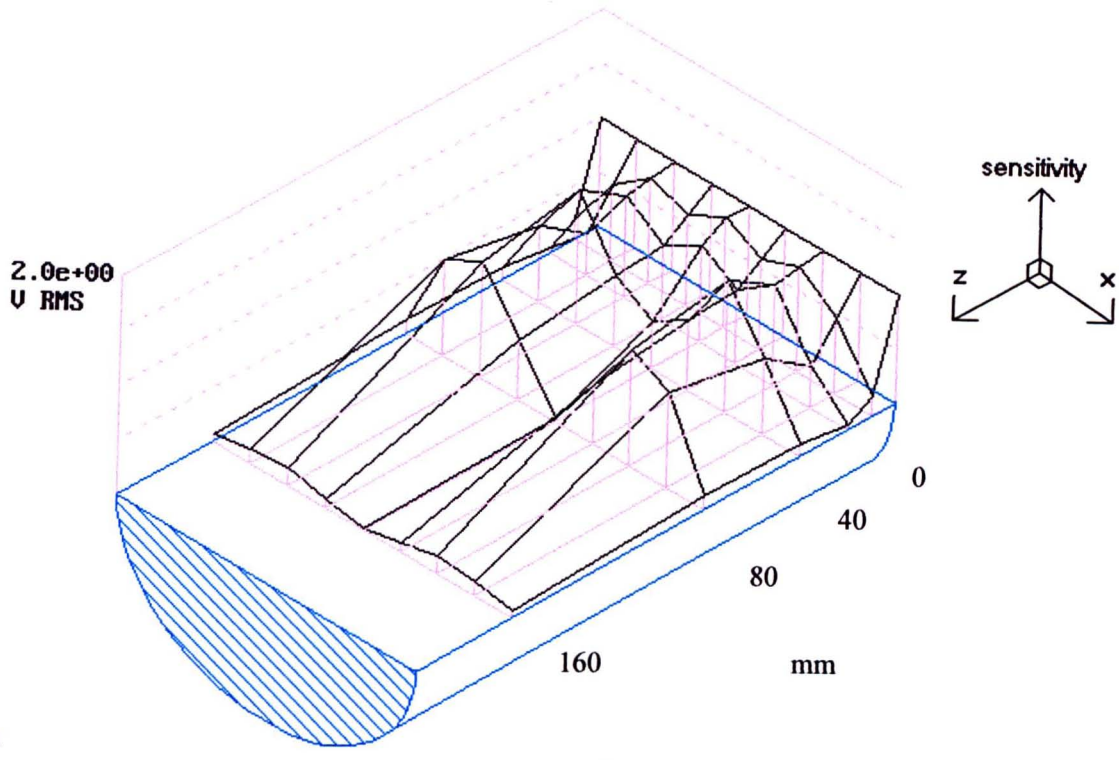

a

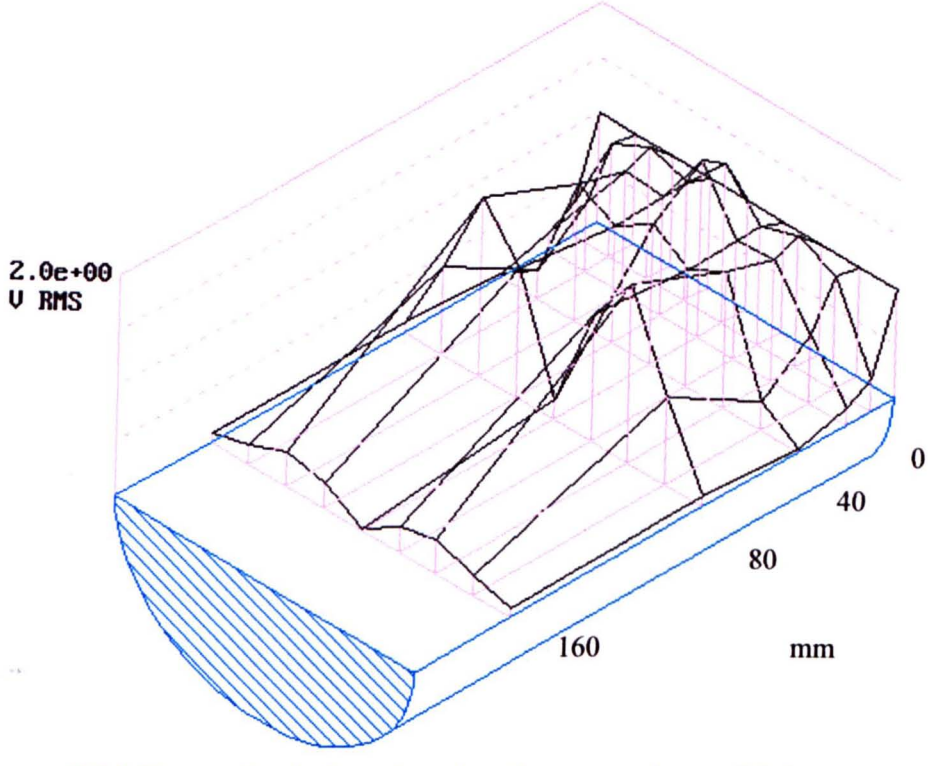

b

Figure 7.5.3 Normalised plots showing the system's sensitivity to a small object placed at different locations in the phantom when the coils are axially displaced. The coils are excited such as to induce the current to flow in the y direction in the plane of the coils. Figures 7.5.3a, b and c show the sensitivity for the coils displaced by 25 mm, 50 mm and 100 mm respectively. *The sensitivity is defined as the RMS of the voltage profile measured at z = 0.*

continued over page

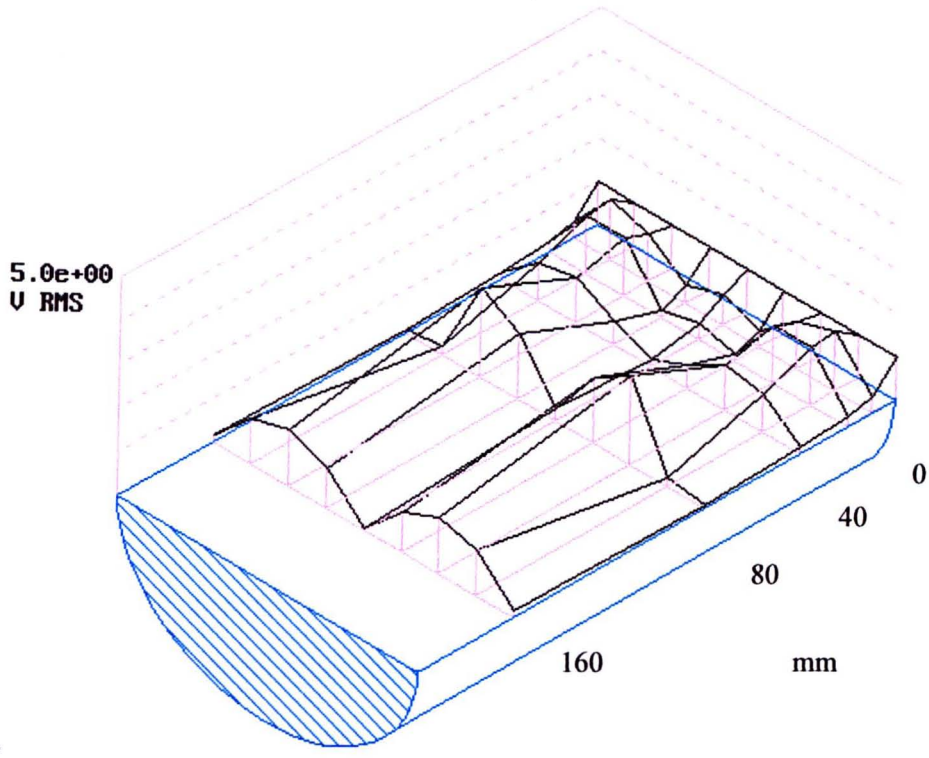

c..

Figure 7.5.3 Normalised plots showing the system's sensitivity to a small object placed at different locations in the phantom when the coils are axially displaced. The coils are excited such as to induce the current to flow in the y direction in the plane of the coils. Figure 7.5.3c shows the sensitivity for the coils displaced by 100 mm. *The sensitivity is defined as the RMS of the voltage profile measured at* $z = 0$.

7.5.2 Techniques used to improve the layer selectivity of the injected current system

A literature search has revealed only a small number of attempts to improve the plane selectivity of impedance imaging systems mainly using injected currents, Guardo *et al* [44] has used 3 layers of electrodes in an injected current system. The top layer was used as current sources, the middle layer senses the potentials, and the bottom layer sinks the current. Guardo's results appear to show that this arrangement gave a small improvement reducing the half sensitivity width to approximately 0.3 diameters compared with Jossinet's 0.4. It would appear that no attempt was made to obtain or use information from other planes. This could perhaps have been achieved using a similar system to Guardo but by exciting a single plane and taking measurements from the middle plane. This arrangement where the excitation plane is distinct from the measurement plane is conceptually very similar to the induced current system where the coils were displaced from the measurement plane.

These results show that it is possible to obtain information from other planes than the plane of measurement but as yet no attempt has been made to use this information to reconstruct either 2-D images with improved axial resolution or 3-D images. It appears that the problem of improving the plane selectivity of the reconstruction algorithm is similar for both the injected and induced current systems. A number of papers have been published on the subject of solving the forward problem for 3-D systems but very few address the task of reconstructing images from 3-D systems, although Morucci[45] has suggested a method.

7.5.3 Direct sensitivity method to reconstruct 3-D images

In an earlier paper by Morucci[46] used a method based on a direct sensitivity matrix. The coefficients of the matrix are defined as the conductivity change for each pixel

divided by the resulting voltage change. This method can be applied to a 2-D or a 3-D system. By solving the forward problem for conductivity discontinuities placed at the location of each pixel or voxel, Morucci finds the coefficients of the reconstruction matrix. The method used to solve the forward problem is the boundary element method but it should be possible to use the FEM to solve the forward problem.

Reconstruction techniques based on direct sensitivity matrices will be computationally expensive but not prohibitively so. In generating the filter described in chapter 6, about 5 days of processing using an I860 accelerator in a PC were required to generate a sensitivity matrix for a 3-D phantom assuming a uniform third dimension. If the solution was repeated for many layers, the computation time would increase rapidly. Once the reconstruction matrix has been found the image generation is relatively fast, as it only requires $P \cdot (E-1) \cdot C$ multiplications, where P is the number of pixels, E is the number of electrodes and C is the number of coils. For a three layered image using 9 coils this would require less than 100 000 multiplications. This reconstruction could be implemented in real time using a single high speed processor.

7.5.4 Modified reconstruction algorithm to generate multi layered images

Another technique to reconstruct 3-D images could be based on a modified version of the current reconstruction algorithm. Even if the current patterns were the same in the coil plane and in the plane of peak sensitivity, the isopotential surfaces are curved in the axial direction. Consequently in moving the electrodes axially from the plane of the coils, it would be necessary to recalculate the position of the isopotential surfaces in the measuring plane. It might be possible to pass the data through a filter that could compensate for the distortion of the potentials and therefore reconstruct images using the same algorithm but operating on filtered data. A further difficulty is that the peak in the sensitivity is not in the plane of the coils so that a modified algorithm would be required derived from the current pattern at the plane of maximum sensitivity.

If this separated layer approach was used, each of the reconstructed layers would be contaminated by structures in the other layers. The problem could be alleviated by adding weighted versions of the other layers to each layer. This is a similar process to backprojection.

7.6 Conclusions

In this chapter the sensitivity of the induced current system to objects out of the plane of measurement has been investigated in detail and it has been shown that the sensitivity is similar to that of the injected current system. It has been shown that with the induced current system the position of peak sensitivity can be moved from the plane of electrodes by moving the coils. This could be advantageous because it means that many layers of information can be recorded from one layer of electrodes by simply moving the coils. This suggests that an induced current system would have advantages over injected current systems because the only way in which an injected current system can separate information about structures out of the plane from those in the plane of measurement is by adding electrodes on different planes. These electrodes could either be current injection or potential sensing or both. With this extra information it should be possible to improve the plane selectivity for the system and produce multi-layered images. A drawback to this method in medical applications is that it would require attaching many more electrodes to the patient.

Chapter 8 Conclusions

8.1 Summary

This study of three dimensional effects in induced current impedance imaging leads to three main conclusions.

A. The most important conclusion is that induced current impedance imaging can be used to reconstruct images from measurements taken from a 3-D body. There is however a major problem associated with image formation in 3-D bodies. The induced current pattern will only approach the state of length invariance if the body is either long or short. For the cylindrical geometries considered, if the length of the body is greater than two diameters, the path of the currents becomes decreasingly length dependent and so the body can be considered long. Under these conditions a 3-D reconstruction algorithm has been devised. For bodies shorter than 0.2 diameters, the induced current patterns become decreasingly length dependent and the body can be considered short. This situation approaches the familiar 2-D case for which reconstruction algorithms exist. Providing the appropriate reconstruction algorithm is used, reconstructed images from both 2-D and 3-D subjects are of a similar quality.

When the body to be investigated is neither long nor short, one of the above criteria, it is still possible to devise reconstruction algorithms, although the performance of such algorithms is critically dependent on the exact axial nature of the body and in principle, each different body requires a separate algorithm. Under these conditions currents in the vicinity of the centre are very small, and the sensitivity to objects at the centre will be poor.

B. It has been demonstrated that a filter based on a sensitivity matrix can be successfully used to enhance the quality of images generated by the 3-D reconstruction algorithm.

C. The sensitivity of the system to out of plane structures has been investigated, and it has been found that the sensitivity of the system falls by a half when structures are displaced by approximately 0.2 diameters from the plane of measurement. It was found that the peak sensitivity for the system could be moved away from the plane of measurement by displacing the plane of the coils from the plane of measurement. This behaviour could possibly be used to obtain 3-D information simply by moving the plane of the coils. It may be possible to use this information to reconstruct 3-D images or to improve the plane selectivity of the system.

8.2 Future work

For bodies which approach a spherical shape, it has been found that induced current patterns generated will have no radial components, but even without radial components of current it may be possible to generate images. These images would be characterised by low centre sensitivity but with good peripheral sensitivity and resolution. A body where this system may be important is the head, which can be regarded as approximately spherical.

Now that the nature of the 3-D problem has been investigated, and to some extent understood, it should be possible to adapt a variety of reconstruction approaches for both 2-D and 3-D. Bouallouche[40] has produced some remarkably good images of 2-D bodies by exciting only one coil. By using the measurements made, it was possible to infer the results of other arbitrary current patterns. Work is required in order to adapt this method so that it can reconstruct images from 3-D bodies. The quality of the images reproduced from only 15 measurements leads to the conclusion that it may be

possible to use a single coil to excite a structure such as the head, and although only inducing circumferential currents, images of reasonable quality may be generated.

Scaife[15] used both real and imaginary measurements to reconstruct permittivity as well as conductivity images. The present reconstruction algorithm will require some modification to reconstruct conductivity and permittivity. The FEM would require major modifications to be capable of modelling both conductivity and permittivity distributions.

The filters developed in chapter 6 significantly improved the quality of the reconstructed images, but neither the filtered nor the unfiltered algorithms are capable of accurately reconstructing images from regions consisting of large areas of alien conductivity. A sensitivity matrix could be found which was based on large area changes in conductivity and this could be used to produce a reconstruction algorithm which would accurately reconstruct images from such conductivity distributions.

References

[1] Henderson R. P. and Webster J. G., "An impedance camera for spatially specific measurements of the thorax," IEEE Trans. Biomed. Eng., BME-25, May 1978, Vol. 3, 250-4.

[2] Brown B. H. and Barber D. C., "Applied potential tomography - a new *in-vivo* medical imaging technique," Proc. Hospital Physicists Annual Conf., Sheffield 1982, Clin. Phys. Physiol. Meas., Vol. 4(1).

[3] Brown B. H Private communication 1995.

[4] Leathard A. D., Brown B. H., Campbell J., Zhang F., Morice A. H. and Tayler. D., "A comparison of ventilatory and cardiac related changes in EIT images of normal human lungs and of lungs with pulmonary emboli," Physiol. meas., 1994, Vol. 15, suppl. A, 137-46.

[5]Erol R. A., Smallwood R. H., Brown B. H., Cherian P. and Bradham K. D., "Measuring oesophageal changes using electrical impedance topography," To be published in Clin. Phys. Physiol. Meas., paper presented at meeting of C.A.I.T, Ankara, 1994

[6] Boone K. and Holder D. S., "A prototype EIT system for imaging action-potential in the brain," To be published in Clin. Phys. Physiol. Meas., paper presented at meeting of C.A.I.T, Ankara, 1994

[7] Osyppka M. and Gersing E., "Problems involved in temperature measurements using EIT," To be published in Clin. Phys. Physiol. Meas., paper presented at meeting of C.A.I.T, Ankara, 1994

[8] Newell J. C., Isaacson D., Saulnier G. J., Cheney M. and Gisser D. G., "Quantitative assessment of pulmonary edema by impedance imaging," To be published in Clin. Phys. Physiol. Meas., paper presented at meeting of C.A.I.T, Ankara, 1994

[9] Purvis W. R., Tozer R. C., Anderson D. K. and Freeston I. L., "Induced current impedance imaging," IEE Proc. - A, March 1993, Vol. 140, No. 2, 135-41.

[10] Dam H. J. W., McClure's Magazine, Jan. 1896.

[11] Haar G. R., "Ultrasound: considerations for its safe and appropriate use," Proc. of the British Med. Ultrasound Soc., British Journal of Radiology, 1987, Vol. 60, No. 714, 612.

[12] Barber D. C. and Brown B. H., "Applied potential tomography," J. Phys. E:Sci. Instrum., 1984, Vol. 17, 723-33.

[13] Record P. M., "Single-plane multi-frequency electrical impedance instrumentation," Physiol. meas., 1994, Vol. 15, suppl. A, 29-35.

[14] Griffths H. and Zhang Z., "A dual-frequency electrical impedance tomography system," Phys. Med. Biol., 1989, Vol. 34, No. 10, 1465-76.

[15] Scaife J. M., Tozer R. C. and Freeston I. L., "Conductivity and permittivity images from an induced current electrical impedance tomography system," Meas. Sci. Technol., Vol. 141, No. 5, Sept. 1994, 356-62

[16] Barber C. C.*, Brown B. H. and Freeston I. L. "Imaging spatial distributions of resistivity using applied potential tomography," Electronics Letters, Oct. 1983, Vol. 19, No. 22.

[17] Purvis W. R., "Impedance imaging using induced currents," PhD thesis, University of Sheffield, Dec. 1990.

[18] Avis N. J. and Barber D. C., "Image reconstruction using non-adjacent drive configurations," Clin. Phys. Physiol. Meas., May 1994, Vol. 15, suppl. 2A, A153-60.

[19] Pidcock M. K., Kuzuoglu M. and Leblebicioglu K., "Analytical and semi-analytical solutions in electrical impedance tomography I: two dimensional problems," Nov. 1994, submitted to Physiol. Meas.

[20] Pidcock M. K., Kuzuoglu M. and Leblebicioglu K., "Analytical and semi-analytical solutions in electrical impedance tomography II: three dimensional problems," Nov. 1994, submitted to Physiol. Meas.

[21] Anderson D. K., Tozer R. C. and Freeston I. L., "An analytic solution of the forward problem for the electrical impedance tomography systems," 1994, submitted to IEE Proc. A.

[22] Silvester P. P. and Ferrari R. L., "Finite Elements For Electrical Engineers," Cambridge University press, 2nd ed., 1990.

[23]Scaife J. M., Private communication.

[24] Low W. F., "The computation of magnetostatic fields in permanent magnet devices" PhD thesis, University of Sheffield, Dec. 1985.

[25] Scaife J. M., "A technique for obtaining conductivity and permittivity images using induced current electrical impedance tomography," PhD thesis, University of Sheffield, Dec. 1991.

[26] Brown B. H. and Seagar A. D., "The Sheffield data collection system," Clin. Phys. Physiol. Meas., 1987, Vol. 8, suppl. A, 91-7.

* The name Barber C. C was mistakenly published in place of Barber D. C.

[27] Tozer R. C., "A low input capacitance sense amplifier for impedance imaging applications," Meas. Sci. Technol., No. 3, 1992, 508-14.

[28] Scaife J. M., Private communication.

[29] Integrated Circuits Data Book, Siliconix, 1990, Ch. 6, 20-30.

[30] Special Purpose Linear Devices Data Book, National Semiconductors, 1989, Ch. 5, 37.

[31] Davies E. R., "Electronics, noise and signal recovery," Academic Press, 151-4.

[32] Mohd-Zainon S., "Design of a surface mount sense amplifier for impedance imaging systems," Bachelor of Engineering thesis, University of Sheffield, 1992.

[33] Press W. H., Teukolsky S. A., Vetterling W. T. and Flannery B. P., "Numerical Recipes in C - The Art of Scientific Computing," Cambridge University Press, Second Ed., 1992.

[34] Hewlett Packard, "3577A Network Analyser - Operating Manual," 1983.

[35] Healey T. J., Tozer R. C. and Freeston I. L., "Impedance imaging of 3-D objects using magnetically induced currents," Proc. 14th Ann. Int. Conf., IEEE EMBS, Paris, 1992, 1719-20,

[36] Barber D. C. and Brown B. H., "Recent developments in applied potential tomography - APT,"Bacharach S. L. (Ed.), "Information Processing in Medical Imaging," Martinus Nijhoff, Dordrecht, 1986, 106-21.

[37] Branston N. M. and Tofts P. S., "Analysis of the distribution of currents induced by a changing magnetic field in a volume conductor," Phys. Med. Biol., 1991, Vol. 36, No. 2, 161-8.

[38] Seagar A. D., Barber D. C. and Brown B. H., "Theoretical limits to sensitivity and resolution in impedance images," Clin. Phys. Physiol. Meas., 1987, Vol. 8, suppl. A, 13-31.

[39] Barber D. C. and Seagar A. D., "Fast reconstrution of resistance images," Clin. Phys. Physiol. Meas., 1987, Vol. 8, suppl. A, 47-54.

[40] Bouallouche A., Private communication.

[41] Jossinet J. and Kardous G., "Physical study of the sensitivity distribution within multi-electrode systems," Clin. Phys. Physiol. Meas., 1987, Vol. 8, suppl. A, 33-7.

[42] Anderson D. K., PhD thesis, to be published.

[43] McAdams E. T., McLaughlin J. A. and McC Anderson J., "Multi-electrode system for electrical impedance tomography," Clin. Phys. Physiol. Meas., May 1994, Vol. 15, suppl. 2A, A101-6.

[44] Guardo R., Boulay C., Murray B. and Bertrand M., "Experimental evaluation of image plane selectivity in electrical impedance tomography," Proc. 11th Ann. Int. Conf., IEEE EMBS, Seattle, 1989, 468-9.

[45] Morucci J. P., Granié M., Lei M. and Chabert M., "Direct sensitivity matrix approach for fast 3-D reconstruction in electrical impedance tomography," To be published in Clin. Phys. Physiol. Meas., paper presented at meeting of C.A.I.T, Ankara, 1994

[46] Morucci J. P., Marsili P.M., Granié M., Shi Y., Lei M. and Dai W. W., "Direct sensitivity matrix approach for fast reconstruction in electrical impedance tomography," Clin. Phys. Physiol. Meas., May 1994, Vol. 15, suppl. 2A, A107-14.

[47] Seagar A. D., "Probing with low frequency electric current," PhD thesis, University of Canterbury, Christchurch, New Zealand, 1983

Appendix 1 The effect of channel mismatch on cmrr

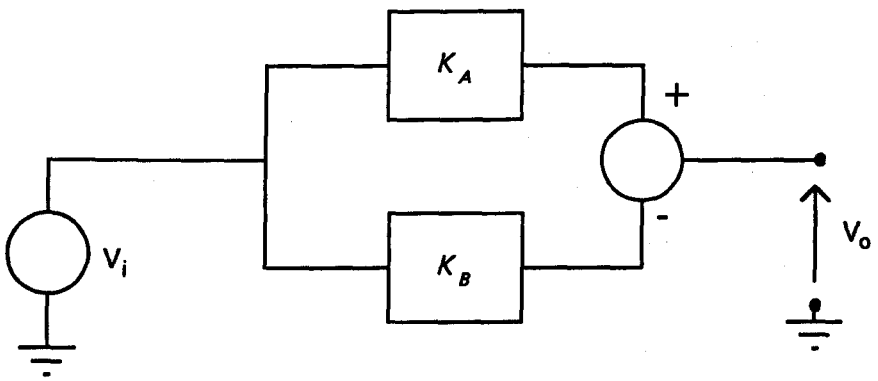

Figure A.1.1. A diagram which represents a system with two channels A and B with two gains K_A and K_B

The output V_o can be found in terms of the input V_i and the two gains

$$V_o = V_i(K_A - K_B) \qquad \text{a.1.1}$$

For a useful system the gains of the channel must be well matched and therefore

$$K_A \approx K_B = K \qquad \text{a.1.2}$$

The cmrr is defined as the differential mode gain divided by the common mode gain. Thus

$$\text{cmrr} = 20 \cdot \lg \frac{|K_A - K_B|}{K} \qquad \text{a.1.3}$$

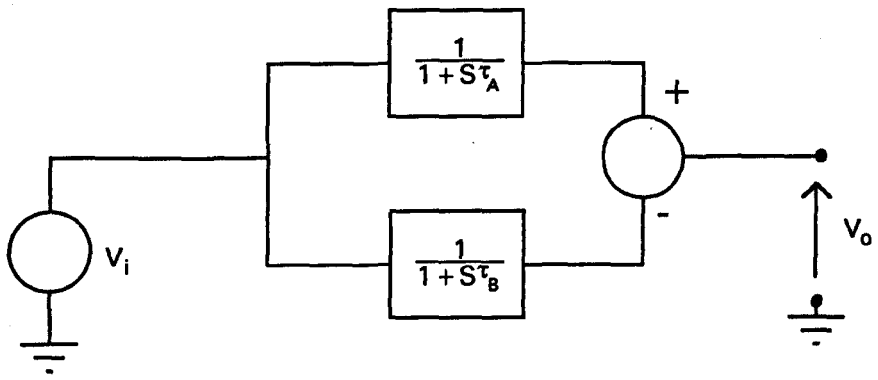

Figure A.1.2. A diagram which represents a system with two channels A and B with two time constants τ_A and τ_B.

If two channels A and B are not perfectly matched then there will be an output V_o

$$V_o = V_i\left(\frac{1}{1+S\tau_A} - \frac{1}{1+S\tau_B}\right) \qquad \text{a.1.4}$$

or

$$V_o = V_i\left(\frac{(1+S\tau_B)-(1+S\tau_A)}{(1+S\tau_A)(1+S\tau_B)}\right) \qquad \text{a.1.5}$$

if the two channels are reasonably matched then

$$\tau_A \approx \tau_B = \tau \qquad \text{a.1.6}$$

then

$$V_o = V_i\left(\frac{S(\tau_B - \tau_A)}{(1+S\tau)^2}\right) \qquad \text{a.1.7}$$

over the useful frequency response of the circuit

$$1 >> S\tau \qquad \text{a.1.8}$$

then the approximation can be made that

$$V_0 \approx V_i S(\tau_B - \tau_A) \qquad \text{a.1.9}$$

The differential gain of the circuit is approximately 1 and therefore the cmrr at a frequency f Hz can be approximated by

$$\text{cmrr} = 20 \cdot \lg\left|2\pi f(\tau_B - \tau_A)\right| \text{ dB} \qquad \text{a.1.8}$$

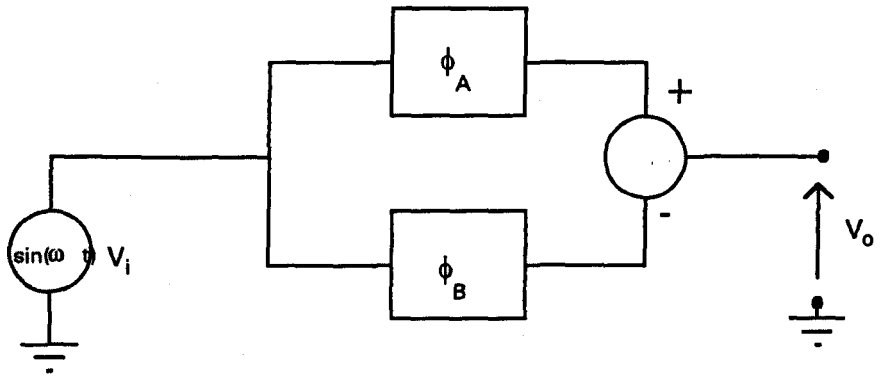

Figure A.1.3. A diagram which represents a system with two channels A and B phase shifts ϕ_A and ϕ_B

$$V_o = V_i\left(\sin(\omega t+\phi_A)-\sin(\omega t+\phi_B)\right) \qquad \text{a.1.10}$$

by trigonometry

$$V_o = V_i\left(2\sin(\frac{\phi_A-\phi_B}{2})\cdot\sin(\frac{2\omega t+\phi_A+\phi_B}{2})\right) \qquad \text{a.1.11}$$

$$V_o = V_i\left(2\sin(\frac{\phi_A-\phi_B}{2})\cdot\sin(\omega t+\phi)\right) \qquad \text{a.1.12}$$

where

$$\phi = \frac{\phi_A+\phi_B}{2} \qquad \text{a.1.13}$$

for a useful system ϕ_A and ϕ_B are similar and therefore

$$(\phi_A-\phi_B) << 1 \qquad \text{a.1.14}$$

so the approximation can be made

$$V_o \approx V_i\left((\phi_A-\phi_B)\cdot\sin(\omega t+\phi)\right) \qquad \text{a.1.15}$$

or

$$\text{cmrr} \approx 20\cdot\lg\left|\frac{\pi(\theta_A-\theta_B)}{180}\right| \qquad \text{a.1.16}$$

Where θ_A and θ_B are the phase shifts in degrees.

Appendix 2 Image reconstruction

The method used by Purvis *et al* [9] to reconstruct the images involves examination of the peripheral voltage gradient caused by an alien pixel in an otherwise homogeneous background. The plane containing the coils was divided up into 30 x 30 pixels but only the pixels which fall in the circular target region were considered. Each pixel in turn is assumed to be the only conductivity discontinuity in the target area. Figure A.2.1 shows a conductivity discontinuity at a pixel P. This pixel interacts with the induced current to behave as a current dipole oriented in the same direction as induced current. The dipole is then viewed as the only source in the target area. A model of this dipole can then be made. The target region is represented by the complex plane Z and a dipole P placed at the centre of the circular bounded region. The potential at any point in the region is given by

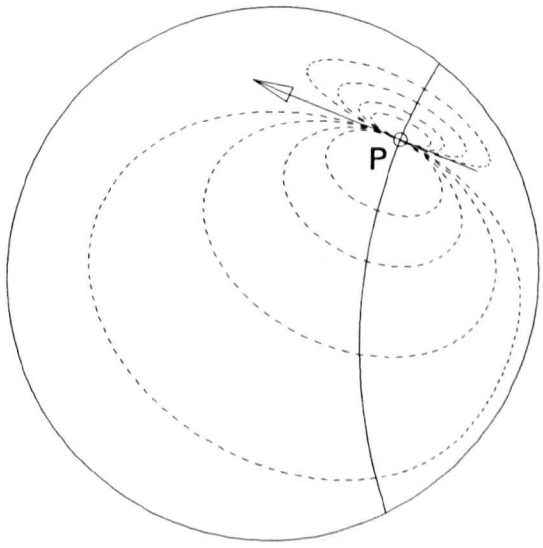

Figure A.2.1 An alien pixel at P generates a dipole in the same direction as the incident induced current, indicated by the arrow. The dashed line represent the current paths and the solid lines represent the normal equipotentials.

$$U = Az\left(1+\frac{R^2}{|z|^2}\right) \qquad \text{A.1}$$

where

$$z = r\cos(\theta-\beta)+jr\sin(\theta-\beta) \qquad \text{A.2}$$

and A is a constant, R is the target region radius, r is the radial position of the point z and θ and β are the angular direction of z and the dipole at P, respectively.

$$w = \frac{\frac{R^2}{d}(z-d)}{z-\frac{R^2}{d}} \qquad \text{A.3}$$

which is a conformal transformation [47] giving the potential distribution for a dipole placed at any position within the target region.

The solid line of figure A.2.1 shows the path of the equipotential which is normal to the dipole. The image reconstruction process uses the shortest path of the equipotential from the dipole to the boundary. This point on the boundary will show the maximum voltage gradient due to this alien pixel and is therefore the most likely to be affected by a discontinuity at the point P. The process is repeated for each pixel, each with a range of current patterns.

The measuring system has only 16 electrodes which means that the potential gradient is only known at 16 discrete points on the boundary, each half way between the electrodes. Spatial quantisation effects are caused if this crude assignment of peripheral potential gradients is used. Reduction in these quantisation effects can be facilitated by making better use of the available information. It is reasonable to assume that voltage profiles contain no useful information above the spatial Nyquist frequency that is implied by the spacing of the electrodes. The estimate of the potential gradient, made by directly subtracting the voltages at each electrode pair to obtain the potential gradient at the midpoint, can be improved by using a low pass interpolating function.

$$V(\gamma) = \sum_{i=\text{int}\,a-m}^{\text{int}\,a+m} V(i)\frac{\sin \pi(\alpha-i)}{\pi(\alpha-i)} \qquad \text{A.4}$$

where:-

V(i) : i^{th} midpoint voltage gradient estimate

m : half the number of electrode (8 in this case)

α : $m\gamma/\pi$

int α : nearest integer value of α

To accommodate the circularly continuous nature of the data the index i is treated as a modulo 16 number. Using the above function an improved estimate for the gradient can be found at any point on the periphery.

Image reconstruction can now be achieved by integrating the value of the interpolated peripheral voltage gradient corresponding to the boundary position for each of the current patterns for all of the pixels. In practice the current patterns are found by weighting the currents for each coil. Hence only three sets of measurement are required because by superposition the result of any current pattern induced by weighted coil currents can be obtained by weighting the individual profiles obtained by driving each coil individually. Thus to reconstruct the image, three matrixes can be formed, c_1 c_2 and c_3, such that the conductivity σ is given by:

$$\sigma = c_1 u_1 + c_2 u_2 + c_3 u_3 \qquad \text{A.5}$$

where u_1, u_2 and u_3 are the base measure taken for each coil.